

**EXPERIMENTAL ELECTRON DENSITY  
RECONSTRUCTION AND ANALYSIS OF TITANIUM  
DIBORIDE AND BINARY VANADIUM BORIDES**

**DISSERTATION**

zur Erlangung des akademischen Grades

Doktor rerum naturalium

(Dr. rer. nat.)

vorgelegt

der Fakultät Mathematik und Naturwissenschaften

der Technischen Universität Dresden

von

M.S. Bürgehan Terlan

geboren am 16.02.1982 in Istanbul, Türkei

Eingereicht am: 18.02.2013

Die Dissertation wurde in der Zeit von November / 2007 bis Dezember / 2012  
am Max-Planck Institut für Chemische Physik fester Stoffe angefertigt.



Tag der Verteidigung: 17.07.2013

Gutachter: Prof. Juri Grin

Gutachter: Prof. Dr. Michael Ruck





*‘Alles Wissen und alle Vermehrung unseres Wissens endet nicht mit einem  
Schlusspunkt, sondern mit Fragezeichen.’*

HERMANN HESSE



## DANKSAGUNG

Die vorliegende Arbeit wurde unter Betreuung von Prof. Juri Grin und Dr. Horst Borrmann am Max-Planck-Institut für Chemische Physik fester Stoffe angefertigt. An dieser Stelle soll all denjenigen herzlicher Dank ausgesprochen werden, die direkt oder indirekt zum Gelingen dieser Arbeit beigetragen haben.

Als erstes möchte ich mich bei meinem Doktorvater Prof. Juri Grin bedanken, der mir vor allem ein sehr interessantes und anspruchsvolles Thema zur Promotion gab und dazu noch sein Vertrauen in mich gesetzt hat. Seine motivierenden, umfassenden und wertvollen Diskussionen haben einen wichtigen Beitrag zum Zustandekommen dieser Arbeit geleistet.

Ein spezielles Wort des Dankes möchte ich an Dr. Horst Borrmann richten für seine wissenschaftlichen, zielgerichteten Betreuung, ständige Diskussionsbereitschaft und schliesslich für die vielen kleinen und grossen Hilfen, die diese Arbeit erweitert, verbessert und anschaulicher gemacht haben. Seine wertvollen Anregungen und Ratschläge habe ich immer geschätzt.

Mein ganz besonderer Dank gilt ausserdem...

... Prof. Dr. Michael Ruck für die Begutachtung meiner Arbeit.

...Dr. Alexey Baranov für seine freundliche Zusammenarbeit und die theoretischen Berechnungen im Rahmen des DFG-Schwerpunktprogramms SPP 1178 'From the electron density to electron pairing, localizability and chemical bonding'.

...Dr. Lev Akselrud, der mit der Entwicklung des Programms WinCSD für die Strukturverfeinerung den Grundstein für meine Arbeit gelegt hat.

...Dr. Marcus Schmidt für seine Freundlichkeit, methodische Ratschläge und Hilfestellung bei der Durchführung von Experimenten.

...Dr. Miroslav Kohout für die wertvollen Diskussionen über die chemische Bindung.

...Dr. Wilder Carillo-Cabrera für die geduldigen elektronenmikroskopischen Untersuchungen.

...Dr. Ulrich Burkhardt für die mühsamen metallographischen Untersuchungen.

...Dr. Gudrun Auffermann für die chemische Analyse.

...Prof. Dr. Mehmet Somer für seine Hilfe und Motivation vor und während meiner Promotion

...Dr. Umut Aydemir, Ms. Carina Börrnert und Mr. Michael Wedel für die Zusammenarbeit

... Dr. Thorsten Goebel und Dr. Thomas Harmening für NMR Untersuchungen

Des Weiteren möchte ich allen Mitgliedern der Kompetenzgruppe „Struktur“ am MPI CPfS für das angenehme Arbeitsklima danken.

Auch geht mein Dank allen, denen ebenfalls ein Wort des Dankes gebührt und die ich hier lediglich vergessen habe.

Ein weiteres Dankeschön gilt für die Deutsche Forschungsgemeinschaft für die finanzielle Unterstützung meiner Dissertation.

Als letztes gilt ein grosser Dank meinen Eltern und meiner Schwester, die mich moralisch immer unterstützt und mir den Rücken gestärkt haben.

# CONTENTS

<b>Symbols and Abbreviations.....</b>	<b>vii</b>
<b>Chapter 1: Experimental Charge Density: Birth, Evolution and Challenge.....</b>	<b>1</b>
1.1 The study of intermetallic borides.....	5
1.1.1 The interest in vanadium-boron system.....	6
1.1.2 The interest in 3d transition metal diborides .....	7
<b>Chapter 2: Experimental Electron Density Analysis from X-ray Diffraction – The Basics .....</b>	<b>11</b>
2.1 Principles of X-ray diffraction .....	11
2.2 Intensity corrections .....	14
2.2.1 Absorption .....	14
2.2.2 Extinction.....	15
2.2.3 Thermal diffuse scattering .....	18
2.3 Structure refinement .....	20
2.4 The independent atom model (IAM).....	21
2.5 The multipole density formalism .....	22
2.6 Residual density .....	24
2.7 Deformation density (DD) .....	25
2.8 The quantum theory of atoms in molecules (QTAIM).....	26
2.8.1 QTAIM atoms.....	26
2.8.2 Critical points and their classification .....	28
2.8.3 Laplacian .....	31
2.8.4 The ellipticity.....	32
2.8.5 The ratio $ \lambda_1 /\lambda_3$ .....	32
2.8.6 The electronic energy density.....	32
2.8.7 The transferability concept .....	33
2.8.8 The electrical field gradient.....	34
2.9 Quantumchemical calculations.....	35
<b>Chapter 3: Synthesis, Characterization and Crystal Structures of Vanadium Borides.....</b>	<b>37</b>

3.1	Synthesis.....	37
3.1.1	Preparation of vanadium boride crystals by Al flux method .....	41
3.1.2	Preparation of vanadium borides by arc-melting.....	43
3.2	Characterization.....	43
3.2.1	X-ray powder diffraction .....	43
3.2.2	Microstructure analysis.....	50
3.3	High resolution single crystal X-ray diffraction.....	52
3.4	Conventional IAM refinement .....	53
3.4.1	Refinement of crystal structure $\text{VB}_2$ .....	54
3.4.2	Refinement of crystal structures $\text{VB}$ , $\text{V}_3\text{B}_4$ and $\text{V}_2\text{B}_3$ .....	57
3.5	Crystal structures of vanadium borides .....	60
3.5.1	Crystal structure of $\text{VB}_2$ .....	60
3.5.2	Crystal structure of $\text{VB}$ .....	62
3.5.3	Crystal structure of $\text{V}_3\text{B}_4$ .....	64
3.5.4	Crystal structure of $\text{V}_2\text{B}_3$ .....	66
3.6	Similarities between the crystal structures of vanadium borides .....	69
3.7	Summary.....	70
<b>Chapter 4:</b>	<b>Electron Density in <math>\text{VB}_2</math></b> .....	<b>71</b>
4.1	Multipole refinement .....	71
4.2	Topological analysis of the electron density in $\text{VB}_2$ .....	74
4.2.1	The B-B interaction.....	76
4.2.2	The B–V interaction .....	78
4.2.3	Atomic electron populations.....	82
4.3	The electric field gradient.....	82
4.4	Summary on $\text{VB}_2$ .....	84
<b>Chapter 5:</b>	<b>Synthesis, Characterization and Reconstructed Electron Density in <math>\text{TiB}_2</math></b> .....	<b>85</b>
5.1	Synthesis.....	85
5.2	Characterization.....	86
5.3	High-resolution single-crystal X-ray diffraction experiment .....	88
5.4	Conventional IAM refinement .....	88
5.5	Crystal structure of $\text{TiB}_2$ .....	89

5.6	Multipole refinement.....	91
5.7	Topological analysis of the electron density .....	93
5.7.1	The B–B interaction .....	95
5.7.2	The B–Ti interaction.....	97
5.7.3	Atomic electron populations.....	99
5.8	The electric field gradient .....	99
5.9	Summary on TiB <sub>2</sub> .....	100
<b>Chapter 6:</b>	<b>Electron Density in VB.....</b>	<b>101</b>
6.1	Multipole refinement.....	101
6.2	Topological analysis of the electron density .....	104
6.2.1	The B–B interaction.....	106
6.2.2	The B–V interaction .....	108
6.2.3	Atomic electron populations.....	110
6.3	Summary on VB.....	111
<b>Chapter 7:</b>	<b>Electron Density in V<sub>3</sub>B<sub>4</sub> .....</b>	<b>113</b>
7.1	Multipole refinement.....	113
7.2	Topological analysis of the electron density .....	116
7.2.1	The B–B interaction .....	119
7.2.2	The B–V interaction .....	120
7.2.3	Atomic Electron Populations.....	123
7.3	Summary on V <sub>3</sub> B <sub>4</sub> .....	125
<b>Chapter 8:</b>	<b>On Similarities and Differences between the Electronic Structures of TiB<sub>2</sub>, VB<sub>2</sub>, VB and V<sub>3</sub>B<sub>4</sub> .....</b>	<b>127</b>
8.1	The B–B interaction .....	127
8.2	Transition metal-boron interactions .....	130
8.3	Atomic electron populations .....	138
8.4	Summary.....	140
<b>Conclusions and Outlook .....</b>		<b>141</b>
<b>References.....</b>		<b>145</b>





## Symbols and Abbreviations

Å	Angstrom	HREM	high resolution electron microscopy
ADP	anisotropic displacement parameters	<i>i.e.</i>	<i>id est</i> ; that is
bcp	bond critical point	IAM	independent atom model
bp	bond path	MEM	maximum entropy method
ccp	cage critical point	MO	molecular orbital
cp	critical point	NMR	nuclear magnetic resonance
DD	deformation density	NQR	nuclear quadrupole resonance
DFG	Deutsche Forschungsgemeinschaft (German Research Association)	IUCr	International Union of Crystallography
DFT	density functional theory	QTAIM	quantum theory of atoms in molecules
e	electron	rcp	ring critical point
<i>e.g.</i>	<i>exempli gratia</i> ; for example	RDF	radial density function
ED	electron density	SAED	selected area electron diffraction
EDD	electron density distribution	SPP	schwerpunktprogramm (priority program)
EFG	electric field gradient	TDS	thermal diffuse scattering
Eq.	equation	TEM	transmission electron microscope
<i>et al.</i>	<i>et alii</i> ; and others	SEM	scanning electron microscope
FIB	focused ion beam	VSCC	valence shell charge concentration
FWHM	full width half maximum	WDXS	wave dispersive X-ray spectroscopy
HF	Hartree-Fock	XRPD	X-ray powder diffraction







# 1 EXPERIMENTAL CHARGE DENSITY: BIRTH, EVOLUTION AND CHALLENGES

Designing of new materials has been of crucial importance for the mankind since it has directly influenced its destiny throughout the history. The race of experimenting with new materials resulted in opening new eras both during antiquity and our period. The remarkable difference between modern and ancient ages is that the former is much more time compressed. A shortening of this development process can be traced back to a better understanding of the relation between structure and chemical or physical properties of the materials.

The first speculations about material structure and the existence of atoms were recorded by Greek philosophers during ancient times.<sup>[1]</sup> But the beginning of the modern atomic model has found its roots by the hypothesis of Dalton and was later developed by Thomson, Rutherford and Bohr. In 1808 Dalton resurrected the Greek idea of atoms as he claimed that elements are composed of discrete atoms linked by bonds. At that time crystallographers were using optical methods for crystal identification but they had no means by which to measure the atom positions. The real breakthrough was achieved in 1895 with the discovery of X-rays by Wilhelm Röntgen which was set as the beginning of the modern crystallography. In 1912 Laue *et al.*<sup>[2]</sup> proved that X-rays have electromagnetic nature and are diffracted by the crystal lattice due to their wavelength comparable to the atom size. One year later Bragg's equation<sup>[3]</sup> was derived by W. H. Bragg and his son W. L. Bragg which enables the absolute determination of lattice parameters. And soon, it was realized that the electron density (ED) distributions in crystals can be obtained from the intensities of the scattered X-rays. Already in 1915, P. J. W. Debye<sup>[4]</sup> stated:



**Figure 1. 1 Peter J. W. Debye Nobel Prize in Chemistry (1936)**

*‘It seems to me that the experimental study of scattered radiation in particular from light atoms, should get more attention, since along this way it should be possible to determine the arrangement of the electrons in the atoms.’*

The accessibility of the ED distribution in crystals with the use of X-ray diffraction is of particular importance as also emphasized by L. Pauling<sup>[5]</sup> in 1932:

*‘The properties of a compound depend on two main factors, the nature of the bonds between the atoms, and the nature of the atomic arrangement’*

Nevertheless, it took a quite long time for X-ray charge density analysis to become a true analytical technique for extracting information about chemical bonding. Several earlier charge density studies clearly indicated the necessity of precise measurements of all reflections to high order in a reasonable period of time. This was hampered primarily due to lack of high intensity X-ray sources and low-temperature measurement techniques. Not until 1960s much better cryogenic techniques and development of high-flux X-ray beam; e.g. by using synchrotron radiation, gave rise to increase of the scattering power and improvement of the resolution of the ED maps since the effect of thermal motion and thermal diffuse scattering (TDS) was vastly reduced.<sup>[6]</sup> More recently, area detectors were introduced after extensive use of scintillation counters. This revolutionary development reduced the data collection time from several weeks to one or couple of days as the data-collection rate is increased by one to two orders of magnitude.<sup>[7]</sup>

The delay of achieving a remarkable progress in the experimental analysis of chemical bonding can not only be traced back to the experimental deficiencies but also to the success of the spherical atom model for the interpretation of X-ray determined charge densities. In most cases, for a routine crystal structure determination the so-called independent atom model (IAM) was used which supposes that scattering occurs by means of spherically averaged ground-state atoms. This conventional structure analysis is sufficient to obtain atomic positions and some information about their static and/or dynamic displacement. Doubtlessly, the success of the spherical atom approximation should not be underestimated since it is still exclusively used worldwide for several tens of thousands of structure determination per year. However, as atoms in a crystal are in a nonspherical environment, meaning that the ED is in fact deviating from spherical shape due to interactions, this assumption indicates some shortcomings in particular when trying to model asphericities. For a more accurate description of the ED, the atomic asphericity should be taken into account which necessitates the use of atom-centered multipolar functions. Starting from the beginning of 1960s this was most successfully accomplished in models by DeMarco and Weiss<sup>[8]</sup>, Dawson<sup>[9]</sup>, Kurki-Suonio.<sup>[10]</sup> Following these studies, Stewart<sup>[11]</sup>,

Hirshfeld<sup>[12]</sup> Hansen & Coppens<sup>[13]</sup> introduced a generalized scattering formalism, based on spherical harmonic density functions centered on each of the atomic nuclei. While all three models have been applied extensively in charge density studies the multipole model by Hansen & Coppens came forward and became a mature technique in charge density refinement.<sup>[14]</sup> In this thesis, all the experimental electron densities are reconstructed using this type of multipole model. More insight on the formalism can be found in Chapter 2.

Hohenberg & Kohn stated that the charge density is a fundamental observable which fully defines the ground-state properties of the system if known at infinite resolution.<sup>[15]</sup> On base of the assumption that all demanded information is inherent in the ED itself, Bader examined the ED closer using the ED gradient  $\nabla\rho(\mathbf{r})$ , ED Laplacian  $\nabla^2\rho(\mathbf{r})$  and local curvatures of the total ED  $\rho(\mathbf{r})$  for the qualitative and quantitative description of bonding in molecular crystals.<sup>[16]</sup> This topological analysis gave birth to the quantum theory of atoms in molecules (QTAIM) and consequently to the opening of a new route in charge density analysis<sup>[17]</sup>. In the present thesis all kinds of atomic interactions are mainly studied within the framework of Bader's QTAIM. Therefore, an extensive insight will be outlined in Chapter 2.

In spite of the technical developments in the field it has been noticed by Coppens that the experimental charge density analysis is still far from a routine technique due to several problems which can not be completely circumvented.<sup>[18]</sup> In the following some of these issues are discussed.

Apart from being subject to experimental errors, the experimental ED is also only known to limited resolution. Some information represented by higher Bragg angles is lost. Consequently, the multipole model is formed by an extrapolation to infinite resolution from a finite set of experimental data. The effect of the omission of terms of the Fourier series with higher diffraction angles on the ED is called the series termination effect. These shortcomings are especially well reflected in DD maps where some detailed features near the atomic nuclei disappear when comparing experiment with theory.<sup>[19]</sup>

Another limitation is that the experimental ED is time averaged over both internal and external vibrations. To compare it with theoretical ED a proper deconvolution of the thermal motion from the experimental ED is required. Since diffraction intensities are reduced at larger scattering angles as a result of destructive interference, much higher accuracy be-

comes crucial for high order reflections. This necessitates the use of low temperature experiments in order to properly separate thermal effects from deformations due to chemical bonding.

Discrepancies in the diffraction data can bias the scale factor which is included into the refinement procedure. The over or underestimation of the scale factor can cause significant misinterpretations in charge density maps.

In principle, for heavy elements the electrons in the inner shells remain essentially unperturbed within the resolution of the X-ray experiment in comparison to those of light atoms. Correspondingly, the frozen-core approximation is routinely used, which assumes that the core ED remains undistorted and mostly asphericities in the outermost shell are accounted for. Recently, it has been shown that already the refinement of individual core expansion/contraction parameters of second row elements leads to a considerable reduction of the residual densities in the  $L$  (core) shell.<sup>[20]</sup> Additional problem is the estimation of electrons belonging to valence or core part. For intermetallic compounds, in particular, much less is known about the bonding situation.

Another challenging issue is synthesis of suitable single crystals for a charge density analysis. Crystals of very small sizes along with the use of the hard radiation is essential in order to minimize absorption and extinction effects.

According to reasons just mentioned above experimental investigations of the ED derived from X-ray diffraction data in contrary to quantum chemical calculations are very limited for intermetallic compounds, in particular. These publications usually cover the charge density evaluations especially on chemical compounds with high application potential like  $\beta'$ -NiAl,  $\gamma$ -TiAl, SrTiO<sub>3</sub>, CoSb<sub>3</sub>, V<sub>3</sub>Si, MgB<sub>2</sub>, MgZn<sub>2</sub> and MgCu<sub>2</sub>.<sup>[21]</sup> In fact, systematical experimental investigations on intermetallic compounds are lacking. One of the main tasks of the present thesis is aimed at filling this gap by comparing several borides of one particular transition metal on one hand side, but also isostructural borides of various metals at the other side. In this respect, similarities and differences between the electron density features in TiB<sub>2</sub>, VB<sub>2</sub>, VB and V<sub>3</sub>B<sub>4</sub> derived from X-ray diffraction data, are analysed in terms of QTAIM and compared with those obtained from quantumchemical calculations. Ultimate target is a transferable model based on typical building blocks for practical applications. More insight on the transferability concept is given in Chapter 2.



In the following, some features of binary vanadium borides and  $3d$  transition metal diborides is outlined which are of particular interest in course of a systematic charge density analysis. In Chapter 2, principles of X-ray diffraction are briefly summarized followed by the experimental methodology of extracting information from a charge density analysis. In Chapter 3, experimental techniques used for the synthesis of vanadium borides are explained. A detailed analysis of crystal structures of vanadium borides are given on base of IAM refinement of high resolution X-ray diffraction data. In the following four chapters, the topological analysis of the experimentally reconstructed ED in  $\text{VB}_2$ ,  $\text{TiB}_2$ ,  $\text{VB}$  and  $\text{V}_3\text{B}_4$  is presented in terms of a multipole model. The results are compared with DFT calculations carried out by Baranov.<sup>[22a]</sup> Finally, in the last Chapter, a comparison between the electronic structures of the respective compounds is given.

### 1.1 The study of intermetallic borides

Boron is one of the most interesting elements of periodic table. It forms great variety of electronic configurations of different stability originating from its ‘deficient’ electron concentration, four valence orbitals and three electrons ( $2s^2 2p^1$ ) leading to an extraordinary bonding versatility. Consequently, boron forms with transition metals compounds with properties varying from high conductivity metals to wide band gap insulators and superconductors, from thermal insulators to thermal conductors and refractory materials, etc.<sup>[23]</sup>

Notwithstanding the great variety of the respective crystal structures and bonding interactions, the nature of chemical bonding in intermetallic borides is not well understood. Particularly, a distinct classification of B–B, B–M and M–M interactions are lacking. The most successful concept of chemical bonding is the Zintl-Klemm model based on a charge transfer from the cationic part of the structure to the anionic one. These electrons are used in the anionic part to form 2c-2e bonds (octet rule). The Zintl-Klemm model allows deriving electron counting rules for a large group of chemical compounds called Zintl phases, especially for compounds with main group elements. For intermetallic borides this description does not work optimally in most cases.<sup>[24]</sup>

In earlier studies, interpretations of the electronic structure were targeted at extending a particular model to all types of borides which mainly resulted in discrepancies in conclusions. There was a considerable debate over the direction of charge transfer. Until late 1960s two main model concepts has been postulated. Some authors advocated the model in

which boron atoms act as donors of electrons to the  $d$ -band of the metal.<sup>[25]</sup> On the other hand, another group proposed that boron atoms are acceptors of electrons from the metal for the formation of B–B bonds.<sup>[26]</sup> Samsonov *et al.*<sup>[27]</sup> and Goryachev *et al.*<sup>[28]</sup> investigated systematically boron compounds of the same structure type with different metals. They calculated the electronic energy spectrum for the diborides of Ti, Zr, Hf, V, Nb, Ta, Cr and Mo. The calculations reveal excess electrons in the electrons states of boron supporting an electron transfer from metal to boron.

Studies concerning the electronic structure of lower borides ( $B/M < 1$ ) are relatively less in the literature. The lower borides are formed primarily from  $d$ -transition metals which have a strong tendency to retain their lattices. Upon the formation of lower transition metals borides, borons are ‘dissolved’ in the interstices of the crystal lattice of the metal; however, they are not able to induce a significant structural change in it. In general, the boron atoms donate electrons to the  $d$ -bands of the transition metals in these compounds as reported in the literature.<sup>[29]</sup>

For tetra- and hexaborides an electron transfer from metal to boron is proposed whereas no certain agreement could be reached for the direction of the charge transfer for dodecaborides.<sup>[30]</sup>

### 1.1.1 The interest in vanadium-boron system

Binary vanadium borides are very suitable model systems for a systematic analysis of transferability concept in intermetallic compounds due to similarities and slight differences according to the respective idealized crystal structures. In Figure 1.2 projections along [100] direction for VB and  $V_3B_4$  and along [001] direction for  $VB_2$  are shown. For the sublattice formed by boron atoms, zig-zag chains are discussed in VB, hexagonal network in  $VB_2$ , but an intermediate situation in  $V_3B_4$ . The crystal structure of the latter compound provides several features which are of particular interest in course of the charge density analysis. For example, there are two inequivalent boron atoms: one (labelled as red) is similar to that in VB, the other one (labelled as blue) resembles that in  $VB_2$  considering the number of neighbouring boron atoms. These similarities and/or small but significant differences should be well reflected in the charge density analysis.

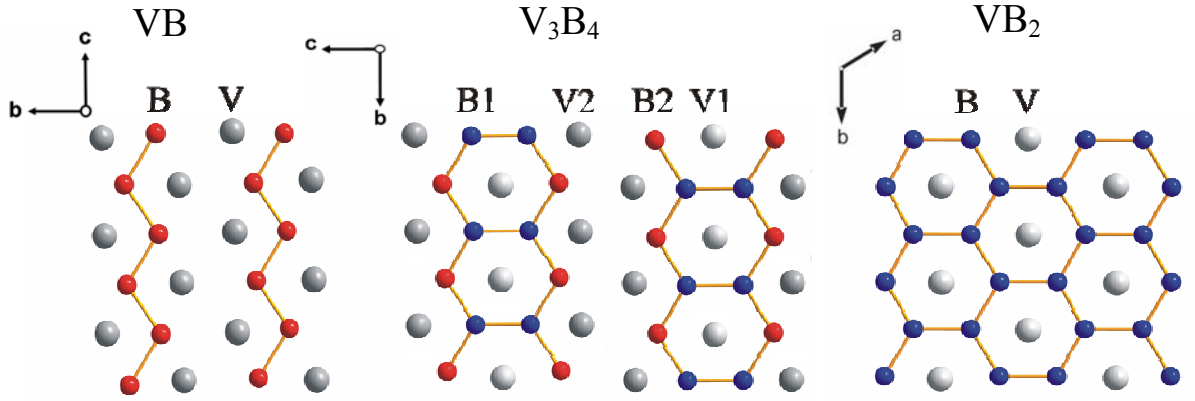


**Figure 1.2:** Crystal structures of vanadium borides.

In general, complete crystal structure determinations of binary vanadium borides are missing except for  $V_2B_3$  and  $V_3B_2$ .<sup>[31]</sup> The most common approach is assigning the structure type and the refining the unit cell parameters which may lead to unrealistic interatomic distances. For example, one of the published B–B interatomic distances in  $V_3B_4$  is extraordinarily short (1.480 Å), although no crystal chemical reason is obvious.<sup>[32]</sup> In principle, characteristic bond lengths of *ca.* 1.7–1.8 Å in the boron substructure are expected accounting for the similar environment of atoms.

### 1.1.2 The interest in 3d transition metal diborides

Diborides of 3d transition metals with  $AlB_2$  structure type has many special mechanical, chemical and physical properties including very high melting temperature, high elastic modulus, high chemical stability and good electrical conductivity.<sup>[33]</sup> Due to the unexpected discovery of superconductivity in  $MgB_2$  with the temperature of critical transition  $T_c \sim 39$  K<sup>[34]</sup> the electronic structure of diborides has been subject of interest from both the theoretical and experimental point of view.<sup>[35]</sup> According to the accepted theoretical concept for the electronic structure, metal atoms donate a part of their valence electrons to boron atoms and these electrons are used to form a hexagonal network.<sup>[35c, 36]</sup> The stability of transition metal diborides rapidly decreases when electrons are used to fill the antibonding *d* bands rather than to be transferred to the boron layer resulting in the reduction of intra-layer interactions.<sup>[37]</sup>

In the  $AlB_2$  crystal structure type, the metal atoms form a simple hexagonal lattice having an axial ratio  $c/a$  slightly greater than unity. At first glance, the boron sublattice seems

to be similar to the graphite structure. However, the chemistry of transition metal diborides proves this statement wrong. The most noticeable property of this class of materials is that they are extremely hard.

One of the important questions concerning the electronic structure is the role of transition metal bonding. General crystallographic models suggest that the exchange of metal affects primarily B–M distance but also causes a slight change in B–B distance. As an example, the B–B and B–M distances of diborides of  $3d$  transition metal atoms with the lowest ( $\text{ScB}_2$ ) and highest atomic number ( $\text{MnB}_2$ ) are highlighted in Figure 1.3.<sup>[38]</sup>

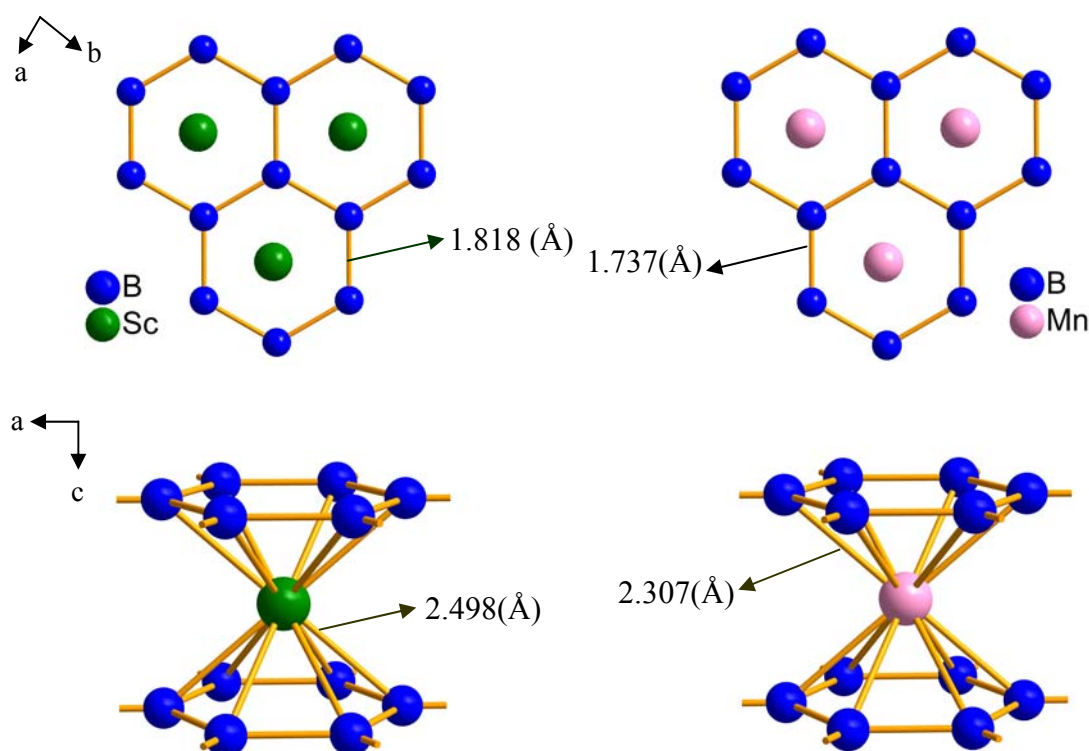


**Figure 1.3:** B–B and B–M distances in  $\text{ScB}_2$  and  $\text{MnB}_2$ .

The cell parameters, interatomic distances and the axial ratios of diborides of  $\text{Sc}$ <sup>[38b]</sup>,  $\text{Ti}$ ,  $\text{V}$ ,  $\text{Cr}$ <sup>[39]</sup> and  $\text{Mn}$ <sup>[38a, 39]</sup> are shown in Figure 1.4. For  $\text{CrB}_2$  and  $\text{MnB}_2$  the crystal structures were not completely determined, but only the structure type was assigned and unit cell parameters were refined. The variation of the axial ratio vs. the atomic number of transition metal atoms is not completely linear. Both cell parameters decrease as the valence increases until  $\text{VB}_2$  where they almost level off. The variation of cell parameter  $c$  is much larger than in cell parameter  $a$ , but it shows a slight maximum to  $\text{CrB}_2$ . The behaviour of

the corresponding axial ratio is similar. Obviously, all these parameters are correlated with the 3d metal but the degree of correlation is presumably varying as the valence increases. This is evidenced *e.g.* by a closer inspection of the respective cell parameter  $c$  and B–M distance which are showing different trends in  $\text{CrB}_2$ . These peculiarities can not be explained straightforwardly by a conventional structure analysis, the "simplicity" of the crystal structures notwithstanding.

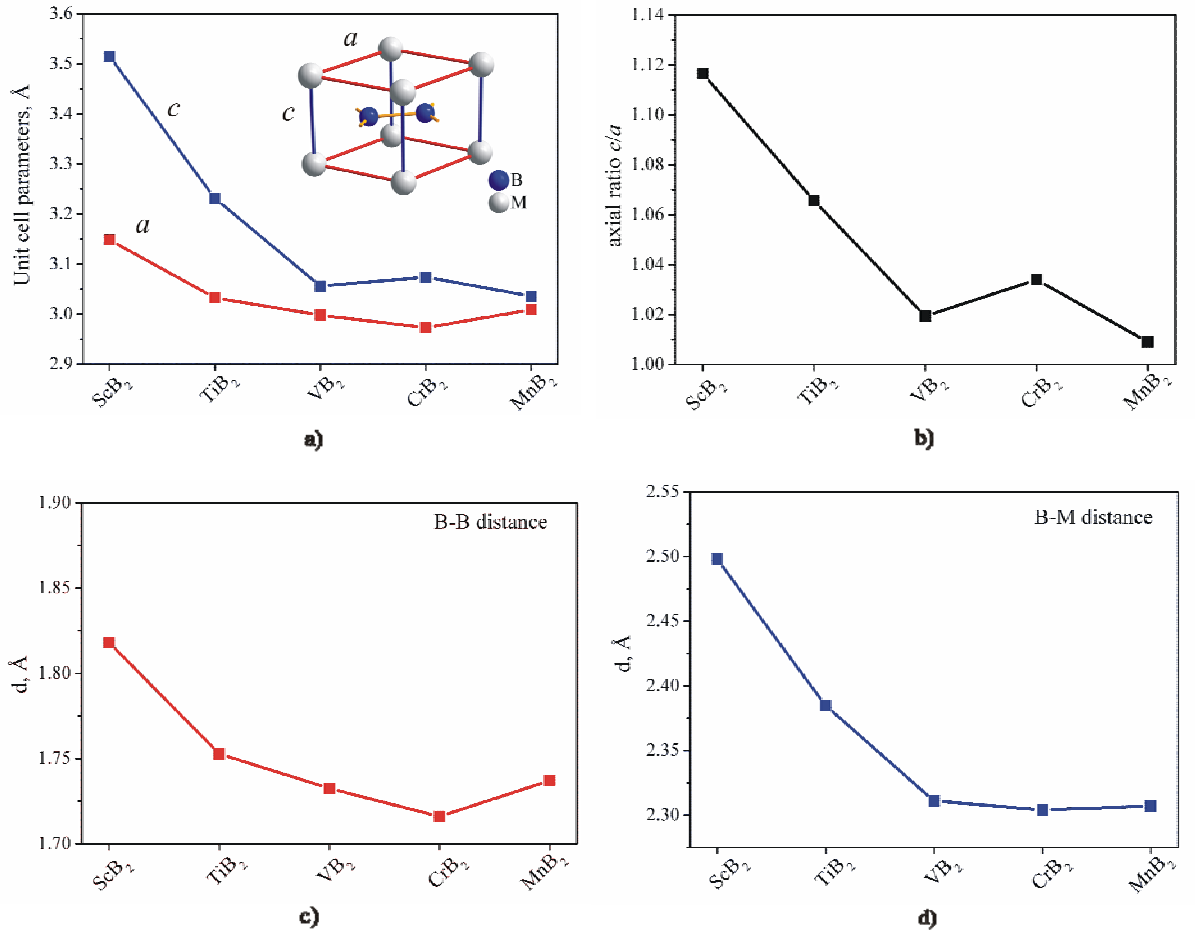


**Figure 1.4:** a) Unit cell and cell parameters of the diborides of 3d transition metals. b) The axial ratio of the cell parameters  $c/a$ . c) B–B distances in boron network plane. d) B–M distances. The values for  $\text{TiB}_2$  are obtained in this work. All other data are taken from the references [38–40].

Transition metal diborides show variations in terms of the naturally occurring crystal defects, *e.g.* vacancy formation. Up to now, it is a well established fact that non-stoichiometry for the diborides of  $s$ ,  $p$  and  $d$  metals is usually due to the cation deficiency. Significant deviations were detected for  $\text{Mg}_{1-x}\text{B}_2$  ( $x \sim 0.04\text{--}0.05$ )<sup>[41]</sup>,  $\text{Al}_{1-x}\text{B}_2$  ( $x \sim 0.1\text{--}0.11$ )

<sup>[42]</sup> and especially for diborides of group V metals  $\text{Nb}_{1-x}\text{B}_2$  and  $\text{Ta}_{1-x}\text{B}_2$  ( $x = 0.01-0.5$ ).<sup>[43]</sup> Vacancies can also appear in the boron position upon doping the boron sublattice with carbon ( $\text{Mg}_{1-x}(\text{B}_{1-y}\text{C}_y)_2$ ;  $x \leq 0.1$ ).<sup>[44]</sup> The published experimental data about Mo-B phase equilibria are quite contradictory.<sup>[45]</sup> Depending on the synthetic route, three different compounds are reported in the composition region near the 'molybdenum diboride'. These are the hexagonal  $\text{MoB}_2$ , the metal deficient  $\text{Mo}_{1-x}\text{B}_2$  or  $\text{Mo}_{2-x}\text{B}_5$  and the boron-deficient  $\text{MoB}_{2-x}$  or  $\text{Mo}_2\text{B}_{5-x}$ . Other diborides of transition metals exist for the stoichiometric composition or the reported width of homogeneity ranges are quite narrow.<sup>[33]</sup>

Studies dealing with the electronic structure and the nature of interatomic interactions for many non-stoichiometric metal diborides are relatively rare. In papers of Shveikin & Ivanovsky <sup>[46]</sup>, Oguchi <sup>[37e]</sup> and Ivanovskii *et al.* <sup>[37a, 47]</sup> the stability of several non-stoichiometric metal diborides are studied by examination of the electronic band structure. But for a long time, the influence of the non-stoichiometry on the structural, chemical and physical properties is mostly ignored. The reason is that XRD, electron beam and conventional chemical analysis techniques for studying possible vacancy ordering effects can not simply be exploited in a routine manner for those materials. Problems are typically induced by extreme hardness of materials giving rise to severe problems during shaping of crystals or grinding of powders for sample preparation. Furthermore, precise boron quantification is mostly hampered by the lack of a boron compound of a well defined composition for being used as a standard. Another important limitation is that the accuracy to which the boron atoms can be located in presence of heavy elements by X-ray diffraction methods is restricted.

## 2 EXPERIMENTAL ELECTRON DENSITY ANALYSIS

### FROM X-RAY DIFFRACTION - THE BASICS

The ED can be reconstructed from diffraction experiments using X-rays, and more recently  $\gamma$ -ray, synchrotron radiation and electron scattering. The aim of this Chapter is to provide an overview about the principles of X-ray diffraction and a background for interpretation of the results. In this respect, an insight into Bader's Quantum theory of atoms in molecules (QTAIM) will be given. Finally, procedures of the quantumchemical calculations which are carried out for a comparison reason are briefly described.

#### 2.1 Principles of X-ray diffraction

X-ray diffraction studies constitute most of our present knowledge of the crystal structures. Basically, a routine crystal structure analysis means the determination of the unit cell (the smallest repeating volume of the lattice) dimensions and the atomic arrangement in the crystal. The crystal structure determination is the resultant of the interaction of X-rays with crystalline matter. X-rays ( $\lambda = 0.5\text{-}3 \text{ \AA}$ ) are scattered by electrons of atoms and ions with an interatomic distance in the region of  $1\text{-}3 \text{ \AA}$  without changing its wavelength. This process is called elastic scattering. The elastically scattered X-rays interfere destructively or constructively depending on the path-difference between neighboring waves. If the difference in the paths traveled by these waves is an integral multiple of the wavelength then they are in phase and interfere constructively. Accordingly, crystals give sharp characteristic interference or diffraction pattern only in allowed positions. The diffraction condition is expressed by Bragg's law which considers the diffracted X-ray beams behaved as if they were reflected from planes passing through points of the crystal lattice (Figure 2.1). A reflection is observed only at certain angles of scattering  $\theta$  where the path difference  $2d \sin \theta$  is an integral multiple of the wavelength:

$$2 d \sin \theta = n \lambda \quad (n = 1, 2, 3 \dots) \quad (\text{Eq. 2-1})$$

In this equation,  $\lambda$  is the wavelength of the radiation used,  $n$  is called the order of diffraction and is an integer,  $d$  is perpendicular spacing between the diffracting lattice planes and  $\theta$  is complement of the scattering angle. The limit of number of the observed reflections de-

depends on both the wavelength used and the unit cell of the crystal. In principle, the larger the unit cell the larger the number of accessible reflections.

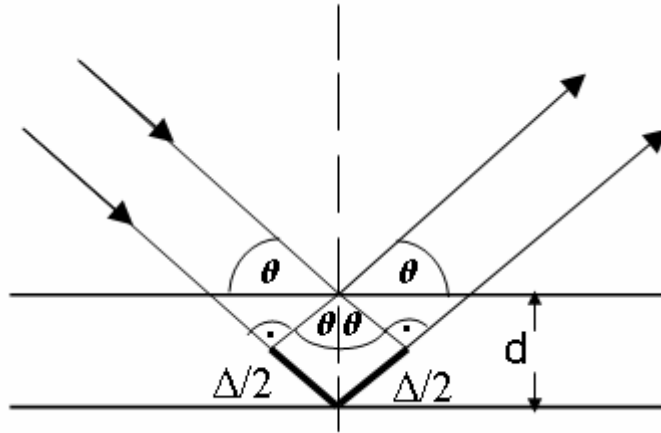


**Figure 2.1** Derivation of Bragg equation.

Another point of view for describing the diffraction phenomenon is the conversion of the coherent X-ray beam, by the three dimensional periodic array of ED in the crystal into the individual structure factors by Fourier transformation. The structure factor  $F(hkl)$  expresses the combined scattering of X-rays for all atoms in the unit cell compared to that for a single electron. Since there is a phase shift between the waves scattered by different atoms with respect to each other a suitable way to express the structure factor is exponentially with an imaginary exponent:

$$F(hkl) = |F(hkl)| e^{i\alpha(hkl)} \quad (\text{Eq. 2.2})$$

, where  $|F|$  or  $|F(hkl)|$  is the amplitude of the scattered wave and  $\alpha(hkl)$  is its phase relative to the chosen origin of the unit cell. Another way to represent the structure factor is making use of the Euler formalism as the sum of cosine term (the real part, A) and a sine term (the imaginary part, B) as an ordinary complex number:

$$\begin{aligned} F(hkl) &= \sum_i f_i [\cos 2\pi(hx_i + ky_i + lz_i) + i \sin 2\pi(hx_i + ky_i + lz_i)] \\ &= A(hkl) + iB(hkl) \end{aligned} \quad (\text{Eq. 2.3})$$

Here,  $f_i$  is the atom form factor and is a measure of the scattering power of an atom for X-rays relative to a single electron under the same conditions (Chapter 2.3). These values are obtained by quantum mechanical calculations and tabulated for every atom and ion both ex-



plicity as well as in polynomial form in International Tables for Crystallography Volume C (Tab. 6.1.1.1-5). Figure 2.2 and Equations 2.4 and 2.5 show the relationship between the scattering amplitude and its phase in the complex plane:

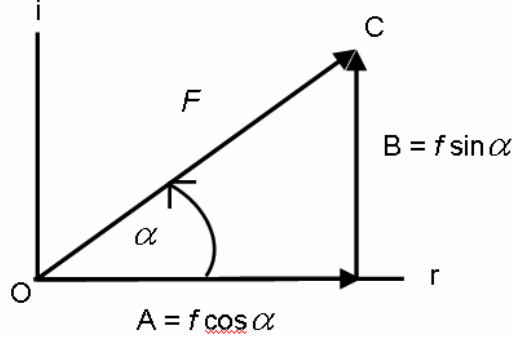


**Figure 2.2** The structure factor  $F(hkl)$  in complex plane;  $\alpha$  is the phase angle and the amplitude  $|F|$  is represented by the length of OC.

$$|F| = \sqrt{A^2 + B^2} \quad (\text{Eq. 2.4})$$

$$\alpha = \arctan \frac{B}{A} \quad (\text{Eq. 2.5})$$

Accordingly, in order to calculate the structure factor, the values of  $x$ ,  $y$  and  $z$  of each atom;  $h$ ,  $k$ ,  $l$  indices, the respective  $\sin \theta/\lambda$  and the scattering factor  $f_i$  for each atom at the corresponding  $\sin \theta/\lambda$  has to be known. However, the measured intensities in a diffraction experiment only give the amplitudes of the structure factors, not the phase angles. The structure amplitudes without the phase information only allow the calculation of unit cell parameters and the crystal space group. In order to determine the atomic positions the phase of the structure factor has to be determined. The problem of getting estimates of the phase angle is the so-called "Phase problem" of X-ray structure analysis. All the methods for solving the phase problem deal with a development of a structural model, which in turn permits calculation of theoretical structure factors and comparison with experimentally observed ones. The structure is refined to give a better agreement between the observed and calculated structure factors. Once the amplitudes of structure factors  $|F(hkl)|$  and their relative phases  $\alpha(hkl)$  are known the ED can be reconstructed  $\rho_{XYZ}$  for every point  $xyz$  in the unit cell of the volume  $V$  through a Fourier synthesis:

$$\rho_{XYZ} = \frac{1}{V} \sum F(hkl) e^{-i2\pi(hX+kY+lZ)} \quad (\text{Eq. 2.6})$$

## 2.2 Intensity corrections

According to the kinematic theory of scattering by Born<sup>[48]</sup> the intensity of the scattered radiation is proportional to the square of the structure factor amplitude:

$$I \sim |F(hkl)|^2 \quad (\text{Eq. 2-7})$$

Although it is actually the energy of the diffracted beam which is measured, the term "intensity" is usually used. In reality, the measured X-ray diffraction intensity does not only include the coherent Bragg intensity which is the elastic part of the total scattering but also other contributions. The proportionality of intensity and structure factors depends on a number of factors for which appropriate corrections are required to be applied to the raw data in order to have a best agreement between the observed and calculated structure factors:

$$|F(hkl)|^2 = k^{-2} y I / [LPA(1 + \alpha)] \quad (\text{Eq. 2-8})$$

In these equations,  $k$  is the scale factor, which transfers the intensity values into an absolute scale; The extinction factor  $0 < y < 1$  corrects for dynamical scattering effects that are responsible from the deviation from the kinematical approximation;  $A$  is the absorption factor, The Lorentz factor ( $L = 1/\sin 2\theta$ ) accounts for the correction based on the fact that for a constant angular velocity of rotation of the crystal, different reciprocal lattice points pass through the sphere of reflection at different rates, thus they have different times-of-reflections opportunity. The Polarization factor  $P$  depends on the degree of monochromator perfection. The thermal diffuse scattering term  $\alpha > 0$  corrects for the inelastic scattering caused by atomic thermal movements that is not removed by the background subtraction.

### 2.2.1 Absorption

When an X-ray passes through a crystal it experiences intensity losses by photoelectric absorption as well as elastic Rayleigh and inelastic Compton scattering of the incident and reflected beam. These effects increase roughly with the fourth power of the atomic number of a scattering atom and with the third power of the wavelength of the radiation. This effect can be summarized as:

$$I = I_o e^{-\mu x} \quad (\text{Eq. 2-9})$$

Here,  $I$  is the diffracted beam intensity,  $I_0$  is the incident beam intensity,  $\mu$  is the linear absorption coefficient and  $x$  is the length of the path which the beam travels within the crystal. If the shape and size of the crystal is known accurately, it is possible to correct for absorption

$$A = V^{-1} \int_V \exp[-\mu(t_0 + t_1)] dV \quad (\text{Eq. 2-10})$$

, where  $t_0$  and  $t_1$  are the path lengths of the incident and reflected beams through the crystal and the integration is over the volume of the crystal.<sup>[49]</sup>

The absorption corrections are of crucial importance for very anisotropic crystals, in particular. If the X-ray data is not corrected for absorption, thermal parameters will compensate by adjusting to values different than the true values. In order to avoid these errors different absorption correction strategies are developed.<sup>[50]</sup> The International Union of Crystallography (IUCr) suggests using the type of correction depending on the value of  $\mu x$ .

### 2.2.2 Extinction

When the X-ray beam travels through a real crystal it experiences an additional attenuation according to the deviations from the "ideally imperfect mosaic crystal structure". The consequence of this effect, called extinction, is that the intensities of strong, mainly low scattering angle reflections are systematically lower than expected ( $|F_{\text{obs}}| < |F_{\text{calc}}|$ ). There are two diffraction theories for the treatment of extinction. According to the kinematical theory of diffraction the interaction between radiation and matter is small enough for incident beam not to be perturbed in the crystal meaning that there is no attenuation of the incident beam and also not any multiple scattering when it passes through the crystal. In fact, the translational symmetry of a crystal does impose constraints on the structure of the X-ray beam, thus leads to its attenuation when traveling inside the crystal. This fact is considered by the dynamical theory which takes the interaction of the incident and scattered beams into account. In this case the intensity of the reflection is reduced until:

$$I_{hkl} \sim |F_{hkl}| \quad (\text{Eq. 2-11})$$

The dynamical theory leads to the kinematical theory in case of X-ray diffraction of ideally perfect crystals and electron diffraction where the dynamical effects become important. This is the case when the effective thickness of the perfect crystal domains  $t$  in a crystal under certain diffraction condition exceeds the so-called extinction length or the coherence length  $\Lambda$ ,

$$t > \Lambda = \frac{V}{(aP)} \frac{1}{|F_{hkl}| \lambda} \quad (\text{Eq. 2-12})$$

,  $V$  is the volume of the unit cell,  $\lambda$  being the wavelength of the X-ray beam,  $a$  is the classical radius of the electron ( $e^2/mc^2$ ),  $P$  is the polarization factor and  $|F_{hkl}|$  is the structure amplitude. As is evident from equation 2-12 the extinction length is smallest for strong reflections and large wavelengths. For the condition  $t < \Lambda$  the diffraction inside a given domain follows the kinematical theory.<sup>[51]</sup>

In principle, the integrated intensities can be calculated by both dynamical and kinematical theories. In fact; real crystals usually do not show a high degree of perfection except some which are highly pure and free of defects. Most crystals possess domain sizes such that

$$I_{hkl} \sim |F_{hkl}|^n \quad (\text{Eq. 2-13})$$

where  $1 < n < 2$  but usually much closer to 2. Therefore, the kinematical theory is almost exclusively used for crystals synthesized in a chemical laboratory. However, in order to make kinematical theory valid extinction has to be corrected

Darwin proposed a model where he presented a real crystal which consist of slightly misaligned mosaic blocks.<sup>[52]</sup> This imperfection is highly desirable since the mosaic structure causes the diffracted beam to have a higher divergence and a lower coherence than the incident beam; hence an additional diffraction of the incident beam is prevented as occurs in perfect crystals. The mosaic crystal is said to be ideally imperfect if extinctions are negligibly small for all reflections. Using the mosaic block representation Darwin distinguished two extinction processes, which he named primary and secondary extinction.

When X-ray beam passes through a single block of a perfect crystal part the scattered beam may be rescattered from bottom sides of the planes back into the incident beam and so on for multiple times (Figure 2.3a). Every reflection corresponds to a phase change of  $\pi/2$ .

X-rays reflected  $n$  times differ in phase by  $\pi$  from those reflected  $n-2$  times. As a consequence, they interfere destructively and cause a reduction of the intensity of the reflected beam. This is due primary extinction and its treatment necessitates the use of dynamical diffraction theory.

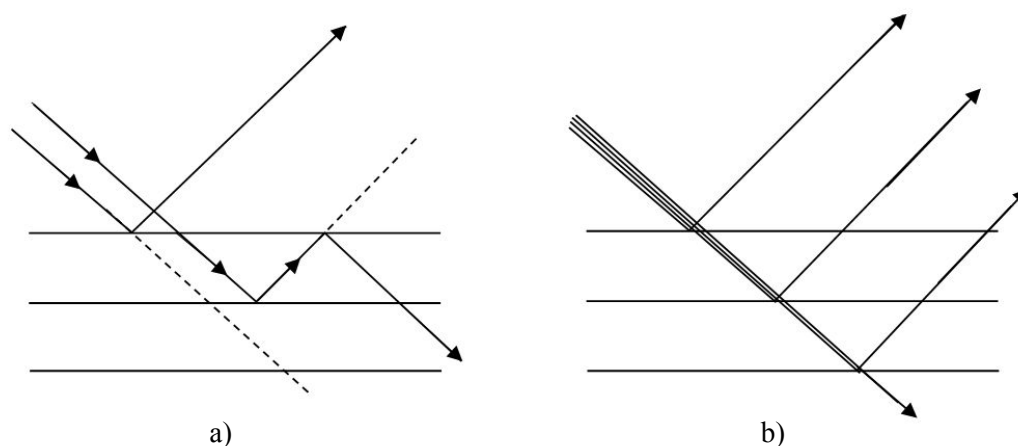


**Figure 2.3** a) Schematic representation of primary extinction within a single domain of a perfect crystal b) Secondary extinction in a mosaic block of an ideally imperfect crystal.

Secondary extinction occurs, when part of the incident beam is diffracted by one mosaic block, hence planes in the following block experiences a reduced primary beam (Figure 2.3b). As a result of this, the intensity contribution of the latter block to the diffracted beam is less than the former one. Extinction of this kind depends on the size of the crystal and alignment of the mosaic blocks with respect to each other which is termed mosaicity. Crystals of smaller size and with less aligned mosaic blocks will have negligible secondary extinction since fewer planes are in position for diffraction condition at a given instant. Large secondary extinction effects can be decreased by submitting the crystals to thermal or mechanical shock for example by dipping the crystal in liquid nitrogen or by grinding their surfaces.

For the treatment of extinction Zachariasen developed a general theory based on Darwin transfer equations, which considers the energy exchange between the incident and reflected rays within the crystal.<sup>[53]</sup> Although the theory was said to be valid for the entire range of crystals from perfect to the ideally mosaic, it had its critics, the most important limitation is due to the theory being of kinematical nature.<sup>[54]</sup> It has only been applied for secondary extinction and the method does not work optimally for larger crystals and in cases of severe primary extinction.<sup>[55]</sup>

A comprehensive treatment of extinction in the quasi-kinematical approximation has been provided by Becker and Coppens who have revised and improved Zachariasen's theory for both primary and secondary extinction.<sup>[56]</sup> The extinction correction is expressed as a function of scattering angle, block size, crystal size and degree of mosaic block disorientation. This formalism was extended to include crystals of non-spherical shape and anisotropy of mosaic spread and particle size.<sup>[57]</sup> In various structure-refinement programs an extinction coefficient, the mosaic spread and a mean block size are determined from the measured intensity according to the primary or secondary extinction models. Uncorrected extinction, like uncorrected absorption can distort the scale factor and/or bias the mean-square displacements towards negative values.

For an X-ray diffraction experiment it is of crucial importance to get accurate structure factors removed from extinction effects in order to reconstruct reliable electron densities. Crystals used for this aim are usually of smaller size and unknown defect structure. A fundamental problem to be solved is how to describe the diffraction process in these cases. In principle, the block size and disorientation characteristics in a crystal can be determined by synchrotron radiation rocking curves.<sup>[58]</sup> Due to the small angular divergence (FWHM  $\sim 20''$  of arc) topographic studies of synchrotron radiation allow one to specify and localize the changes in orientation and spacing of crystal lattice planes which give rise to local differences in either diffracted beam direction or intensity.<sup>[59]</sup> Recently, high-resolution electron microscopy (HREM) is also extensively used for the determination of structures of perfect crystal regions, crystals defects with atomic resolution.<sup>[60]</sup>

### **2.2.3 Thermal diffuse scattering**

In general, diffuse scattering arises from a deviation from the regular periodic character of crystal lattice. The inelastic thermal diffuse scattering (TDS), on the other hand, is another kind of contribution to the total scattering originated by long range lattice vibrations which are temperature dependent. The thermal vibrations in a crystal cause the elastic Bragg scattering intensity to fall off due to destructive interference and the inelastic TDS intensity to build up according to energy exchanges between the scattered beams and the lattice vibration modes. As a result, a variable diffuse background forms over the entire reciprocal lattice in addition with a sharp maxima in the region of the Bragg reflections, the TDS intensity being proportional to the Bragg intensity:

$$I_{\text{meas}} = I_{\text{Bragg}} + I_{\text{TDS}} = I_{\text{Bragg}}(1 + \alpha), \quad \alpha = I_{\text{TDS}} / I_{\text{Bragg}} \quad (\text{Eq. 2-15})$$

It is possible to approximate  $\alpha$  through the equation

$$\alpha \sim T \left[ (\sin \theta / \lambda) \right]^2 v_s^{-2} \quad (\text{Eq. 2-15})$$

where  $T$  is the absolute temperature and  $v_s$  is the mean velocity of the sound in the crystal, which is related to the "hardness" of the crystal and can be calculated if the elastic constants of the crystal are known.<sup>[61]</sup> Elastic constants can not be measured easily. Therefore, these values are available for only relatively few crystals. Blessing estimated  $\alpha$  values empirically without using the elastic constants by fitting TDS peak by triangle, exponential, Gaussian or Lorentzian functions.<sup>[62]</sup>

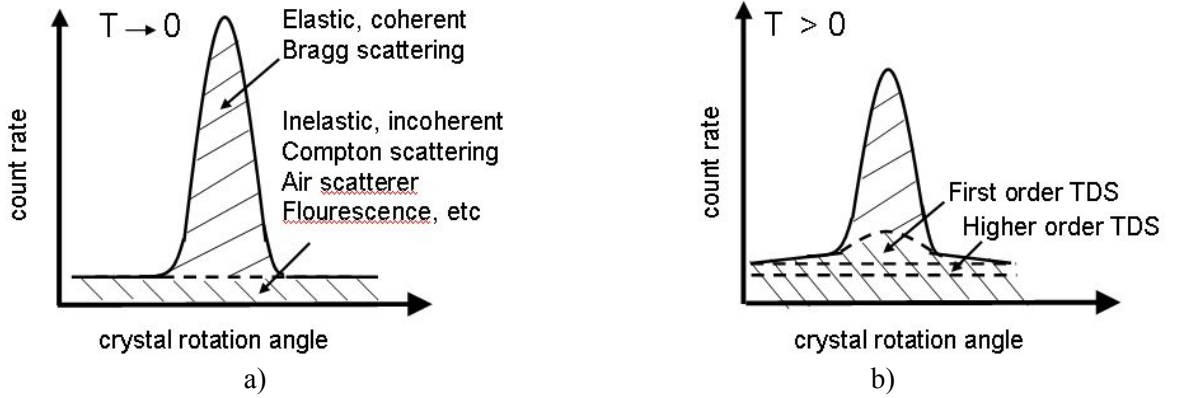


**Figure 2.4:** Intensity profiles without (a) and with (b) TDS contribution.

As shown in Figure 2.4 the inelastic TDS process give rise to a broader intensity profile than the Bragg reflection since it includes both absorption and emission interactions with the Bragg scattering and increases the wavelength spread of the scattered beam. First order scattering is a one-phonon scattering due to acoustic modes and is quite strongly peaked at reciprocal lattice points. The TDS due to optic modes is less important. Higher order TDS is also relatively less peaked. It is part of the background formed by inelastic Compton scattering, fluorescence and contributions from air scattering which intensity vary very slowly in reciprocal space. The subtraction of background from the peak intensity removes the broad part of the TDS but not the maximum below the Bragg peak. The TDS is relatively weak at great distances from the reciprocal lattice points. In general, it is anisotropically distributed because all crystals, even those of cubic symmetry have anisotropic mechanical elasticity.

In order to determine the temperature factors and ED distributions accurately, the contribution of TDS should be determined and separated from elastic scattering, particularly in cases, where the TDS contribution to the total intensity is pronounced. This is experimentally carried out by  $\gamma$ -ray Mössbauer spectroscopy which has a much smaller width of the resonance emission line ( $\sim 10^{-8}$  eV) than the intrinsic energy spread of X-ray line, (1-5 eV).<sup>[63]</sup> Accordingly, inelastic scattering of energy transfer ( $\sim 0.1$  eV) which is larger than the resonant width of Mössbauer lines is not absorbed, thus separated from the elastic scattering.

Nilsson studied the effect of neglecting a TDS correction on a structure investigation and concluded that the temperature factors of soft materials such as molecular crystals calculated in this manner become smaller.<sup>[64]</sup>

### 2.3 Structure refinement

Structure refinement is the process where it is aimed to get the best possible agreement between the observed and calculated structure factors by systematic variation of parameters according to a given model. The most commonly used algorithm for this purpose is the method of least squares. According to this method; variables for the assumed model are optimized by minimizing the sum of the squares of the deviations between the observed and calculated structure factors:

$$\sum_{hkl} w(F_o^2 - F_c^2)^2 = \min \quad (\text{Eq. 2-16})$$

Since not all the data is measured with the same accuracy a weight  $w$  is assigned to each measurement. In many cases, it is sufficient to define a weight of the form:

$$w = 1 / \sigma^2 \quad (\text{Eq. 2-17})$$

In this equation  $\sigma$  is the error estimate based on the counting statistics of the diffractometer measurement. In general, it is larger for weak reflections than for strong ones.

A measure of the disagreement between observed and calculated structure amplitudes is given by the  $R_{(F)}$ -value:

$$R_{(F)} = \sqrt{\frac{\sum_{hkl} w(F_o^2 - F_c^2)^2}{\sum_{hkl} w(F_o^2)^2}} \quad (\text{Eq. 2-18})$$



After each minimization of the discrepancy a scale factor is determined in order to compare observed and calculated amplitudes directly.

$$k = \frac{\sum F_o^2}{\sum F_c^2} \quad (\text{Eq. 2-19})$$

## 2.4 The independent atom model (IAM)

The simplest approximation for the derivation of structure factor relies on the superposition of isolated spherical atomic densities. This is the independent atom model (IAM) where core electron distribution can be fairly well described by spherical scattering amplitudes. The Fourier transformation of the spherical atomic density  $\rho_j^{at}$  in the unit cell gives the atomic form factors,  $f_j(hkl)$ :

$$f_j(hkl) = \int_{V_j} \rho_j^{at}(xyz) \cdot e^{2\pi i(hX+kY+lZ)} dV_j \quad (\text{Eq. 2-20})$$

The atomic form factor or the atomic scattering factor depends upon the nature of the atom, the direction of scattering, the wavelength of X-rays and the thermal vibrations of the atom. Figure 2.5 shows the atomic form factors of vanadium and boron as a function of  $\sin \theta/\lambda$ . They are normalized for the number of electrons.

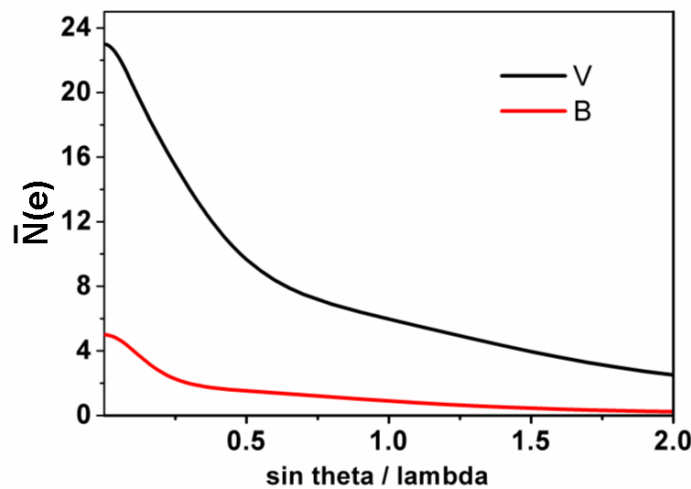


**Figure 2.5** Atomic form factors for vanadium and boron as a function of  $\sin \theta/\lambda$ .

There is a great fall-off of atomic form factors at higher angles due to both interference effects originating from path differences of the scattered radiation and thermal vibrations of the respective atoms. For light atoms it is almost not necessary to measure data at higher angle whereas important information can still be extracted for heavier elements from high order reflections. In general, it is difficult to locate light elements by means of heavier ones.

The IAM is very good approach especially for heavy elements where it is only intended to determine the atomic positions. On the other hand, it is a poor approximation for light elements for which the contribution of the valence electrons to the total scattering is more pronounced. The reason is that IAM does not account for deviations from sphericity due to chemical bonding. The scattering of valence electrons are concentrated in low  $\sin \theta/\lambda$  values, while core electrons scatter in the high order region of reciprocal space. Therefore, in some cases, positional and thermal parameters together with the scale factor are refined using high order reflections in order to reduce bias in the structural parameters due to insufficient approximation of the ED.<sup>[11a]</sup>

## 2.5 The multipole density formalism

Hansen & Coppens described a formalism of density representations with pseudoatoms which is based on an algorithm to account for the density deformations due to chemical bonding.<sup>[13]</sup> This formalism expresses the static ED in the crystal by a superposition of aspherical pseudoatoms as

$$\rho_{at}(r) = P_c \rho_{core}(r) + P_v \kappa^3 \rho_{spher, valence}(\kappa r) + \sum_{l=0}^{l_{max}} \kappa'^3 R_l(\kappa' r) \sum_{m=0}^l P_{lm\pm} y_{lm\pm}(\theta/\varphi) \quad (\text{Eq. 2-21})$$

In this expression, both  $\rho_{core}$  and  $\rho_{spher, valence}$  were used to describe the spherical core and valence densities and calculated from atomic wave functions and normalized to one electron. The core population  $P_c$  is usually kept fixed at the filled-shell value. Due to the variation in the electronegativity, the parameter  $P_v$  will be different than that of the neutral atom. Since the crystal as a whole is neutral the total charge has to be kept constant. Accordingly, it is possible to observe the charge transfer by application of an electroneutrality constraint. The change in the atomic electron population effects the electron-electron re-

pulsion, thus the radial dependence of the charge density on the atom. Correspondingly, the valence function is allowed to expand ( $\kappa < 1$ ) or contract ( $\kappa > 1$ ) by the adjustment of the variable radial parameter  $\kappa$ .<sup>[65]</sup> In order to take asphericity into account, a third term has been introduced. Here the valence ED of each atom is decomposed into convergent Laplace series over the real spherical harmonic angular functions  $y_{lm\pm}$  centered at the nuclear positions satisfying the symmetry of the local atomic environment. The terms in the series are called multipoles and  $l$  is the order of multipole expansion. The radial dependence of the atomic electron distribution is given by normalized Slater-type radial functions in the form

$$R_l(r) = \kappa'^3 \frac{\zeta^{n_l+3}}{(n_l+2)!} (\kappa' r)^{n_l} \exp(-\kappa' \zeta r) \quad (\text{Eq. 2-22})$$

where  $r$  is the radial coordinate,  $\zeta$  is the single Slater exponent, which starting values can be modified by  $\kappa'$ , such that  $\zeta' = \kappa' \zeta$  and the values of  $n_l$  has to obey Poisson's equation ( $n_l \geq l$ ).<sup>[66]</sup> Finally, the electron populations  $P_v$ ,  $P_{lm}$ , both with  $\kappa$  and  $\kappa'$  are refinable parameters in course of multipole refinement where the values for parameters  $n_l$  and  $\zeta$  can be chosen according to rules provided by Hansen & Coppens.<sup>[13]</sup>

Table 2.1 summarizes all parameters which are subject to a refinement in course of a routine structure and charge density analysis. As a rule of thumb, for a reasonable classical structure refinement, the reflection-parameter ratio has to exceed at least ten. Therefore, X-ray data up to high resolution is of crucial importance to allow confidence in the results.<sup>[6e]</sup>

**Table 2.1** Refined parameters in the conventional IAM and multipole model.

Conventional Parameters	Charge Density Parameters
Scale factor $k$	<u>Valence-shell parameters:</u>
Positional parameters $x, y, z$	Population parameter, $P_v$
Harmonic and anharmonic thermal parameters	Expansion-contraction parameters, $\kappa$
Isotropic and anisotropic extinction parameters	<u>Deformation parameters:</u>
Occupancy parameters	Population parameters, $P_{lm}$
	Expansion-contraction parameters, $\kappa'$

The refined parameters in the multipole formalism provide a description of the static density which can be biased in case of inadequate deconvolution of the thermal motion. A concise model should result from an independent analysis of static and dynamic parameters since they are both capable of representing asphericities.

An important problem with the multipole model is that the number of refined parameters is considerably larger as compared for an IAM refinement. Furthermore, these have to be fitted to only a few percent of diffracted intensity, thus a stable solution might not be existed. In those cases, either relation between the multipole parameters are employed which go beyond symmetry (chemical constraints) or physically most insignificant parameters are excluded. As a result, the multipole model might exhibit artefacts due to these restrictions.

As an alternative to the multipole formalism the maximum entropy method (MEM) is introduced by Collins into crystallography.<sup>[67]</sup> MEM is in principle a model-independent approach unlike the multipole model, and reconstructs the ED on a three-dimensional grid using the observed structure factors as a constraint in the maximization of the entropy.<sup>[68]</sup> A problem with MEM is that this model-free approach does not allow the deconvolution of the ED from the thermal motion unlike the Hansen & Coppens multipole model.<sup>[69]</sup>

## 2.6 Residual density

The success of the model used for the refinement process can be tested by the residual ED which is the Fourier summation of differences of structure factors from observations calculated with model phases and those from the refinement model ( $F_{\text{obs}} - F_{\text{calc}}$ ). The features of this so-called residual or difference density map represent the shortcomings of the least-squares minimization. Accordingly, a flat and featureless residual map is indicative of the adequacy of the model. Here, the term 'featureless' means at least 'randomly distributed' residual density which can be assigned to experimental noise. In general, IAM refinement yields residuals especially in the bonding region which vanishes or gets smaller after introducing a multipole model. Strong residuals in the vicinity of the core or in the bonding region are generally a sign of unadequate model while experimental errors mostly yield residuals in larger distances to atom positions.

## 2.7 Deformation density (DD)

In principle, the total density is dominated by core electrons and the density value of bonding regions is by far smaller. Therefore, analysis of the total density generally does not provide much information about the chemical bonding. To illustrate bonding effects or accumulation of density in the lone pairs, the most widely used function is the deformation density which is simply the difference between the total density and spherically averaged hypothetical reference state:

$$\Delta\rho(r) = \rho(r) - \rho_p(r) \quad (\text{Eq. 2-23})$$

In this equation  $\rho_p(r)$  is the promolecule which represents the molecule before the bond formation. Accordingly; the adequacy of a DD map depends on the accuracy of the structural parameters of this promolecule. Most accurately, such parameters can be obtained by neutron diffraction. However, the use of different data set for a single refinement lead to scaling problems since the atomic displacement parameters obtained from X-ray and neutron diffraction show differences.

Another strategy for developing deformation densities is the refinement of high-order data which includes information about the core-region electrons. When difference Fourier synthesis is carried out using all diffraction data, the valence part of the ED is emphasized:

$$\Delta\rho_{\text{deformation}}^{X-X}(r) = \frac{1}{V} \sum_H (F_{\text{obs},X} - F_{\text{calc},X \text{ high order}}) \exp(-2\pi i H \cdot r) \quad (\text{Eq. 2-24})$$

Since valence electrons scatter mainly in the low order region of the data set this procedure yields parameters less biased by bonding effects.<sup>[70]</sup> The drawback of this method is the lack of knowledge for a proper cut-off limit of the high-order refinement for different systems. In this thesis, the deformation ED is obtained by the difference between the static ED fitted to the multipole model and the promolecule density fitted only to the spherical part of the multipole model.

The early work in ED studies was almost exclusively based on the analysis of the deformation density. With the advent of high flux neutron beams it was possible to obtain directly information on the nuclear positions without being influenced by the electron dis-

tribution since neutrons interact with rather atomic nuclei. The combination of this technique with X-ray diffraction is effectively used in order to separate effects of thermal vibrations from the effects of chemical bonding. However, treatment of data obtained from different experimental conditions can be problematic; inappropriate treatment of thermal diffuse scattering (TDS) extinction and absorption effects may lead to discrepancies between X-ray and neutron displacement parameters.<sup>[71]</sup>

Despite the fact that DD maps allows a great diagnostic potential and confirms long-used chemical concepts special care needs to be taken when extracting information about bonding. Incorrect assumption of spherical atoms in the promolecule might lead to negative or very small densities.<sup>[6c, 72]</sup> A weakness of DD is that most of the uncertainty in the deformation densities is directly associated with the uncertainty in the value of the scale factor.<sup>[12]</sup> For elements with more than half-filled valence shells, bonding features in the DD maps may absent, because the reference atoms may contain excess electrons in the orbitals which participates in bond formations.<sup>[73]</sup> Furthermore, in regions of very diffuse density, the absolute values of the deformation density peaks and troughs are not considered as reliable, but it still allows a qualitative comparison.

## 2.8 The quantum theory of atoms in molecules (QTAIM)

Bader<sup>[17]</sup> designed a topological analysis based on a physical observable, the ED distribution  $\rho(r)$  unlike the quantum wave function in the Schrödinger equation which is used in most theoretical calculations and is not observable.<sup>[74]</sup> Important aspects of Bader's theory are that it provides a procedure to partition a molecular structure into submolecular fragments and also allows proper definitions to long used concepts, which are essential to the description of a chemical system. This is achieved by giving a qualitative and quantitative description for atoms as well as different type of interactions by making use of the first and second partial derivatives of the ED function  $\rho(r)$  which leads to the ED gradient vector field  $\nabla\rho(r)$  and the Laplacian  $\nabla^2\rho(r)$ .

### 2.8.1 QTAIM atoms

The topology of  $\rho(r)$  can be well characterized in terms of its derived vector field  $\nabla\rho(r)$ .<sup>[75]</sup> The gradient vector field of the charge density in the Cartesian coordinate system with the unit vectors  $i, j$  and  $k$  is defined as

$$\nabla\rho(\mathbf{r}) = \mathbf{i}\frac{\partial\rho(\mathbf{r})}{\partial x} + \mathbf{j}\frac{\partial\rho(\mathbf{r})}{\partial y} + \mathbf{k}\frac{\partial\rho(\mathbf{r})}{\partial z} \quad (\text{Eq. 2-24})$$

It is represented through a display of the gradient vectors also called the trajectories following the direction of the largest increase in  $\rho(\mathbf{r})$ , being perpendicular to lines of constant density. Every trajectory must originate or terminate at a point where  $\nabla\rho(\mathbf{r})$  vanishes. The areas around nuclear positions are separated by the unique surfaces  $S(\mathbf{r})$  that is not crossed by any gradient lines of the ED  $\rho(\mathbf{r})$ :

$$\nabla\rho(\mathbf{r}) \cdot \mathbf{n}(\mathbf{r}) = 0 \quad (\text{Eq. 2-25})$$

In this equation  $\mathbf{n}(\mathbf{r})$  represents a unit vector perpendicular to the surface at  $\mathbf{r}$ . Since it has a vanishing scalar product this boundary is also called the zero-(ED-gradient) flux surface. This set of surfaces partition a molecule or extended solid into chemically identifiable atomic-like fragments which are called atomic basin. Integration of the model ED over the atomic basins allows the atomic electron populations to be estimated. Within this context an atom is defined as a union of a single attractor, *e.g.* the atomic nucleus and the region containing all gradient paths terminating at the corresponding attractor, the electronic basin. This partitioning provides a comparison between topological properties of different fragments in a system. The sum of contributions of any property from these fragments may be equal to the corresponding property of the total system.

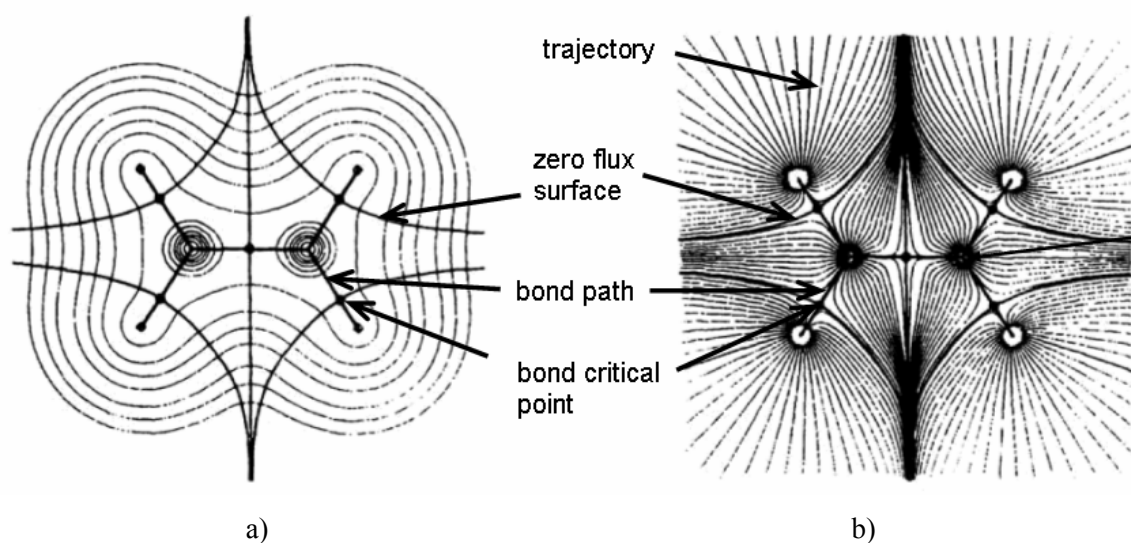


**Figure 2.6** a) A superposition of trajectories associated with the bond paths on a contour map of a charge density in the plane of the ethylene molecule. b) The corresponding gradient vector field in the same plane as shown in a).

It is evident from Figure 2.6 that some gradient paths are connecting certain pairs of nuclei. These are termed bond paths and their presence is considered as a sufficient condition for two nuclei to be bonded. However, they do not represent a bond. As will be demonstrated in the next section, the interactions between the atoms can be characterized in terms of ED properties at the so-called bond critical point.

### 2.8.2 Critical points and their classification

QTAIM not only provides a new definition of an atom but also allows the concept of the chemical bonding to be deduced from the ED topology. The charge density  $\rho(r)$  is a physical quantity which has a definite value at each point of the three-dimensional direct space. It is a scalar field and its topological properties can be determined using the number and kind of its critical points (cp).

In general,  $\rho(r)$  exhibits local maxima only at nuclear positions according to the observations based on experimental results obtained from X-ray diffraction studies on crystals and theoretical calculations. These are the points where a gradient path  $\nabla\rho(r)$  terminates. Gradient paths originate and terminate in an isolated molecule at points where the first derivatives of  $\rho(r)$  vanish. These locations of extrema are associated with a point in space called a critical point which describes and quantifies important interactions between atoms. Critical points are distinguished according to the nature of the extremum (maxima, minima or saddles). In order to analyse these extrema the curvature of  $\rho(r)$  at the corresponding point has to be determined which necessitates the analysis of nine second-order derivatives of  $\rho(r)$  in three dimensional form. This is the so-called  $3 \times 3$  array Hessian matrix of the charge density:

$$H(r) = \begin{bmatrix} \frac{\partial^2 \rho(r)}{\partial^2 x^2} & \frac{\partial^2 \rho(r)}{\partial x \partial y} & \frac{\partial^2 \rho(r)}{\partial x \partial z} \\ \frac{\partial^2 \rho(r)}{\partial y \partial x} & \frac{\partial^2 \rho(r)}{\partial^2 y^2} & \frac{\partial^2 \rho(r)}{\partial y \partial z} \\ \frac{\partial^2 \rho(r)}{\partial z \partial x} & \frac{\partial^2 \rho(r)}{\partial z \partial y} & \frac{\partial^2 \rho(r)}{\partial^2 z^2} \end{bmatrix} \quad (\text{Eq. 2-26})$$

Since it is real and symmetric  $H(r)$  can be diagonalized. The diagonalized form of  $H(r)$  is denoted by the matrix



$$H(r) = \begin{bmatrix} \frac{\partial^2 \rho(r)}{\partial^2 x^2} & 0 & 0 \\ 0 & \frac{\partial^2 \rho(r)}{\partial^2 y^2} & 0 \\ 0 & 0 & \frac{\partial^2 \rho(r)}{\partial^2 z^2} \end{bmatrix} = \begin{bmatrix} \lambda_1 & 0 & 0 \\ 0 & \lambda_2 & 0 \\ 0 & 0 & \lambda_3 \end{bmatrix} \quad (\text{Eq. 2-27})$$

In diagonalized form, the Hessian matrix provides three eigenvalues  $\lambda_1$ ,  $\lambda_2$  and  $\lambda_3$  which characterize the ED curvature. The classification of the critical points is then carried out according to their rank  $w$  and signature  $\sigma$ . The rank is the number of non-zero eigenvalues of the ED curvature whereas the signature is the sum of the algebraic signs of the eigenvalues.

A critical point with  $w < 3$  and with at least one zero curvature is said to be degenerate. Degenerate critical points can vanish or bifurcate into a number of non-degenerate or stable ( $w = 3$ ) critical points due to small changes in the charge density. The existence of degenerate critical points indicates the onset of structural changes in a molecule.

There are four possible types of critical points in a three dimensional scalar distribution of rank three which are listed in Table 2.2. At a critical point where all curvatures are negative ( $w = 3$ ,  $\sigma = -3$ )  $\rho(r)$  exhibits a local maximum. This typically occurs at nuclear positions.

**Table 2.2** Classification of critical points according to their rank and signature.

$w, \sigma$	$\lambda_i$	Type
(3, -3)	all $\lambda_i < 0$	nuclear position
(3, -1)	two $\lambda_i < 0$ one $\lambda_i > 0$	bond critical point (bcp)
(3, +1)	two $\lambda_i < 0$ one $\lambda_i > 0$	ring critical point (rccp)
(3, +3)	all $\lambda_i > 0$	cage critical point (ccp)

The interaction between two atoms results in the formation of the bond critical point (3, -1) cp when at  $r_c$   $\rho(r)$  is a maximum in the plane defined by the axes corresponding to the negative curvatures  $\lambda_1$  and  $\lambda_2$ ;  $\rho(r)$  is a minimum at  $r_c$  along the third axis of the positive curvature  $\lambda_3$  which is perpendicular to this plane. The existence of the (3, -1) cp between two atoms is a

necessary condition for the chemical bond to be present. Gradient paths which originate at the bond critical point and terminate at each of the two nuclei define the bond path. The formation of a bond path indicates the accumulation of ED, thus it is the line of maximum density between linking two atoms. The bond path is not necessarily a straight line, it can be bent. Bent bonds indicates that there is strain in the bond.<sup>[76]</sup> The distance between the line connecting two atoms and the bond critical point is a measure of degree of bond-bending.

The cp type of (3, +1) or ring critical point (rcp) is present at the center of a ring of bonded atoms and arises when two curvatures are positive and at  $r_c$   $\rho(r)$  is a minimum in the plane defined by the axes corresponding to the positive curvatures;  $\rho(r)$  is a maximum at  $r_c$  along the third axis which perpendicular to this plane.

Finally, the (3, +3) cp or cage critical point (ccp); where all curvatures are positive and  $\rho(r)$  is a local minimum at  $r_c$ , is found at the centre of the cage structure which is bounded by ring surfaces.

In an isolated molecule, or cluster of atoms for a number of different types of critical points  $m(w, \sigma)$ , the Poincaré-Hopf relationship<sup>[77, 78]</sup> holds

$$m(3, -3) - m(3, -1) + m(3, +1) - m(3, +3) = 1 \quad (\text{Eq. 2-27})$$

While QTAIM was initially developed for the analysis of theoretical densities, it has been shown also to be a powerful tool for classification of chemical bonding based on experimental ED. It allows a comparison between theory and experiment, hence a bridge between two methods. ED distribution differences can be classified as quantitative and qualitative.<sup>[79]</sup> If the number and type of the critical points is the same for two models but only the values differ, the difference is regarded to be only quantitative. If there are not equal numbers of saddle points, maxima and minima, this case corresponds to a qualitative difference. However, for structures involving transition metals the magnitudes of the eigenvalues might be too small leading to uncertainties in estimation of the true cp type since EDs is very flat in interatomic regions. In those cases, two models might differ quantitatively only slightly, discrepancies due to different type of cps notwithstanding.

### 2.8.3 Laplacian

An important function of the ED is its Laplacian, which is the sum of the diagonal elements of the Hessian matrix and defined as

$$\nabla^2 \rho(\mathbf{r}) = \frac{\partial^2 \rho(\mathbf{r})}{\partial x^2} + \frac{\partial^2 \rho(\mathbf{r})}{\partial y^2} + \frac{\partial^2 \rho(\mathbf{r})}{\partial z^2} = \lambda_1 + \lambda_2 + \lambda_3 \quad (\text{Eq. 2-28})$$

The sign of the  $\nabla^2 \rho(\mathbf{r})$  can be related to the character of the atomic interactions, *i.e.*, the character of the chemical bond. It depends on the relation between the principal curvatures of the ED and characterizes the concentration or depletion of electrons at each point,  $r$ . At the bcp, negative  $\lambda_1$  and  $\lambda_2$  values indicate that there is a contraction of ED toward the bcp, perpendicular to the bond path and the positive  $\lambda_3$  value measures the degree of ED contraction toward each of the neighboring nuclei. The formation of a chemical bond is a result of a competition between perpendicular contractions of  $\rho(\mathbf{r})$  leading to a concentration of ED along the bond path and the expansion of  $\rho(\mathbf{r})$  leading to concentration of ED in the basins of neighbouring atoms. The sign of the Laplacian at  $r$  depends on which of the two competing effects dominates. If the positive curvature dominates, thus  $\nabla^2 \rho(\mathbf{r})$  is positive at the bcp, the ED is depleted in the interaction surfaces and concentrated in each of atomic basins separately which is typical of closed shell interactions (*i.e.*, ionic and van der Waals interactions). This picture is characterized by a relatively low value of  $\rho(\mathbf{r})$ . Small values for  $\rho(\mathbf{r})$  in closed shell interactions are not necessarily an implication of weak interactions. For highly ionic interactions these values may be small. Nevertheless, the transfer of charge from one atomic basin to the other may result in a strong interaction. In cases, where negative curvatures dominate ( $\nabla^2 \rho(\mathbf{r}_b) < 0$ ) the ED is locally concentrated at the bcp. This is the case when shared interactions (covalent bonds) are present. The deviation of the bcp from the midpoint of the bond path is an indication of polarity of the bond.

The ED distribution of an isolated atom has a single maximum corresponding to the nucleus position and decays exponentially with distance from the atom. On the other hand, Laplacian distribution in the outer shell of an atom is characterized by alternating shells where the ED is locally concentrated ( $\nabla^2 \rho(\mathbf{r}) < 0$ ) and depleted ( $\nabla^2 \rho(\mathbf{r}) > 0$ ). The portion of the outermost shell over which the Laplacian has a negative sign, is termed as the valence shell charge concentration (VSCC). Charge concentrations in the Laplacian distribution should not be mixed with the localized electron pairs.<sup>[16d]</sup> In general, formation of a chemi-

cal bond leads to structurization of ED Laplacian distribution.<sup>[80]</sup> For  $3d$  transition metals, asphericity of the Laplacian distribution generally indicates the participation of  $3d$  orbitals in transition metal bonding.

Positive Laplacian, though associated with charge depletion, cannot be considered as a clear-cut sign of closed-shell interaction for transition metals.<sup>[81]</sup> The reason is that the one-to-one correspondence of  $\nabla^2\rho(r)$  distribution with the shell structure is lost and as a result, the bcps fall almost without exception in a zone of charge depletion due to the lack a distinct charge concentration in the outermost shell.<sup>[82]</sup>

### 2.8.4 The ellipticity

An important property of  $\rho(r)$  at the bcp is the ratio of its negative curvatures along axes perpendicular to the bond path which corresponds to the quantitative measure of preferential concentration of electrons in a plane perpendicular to the bond path.

$$\varepsilon = (\lambda_1 / \lambda_2) - 1 \quad (\text{Eq. 2-29})$$

In this equation  $\varepsilon$  is called the bond ellipticity. It gives a quantitative generalization of the concept of  $\sigma$  and  $\pi$  character of a bond. For a cylindrically symmetric bond the axes associated with  $\lambda_1$  and  $\lambda_2$  are symmetrically equivalent which result in  $\lambda_1 / \lambda_2 = 1$  and  $\varepsilon = 0$ . Ellipticity values differ from zero *e.g.* for double bonds which have a  $\pi$  contribution as an indication of deviation from cylindrical symmetry of the bond. Such deviations can be observed in DD maps. However, a precise quantification is not possible in those cases.

### 2.8.5 The ratio $|\lambda_1|/\lambda_3$

Another topological quantity used particularly for homoatomic interactions is the ratio between the magnitude of the largest perpendicular contraction of ED  $|\lambda_1|$  at the (3, -1) critical point and the parallel contraction of ED  $\lambda_3$  towards the nuclei. The ratio  $|\lambda_1|/\lambda_3$  increases with bond strength for shared-type interactions.

### 2.8.6 The electronic energy density

Further information about the bonding type can be extracted from the local electron energy densities [ $G(r)$  = kinetic energy density,  $V(r)$  = potential energy density]. The local

energy density is calculated from the Laplacian function using the approximation for  $G(r)$  proposed by Kirzhnits<sup>[83]</sup> in combination with the local virial theorem from which  $V(r)$  is estimated:<sup>[84]</sup>

$$2G(r) + V(r) = (\hbar / 4m) \nabla^2 \rho(r) \quad (\text{Eq. 2-30})$$

Here,  $m$  is the electron mass,  $G(r)$  and  $V(r)$  describe the local contributions to the electronic kinetic and potential energies;  $G(r) > 0$  and  $V(r) < 0$  everywhere in the equilibrium system.<sup>[85]</sup> Cremer and Kraka used energetic considerations for the characterization of the chemical bond.<sup>[86]</sup> The local energy densities  $G(r)$  and  $V(r)$  can be compared in the bonding region through the equation:

$$H(r) = G(r) + V(r) \quad (\text{Eq. 2-31})$$

The sign of the total electronic energy density  $H(r)$  gives a straightforward criterion for the recognition of the atomic interaction type. Since  $V(r)$  is always negative and  $G(r)$  always positive, the sign of the energy density  $H(r)$  reveals whether  $V(r)$  or  $G(r)$  dominates in the bonding region. In shared type atomic interactions  $V(r)$  dominates and  $H(r)$  is negative. In closed-shell type interactions the local kinetic energy outweighs the potential energy and  $H(r)$  is positive.

### 2.8.7 The transferability concept

Bader states in his theory that two resembling molecular fragments in different environments enclosed by a zero-flux surface can be substituted when there is negligible changes in their electron-density properties.<sup>[17]</sup> This concept is the so-called transferability of submolecular fragments. Taking the advantage of the transferability, larger functional groups can be built from a limited number of known pseudoatomic densities keeping the multipole populations the same for the resembling pseudoatoms. In cases, where the transferred functional groups undergo minor changes, the ED properties of these new groups can be predicted. One important question is to what extent these transferred functional groups can be preserved in different resembling chemical environments since every transfer causes small perturbations in the density and hence in its properties.

As a consequence of experimental verification of transferability, 'deformation density databanks' are established with averaged multipole populations for each chemically unique and transferable pseudoatom.<sup>[69, 87]</sup> The experimental examination of transferability of atomic densities utilizing high resolution X-ray diffraction method was first carried out for molecular crystals<sup>[87]</sup> These compounds are more suitable for an experimental ED analysis as compared to extended solids for various reasons.<sup>[88]</sup> First of all, non-stoichiometry of the compositions and the related defect structure are quite debatable in extended solids<sup>[47]</sup> Furthermore, studies of compounds including heavier elements demand a much higher accuracy of the diffraction data since the scattering contribution from valence electrons form a smaller part of the diffraction intensity relative to the dominating core contribution.<sup>[89]</sup> Additional problems are typically induced by high-symmetry space groups along with symmetry-restrictions for the atomic sites involved. Structures with small unit cells yield very few low-order reflections which can be biased by systematic errors like extinction and/or absorption.

Transferability of the pseudoatomic atomic densities offers important advantages from experimental point of view. First of all, it is possible to determine accurate ED in a reasonable time from 'normal resolution' data as experimentally inaccessible multipole parameters are kept at theoretically predicted values. The decrease in the number of variables used also reduces the correlations between the parameters refined.

### 2.8.8 The electrical field gradient

The electric-field gradient (EFG) at nuclear positions is an important characteristic which arise from the non-spherical charge distribution due to the interaction of the nuclear charge density moments with the multipole moments of the ED relative to the nuclei. Experimentally, the EFG can be detected for crystals containing nuclei with nuclear spin  $I > 1/2$  via its interaction with the quadrupolar moment of the nucleus. For this, the quadrupolar frequency is measured with techniques such as nuclear magnetic resonance (NMR) or Mössbauer spectroscopy. The quadrupolar frequency of a nucleus  $\nu_{aa}$  is related to the EFG  $\nabla E_{aa}$  through the equation

$$\nabla E_{aa} [V / m^2] = \frac{h}{eQ} \frac{2I(2I-1)}{3} \times 10^6 \nu_{aa} [MHz] \quad (\text{Eq. 2-32})$$

where  $h$  is the Planck constant ( $6.626075 \times 10^{-34} \text{ J s}$ ),  $e = 1.60210^{-19} \text{ C}$  is the elementary charge,  $v_{\alpha\alpha}$  is the nuclear quadrupolar moment in Barn ( $1\text{b} = 10^{-28} \text{ m}^2$ ), which is well known for all nuclei and  $I$  is the nuclear spin. The sign of EFG is often understood to be the sign of the largest component  $\nabla E_{zz}$ .

It is possible to determine the EFG from the multipole model using a simple approximation of the electronic contribution to the EFG in the form<sup>[90]</sup>

$$\nabla E_{zz} = -(e / 4\pi\epsilon_0)[6 \times 3^{1/2} \alpha^3 / 5n_2(n_2 + 1)(n_2 + 2)]P_{20} \quad (\text{Eq. 2-33})$$

In this equation,  $P_{20}$  is the electron population of the quadrupole density term, and  $n_2$  is the power index in the quadrupole component of the pseudoatom ED radial part and  $\alpha$  is a model parameter determined by least squares in units of  $\text{m}^{-1}$ .

The contributions to the EFG originate mainly from the atomic valence-shell asphericity and peripheral (lattice) contributions due to the surrounding atoms. The latter is important when short interatomic distances are present in the crystal. On the other hand, for transition metal atoms, the contribution of the valence shell to the EFG is more pronounced. In general, the EFG is particularly sensitive at distances close to the nucleus and is difficult to extract from the X-ray experiment due to the resolution limit of the data. Since the thermal motion is deconvoluted from the ED density, the EFG value obtained from the multipole parameters accounts for the static crystal. On the other hand, the spectroscopic data is affected by vibrations. Therefore, there may be a systematic difference between the two set of values.

## 2.9 Quantumchemical calculations

In this thesis, the experimentally reconstructed ED, in case of all structures investigated, is compared with DFT calculations which are carried out by Baranov.<sup>[22a]</sup> The scalar-relativistic all-electron full-potential DFT calculations employing (L)APW+lo+LO basis set are done using LDA Perdew-Wang<sup>[22b]</sup> exchange-correlation functional with the Elk program.<sup>[22c]</sup> The  $R \times G$   $k_{\text{max}}$  parameter is set to 10 and the MT-sphere radii are 2.0 a.u. for Ti and V and 1.45 a.u. for B. The planewave expansion cut-off for potential and density is  $G_{\text{max}} = 26 \text{ a.u.}^{-1}$  and the multipole expansion cut-off for potential, density and wave function is set to  $l_{\text{max}} = 12$ . APW radial functions with  $l = 2$  for metal atoms and for all  $l$  for B atoms are linearized to the first order to achieve acceptable smoothness of the electron den-

sity Laplacian. Meshes of 80, 80, 92 and 480 irreducible  $k$  points are used for  $\text{TiB}_2$ ,  $\text{VB}_2$ ,  $\text{V}_3\text{B}_4$  and  $\text{VB}$ , respectively. The calculation, topological analysis and evaluation of critical points of electron density is done with the program DGrid<sup>[22d]</sup> on a discrete grid with the mesh size of  $\approx 0.05$  a.u.



### 3 SYNTHESIS, CHARACTERIZATION AND CRYSTAL STRUCTURE OF VANADIUM BORIDES

For the very hard materials such as vanadium borides, single crystals have to be obtained directly from the synthetic experiments as severe problems arise from any kind of crystal shaping in order to reduce the crystal size. In this section, the efforts for obtaining suitable vanadium boride single crystals for a charge density analysis are presented. The homogeneity range and the microstructure of the compounds are examined by X-ray powder diffraction and Wavelength dispersive X-ray spectroscopy analyses (WDXS), respectively. Crystal structures of  $\text{VB}_2$ ,  $\text{VB}$ ,  $\text{V}_3\text{B}_4$  and  $\text{VB}_2$  based on single crystal X-ray diffraction data are described in detail.

#### 3.1 Synthesis

It is, in general, a challenging task to prepare homogeneous, single phase transition metal borides due to their unusual high melting point. Figure 3.1 shows the most recently published V–B phase diagram<sup>[91]</sup> which is based on the the optimization of the thermochemical and experimental data.<sup>[92]</sup> In the vanadium-boron system the binary phases  $\text{V}_3\text{B}_2$ ,  $\text{VB}$ ,  $\text{V}_5\text{B}_6$ ,  $\text{V}_2\text{B}_3$ ,  $\text{V}_3\text{B}_4$ , and  $\text{VB}_2$  have been reported so far.

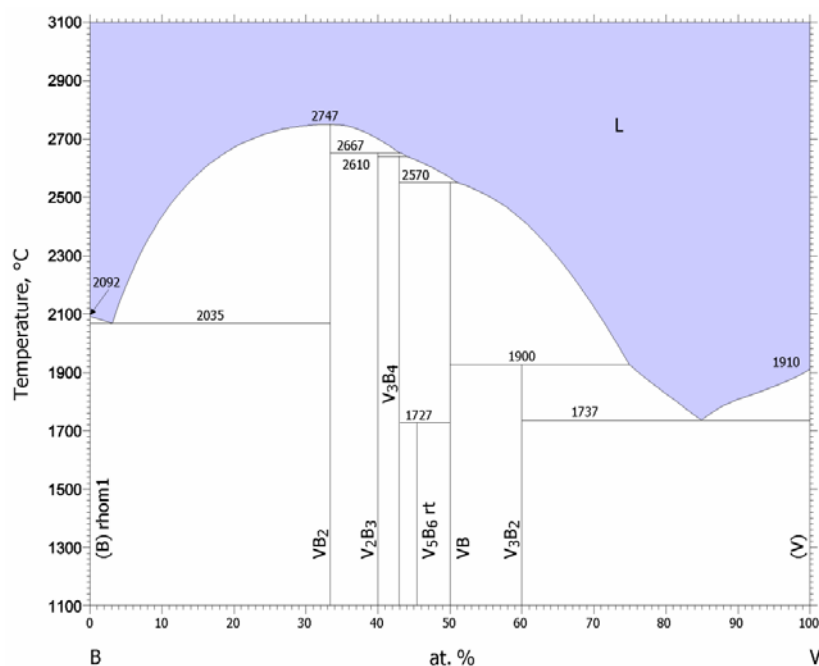


Figure 3.1 V-B phase diagram.<sup>[91]</sup>

It is apparent from the phase diagram that all binary vanadium borides form above 2500 °C except  $V_3B_2$  and  $V_5B_6$ .  $VB_2$  has the highest melting temperature (2747 °C) compared to other phases. Besides, it is a congruent melting phase. The reaction types for all phases in V–B system is summarized in Table 3.1. On the vanadium-rich side where VB appears, there are contradictory results about its formation. Rostoker *et al.*<sup>[93]</sup> reported that VB forms by a peritectic reaction between the liquid and  $VB_2$  whereas Rudy *et al.*<sup>[92b]</sup> claimed that there is a peritectic reaction between the liquid and  $V_3B_4$ . Blumenthal *et al.*<sup>[94]</sup> and most recently de Lima *et al.*<sup>[95]</sup> suggested a congruent formation for this phase. The phases  $V_3B_4$  and  $V_2B_3$  as well as the  $V_3B_2$  at the very vanadium rich part of the phases diagram form from the liquid through the peritectic reactions.

**Table 3.1** Reactions of the V–B system and compositions of the liquid phase (at. % B) based on different studies.

	(at. % B)	Reaction type	Reference
$L \rightleftharpoons VB_2 + B$	95	eutectic	De Lima <sup>[95]</sup> ,
$L \rightleftharpoons VB_2$	67	congruent	Rudy <sup>[92b]</sup> , de Lima <sup>[95]</sup> , Norton <sup>[96]</sup> , Kieffer <sup>[97]</sup> , Post <sup>[98]</sup>
$VB_2 + L \rightleftharpoons V_2B_3$	57, 58	peritectic	De Lima <sup>[95]</sup> , Spear <sup>[92a]</sup>
$V_2B_3 + L \rightleftharpoons V_3B_4$	54, 56	peritectic	Spear <sup>[92a]</sup> , De Lima <sup>[95]</sup>
$V_3B_4 + L \rightleftharpoons V_5B_6$	52-56	peritectic	Nunes <sup>[99]</sup>
$V_3B_4 + VB \rightleftharpoons V_5B_6$	—	peritectoid	Spear <sup>[92a]</sup>
$V_3B_4 + L \rightleftharpoons VB$	47	peritectic	Rudy <sup>[92b]</sup>
$VB_2 + L \rightleftharpoons VB$	—	peritectic	Rostoker <sup>[93]</sup>
$L \rightleftharpoons VB$	50	congruent	Blumenthal <sup>[94]</sup> , De Lima <sup>[95]</sup>
$VB + L \rightleftharpoons V_3B_2$	19, 26	peritectic	De Lima <sup>[95]</sup> , Rudy <sup>[92b]</sup>
$L \rightleftharpoons V_3B_2$	40	congruent	Nowotny <sup>[92c]</sup>
$L \rightleftharpoons V + V_3B_2$	12	eutectic	De Lima <sup>[95]</sup>

It is evident from the phase diagram that the respective formation temperatures of the intermediate phases  $V_3B_4$  and  $V_2B_3$ , in particular, are too close to each other.<sup>[100]</sup> The proximity of the formation temperatures together with the incongruent decomposition

complicates the preparation of homogenous single crystals of the respective phases using conventional synthesis methods.

There are also contradictory results on the formation reaction of  $V_5B_6$ . According to the phase diagram shown in Figure 3.1 a solid-state formation (peritectoid reaction) is proposed. However, careful studies by de Nunes *et al.* showed that  $V_5B_6$  phase is formed from the liquid through the peritectic reaction.<sup>[99]</sup>

For large scale production generally metal borides are prepared by carbothermal reduction of metal oxides at temperatures above 1400 °C according to the reaction:<sup>[101]</sup>



Depending on the desired reaction product carbon, metal carbide or boron are included in the starting materials of the reaction given above.<sup>[102]</sup> However, the reaction product includes often carbon and oxygen as an impurity; therefore high temperature purification is necessary.<sup>[33]</sup>

There are several methods for the preparation of vanadium borides on laboratory scale. One of the major phase studies in the system was performed by direct synthesis by arc-melting experiments just by mixing stoichiometric amounts of the respective elements at high temperatures.<sup>[92, 95, 103]</sup> In principle, at high temperatures generally thermodynamically the most stable compound is formed as there is little room for kinetic control. On the other hand, the synthesis of single-phase intermediate compounds showing slight differences in their formation temperatures is mostly hampered due to lack of temperature control. Furthermore, fast cooling does not provide a favourable environment for crystal growth.

Another method of obtaining vanadium boride single crystals is the vapour deposition method. This method is applied for the synthesis of  $VB_2$  where boron trichloride-hydrogen mixture and vanadium sulfides or chlorides were used as the educts.<sup>[104]</sup> The purity of the products synthesized depends primarily upon the purity of the starting materials in particular of  $H_2$ . Campbell *et al.* synthesized vanadium borides according to a similar reaction also with the use of vapour-phase deposition.<sup>[105]</sup>



Further methods for the synthesis of vanadium borides are the borothermic reaction of vanadium oxide ( $V_2O_3$ )<sup>[101]</sup> and solid state reaction between vanadium chloride and  $MgB_2$ ,  $NaBH_4$  or  $LiBH_4$ .<sup>[106]</sup>

In principle, high temperatures enhance the diffusion of reactants. In cases where high temperatures are not enough to overcome the activation energy barrier for the formation of desired products, starting materials are ground to powders to expose fresh surfaces. Unfortunately, grinding of reactants introduces contaminants, in particular for very hard materials. The development of a method which allows the reactions to be carried out at lower temperatures would be a highly desirable achievement since along this way problems like the need of a construction of a high temperature apparatus or grinding of very hard starting materials can be circumvented. The so-called “flux method” or “auxiliary metal bath technique” provides high diffusion rates of reactants achieved by simply allowing starting materials to react in a solvent. Consequently; for a reaction to take place activation barriers can be overcome at lower temperatures and new compounds can be synthesized. Recently, there are an increasing number of studies where single crystals of vanadium borides are synthesized from solution. In this method, the starting materials react in a metal solvent from which the crystals can subsequently be extracted.<sup>[107]</sup>

Both the quality as well as the size of the crystal is an important consideration for charge density experiments. In cases of strong absorption and extinction effects, very small crystals (below around  $100\ \mu m$ ) with well defined faces are highly desirable. An important advantage of the metal-flux method is that slow cooling of the saturated solution provides a favourable environment for crystal growth.

Kieffer was the first who mentioned in his papers about several key requirements to be fulfilled by the solvent metal.<sup>[108]</sup> First of all, the metal should have a reasonable low melting point and low vapour pressure at the temperature of the synthesis so that conventional heating equipment and containers can be used. It should be able to dissolve the starting components at the synthesis temperature to some extent at least. However, it should not react with starting components in order to form compounds more stable than the desired product. Finally, it should be possible to separate the metal from the reaction products either by chemical dissolution, distilling it in vacuum or by mechanical removal.

Aluminium metal has been shown a useful flux in the synthesis of vanadium borides since it meets these characteristics which are mentioned above.<sup>[31a, 45a, 109]</sup> It melts at 660 °C and dissolves both vanadium and boron at elevated temperatures according to the respective phase diagrams.<sup>[110]</sup> Furthermore, it can be easily removed by a nonoxidizing acid in which borides are characterized by a general inertness.<sup>[111]</sup> In general, for transition metal borides resistance against hydrochloric acid (HCl) and sulphuric acid (H<sub>2</sub>SO<sub>4</sub>) increases with increasing atomic number in any group or period. On the other hand, all borides dissolve in oxidising acid mixtures, *e.g.* aqua regia, HNO<sub>3</sub>-H<sub>2</sub>SO<sub>4</sub>, HNO<sub>3</sub>-H<sub>2</sub>O<sub>2</sub>, *etc.* Hot concentrated sulphuric acid attacks all borides yielding sulphur dioxide.<sup>[112]</sup> Similarly, hydrofluoric acid and nitric acid dissolves transition metal borides.

The formation of Al<sub>1-x</sub>B<sub>2</sub> as an impurity by Al flux-synthesis of intermetallic borides is investigated. Thermodynamic analyses carried out at a temperature range between 675 °C to 900 °C indicate that formation of ZrB<sub>2</sub>, TiB<sub>2</sub> and VB<sub>2</sub> in Al solution is more favored in comparison to that of Al<sub>1-x</sub>B<sub>2</sub>.<sup>[113]</sup> Higashi *et al.*<sup>[45a]</sup> studied the solubility of aluminium in various metal borides including TiB<sub>2</sub>, ZrB<sub>2</sub>, HfB<sub>2</sub>, VB, V<sub>3</sub>B<sub>4</sub>, NbB<sub>2</sub>, TaB and W<sub>2</sub>B<sub>5</sub> by a synthesis from the aluminium melt at elevated temperatures. The solubility of Al in these borides is reported 0.1 wt. % maximum. Accordingly, Al<sub>1-x</sub>B<sub>2</sub> do not form mixed crystals with the respective borides.

### **3.1.1 Preparation of vanadium boride crystals by Al flux method**

In the present work, the "LORA" model high temperature furnace produced by HTM Reetz GmbH is used for the preparation of vanadium borides via aluminium flux method as shown in Figure 3.2. The corund crucible which includes mixture of starting materials is placed in a tube which is the essential part of the furnace. This tube made of sintered aluminium oxide enables operation in inert atmospheres up to 1800 °C. The diameter and the length of the tube are 32 mm and 600mm, respectively. The molybdenum heating conductor is directly wound on this tube. To protect the heating conductor from oxidation, it is enclosed in stainless steel housing and the chamber is purged with nitrogen. The temperature is measured directly at the sample with a type-C (W5% Re / W26% Re) thermocouple which capability of measuring temperatures are varying in the range of 0 °C - 2319 °C.

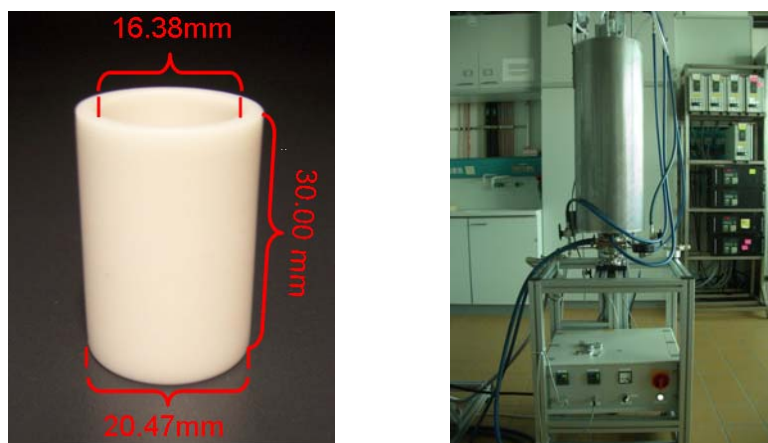


**Figure 3.2** The corund crucible (left) and high temperature furnace for Al flux experiments (right).

The starting materials used for the reactions are vanadium powder, crystalline boron powder and aluminium metal chips (purity grades: V — 99.99 %; cryst. B — 99.995 %; Al — 99.995 %). They are weighted various amounts and placed in corund crucible in an argon-filled glove box. For the synthesis, the amounts of aluminium and vanadium are kept constant at 3.71 g and 250 mg, respectively ( $\text{Al/V}=28.1$ ), whereas the boron content is varied according to desired composition. The samples are transferred from the glove box to the furnace in a sealed metal container in order to prevent the formation of oxide layers on the surfaces. In a typical procedure the mixtures are tempered in the furnace under argon atmosphere at 1500 °C. The melt is cooled during 6h from 1500 °C to 660 °C. Excess aluminium is dissolved in diluted hydrochloric acid within 4-5 days. The reaction product consists of metallic shining, well-shaped crystals besides which transparent impurities are detected (Figure 3.3).

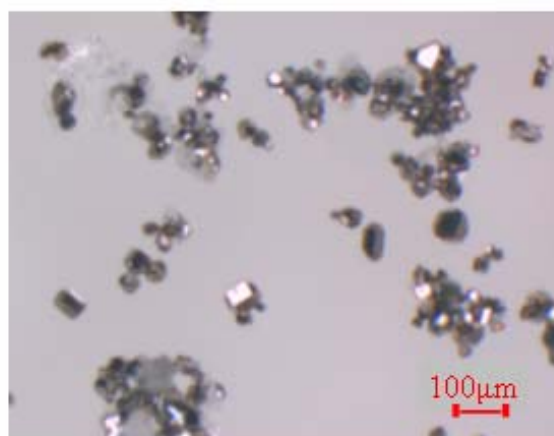


**Figure 3.3:** VB<sub>2</sub> crystals synthesized by Al flux.

Attempts for the synthesis of  $V_3B_4$ ,  $V_2B_3$  and  $V_5B_6$  do not yield the desirable reaction products using the reaction route described above. For the synthesis of  $V_3B_4$  and  $V_2B_3$  samples are maintained 12 h at 1500 °C, cooled at a rate of 5 K/min to 1100 °C. After second soaking of 24 h at this temperature, the melt is slowly cooled during 10 h from 1100 °C to 660 °C. For the synthesis of  $V_5B_6$  the samples are heated for 6 h at 1500 °C, the melt is cooled at a rate of 5 K/min down to 1100 °C, maintained for 12 h at 1100 °C and finally cooled at a rate of 1 K/min down to 660 °C.

### 3.1.2 Preparation of vanadium borides by arc-melting

The starting materials are vanadium powder, amorphous boron powder (purity grades: V—99.99 %; amorph. B—95 %, Mg max. 0.8 %). For the synthesis, the amount of vanadium is kept constant at 150 mg while the boron content is varied with desired composition. The components are thoroughly mixed and pressed into pellets which are melted on a copper hearth with a tungsten electrode. The sample pellets of about 1 cm in diameter and 0.3 mm in height are small enough to ensure that the entire sample is in the liquid state during arc-melting. The pellets are inverted and remelted to homogenize through whole sample. As will be discussed in the following section some samples contain mixtures of several phases. These are placed in evacuated and sealed Ta ampoules and annealed for one week at 1500 °C after the arc-melting preparation in the same furnace as used for the Al flux synthesis.

## 3.2 Characterization

### 3.2.1 X-ray powder diffraction

For X-ray powder diffraction (XRPD) experiments the samples are finely ground in WC mortar which is damaged due to the extreme hardness of the materials. Phase analysis is performed on Guinier powder data (Huber G670 Image Plate Camera,  $CuK\alpha_1$  radiation,  $\lambda = 1.54060$  Å, graphite monochromator,  $5^\circ \leq 2\theta \leq 100^\circ$ ,  $\Delta 2\theta = 0.005$ ). Using WinCSD program package<sup>[114]</sup>, the unit cell parameters are calculated from a least-square refinement where Si is used as internal standard ( $a = 5.430825(11)$  for  $\lambda = 1.54060$  Å at 298.1 K).<sup>[115]</sup>

Figure 3.4 shows the X-ray diffraction powder patterns of binary vanadium borides prepared using both Al flux method as well as by arc-melting together with the calculated positions of the diffraction lines from the single-crystal refinements carried out in the pre-

sent work except for that of  $V_3B_2$  which is taken from Riabov *et al.*<sup>[31b]</sup> Tungsten carbide (WC) observed in the powder pattern of each compound, points to the extreme hardness of the materials.

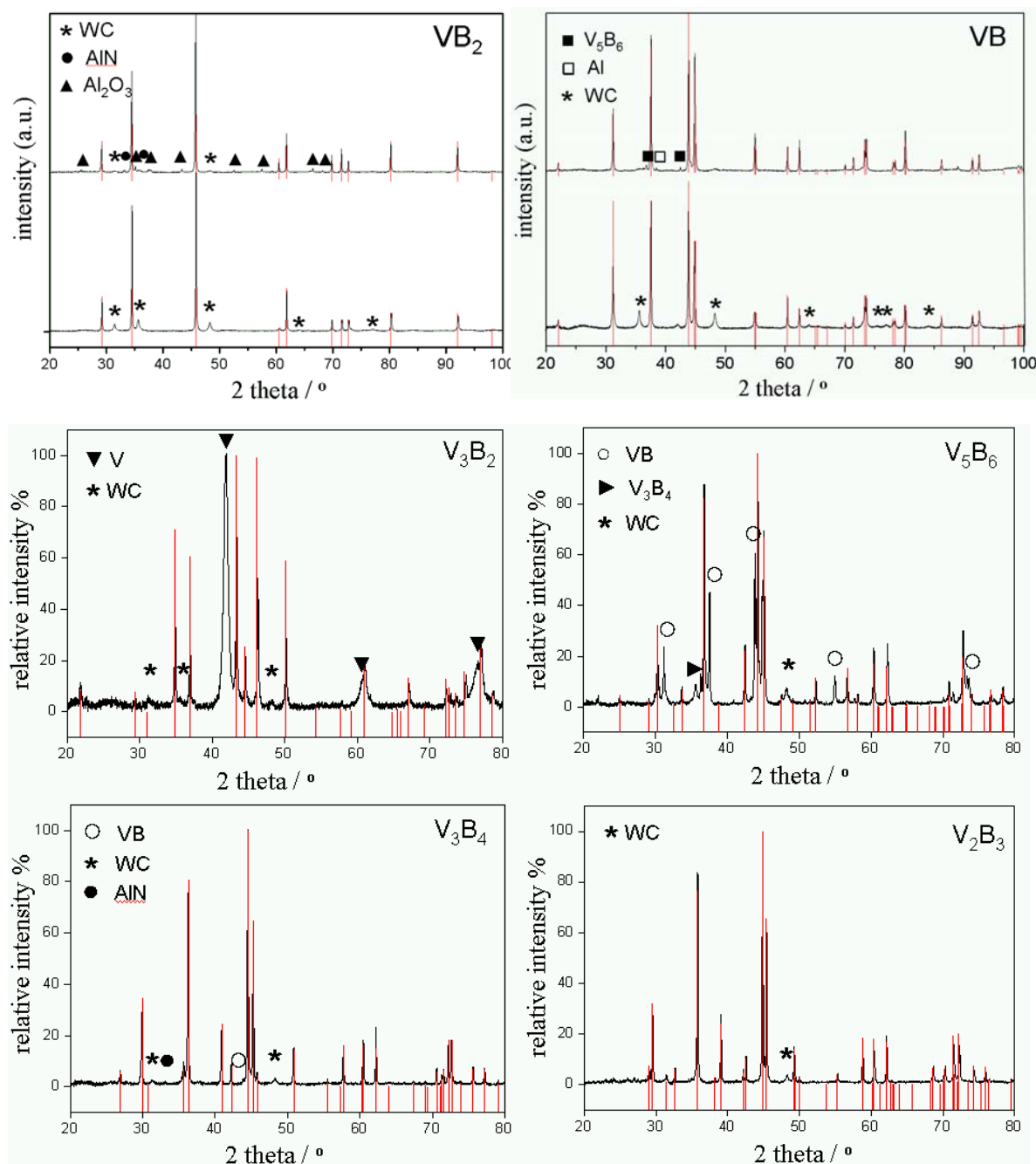


**Figure 3.4:** Observed X-ray powder diffraction data and calculated diffraction peak's positions lines from single crystal refinement (red) for binary vanadium borides. In case of VB<sub>2</sub> and VB, diffractograms in the upper part and lower part show diffraction data of samples prepared using Al melt and by arc-melting, respectively.



Sufficient non-overlapping powder diffraction lines are identified for the unit cell refinement for all six binary vanadium borides. A pseudo-Voigt function is chosen to describe the line shape of the diffraction peaks. Peak positions are corrected for peak asymmetry. The calculated lattice parameters and estimated standard deviations were averaged on different samples. Table 3.2 summarizes the space group and the lattice parameters of all known binary vanadium borides according to X-ray powder diffraction results. The unit cell dimensions are generally in good agreement with previously published data. The lattice parameters of VB, V<sub>3</sub>B<sub>4</sub>, V<sub>2</sub>B<sub>3</sub> and VB<sub>2</sub> obtained from powder X-ray diffraction experiments are used for the respective single crystal refinements.

**Table 3.2:** Lattice parameters of vanadium borides.

Compound	Space group	Lattice parameters (Å)		
		This work	References	
VB <sub>2</sub>	<i>P6/mmm</i>	$a = 2.9977(2)$ $c = 3.0560(3)$	$a = 2.998(1)$ $c = 3.056(1)$	Spear <i>et. al.</i> <sup>[92a]</sup>
V <sub>2</sub> B <sub>3</sub>	<i>Cmcm</i>	$a = 3.0660(3)$ $b = 18.428(1)$ $c = 2.9843(2)$	$a = 3.0599(4)$ $b = 18.429(2)$ $c = 2.9839(4)$	Yu <i>et. al.</i> <sup>[31a]</sup>
V <sub>3</sub> B <sub>4</sub>	<i>Immm</i>	$a = 2.9821(2)$ $b = 3.0601(2)$ $c = 13.2251(5)$	$a = 2.981(1)$ $b = 3.058(1)$ $c = 13.220(4)$	Spear <i>et. al.</i> <sup>[92a]</sup>
V <sub>5</sub> B <sub>6</sub>	<i>Cmmm</i>	$a = 2.9860(2)$ $b = 21.260(4)$ $c = 3.0645(6)$	$a = 2.9773(2)$ $b = 21.242(2)$ $c = 3.0613(2)$	Bolmgren <i>et. al.</i> <sup>[116]</sup>
VB	<i>Cmcm</i>	$a = 3.0616(2)$ $b = 8.0495(3)$ $c = 2.9733(2)$	$a = 3.060(3)$ $b = 8.048(3)$ $c = 2.972(1)$	Spear <i>et. al.</i> <sup>[92a]</sup>
V <sub>3</sub> B <sub>2</sub>	<i>P4/mbm</i>	$a = 5.7437(6)$ $c = 3.0324(5)$	$a = 5.755(2)$ $c = 3.038(2)$	Riabov <i>et. al.</i> <sup>[31b]</sup>

Table 3.3 shows the variation of the reaction products synthesized using Al flux with respect to the nominal composition in at. % based upon the XRPD analysis. VB<sub>2</sub> crystals are isolated from the melt when atomic ratios B/V = 1.86-2.6 are used. It is possible to obtain single phase of V<sub>2</sub>B<sub>3</sub> for the starting ratio B/V = 1.62 while V<sub>3</sub>B<sub>4</sub> is observed in the reaction product together with a small amount of VB when the starting ratios between B/V = 1.1-1.18 are used.

**Table 3.3:** Strength of relative intensities of X-ray diffraction patterns of vanadium borides synthesized via Al flux: w = weak; m = medium; s = strong.

Nominal composition at.% B	Phases present				
	VB	V <sub>5</sub> B <sub>6</sub>	V <sub>3</sub> B <sub>4</sub>	V <sub>2</sub> B <sub>3</sub>	VB <sub>2</sub>
40**	s	w			
45	m		m		
45.45*	w	w	m		
46*	w	w	m		
47	w		m		
48	w		m		
49	w		m		
50	m		m		
51	w		m	w	
52.38**	w		s		
52.83**	w		s		
53.27**	w		s		
53.70**	w		s		
54			m	m	
54.13**			s		
54.55			m	m	
56				m	w
57				m	w
58.33				m	
58.46**			w	s	
59				m	m
60				w	m
61.04**				s	w
61.90**				s	
62				w	m
63				w	s
65					s
66					s
66.67					s
68.75					s
69.70					s
70.59					s
71.43					s
72.22					s

Reaction protocol for the samples: \* 30 K/min up to 1500 °C, 6 h at 1500 °C, 5 K/min down to 1100 °C, 12 h at 1100 °C, 1 K/min down to 660 °C; \*\* 30 K/min up to 1500 °C, 12 h at 1500 °C, 5K/min down to 660 °C, for all other reactions: 30 K/min up to 1500 °C, 6 h at 1500°C, 10 K/min down to 660 °C.

The efforts for the synthesis of VB, V<sub>3</sub>B<sub>2</sub> and V<sub>5</sub>B<sub>6</sub> end up with a number of by-products belonging to the Al-V system. The diffraction lines for V<sub>3</sub>B<sub>2</sub> do not appear in any end

products. Furthermore,  $V_5B_6$  is detected only in few cases but only together with VB and/or  $V_3B_4$ . Possible explanation for the unobserved diffraction lines of  $V_5B_6$  is the weakness of the respective reflection intensities which have gone unnoticed as a result of peak overlapping.  $V_3B_2$  phase is not observed in the samples synthesized by Al flux. The X-ray diffractograms indicate also the presence of AlV,  $AlV_3$ ,  $Al_{45}V_7$  and  $Al_4V_{23}$  in some samples together with a small amount of  $Al_2O_3$ , AlN. In general, the amount of these by-products varies according to composition of the starting materials.

Table 3.4 summarizes the experimental results based upon the XRPD analysis for samples synthesized by arc-melting.  $V_3B_2$  phase is also detected in the reaction product together with VB.

**Table 3.4:** Strength of relative intensities of phases present in the X-ray powder diffraction diagrams of samples synthesized by arc-melting: w = weak; m = medium; s = strong.

Nominal composition at.% B	Phases present					
	$V_3B_2$	VB	$V_5B_6$	$V_3B_4$	$V_2B_3$	$VB_2$
40	s	m				
45	s	m				
48	m	m		s		s
49		s		w		
50		s				
51		s				
52	w	m	m			
53	w	m	m			
54.55	w	m	m			
56	w	m	m			
57.14		w	m	m		
59		w	w	s		w
60		w	w	m		w
61				m	w	m
62		m	m	m		s
63		w	w	m		s
64		w		w	m	s
65		w		w	m	s
66				w	w	s
66.67					w	s
68						s
69						s
70.5						s
71						s
72.5						s
73						s
73.5						s

Only VB and VB<sub>2</sub> can be obtained in nearly pure form using arc-melting. For all other cases additional vanadium borides are identified in the powder patterns. In those cases the powder lines are mostly overlapping, which complicates the identification of the phases.

### 3.2.1.1 Homogeneity ranges

Special attention is paid in the examination of the homogeneity ranges of vanadium borides since the reported investigations reveal that they supposed to be quite small if there exist any. Rudy *et al.* and Spear *et al.* observed only minor changes in sample composition.<sup>[92a, 92b]</sup> Figure 3.5 shows the lattice parameters of several VB<sub>2</sub> samples with respect to the variation of B/V atomic ratios. The samples are synthesized by Al flux or arc-melting using crystalline or amorphous boron.

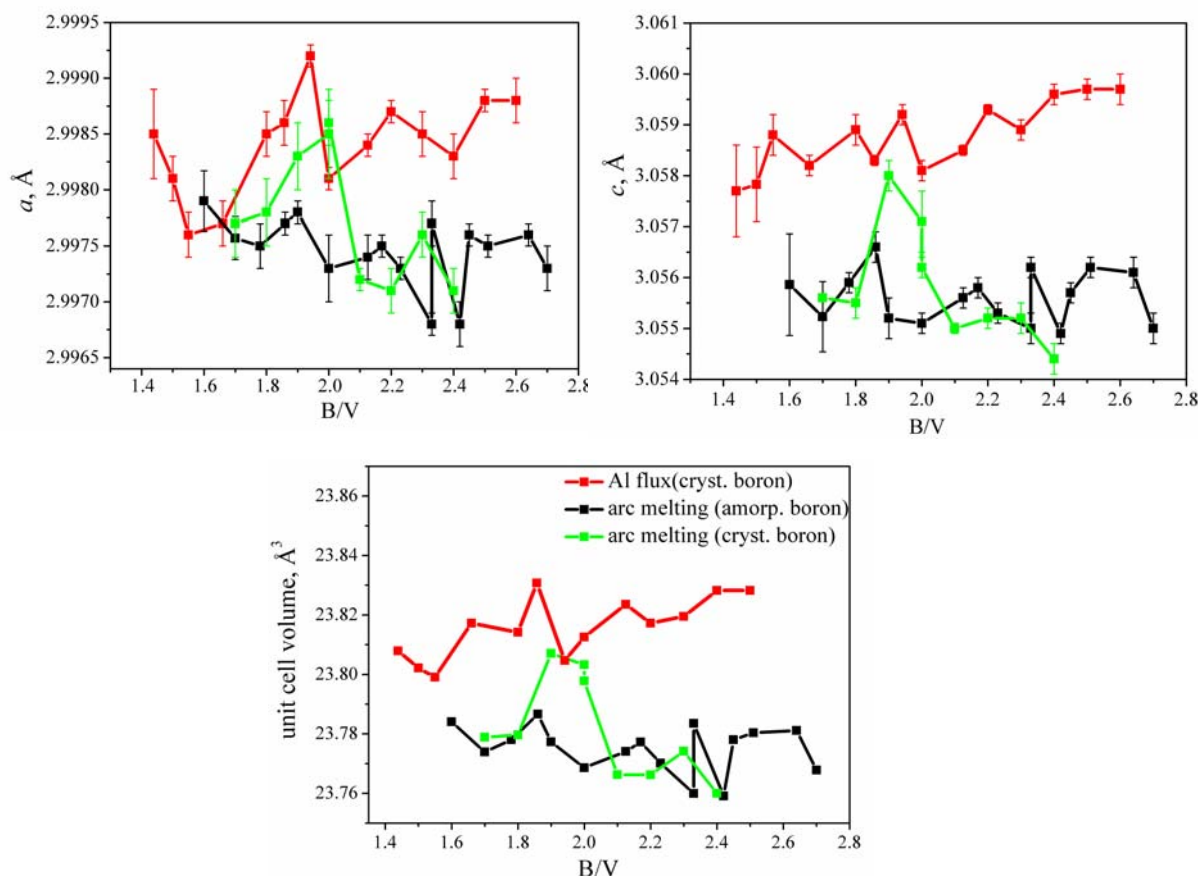


**Figure 3.5:** Cell volumes (Å<sup>3</sup>) and cell parameters (Å) of VB<sub>2</sub> samples vs. B/V molar ratio. The error bars for e.s.d.s for the cell volume are smaller than the square-shaped data points.

Obviously, there are slight changes between the cell parameters of VB<sub>2</sub> samples depending on which synthesis method or starting material is used. Taking the anisotropic

nature of the crystal structure into account, as will be discussed later, different tendencies are expected when changes in both cell parameters  $a$  and  $c$  are compared. However, the small variations observed in the present case do not indicate such a clear trend, thus any significant variation of composition.

A possible explanation for the slight changes between the cell parameters would be that the samples are not in equilibrium neither by arc-melting, nor by Al-flux preparation giving rise to small variations of the peak shapes of the respective reflections. Additional reasons can be the difficulty of reproducing samples with comparable crystallinity and / or structural changes like defects which are probably introduced during excessive grinding of very hard powders. It is worth to mention that X-ray single crystal refinement of  $\text{VB}_2$  structure also do indicate not any significant deviation from the ideal stoichiometry as will be reported in subsection 3.4.1

The investigation of the homogeneity range for VB does not reveal any significant change in cell parameters with respect to variation of the B/V atomic ratios (Figure 3.6).

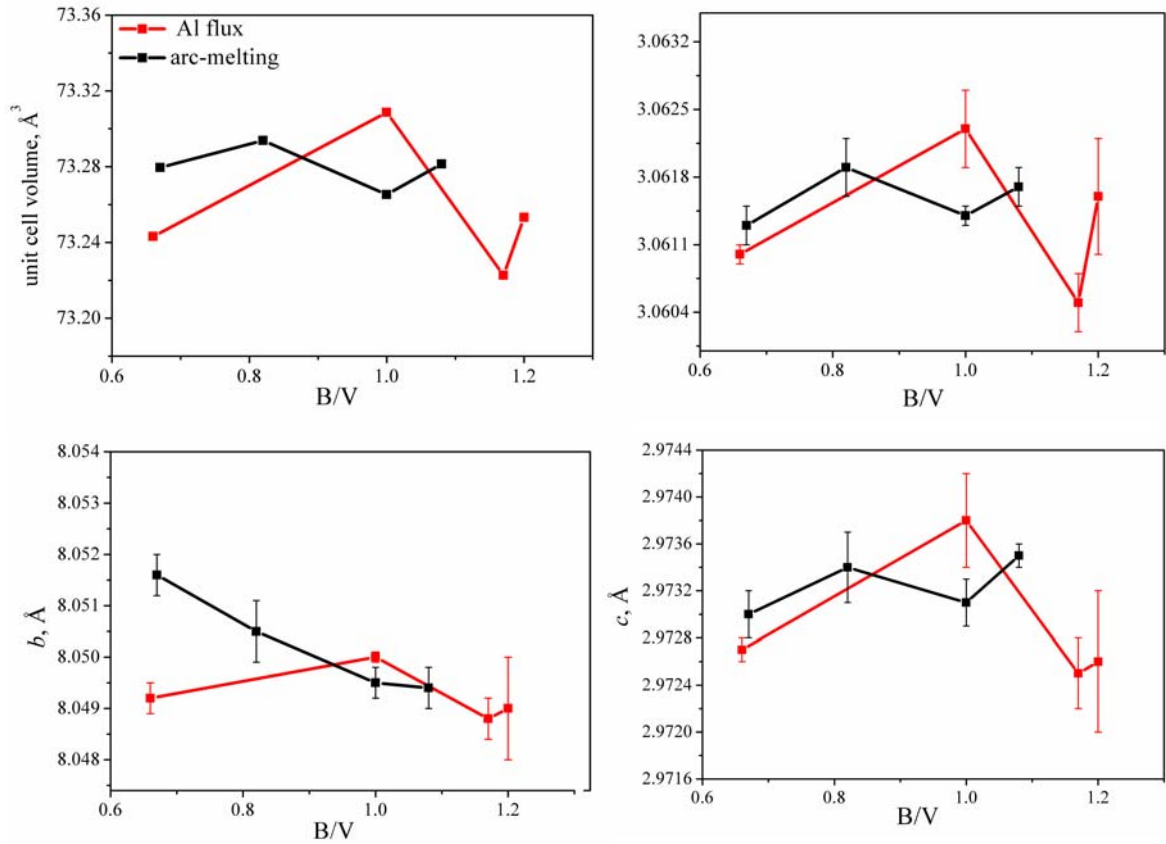


**Figure 3.6:** Unit cell volumes ( $\text{\AA}^3$ ) and cell parameters ( $\text{\AA}$ ) of VB samples vs. B/V atomic ratio. The error bars for e.s.ds for the cell volume are smaller than the square-shaped data points.

The homogeneity range examination of cell parameters for  $V_2B_3$  and  $V_3B_4$  is mostly hampered by the overlapping powder lines especially for the arc-melted samples. After the exclusion of these peaks there is not many left to draw any reliable conclusion. Therefore, cell parameters of these compounds are calculated considering the samples synthesized by Al flux method. Variation of nominal composition does not indicate any considerable change in the cell volume (Figure 3.7).

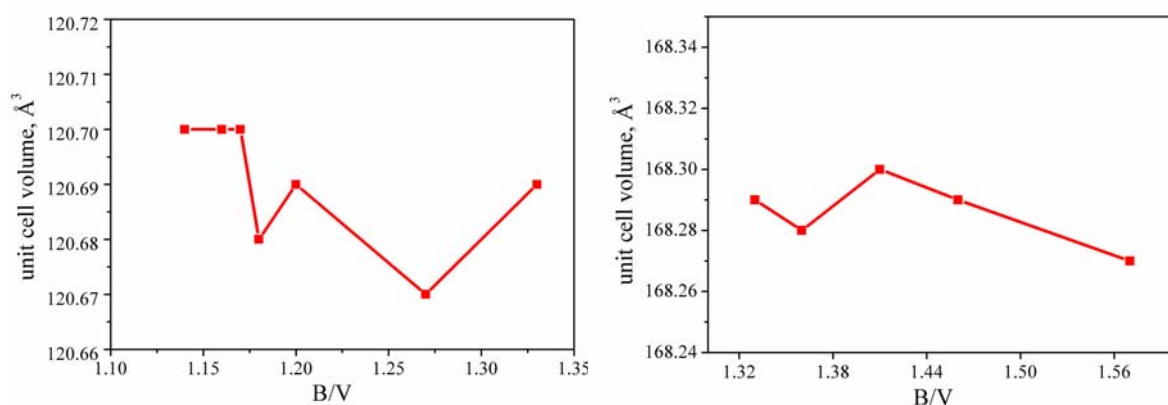


**Figure 3.7:** Cell volumes ( $\text{\AA}^3$ ) of  $V_3B_4$  (left) and  $V_2B_3$  (right) samples vs. B/V molar ratio. The error bars for e.s.ds for the cell volume are smaller than the square-shaped data points.

Due to severe overlapping problems in case of arc-melted samples, several powder lines remained unresolved in the indexing process of  $V_3B_2$  and  $V_5B_6$ . Unfortunately, the products precipitated from aluminium solution in the respective composition range end up with a number of by-products belonging to the Al-V system. These factors give rise to uncertainties in estimation of accurate lattice parameters of  $V_3B_2$  and  $V_5B_6$ .

### 3.2.2 Microstructure analysis

For metallographic investigations vanadium boride samples are mounted in conductive resin (PolyFast, Struers) suitable for analyses on a scanning electron microscope. Microstructure have been prepared by conventional, multi-step grinding and polishing processes with final polishing using  $0.25 \mu\text{m}$  diamond powder and water based lubricant. Light optical microscopy (Axioplan2, Zeiss) as well as scanning electron microscopy (Philips XL30 with  $\text{LaB}_6$  cathode, FEI) confirm the homogeneity of the microstructure. Wavelength dispersive X-ray spectroscopy analyses (WDXS) are performed with a Cameca SX100 electron microprobe with tungsten cathode.

**Table 3.5** Atomic compositions of V-B alloys.

Compound	Nominal composition		Composition detected by WDXS	
	at.% V	at.% B	at.% V	at.% B
$V_{1.00(1)}B_{0.99(1)}$	49	51	$50.17 \pm 0.25$	$49.83 \pm 0.25$
$V_{1.00(1)}B_{0.99(1)}$	48	52	$50.14 \pm 0.20$	$49.86 \pm 0.20$
$V_{4.80(1)}B_{6.05(1)}$	45.45	54.55	$44.25 \pm 0.16$	$55.75 \pm 0.16$
$V_{2.96(1)}B_{4.03(1)}$	44	56	$42.36 \pm 0.17$	$57.64 \pm 0.17$
$V_{1.94(1)}B_{3.06(1)}$	40	60	$38.74 \pm 0.29$	$61.26 \pm 0.29$
$V_{0.98(1)}B_{2.01(1)}$	33.33	66.66	$32.54 \pm 0.11$	$67.46 \pm 0.12$
$V_{0.98(1)}B_{2.02(1)}$	31	69	$32.50 \pm 0.25$	$67.50 \pm 0.25$

Investigations reveal not any significant deviation from the ideal stoichiometry for VB and  $VB_2$  whereas slight deviations are observed for  $V_3B_4$  and  $V_2B_3$  (Table 3.5). The largest deviation from ideal stoichiometry is observed for  $V_5B_6$ . The compositions of VB and  $VB_2$  samples prepared both with excess boron as well as with excess vanadium are identical within the standard deviations. Thus, they do not indicate any significant homogeneity range. This is in line with the results obtained from XRPD. No additional elements besides vanadium and boron are found. Figure 3.8 shows SEM images of VB,  $V_3B_4$ ,  $V_2B_3$  and  $VB_2$  crystals synthesized by Al flux method. The dimensions of the crystals are mostly below  $100\ \mu\text{m}$ . In few cases, it is possible to grow larger crystals with *ca.* 1mm in length.

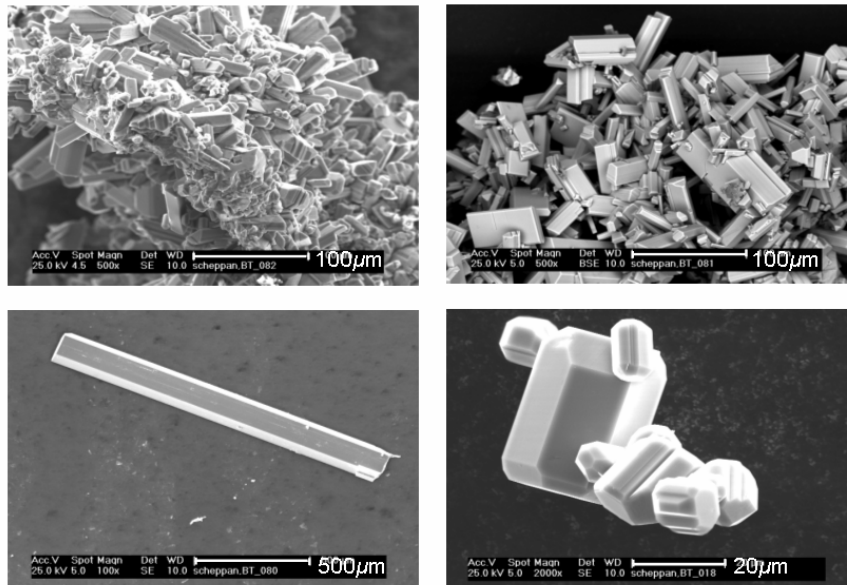


**Figure 3.8** SEM images of vanadium boride crystals synthesized by aluminium flux method. First row: VB (left) and  $V_3B_4$  (right). Second row:  $V_2B_3$  (left) and  $VB_2$  (right).

### 3.3 High resolution single crystal X-ray diffraction

X-ray single crystal diffraction measurements up to high resolution are carried out for  $\text{VB}_2$ ,  $\text{V}_2\text{B}_3$ ,  $\text{V}_3\text{B}_4$  and  $\text{VB}$  crystals as depicted in Figure 3.9. The size of the  $\text{V}_3\text{B}_4$  and  $\text{VB}$  crystals depicted are around 50  $\mu\text{m}$  in length, while for  $\text{VB}_2$  and  $\text{V}_2\text{B}_3$  even smaller crystals are used. For comparison also a larger crystal of  $\text{VB}_2$  is examined. The crystal structure investigations are performed at room temperature on a microfocus rotating anode diffractometer (100  $\mu\text{m}$ ), Ag  $K\alpha$  radiation  $\lambda = 0.56087 \text{ \AA}$ , mirror optics and image plate detector in Weissenberg-type arrangement.

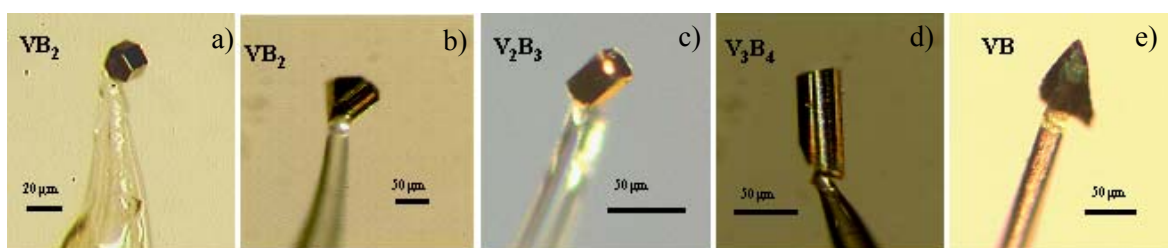


**Figure 3.9** Small  $\text{VB}_2$  crystal depicted in a). For comparison larger  $\text{VB}_2$  crystal shown in b) was investigated. A typical crystal of  $\text{V}_2\text{B}_3$ ,  $\text{V}_3\text{B}_4$  and  $\text{VB}$  is depicted in c), d) and e).

Severe absorption effects are remarkably reduced by the use of hard radiation. Quite high diffraction limits are achieved (Figure 3.10). The data sets are measured up to  $\sin \theta / \lambda = 1.72 \text{ \AA}^{-1}$  for  $\text{VB}_2$ ,  $\text{V}_3\text{B}_4$  and  $\text{V}_2\text{B}_3$ .

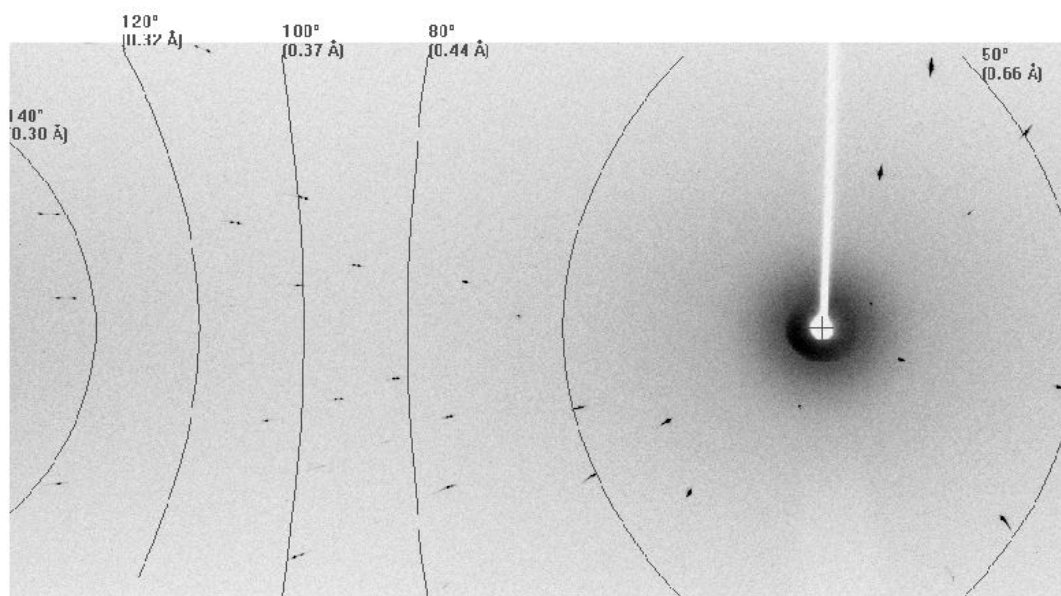


**Figure 3.10** A typical diffraction image from small  $\text{VB}_2$  crystal depicted in Figure 3.9 a).



The data collection and evaluation information is given in Table 3.6. The overall completeness based on Laue symmetry is more than 97% for  $\text{VB}_2$ ,  $\text{V}_3\text{B}_4$  and  $\text{V}_2\text{B}_3$ . A quite fair number of reflections are collected, high symmetry of the compounds notwithstanding. In general,  $R_{(\text{int})}$  which reflects the data quality increases with the amount of reflections along with the series  $\text{VB}_2$ -VB- $\text{V}_3\text{B}_4$  and  $\text{V}_2\text{B}_3$ . The  $R_{(\text{int})}$  for the data set of the larger  $\text{VB}_2$  crystal is higher than that of the smaller  $\text{VB}_2$  crystal.

**Table 3.6** X-ray single crystal measurement data.

	$\text{VB}_2$	$\text{VB}_2^*$	VB	$\text{V}_3\text{B}_4$	$\text{V}_2\text{B}_3$
Measured range	$-7 \leq h \leq 6;$ $-9 \leq k \leq 8;$ $-10 \leq l \leq 10$	$-6 \leq h \leq 9;$ $-8 \leq k \leq 10;$ $-5 \leq l \leq 9$	$-9 \leq h \leq 10;$ $-26 \leq k \leq 25;$ $-9 \leq l \leq 8$	$-9 \leq h \leq 8;$ $-9 \leq k \leq 8;$ $-44 \leq l \leq 43$	$-9 \leq h \leq 10;$ $-59 \leq k \leq 61;$ $-10 \leq l \leq 10$
$2 \theta_{\text{max}}(^{\circ}) /$ $(\sin \theta_{\text{max}}) / \lambda (\text{\AA}^{-1})$	149.37 / 1.72	149.37 / 1.720	138.22 / 1.67	153.44 / 1.735	150.75 / 1.725
No. of measured / unique reflections	2109 / 246	1769 / 242	3270 / 774	5786 / 1343	11644 / 2049
$R_{(\text{int})}$	0.0165	0.0221	0.0199	0.0194	0.0208
Completeness (%)	98.8	97.6	94.6	98.2	97.1

\* Also a larger crystal of  $\text{VB}_2$  ( $\sim 50 \mu\text{m}$ ) is measured.  $R_{(\text{int})}$  is simply the  $R$ -factor between the amplitudes of Friedel pairs.

### 3.4 Conventional IAM refinement

In this section, the focus will be on data analysis and strategies of spherical refinement. Refinement steps are presented in order to get the best agreement between the observed and calculated structure factors prior to the introduction of a multipole model. A thermal diffuse scattering (TDS) correction is not carried out for the respective data sets. The reason is that for the very hard materials such as vanadium borides the contribution of inelastic TDS to the total intensity is expected to be negligible.

All conventional structure refinements are performed with the WinCSD software program.<sup>[114]</sup> Least-squares refinements are performed by minimizing the difference between the observed ( $F_{\text{obs}}$ ) and the calculated structure factors ( $F_{\text{calc}}$ ) since it gives a slightly better refinement results than if the model is refined against intensity ( $F^2$ ). Complete data set is used. The observations are weighted according to their counting statistical variances as

given in equation 2.17 in Chapter 2. In case of all refinements, anisotropic extinction model reduces the  $R_{(F)}$  value more than the isotropic approximation of extinction. In order to treat extinction anisotropically each reflection needs to be processed with its individual path length in the calculation. Accordingly, the unmerged data is used during conventional refinement. The scale factor is kept free throughout the refinement until the convergence is achieved. Table 3.7 gives the number of unique reflections and the refined parameters. As a rule of thumb, the reflection-to-parameter ratio should be at least ten. This condition is by far satisfied for all data sets.

**Table 3.7** IAM refinement details.

Compound	No. of measured / unique reflections	No. of refined Parameters
VB <sub>2</sub> (~20 $\mu$ m)	2109 / 246	14
VB <sub>2</sub> (~50 $\mu$ m)	1769 / 242	14
VB	3270 / 774	24
V <sub>3</sub> B <sub>4</sub>	5786 / 1343	31
V <sub>2</sub> B <sub>3</sub>	11644 / 2049	35

### 3.4.1 Refinement of crystal structure VB<sub>2</sub>

The refined parameters for VB<sub>2</sub> are the scale factor, the displacement parameters of both atoms and finally two width parameters of a gaussian mosaic distribution for anisotropic extinction according to the Becker-Coppens formalism.<sup>[57]</sup> The refinement with isotropic description of the atomic displacement gives the  $R_{(F)}$  value of 1.90% without accounting for extinction. Application of the anisotropic extinction model already reduces the  $R_{(F)}$  to 1.38%. At this stage the refinement of the occupancies of both atom positions indicates that there is not any deviation from the exact stoichiometry. On account of this, the occupancies are kept at unity throughout the refinement. From this step on, extinction and ADPs are refined separately. Introducing the anisotropic approximation of atomic displacement leads to a small reduction of the reliability factor ( $R_{(F)}$  value drops to 1.35%). The final achievement for the unmerged data is obtained applying the anharmonic description of the

atomic displacement for V and B up to the fourth tensor:  $R_{(F)}$  droppes to 1.11%. Finally, at the last stage the data is merged ( $R_{(F)} = 0.97\%$ ).

A fundamental limitation on the accuracy of the measured intensities is that they are weaker at higher diffraction angles but possess information of equal importance as lower resolution. This explains why special care needs to be taken for the precision of these observables. Data analysis on the basis of the conventional spherical refinement after merging revealed that at the very high resolution the difference between the observed and calculated structure factors becomes pronounced. As shown in Figure 3.11 some observed structure factors are considerably smaller than the calculated ones at very high  $\sin \theta / \lambda$ .

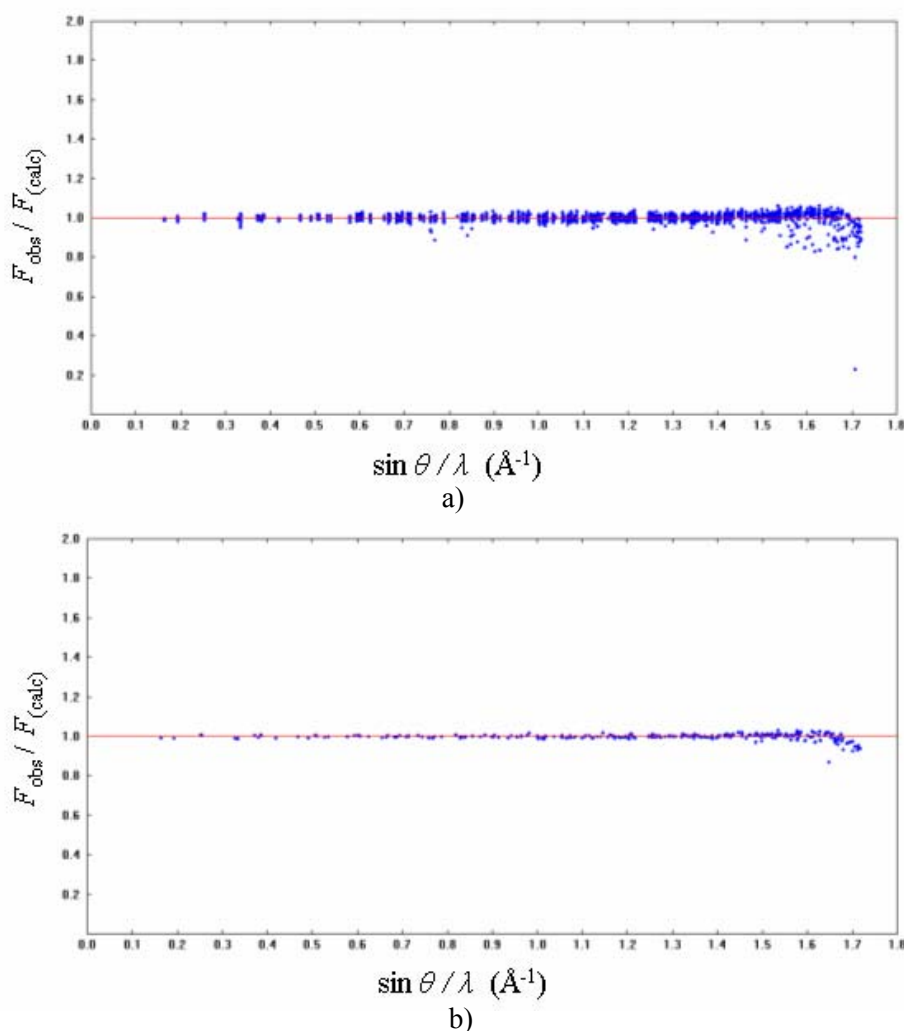


**Figure 3.11**  $F_{\text{obs}} / F_{\text{calc}}$  vs.  $\sin \theta / \lambda$  for unmerged (a) and merged (b) data according to IAM refinement.

As reflected in reliability factors  $R_{(F)}$  values the difference between the observed and calculated structure factors arises suddenly at very high resolution (Figure 3.12). Since the scattering power is a function of the crystal volume the accuracy of weak reflections can be improved by using a larger crystal. However, the use of a larger crystal does not provide any significant improvement.

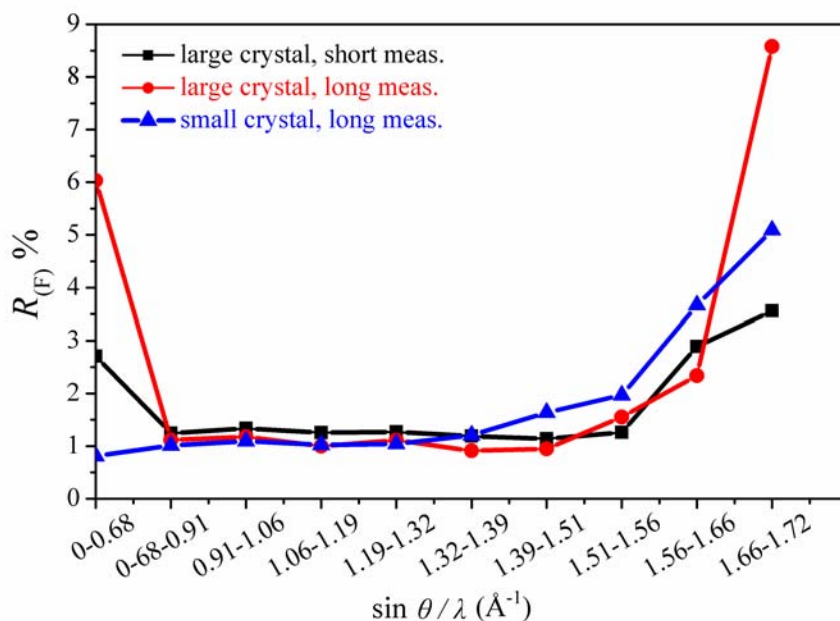


**Figure 3.12** Analysis of variance of  $R_{(F)}$  for reflections employed in the spherical refinement of  $\text{VB}_2$ .

For weak reflections the uncertainty in the background correction contributes significantly to the uncertainty of the final intensity. To increase the precision of the data measurement it is of great importance to spend the same time as well for measuring the background. In the particular case, however, increase of the measuring time does not have any reducing effect on  $R_{(F)}$  values (Figure 3.12).

The final attempt to reduce the deviation at very high diffraction angles is to vary the integration box size. The interval of integration depends on the primary beam divergence and its wave dispersion, on crystal mosaic block disorientation and on the scattering angle. Reflection integration limits are obtained by an analysis of the anisotropic variation and scattering angle dependence of peak widths based on principles of the convolution synthesis of peak profiles.<sup>[117]</sup> Figure 3.13 shows the variation of  $R_{(F)}$  values to different integration box size in the data range of  $\sin \theta / \lambda = 1.66 - 1.72 \text{ \AA}^{-1}$ . It provides only minor improvement. Extinction correction does not provide any improvement since the corre-

sponding resolution is certainly outside of the limit where extinction effects may be pronounced.

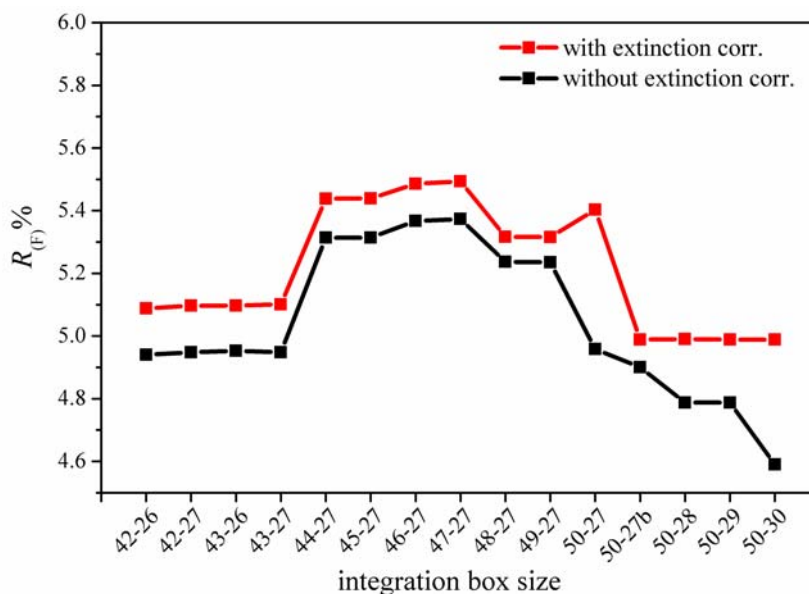


**Figure 3.13**  $R_{(F)}(\%)$  vs. integration box size.

A possible explanation for the sudden rise of  $R_{(F)}$  at higher diffraction angles might be a systematical error caused by the sharp increase of reflection width due to the spatial intensity distribution or angular divergence of the incident X-ray at high angles as analysed by Blessing.<sup>[118]</sup> Choosing the correct weights for those observations in the least square procedure deserves serious consideration.<sup>[119]</sup>

### 3.4.2 Refinement of crystal structures VB, $V_3B_4$ and $V_2B_3$

For the refinement of VB,  $V_3B_4$  and  $V_2B_3$  structures a similar refinement strategy is applied such as for VB<sub>2</sub>. The reliability factors  $R_{(F)}$  which are obtained at different stages and the final convergence are summarized in Table 3.8. The  $R_{(F)}$  values of the final convergence increase along with VB,  $V_3B_4$  and  $V_2B_3$ . The final refinement is carried out on full occupancy of all atomic positions since there is not any occupational disorder observed for any of the atom positions. These results are supported by XRPD experiments where no indication of any homogeneity range is found. Anisotropic extinction correction is applied after the introduction of isotropic description of ADPs and refined again separately from the ADPs during the following steps until the final convergence is achieved.

**Table 3.8**  $R_{(F)}$  (%) values at several steps of the refinement of VB,  $V_3B_4$  and  $V_2B_3$  structures. The final  $R_{(F)}$  value is obtained after data merging.

Compound	Isotropic description of ADPs	Anis. extinction correction	Anis. description of ADPs	Anharm. description of ADPs (3 <sup>rd</sup> rank)	Anharm. description of ADPs (4 <sup>th</sup> rank)	Final $R_{(F)}$
VB	2.30	1.56	1.50	1.50	1.34	1.23
$V_3B_4$	2.51	2.33	2.07	2.07	1.90	1.86
$V_2B_3$	2.80	2.25	2.22	2.22	1.85	1.76

The influence of anharmonic contributions to  $R_{(F)}$  has been investigated. The corresponding anharmonicity values for each data set will be given in the subsection 3.6 together with the crystal structure descriptions. The third-order anharmonic contribution yield values close to zero which is also well reflected in  $R_{(F)}$  values where not any discernable change is present (Table 3.8). Accordingly, they are kept unrefined in order to reduce the number of refined parameters. The use of fourth-order model for metal leads to a considerable reduction in  $R_{(F)}$  whereas no substantial improvement is achieved for boron. Of course; the physical significance of the anharmonic approximation is certainly doubtful due to extreme hardness of the materials. It has to be emphasized that in presence of a few numbers of refineable positional parameters the systematic errors may rather choose to contribute to the ADPs. Furthermore, due to similar dependence of basis functions on scattering vector components the anharmonic description of thermal motion is remarkably successful in representing bonding effects in valence charge density.<sup>[120]</sup> Reliable information about anharmonicity has to be obtained from temperature dependent diffraction experiments and complemented with results from independent analysis by IR and Raman spectroscopy or *ab-initio* calculations of vibrational properties.<sup>[121]</sup> In harmonic models the mean-square amplitudes measured at high temperatures are extrapolated to zero at 0 K. Deviations from zero mean-square amplitudes at zero K is an indication of anharmonicity.

As also observed by  $VB_2$  discrepancy between the observed and calculated structure factors at high diffraction angles becomes pronounced. The number of such reflections increased along the series VB- $V_3B_4$ - $V_2B_3$  and extended to lower resolutions (Figure 3.14).

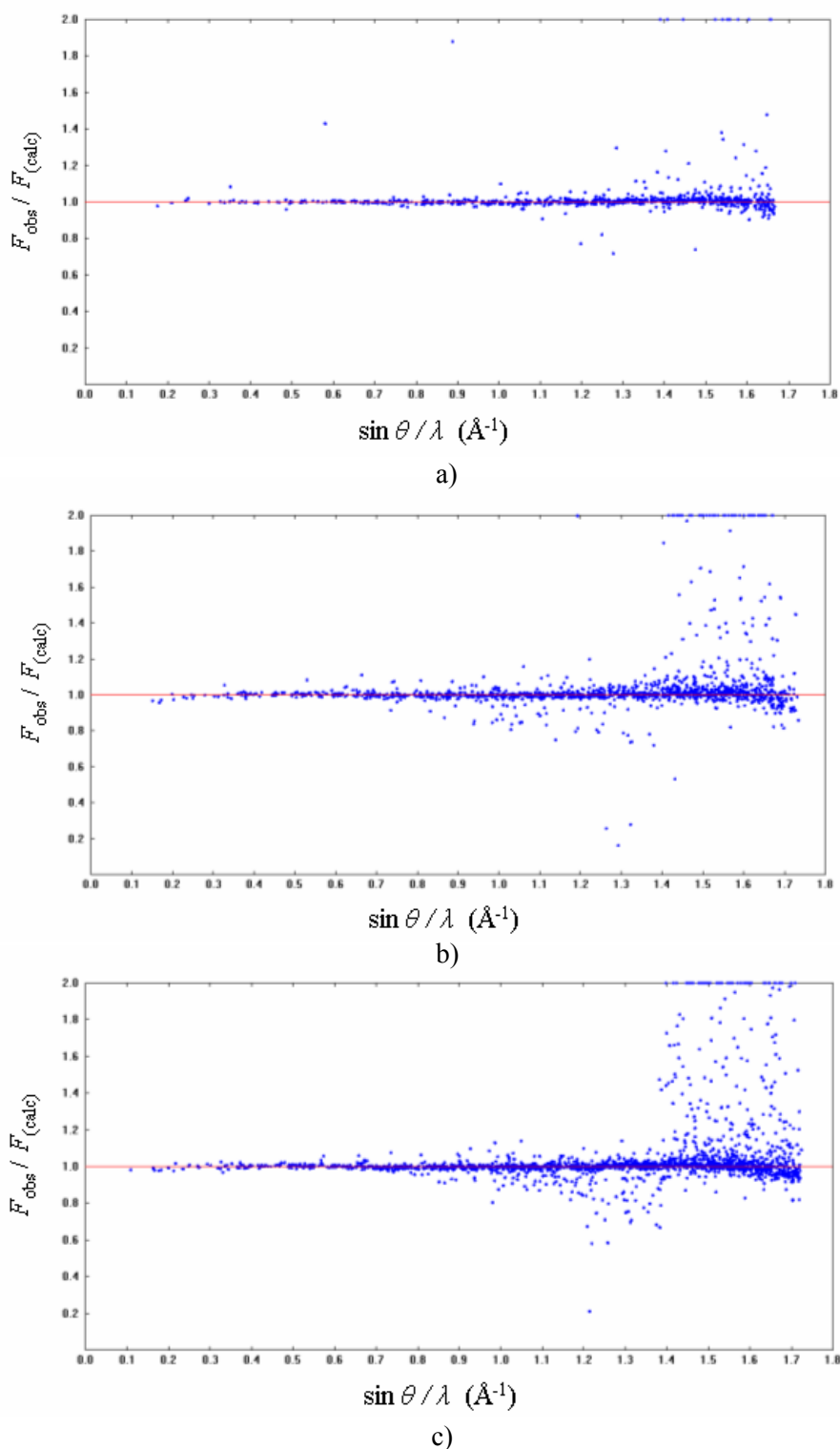


**Figure 3.14**  $F_{\text{obs}}/F_{\text{calc}}$  vs.  $\sin \theta / \lambda$  for VB in a), for  $\text{V}_3\text{B}_4$  in b) and for  $\text{V}_2\text{B}_3$  in c).

The number of most rejected outlier reflections ( $F_{\text{obs}}/F_{\text{calc}} < 0.5$  or  $F_{\text{obs}}/F_{\text{calc}} > 1.50$ ) are 16, 47, and 70 for VB,  $\text{V}_3\text{B}_4$  and  $\text{V}_2\text{B}_3$ . These are detected in the range of  $\sin \theta / \lambda = 0.8$ -1.72. The final convergence by the refinement of  $\text{V}_3\text{B}_4$  and  $\text{V}_2\text{B}_3$  is achieved by excluding the respective outliers.

### 3.5 Crystal structures of vanadium borides

In this section, a detailed description for the structural models of vanadium borides are given obtained by the spherical refinement of the single crystal X-ray diffraction data.

#### 3.5.1 Crystal structure of $\text{VB}_2$

In the  $\text{VB}_2$  structure the fundamental units are trigonal prism of the metal atoms with a boron atom at the center as shown in Figure 3.15.  $\text{VB}_2$  is like all other  $\text{AlB}_2$ -type structures the ultimate structure obtainable where all metal atoms form trigonal prisms. The prisms extend parallel to the  $[001]$  axis and are packed together so as to share the faces. The triangular faces of the prisms are parallel to the  $(001)$  planes. The structure can be described from another point of view as following: Both metal and boron atoms form layers which have hexagonal close-packed arrangement. In that respect, each metal atom has six equidistant neighbours in the  $(001)$  plane and two neighbours located above and below  $(001)$  plane at slightly larger distance. Accordingly, the space to accommodate vanadium atoms above and below the hexagonal network is larger. Vanadium atoms form a simple hexagonal lattice having an axial ratio deviating slightly from unity. The boron atoms which are located in between metal sheets have three close neighbours in the plane. The trigonal prisms of vanadium atoms are arranged in such a way that the boron atoms form hexagonal nets. Accordingly,  $\text{VB}_2$  is the first type among known binary vanadium borides where a discernible extended boron lattice occurs.

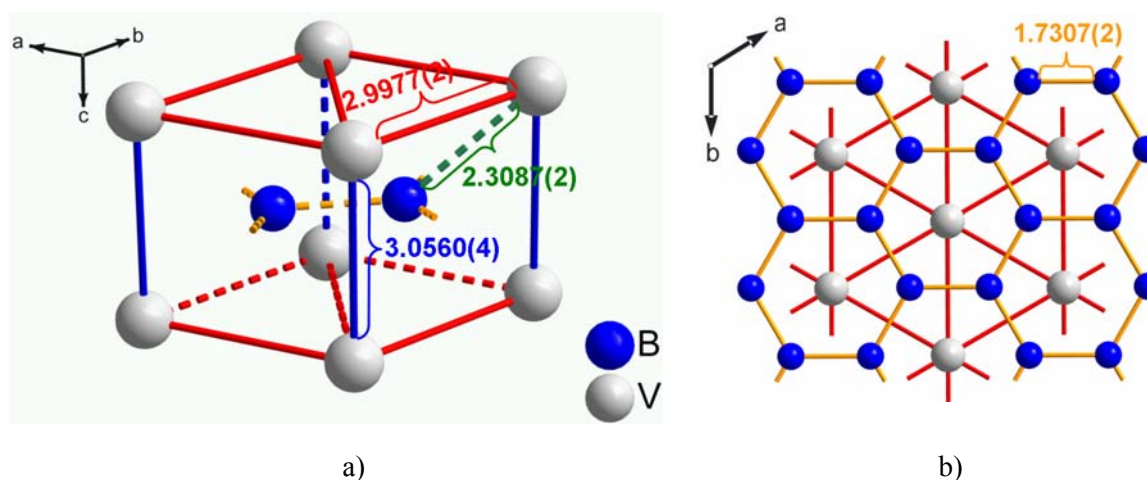


**Figure 3.15** Interatomic distances (Å) in  $\text{VB}_2$ . a) The view is perpendicular to the B-atom plane. (b) The view is perpendicular to the B-atom plane.



The ADPs of  $\text{VB}_2$  indicates that the movement of the metal atoms are more restricted in all three directions compared to boron atoms as shown in Table 3.9. Detailed investigations on the isostructural phases  $\text{TiB}_2$ <sup>[122]</sup> and  $\text{MgB}_2$ <sup>[21f]</sup> reveal that the displacement parameters for the metal position is smaller than that for the boron position while for  $\text{AlB}_2$ <sup>130</sup> it is the other way around. It is clear from Figure 3.15 that the space for the accommodation of vanadium atom along the [001] direction is slightly larger than in other directions, which in turn provides more freedom of movement for vanadium atoms along that direction compared to in plane. Similarly, boron atoms also vibrate more easily along the [001] direction. However, the corresponding difference between  $B_{11}$  and  $B_{33}$  is significantly larger than that between vanadium atoms indicating that existing forces between boron atoms in B-plane is presumably stronger.

**Table 3.9** Atomic positions and anisotropic ADPs in the crystal structure of  $\text{VB}_2$ .

Atom	$x/a$	$y/b$	$z/c$	$B(\text{eq})^*$	$B_{11}$	$B_{22}$	$B_{33}$	$B_{12}$
V	0	0	0	0.152(2)	0.115(3)	$B_{11}$	0.155(4)	$\frac{1}{2} B_{11}$
B	$\frac{1}{3}$	$\frac{2}{3}$	$\frac{1}{2}$	0.261(7)	0.185(8)	$B_{11}$	0.320(8)	$\frac{1}{2} B_{11}$

$$^*B(\text{eq}) = 1/3[B_{11}a^{*2}a^2 + \dots 2B_{23}b^*c^*bc \cos \alpha]$$

As already described by the refinement procedure, introduction of the anharmonic description of the fourth tensor to the ADPs leads to a considerable reduction of the  $R_{\text{(F)}}$ . Owing to the symmetry restrictions third order anharmonic parameters of only boron differs from zero. However, the  $R_{\text{(F)}}$  does not change at all after refining these parameters since their absolute values are insignificantly small. Accordingly, they are kept fixed throughout the refinement. Introducing the anharmonic description of the fourth order yields reasonable values for vanadium atoms while the corresponding standard deviations of boron atoms turns out to be relatively larger; therefore B atom is refined only anisotropically (Table 3.10).

**Table 3.10** Anharmonic ADPs ( $\text{\AA}^4$ ) in the crystal structure of  $\text{VB}_2$ .

Atom	$D_{1111}$	$D_{3333}$	$D_{1133}$
V	-3.9(2)	-1.6(1)	-0.76(6)
B	kept fixed		

### 3.5.2 Crystal structure of VB

The VB is a representative of TII structure type. For other metal monoboride representatives of this structure type, the crystal structures are mostly not determined, but only the structure type is assigned and unit cell parameters are refined except for CrB.<sup>[123]</sup> The crystal structure is based on double metal layers containing  $BV_6$  prisms. These metal layers are stacked with the triangular prism faces in common and are shifted one half of the prism axis. The rectangular face of this trigonal prism is also the base of a pyramid. The apex of the pyramid is a part of neighbouring trigonal prism. The  $BV_6$  prisms form columns by sharing rectangular faces and extend along the  $[001]$  direction. Each  $BV_6$  prism includes one boron atom. They form zig-zag chains also extending along the  $[001]$  direction as shown in Figure 3.16.

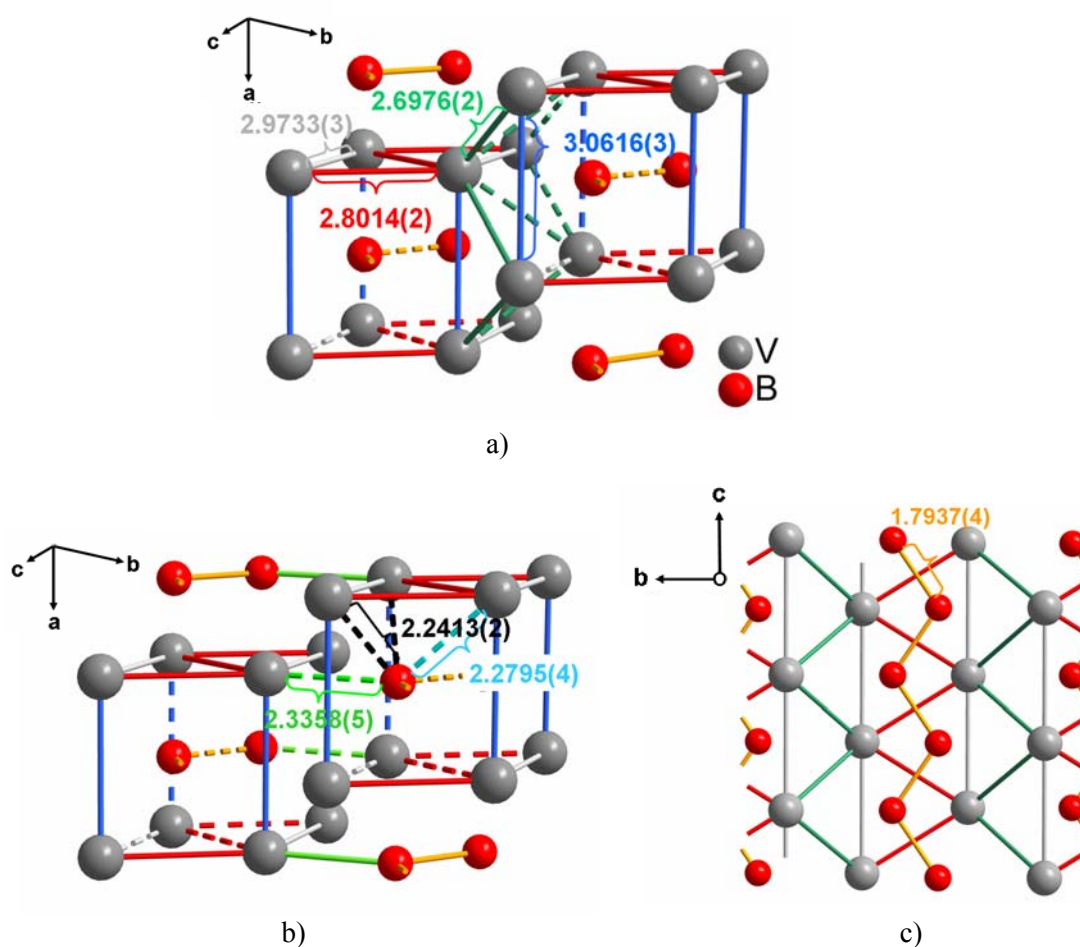


**Figure 3.16** Interatomic distances (Å) in the crystal structure of VB. a) V–V distances. The view is parallel to the B–B zig-zag chain. b) B–V distances. The view is the same as in a). c) B–B distances. The view is perpendicular to the B–B zig-zag chain.

The trigonal prisms formed by vanadium atoms are distorted. There are two different V–V distances in (100) metal plane; one is drawn in gray, the other one in red (Figure 3.16). The vanadium atoms connected by the gray line have a shorter distance ( $\sim 2.24$  Å) to the boron atom sitting in the trigonal prism compared to the other B–V distance ( $\sim 2.28$  Å) drawn in blue. In other words, the position of the boron atom is shifted from the center of the trigonal prism near to the base of rectangular pyramide. Consequently, the boron atom is not placed exactly at the center of the trigonal prism. Accordingly, the bond angle of the B–B chain is reduced as compared to that in boron network in VB<sub>2</sub>.

**Table 3.11** Atomic positions and anisotropic ADPs (Å<sup>2</sup>) of VB.

Atom	$x/a$	$y/b$	$z/c$	$B(\text{eq})^*$	$B_{11}$	$B_{22}$	$B_{33}$
V	0	0.14749(1)	0.25	0.134(2)	0.140(4)	0.122(4)	0.139(4)
B	0	0.43767(6)	0.25	0.2785(5)	0.301(8)	0.292(9)	0.262(8)

$$^* B(\text{eq}) = 1/3[B_{11} a^{*2} a^2 + \dots 2 B_{23} b^* c^* b c \cos \alpha]$$

The ADPs of VB indicate that the movement of the metal is more restricted in all three directions in comparison to boron as also observed by VB<sub>2</sub> (Table 3.11). However, the anisotropy is less pronounced. As shown in Figure 3.16 vanadium atoms have closer distances in rectangular pyramids along [010] direction which is also reflected in the relatively smaller ADP in the same direction. The displacement of boron atoms along the B–B zig-zag chain is smaller than in other directions. Similar situation is observed by borons in VB<sub>2</sub> which displacement in B-network is also considerably smaller. This is presumably due to the strong forces existing between boron atoms in planes or along chains, which in turn restrict their movement in the corresponding directions.

Third-order anharmonic parameters for both atoms positions are close to zero. Therefore, only fourth order parameters are refined within the anharmonic description (Table 3.12). The fourth-order ADPs for the boron positions are smaller than their error estimates. Therefore, the displacement of boron is described only in harmonic motion.

**Table 3.12** Anharmonic ADPs (Å<sup>4</sup>) of in the crystal structure of VB.

Atom	$D_{1111}$	$D_{2222}$	$D_{3333}$	$D_{1122}$	$D_{1133}$	$D_{2233}$
V	-1.6(1)	–	-1.5(1)	–	-0.46(4)	—
B	kept fixed					

### 3.5.3 Crystal structure of $V_3B_4$

The  $V_3B_4$  is a representative of  $Ta_3B_4$  structure type. The crystal structure can be described as a combination of trigonal prism units and rectangular pyramids built by vanadium atoms similar to VB. In this structure type, the boron atoms of different chains are closer to each other, thus forming a double chain (Figure 3.17). There are two inequivalent boron positions. B2 atom is more responsible for the formation of the zig-zag chain, whereas B1 is linking both chains. Also two inequivalent positions exist for vanadium atoms: V1 is located below and above the boron double chain; V2 is sitting at the corner of the rectangular base of the rectangular pyramids.

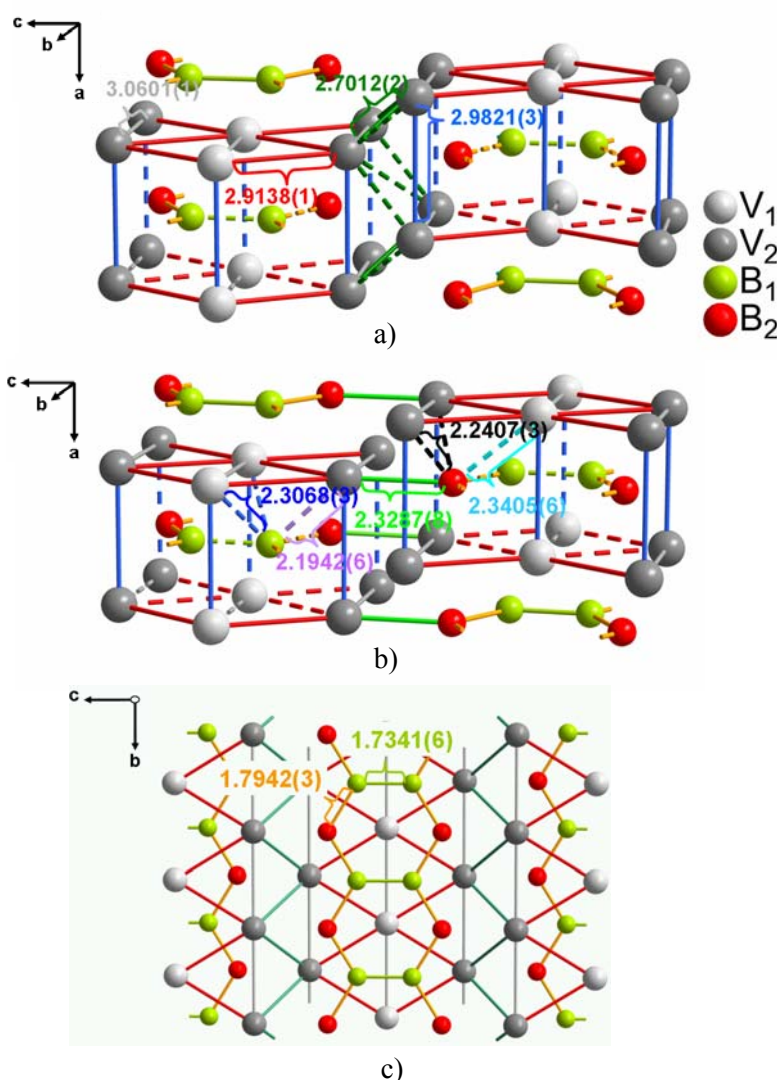


**Figure 3.17:** Interatomic distances (Å) in the crystal structure of  $V_3B_4$ . a) V-V distances. The view is parallel to the B-B zig-zag double chain. b) B-V distances. The view is the same as in a). c) B-B distances. The view is perpendicular to the B-B zig-zag double chain.

The shortest V–V interatomic distance which is drawn in dark green is  $\sim 2.70$  Å (Figure 3.17). The respective interatomic line connects the metal layers which are shifted along [100] direction. The trigonal prisms are distorted. The boron atoms which are sitting inside are located closer to the vanadium atoms which form the base of the rectangular pyramids. As a result, the boron double chains are slightly compressed along [010] axis as observed by the boron zig-zag chain of VB. The bond angle is smaller than  $120^\circ$ .

Kiessling claimed that the B1–B1 distances in isostructural  $\text{Ta}_3\text{B}_4$ ,  $\text{Cb}_3\text{B}_4$ ,  $\text{Mn}_3\text{B}_4$  and  $\text{Cr}_3\text{B}_4$  compounds are shorter (1.45–1.55 Å) than the characteristic bond lengths (1.73–1.8 Å).<sup>[25b, 124]</sup> These values are considerably shorter than any B–B distance previously reported. He concluded that these short distances are indication of B–B double bonds since the double bond radius for boron is 0.76 Å according to Pauling.<sup>[125]</sup> It has been asserted by several authors that this short B–B distance is also present in  $\text{V}_3\text{B}_4$ . In all these studies, the structure determination is based only on assigning the structure type and the refining unit cell parameters.<sup>[32, 126]</sup> In contrary, Elfstrom claimed that in  $\text{Cr}_3\text{B}_4$  no such abnormally short B–B distances exist.<sup>[127]</sup> The complete structure determination in the present work reveal that the corresponding distances in  $\text{V}_3\text{B}_4$  are not remarkably shorter; they are similar to the characteristic B–B bond length.

**Table 3.13** Atomic positions and anisotropic ADPs ( $\text{\AA}^2$ ) in the crystal structure of  $\text{V}_3\text{B}_4$ .

Atom	$x/a$	$y/b$	$z/c$	$B(\text{eq})$	$B_{11}$	$B_{22}$	$B_{33}$
V(1)	0	0	0	0.123(3)	0.096(5)	0.136(4)	0.137(4)
V(2)	1/2	0	0.31250(1)	0.130(2)	0.094(3)	0.163(3)	0.133(3)
B(1)	0	0	0.43441(4)	0.270(7)	0.26(1)	0.28(1)	0.27(1)
B(2)	1/2	0	0.13641(4)	0.296(7)	0.29(1)	0.29(1)	0.31(1)

$$^*B(\text{eq}) = 1/3[B_{11}a^{*2}a^2 + \dots + 2B_{23}b^*c^*bc \cos \alpha]$$

Table 3.13 summarizes the atomic positions and the ADPs in  $\text{V}_3\text{B}_4$ . In general, the displacement of both vanadium atoms is more restricted along [100] axis in contrary to those observed in VB and  $\text{VB}_2$ . V1 atom which is located in the middle of the double chain has less displacement than V2 atoms forming the rectangular pyramids along the [010] axis. The displacement of B atoms is closer to each other in all directions. There is not any con-

siderable reduction of displacement in the (100) boron layer in neither [010], nor [001] direction in contrary to the ADPs of borons in VB and VB<sub>2</sub> which show variations in different directions.

Only fourth-order parameters are refined within the anharmonic description of the ADPs since third order anharmonic parameters for both atoms positions are close to zero (Table 3.14). The  $D_{3333}$  for both V atoms is also not refined according to the same reason. The fourth order ADPs for both boron positions are ignored due to high standard deviations.

**Table 3.14** Anharmonic ADPs ( $\text{\AA}^4$ ) in the crystal structure of V<sub>3</sub>B<sub>4</sub>.

Atom	$D_{1111}$	$D_{2222}$	$D_{1122}$	$D_{1133}$	$D_{2233}$
V1	-2.1(4)	-2.0(3)	-0.7(1)	–	–
V2	-2.0(3)	1.0(2)	-0.5(1)	–	–
B1-B2	kept fixed				

### 3.5.4 Crystal structure of V<sub>2</sub>B<sub>3</sub>

Similar to other vanadium borides previously described, the V<sub>2</sub>B<sub>3</sub> structure consists of trigonal prism units and rectangular pyramids formed by vanadium atoms (Figure 3.18). The atom distances are in agreement with previously published data.<sup>[31a]</sup> Boron atoms are sitting in trigonal prisms formed by vanadium atoms and form the triple chains which are extending along the [001] axis. The boron layers are shifted along [100] with respect to each other. There are three inequivalent boron atom positions; B3 is responsible for the formation of the zig-zag chain more analogous to VB, a second one B1 analogous to VB<sub>2</sub>. The third boron atom is linking two different motifs. There are two vanadium positions: first one V1 is situated below and above the boron double triple chain; second one V2 is located at the base corners of the rectangular pyramid. There are two types of trigonal prisms: one is formed only by V1 atoms; second one consists of both types of vanadium atoms. Both trigonal prism types are distorted whereas the volume of the trigonal prism unit formed only by V1 atoms is larger. B2 and B3 atoms are shifted from the center of the trigonal prisms near to the base of the rectangular pyramide. As a result, the boron triple chain is compressed along the [001] axis, as also observed by VB and V<sub>3</sub>B<sub>4</sub>. B(1) is also

not sitting exact at the center of the trigonal prism formed by V1 and V2 atoms. However, the position away from the middle point of the prism is relatively less in comparison to other borons.

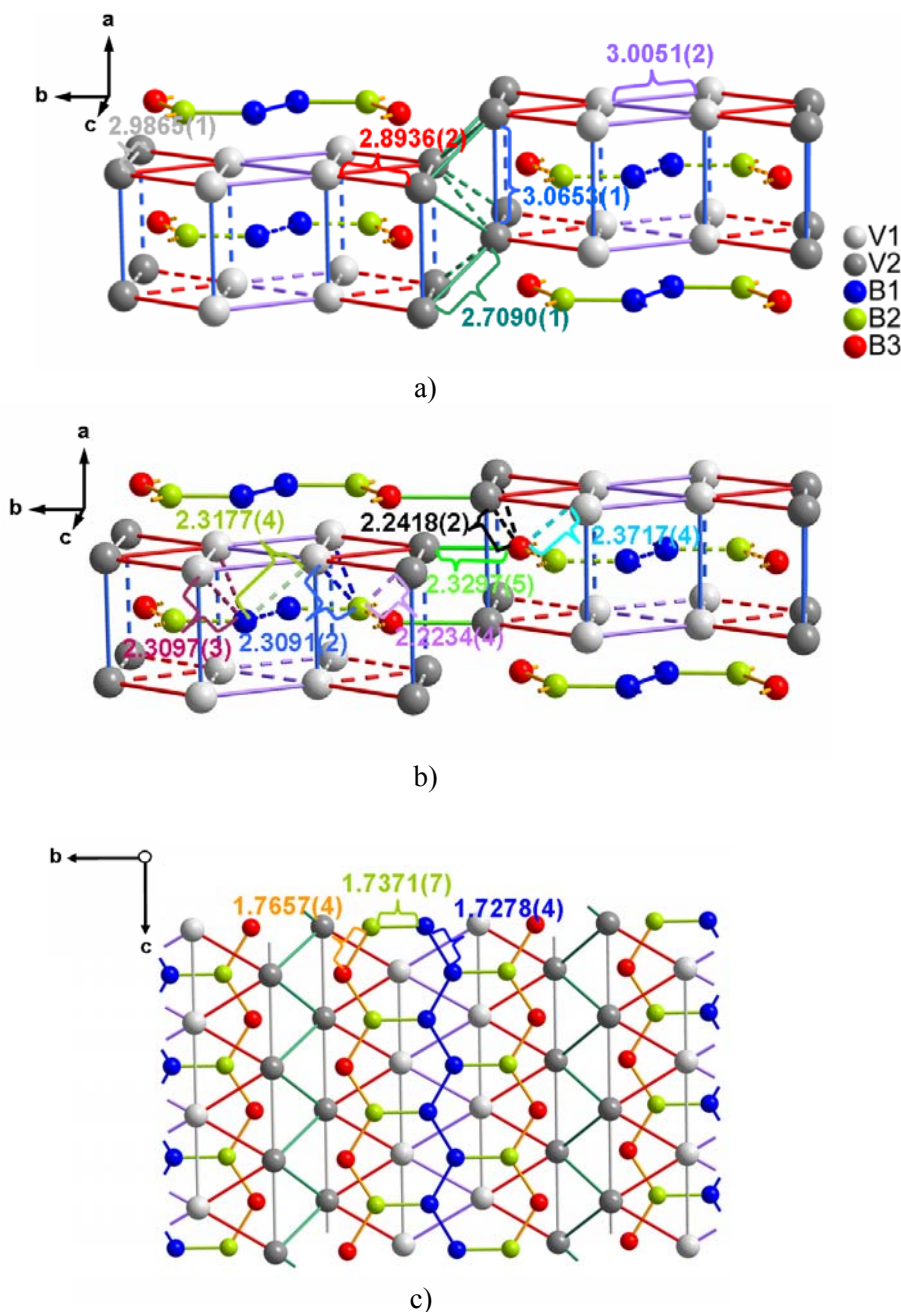


**Figure 3.18** Interatomic distances (Å) in the crystal structure of  $V_2B_3$ . a) V-V distances. The view is parallel to the B-B zig-zag triple chain). b) The B-V distances. The view is parallel to the plane as shown in a). c) The B-B distances. The view is perpendicular to the B-B zig-zag triple chain.

Table 3.15 summarizes the atomic positions and the ADPs of  $V_2B_3$ . Obviously, V1 displaces more easily in the (100) metal plane in contrary to the vanadium atom in  $VB_2$  which movement is relatively more restricted in corresponding directions. For V2 the displacement along [010] is relatively smaller indicating the restriction of motion in the respective direction for those vanadium atoms forming the rectangular pyramide as also observed by VB. The displacement of B1 and B2 are relatively more restricted along [010] and [001] axis whereas for B3 the most noticeable reduction in the vibration is along [001] direction.

**Table 3.15** Atomic positions and anisotropic ADPs ( $\text{\AA}^2$ ) in the crystal structure of  $V_2B_3$ .

Atom	$x/a$	$y/b$	$z/c$	$B(\text{eq})^*$	$B_{11}$	$B_{22}$	$B_{33}$
V(1)	0	0.42934(1)	$\frac{1}{4}$	0.135(2)	0.126(3)	0.133(3)	0.148(3)
V(2)	0	0.70499(1)	$\frac{1}{4}$	0.126(2)	0.126(3)	0.111(3)	0.141(3)
B(1)	0	0.02356(2)	$\frac{1}{4}$	0.255(5)	0.306(9)	0.220(9)	0.239(8)
B(2)	0	0.11769(2)	$\frac{1}{4}$	0.257(5)	0.307(9)	0.216(9)	0.248(8)
B(3)	0	0.83125(2)	$\frac{1}{4}$	0.281(5)	0.297(9)	0.296(9)	0.248(8)

$$^*B(\text{eq}) = 1/3[B_{11}a^{*2}a^2 + \dots + 2B_{23}b^*c^*bc \cos \alpha]$$

Refining the third order anharmonic ADPs yields values near zero. Hence, only fourth order parameters are refined within the anharmonic description (Table 3.16). The  $D_{2222}$  for both V atoms is also not refined according to the same reason. The fourth order ADPs for both boron positions yield very high standard deviations. Accordingly, they are also not included in the model.

**Table 3.16** Anharmonic ADPs ( $\text{\AA}^4$ ) in the crystal structure of  $V_2B_3$ .

Atom	$D_{1111}$	$D_{3333}$	$D_{1122}$	$D_{1133}$	$D_{2233}$
V1	-2.5(1)	-1.9(1)	–	-0.9(1)	–
V2	-1.9(1)	1.7(1)	–	-0.7(1)	–
B1-B2-B3	kept fixed				



### 3.6 Similarities between the crystal structures of vanadium borides

The structural analysis of the vanadium borides based on IAM refinement verifies that there are slight variations in the resembling atomic arrangements of different vanadium borides. As also stated in previous sections the boron atoms in VB, V<sub>3</sub>B<sub>4</sub> and V<sub>2</sub>B<sub>3</sub> are shifted from the centers of the trigonal prisms which induces slight differences in B–B angles and distances.

**Table 3.17** Geometric parameters in vanadium borides.  $d(\text{B–B})$  is the B–B interatomic distance whereas  $\alpha$  is the angle formed by boron atoms along the respective zig-zag chains. The bond angle of the central zig-zag chain is denoted by an asterisk. The volumes (V) of vanadium-trigonal prism units are also given for a comparison reason.

	$d(\text{B–B})$ (Å)	$\alpha$ (°)	V (Å <sup>3</sup> )
VB <sub>2</sub>	1.7307(2)	120.00	11.891
	1.7278(8)	119.73(3) *	11.917
V <sub>2</sub> B <sub>3</sub>	1.7371(7)	115.50(3)	11.344
	1.7657(4)		
V <sub>3</sub> B <sub>4</sub>	1.7341(6)	117.04(2)	11.315
	1.7942(3)		
VB	1.7939(4)	111.99(3)	10.807

A comparison between B–B distances and angles in VB<sub>2</sub>, V<sub>3</sub>B<sub>4</sub>, V<sub>2</sub>B<sub>3</sub> and VB structures is given in Table 3.17. In general, B–B distances tend to decrease with increasing boron content. Conversely, the B–B bond angles tend to decrease with decreasing boron content. The volume of the vanadium-trigonal prism units increases towards higher borides. The shortest B–B distance is found in V<sub>2</sub>B<sub>3</sub> which seems to be very close to that in VB<sub>2</sub>. V<sub>3</sub>B<sub>4</sub> has two B–B distances: The larger one is very similar to that in VB whereas the shorter one is close to the B–B distances both in VB<sub>2</sub> and in the central zig-zag chain of V<sub>2</sub>B<sub>3</sub>.

### 3.7 Summary

Single crystals of vanadium boride are synthesized by both Al flux method and arc-melting. According to X-ray powder diffraction results,  $\text{VB}_2$  and  $\text{V}_2\text{B}_3$  phases can be obtained nearly in pure form from the Al melt whereas arc melting synthesis allows preparation of VB and  $\text{VB}_2$  crystals as single phase. The efforts for the synthesis of other vanadium borides end up mostly with a number of by-products belonging to the Al-V system and / or additional vanadium borides. In those cases, the powder lines are mostly overlapping which in turn complicates the identification of the respective phases. Careful investigations about the homogeneity range using X-ray powder diffraction in accordance with WDXS ensure that there is not any clear indication of a deviation from ideal stoichiometry for  $\text{VB}_2$  and VB which is also supported by the single crystal refinement. On the other hand, the homogeneity range examination of other vanadium borides is mostly hampered due to the overlapping X-ray powder diffraction lines.

High resolution X-ray single crystal diffraction measurements are carried out for  $\text{VB}_2$ ,  $\text{V}_2\text{B}_3$ ,  $\text{V}_3\text{B}_4$  and VB crystals. The IAM refinements yield quite small reliability factors  $R_{\text{(F)}}$ . Data analysis after the conventional refinement reveals that the difference between the observed and calculated structure factors arises suddenly at very high resolution. Varying of the integration box size does not provide any improvement. Accordingly, the most disagreeable reflections in data sets of  $\text{V}_3\text{B}_4$  and  $\text{V}_2\text{B}_3$  are excluded in the refinement.

Crystal structures of the respective vanadium borides are discussed in light of the IAM refinement. Several fragments of different vanadium boride structures exhibit correlations in their geometric parameters. These are well reflected in B–B distances and angles, in particular. A closer inspection of the respective electronic structures via charge density analysis is expected to reflect these structural features.

## 4 ELECTRON DENSITY IN VB<sub>2</sub>

In this section, first a procedure for the multipole refinement of VB<sub>2</sub> structure is outlined. A topological analysis of the reconstructed ED is carried out based on Bader's QTAIM. Investigations are focused on the B–B and B–V interactions, in particular. Furthermore, a comparison between experiment and theory is given. All the multipole refinements carried out in this thesis are performed with WinCSD program package.<sup>[114]</sup> The ED is reconstructed with *WinXPRO* program.<sup>[128]</sup> For testing the results residual densities were calculated using XD2006 program package.<sup>[129]</sup>

### 4.1 Multipole refinement

The results of the Independent atom model (IAM) refinement suggest that VB<sub>2</sub> is a relatively good candidate for a charge density analysis compared to other vanadium borides according to the lower residual factor  $R_{(F)}$  obtained. This structure also offers another advantage in terms of the relatively low number of the multipole parameters to be refined due to its higher symmetry. In addition to the conventional IAM parameters, two valence, five multipole and four expansion and contraction (two for each atom) parameters have to be refined in the framework of the multipole formalism.

The V and B atoms have site symmetry  $6/mmm$  and  $\bar{6}m2$ , respectively. Therefore, the multipole expansion is terminated at the hexadecapole level for each atom. The contributing multipoles for V atoms are  $P_v$ ,  $P_{20}$  and  $P_{40}$ . For B atoms,  $P_v$ ,  $P_{20}$ ,  $P_{33}$  and  $P_{40}$  are allowed by symmetry. The core and valence EDs are constructed by the Hartree-Fock wavefunctions taken from Clementi and Roetti.<sup>[130]</sup> The respective radial-function parameters  $n_2 = 2$ ,  $n_4 = 4$  and  $\zeta_V = 4.4$  for V and  $n_2 = 2$ ,  $n_3 = 3$ ,  $n_4 = 4$  and  $\zeta_B = 2.53$  for B have been used.

Prior to the multipole refinement all parameters used in the spherical model are fixed. In the multipole model  $4s^2$ ,  $3d^3$  and  $2s^2$ ,  $2p^1$  scattering contributions are included in the valence functions for V and B, respectively. This gives electron populations  $P_v$  of 5 e<sup>−</sup> for V and 3 e<sup>−</sup> for B as starting values. First, only displacement parameters and the scale factor are refined using all data keeping  $P_v$  parameters fixed ( $R_{(F)} = 0.94\%$ ). After this, the  $P_v$  parameters are refined for both atom positions using low order data up to  $(\sin \theta / \lambda) \leq 0.8 \text{ \AA}^{-1}$

keeping  $\kappa$ ,  $\kappa'$  and all multipole parameters fixed. The same statistical weighting scheme ( $w = 1 / \sigma^2 F$ ) is used as in the IAM refinement. The electron populations for both atoms indicate that there is charge transfer from vanadium to boron. The electroneutrality condition is imposed for the unit cell. The  $P_{lm\pm}$  parameters together with  $\kappa$  and  $\kappa'$  are refined using  $(\sin \theta / \lambda) \leq 0.8 \text{ \AA}^{-1}$ . Subsequently, they are fixed and the  $P_v$  parameters and the thermal parameters are refined step by step using the same part of the data set as before. Such a procedure is repeated several times until the final convergence is achieved. The  $R_{(F)}$  value for the whole data set drops to 0.74%. The multipole refinement at this stage gives the final model which is used for reconstruction of the ED. The multipole, expansion and contraction parameters are summarized in Table 4.1.

**Table 4.1** Multipole, expansion and contraction parameters of VB<sub>2</sub>.

	V (in $6/mmm$ )	B (in $\bar{6}m2$ )
$P_v$	4.706	3.147
$P_{20}$	0.024(2)	0.002(2)
$P_{33-}$	—	0.229(2)
$P_{40}$	-0.015(2)	-0.093(2)
$\kappa$	0.984(2)	0.986(2)
$\kappa'$	1.258(2)	0.808(2)

The use of multipole model instead of spherical treatment of atoms reduce the  $R_{(F)}$  value from 0.47% to 0.36% for the first 35 low order reflections up to  $(\sin \theta / \lambda) \leq 0.8 \text{ \AA}^{-1}$ . Figure 4.1 demonstrates this improvement in the fit by the ratio of observed and calculated structure factors  $F_{\text{obs}} / F_{\text{calc}}$  as a function of  $(\sin \theta / \lambda)$ .

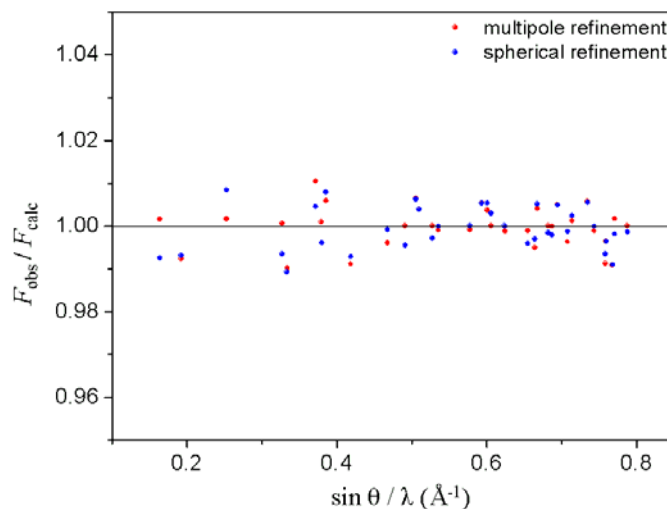


**Figure 4.1**  $F_{\text{obs}} / F_{\text{calc}}$  vs.  $\sin \theta / \lambda$  after conventional (red) and multipole (blue) refinement.

Figure 4.2 shows density residuals with the max. and min. values of 0.643 / -0.114 in the vicinity of boron atom and in the B–B internuclear region after the IAM refinement. The use of multipole model instead provides a featureless residual density map with the max. and min. values of 0.067 / -0.058.

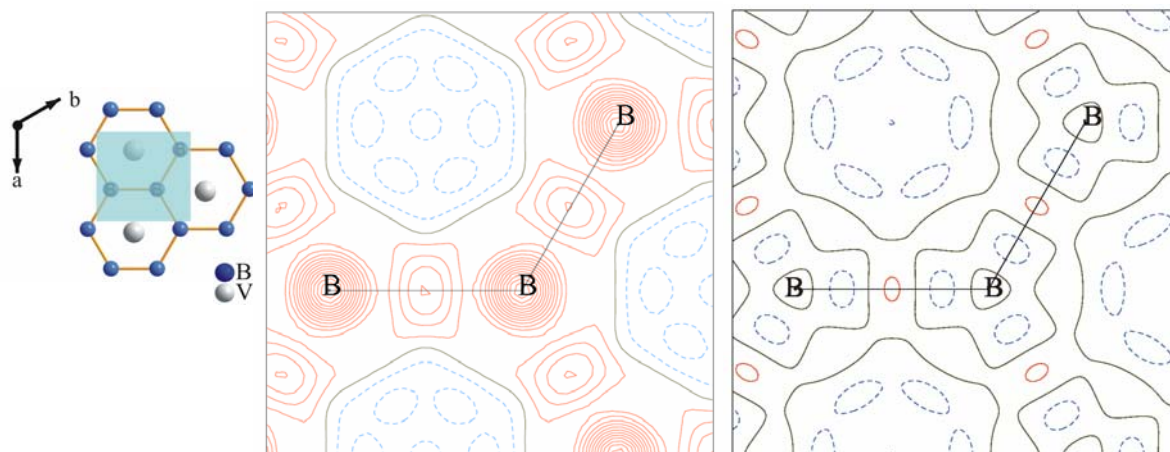


**Figure 4.2** Residual density distribution in B-atom plane after IAM (left) and multipole (right) refinement; data cut-off at  $\sin \theta/\lambda=0.9 \text{ \AA}^{-1}$ ; contour level step width:  $0.05 \text{ e\AA}^{-3}$ . Solid red and dashed blue lines correspond to positive and negative values, respectively, whereas solid black line is the zero contour.

The use of the multipole model instead of simple spherical atoms induced some changes in the ADPs of both vanadium and boron atoms. The harmonic room-temperature amplitude of the V-atom displacement along [001] and in the (001) plane is reduced whereas those of the boron atoms in the same directions are increased (Table 4.2).

**Table 4.2** The harmonic ( $\text{\AA}^2$ ) and anharmonic ( $\text{\AA}^4$ ) ADPs due to IAM and multipole refinement.

		$B(\text{eq})^*$	$B_{11}$	$B_{33}$	$D_{1111}$	$D_{3333}$	$D_{1133}$
IAM Refinement	V	0.152(2)	0.115(3)	0.155(4)	-3.9(2)	-1.6(1)	-0.8(1)
	B	0.261(4)	0.185(4)	0.320(8)		kept fixed	
Multipole Refinement	V	0.129(2)	0.095(3)	0.125(4)	-4.2(2)	-2.1(1)	-0.9(1)
	B	0.271(4)	0.193(4)	0.332(8)		kept fixed	

\*  $B(\text{eq}) = 1/3[B_{11}a^{*2}a^2 + \dots + 2B_{23}b^*c^*bc \cos \alpha]$

## 4.2 Topological analysis of the electron density in $\text{VB}_2$

Figure 4.3 shows the total ED for  $\text{VB}_2$  in some selected planes reconstructed from experiment as well as from theoretical calculations for a comparison reason.

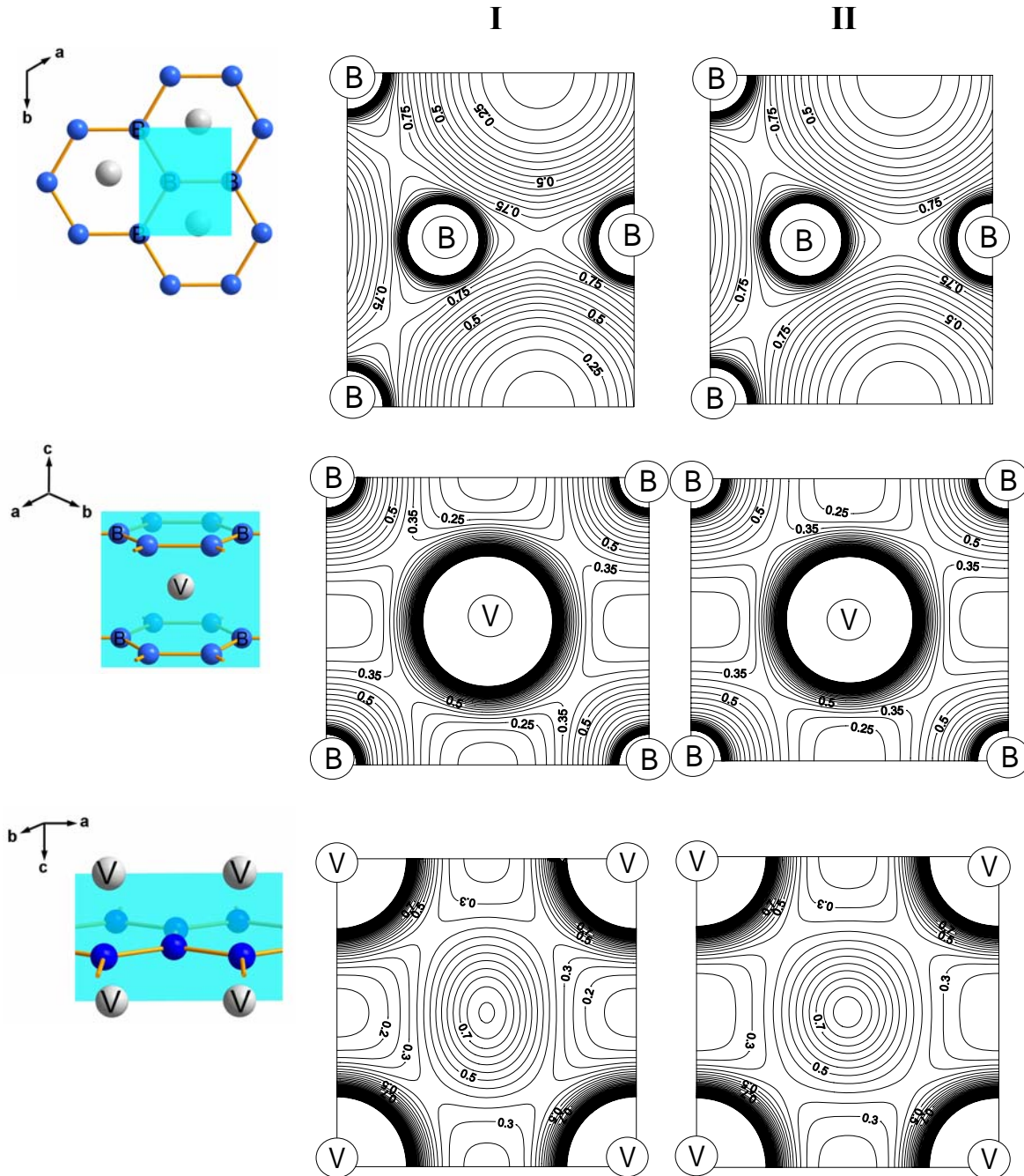


**Figure 4.3** The total ED maps for  $\text{VB}_2$  in planes as shown: (I) reconstructed from the X-ray data, (II) calculated by DFT method. The isoline interval is  $0.05 \text{ e } \text{\AA}^{-3}$ .

The topological features of the reconstructed total ED are in markedly good agreement with the results of the quantum chemical calculations (Figure 4.3). However, it should be considered that the total ED values are dominated, particularly, from those in the core region so that the values in the bonding regions are much smaller. This underlines the necessity of a close inspection of the density based properties like the Laplacian, bond paths, critical points (cp) and also deformation densities in order to have better understanding of the chemical bond.

Table 4.3 indicates that all of the cp types are present in the ED of VB<sub>2</sub>. Some of their positions are restricted by the space group symmetry. The number of the different cp types fulfills the Poincare-Hopf condition.<sup>[131]</sup> No non-nuclear attractors were found.

**Table 4.3** Topological characteristics of the critical points determined from reconstructed experimental data and theoretical calculations. Theoretical values are denoted by an asterisk.

Wyckoff notation and position of cp	$\rho(r_{cp})(e \text{ \AA}^{-3})$	$\nabla^2 \rho(r_{cp})(e \text{ \AA}^{-5})$	$\lambda_1(e \text{ \AA}^{-5})$	$\lambda_2(e \text{ \AA}^{-5})$	$\lambda_3(e \text{ \AA}^{-5})$	Type of cp
3g (0.5,0.5,0.5)	0.812	-3.098	-3.285	-1.897	2.082	3, -1
3g (0.5,0.5,0.5)*	0.831	-4.480	-3.12	-2.757	1.395	3, -1
12o (0.823, 0.177, 0.240)	0.364	2.953	-1.029	-0.101	4.085	3, -1
12o (0.832, 0.168, 0.261)*	0.393	2.299	-1.072	-0.195	3.567	3, -1
12n (0, 0.692, 0.243)	0.364	2.744	-0.964	0.118	3.591	3, +1
12n (0,0.712,0.268)*	0.384	2.430	-1.027	0.183	3.273	3, +1
3f (0, 0.5, 0)	0.232	1.050	-0.130	0.552	0.629	3, +1
3f (0, 0.5, 0)*	0.220	1.048	-0.065	0.523	0.593	3, +1
2c (0.333, 0.667, 0)	0.213	1.168	0.150	0.150	0.870	3, +3
2c (0.333, 0.667, 0)*	0.211	0.954	0.072	0.072	0.809	3, +3
1b (0,0,0.5)	0.124	1.732	0.465	0.465	0.802	3, +3
1b (0,0,0.5)*	0.206	1.424	0.547	0.547	0.330	3, +3

Comparison of the ED at cps both from experiment and theory reveal that the same number and type of critical points are obtained. There are only minor quantitative differences in ED values at critical points. Experimental topological descriptors agree with the values of theory by  $\pm 0.08 e \text{ \AA}^{-3}$  for  $\rho(r_{cp})$  and  $\pm 1.4 e \text{ \AA}^{-5}$  for  $\nabla^2 \rho(r_{cp})$ .

### 4.2.1 The B–B interaction

The examination of the principle curvatures of ED at critical points provides valuable information about atomic interactions. Topological analysis of ED indicates a bcp between boron atoms in VB<sub>2</sub> (Figure 4.4). At the bond critical point (bcp) the principal curvature along the bond path  $\lambda_3$  is positive and reaches its minimum. The axis of this single positive curvature is perpendicular to the plane defined by the respective axes of the remaining two negative curvatures  $\lambda_1$  and  $\lambda_2$ . The ED is a maximum at bcp in this plane. The sum of the principle curvatures of ED at this bcp is negative, clearly indicating the concentration of the ED in the boron internuclear region (Table 4.4). Such a situation is typical for covalent bonds.

Figure 4.4 shows the deformation ED and the gradient field  $\nabla\rho(r)$  of ED in the boron network plane together with the B–B bond paths. The bond paths are coincident with the interatomic lines due to the high local symmetry of atomic position. The DD map on the same plane reveals that the ED is predominantly accumulated in the B–B interatomic region.

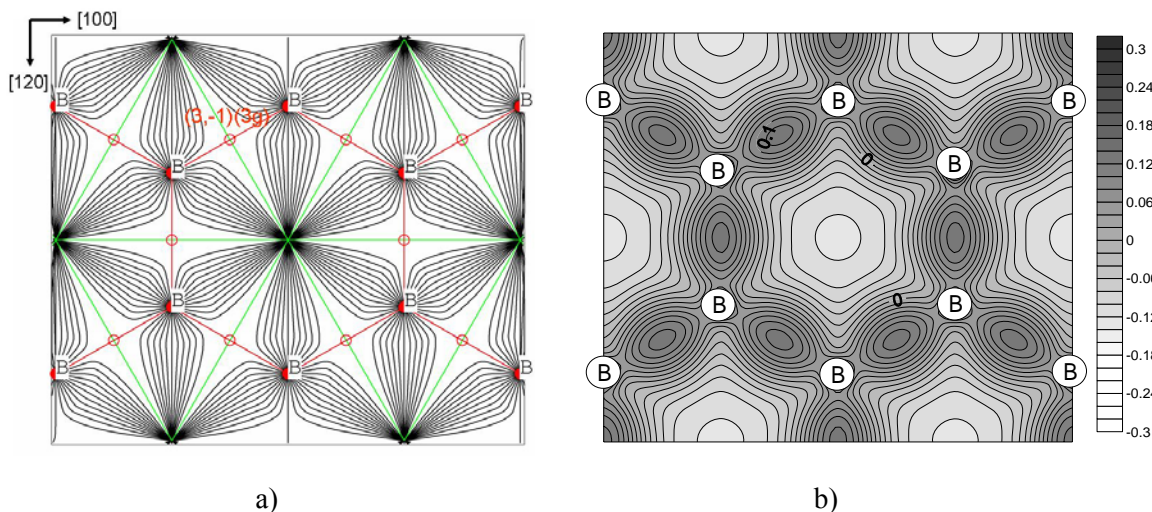


**Figure 4.4** a) The  $\nabla\rho(r)$  field of the ED in the B–atom plane in VB<sub>2</sub>. The B–B bond paths are drawn in red. The bond critical points are denoted by circles. b) The deformation ED map (left) in the same plane. The isoline interval is 0.02 e a.u.<sup>-3</sup>.

Some other selected properties of B–B bond are given in Table 4.4. An important quantity which is in relation with the principle curvatures of the ED is the ratio of largest perpendicular contraction at the bcp  $\lambda_1$  and the parallel contraction towards the nuclei  $\lambda_3$ .  $|\lambda_1| / \lambda_3$  ratio is a measure for the bond strength for homoatomic interactions. If  $\lambda_1$  domi-



nates, the ED is locally concentrated in the region of the bond critical point. If the positive curvature ( $\lambda_3$ ) dominates, ED is concentrated separately in each atomic basin. In the present case, both the theoretical and experimental  $|\lambda_1| / \lambda_3$  ratio is larger than unity indicating a strong B–B interaction in the boron network.

**Table 4.4** Topological properties of B–B bond critical point in VB<sub>2</sub> determined from the reconstructed experimental (first row) and theoretically calculated (second row) ED.

	$\rho(r_b)$ (e Å <sup>-3</sup> )	$\nabla^2 \rho(r_b)$ (e Å <sup>-5</sup> )	$\lambda_1$ (e Å <sup>-5</sup> )	$\lambda_2$ (e Å <sup>-5</sup> )	$\lambda_3$ (e Å <sup>-5</sup> )	$\varepsilon(r_b)$	$ \lambda_1  / \lambda_3$
Exp.	0.812	-3.098	-3.285	-1.897	2.082	0.731	1.58
Theory	0.823	-3.856	-2.91	-2.554	1.591	0.140	1.83

A commonly used topological index of a bcp is the ellipticity which is the ratio of its negative curvatures along the axes perpendicular to the bond path ( $\varepsilon = \lambda_1/\lambda_2 - 1$ ). Values above zero indicate deviations from cylindrical symmetry of the bond. Experimentally determined ellipticity value at B–B bcp is significantly larger than the theoretical one. The elliptical nature of the B–B bonds may indicate relevant  $\pi$ -density contributions to the bond. The topology of DD in Figure 4.5 explicitly confirms the deviation from the cylindrical symmetry of B–B bond. The isolines of ED are elongated along the [001] direction.

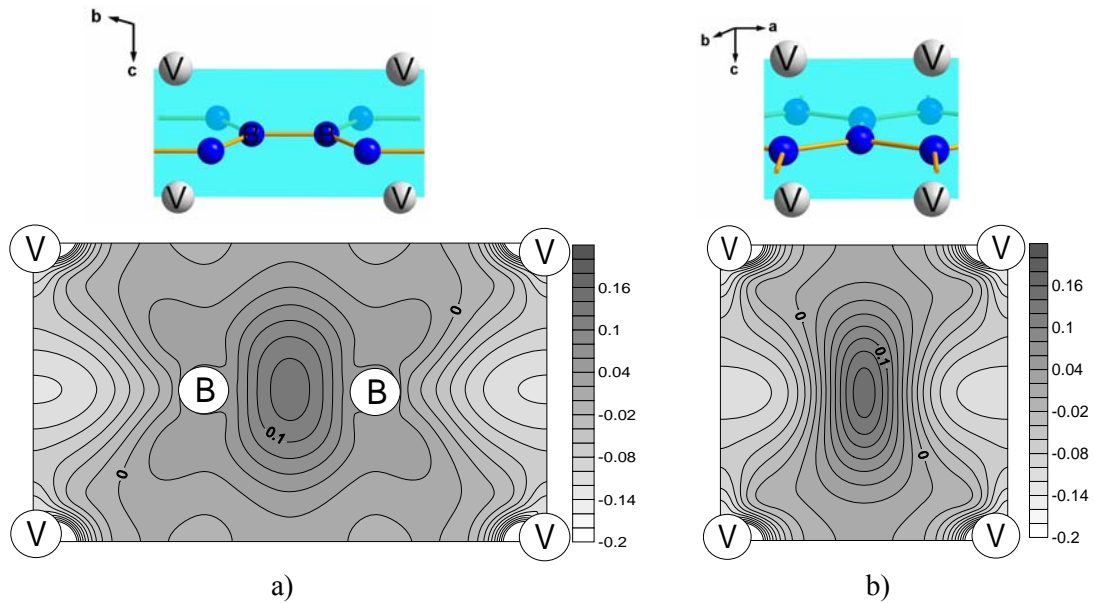


**Figure 4.5** a) Deformation electron densities in VB<sub>2</sub> a) in (1 $\bar{1}$ 0) plane; (b) in (100) plane. The iso-line interval is 0.02 e a.u.<sup>-3</sup>

The distribution of ED Laplacian  $\nabla^2\rho(r)$ , as a second derivative function, is capable of analysing fine details in the topology of ED. According to both theory and experiment there are two minimas along B–B bond path as shown in Figure 4.6. These are originating from two valence shell charge concentrations in the B–B interatomic region. Experimental results indicate that the curve is more contracted in the valence region in comparison to theory indicating that the valence shell is more pronounced.

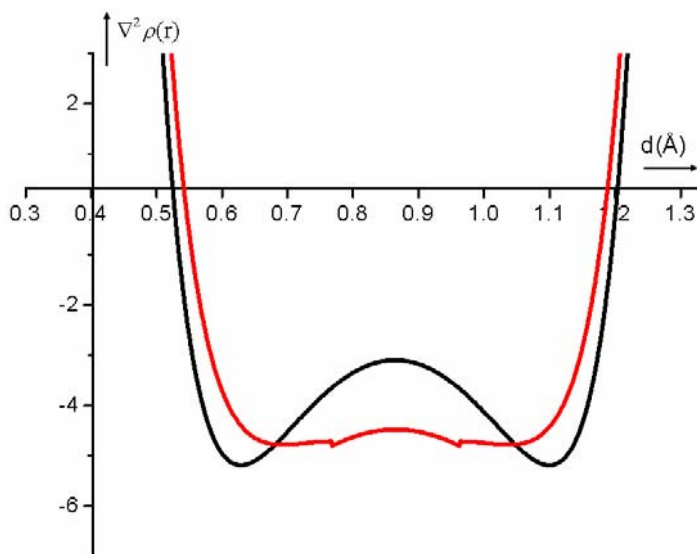


**Figure 4.6** Laplacian distribution  $L(r) = -\nabla^2\rho(r)$  along B–B bond path. The bcp is located at a distance of 0.875 Å from both B-atoms (at 0 Å and 1.7499 Å, respectively) exactly in the middle of the bond path. The non-continuous behaviour of the theoretical values is an artefact originating from the APW basis set used for the theoretical calculation.

#### 4.2.2 The B–V interaction

In the topological analysis of both experimentally and theoretically derived ED, a second bcp (at the 12o position) is found in B–V interatomic region. The magnitude of ED at the bcp is less than half compared to that found at the B–B bcp. The sign of the  $\nabla^2\rho$  at the B–V bcp is positive but its magnitude is considerably smaller in comparison to those found in strong ionic interactions. It has to be stressed that, one of the principal curvatures of the ED,  $\lambda_2$ , is definitively smaller than the other two curvatures (Table 4.5). There is also a ring critical point (rcp) located at the 12n position on the three membered ring surface that result from the formation of B–B and B–V bond paths. Similarly, one of the principle curvatures  $\lambda_2$  of the ED at this rcp is considerable smaller than the other two (Table 4.3).

**Table 4.5** Experimentally and theoretically determined topological properties of the B–V bond in VB<sub>2</sub>.  $d(\text{bcp})$  is the distance between the B–V bcp and the B–V interatomic line.

	$d(\text{bcp})$ (Å)	$\rho(r_b)$ (e Å <sup>-3</sup> )	$\nabla^2\rho(r_b)$ (e Å <sup>-5</sup> )	$\lambda_1$ (e Å <sup>-5</sup> )	$\lambda_2$ (e Å <sup>-5</sup> )	$\lambda_3$ (e Å <sup>-5</sup> )	$\varepsilon(r_b)$
Exp.	0.059	0.364	2.953	-1.029	-0.101	4.085	9.188
Theory	0.063	0.393	2.299	-1.072	-0.195	3.567	4.497

Since the sign of the Laplacian is not informative for the interpretation of atomic interactions in case of transition metal bonding the local energy density  $H(r)$  is mostly used for a qualitative description of bonding. In a stable system, negative  $H(r)$  at the bcp is an additional requirement for the existence of a covalent bond. At the bcp along the B–V bond path the potential energy  $V(r)$  is dominating leading to  $H(r) = -0.013$  a.u. Accordingly, energetic considerations indicate that B–V bond is of covalent nature. This result is also supported by the magnitude of the ED Laplacian at the respective bcp which is considerably small as generally observed by strong ionic interactions.

As a result of the large difference between the principle curvatures of ED very high bond ellipticity at the B–V bcp is obtained which does not provide any meaningful information about the  $\pi$  character of the bond.

The experimental DD map on the  $(1\bar{1}0)$  plane indicates some ED accumulation in the B–V internuclear region which is smaller to that observed in B–B interatomic region (Figure 4.7a). Besides, the ED is depleted in regions between the metal atoms along the  $[001]$  axis. For the investigation of the transition metal bonding the density Laplacian is advantageous over deformation ED since it indicates charge concentrations without requiring a reference state, and allows –unlike DD maps– not only to analyse the internuclear space but also the vicinity of nuclei. The contour plot of the density Laplacian in the  $(1\bar{1}0)$  plane indicates a structurization in the penultimate shell of vanadium atom as shown in Figure 4.7(c and d). The theoretical calculations correlate well with experiment; according to both methods charge concentrations around the metal atom are directed towards the borons where they face a charge concentration which in turn supports an interaction between the boron and vanadium atoms (Figure 4.7b).

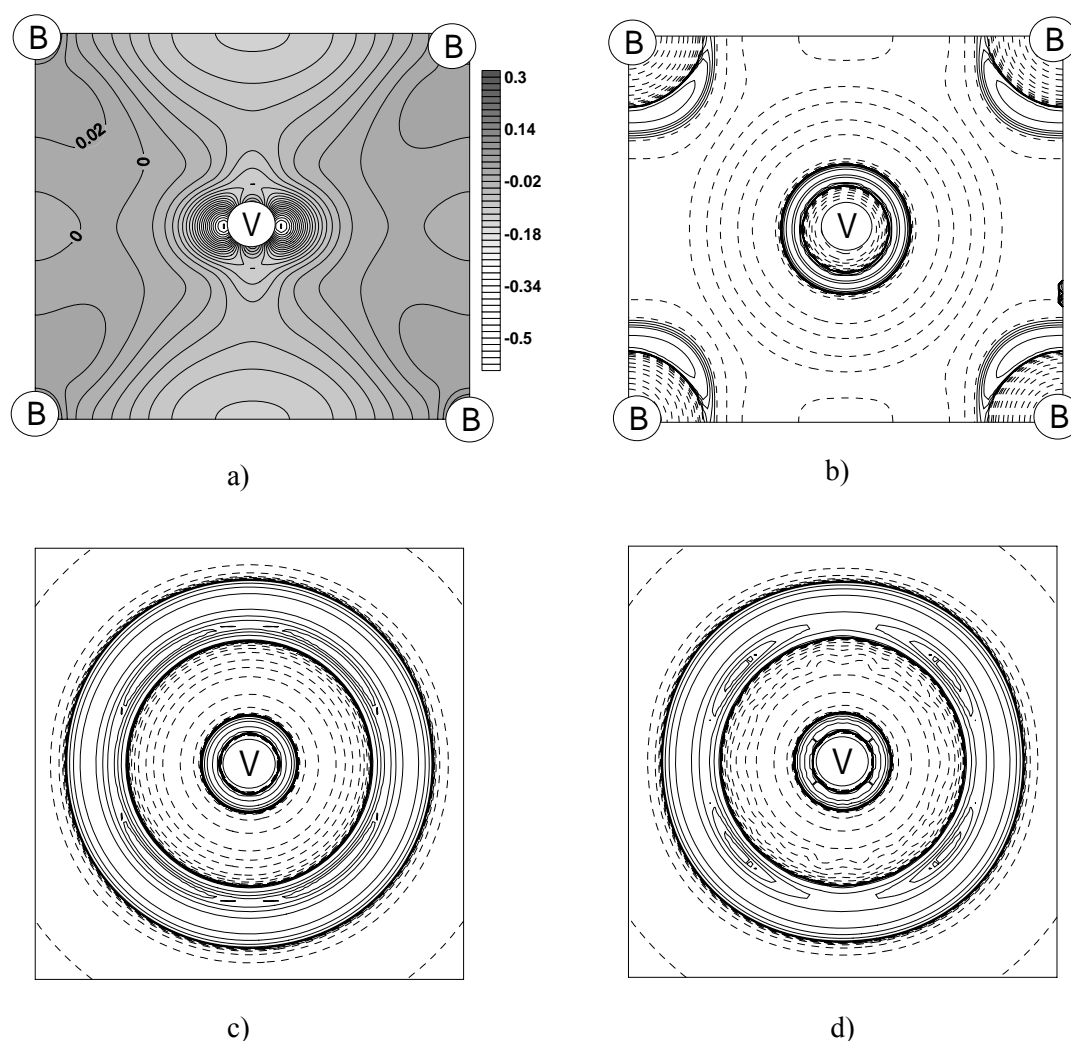


**Figure 4.7** a) The experimental deformation ED of VB<sub>2</sub> in  $(1\bar{1}0)$  plane. The isoline interval is 0.02 e a.u.<sup>-3</sup>. b) The experimental ED Laplacian of VB<sub>2</sub> in the same plane of (I). c) An enlarged view of the vanadium atom shown in b). d) The ED Laplacian calculated within DFT in the same plane of c). Solid and broken lines represent negative and positive Laplacian values, respectively. Isolines intervals for b) are  $\pm 2 \times 10^n$ ,  $\pm 4 \times 10^n$ ,  $\pm 8 \times 10^n$  e Å<sup>-5</sup> where  $n = 0, 4, 3, 2, 1$ . Additional isolines are -1, -0.75, -0.5 and -0.25 e Å<sup>-5</sup> for b) and -250, -275 and -288 e Å<sup>-5</sup> for c) and d).

Figure 4.8 shows the gradient field of the ED in  $(1\bar{1}0)$  plane. The B–V bond path is slightly curved. The distance of the B–V bcp from the respective internuclear line is 0.059 Å. The bcp is shifted along the bond path towards the boron atom which indicates the polarity of the B–V bond. The bond path length from bcp to the V nucleus is 1.174 Å whereas it is 1.139 Å between bcp and the B nucleus. Accordingly, the boundary surface between two atoms is closer to the boron atom.

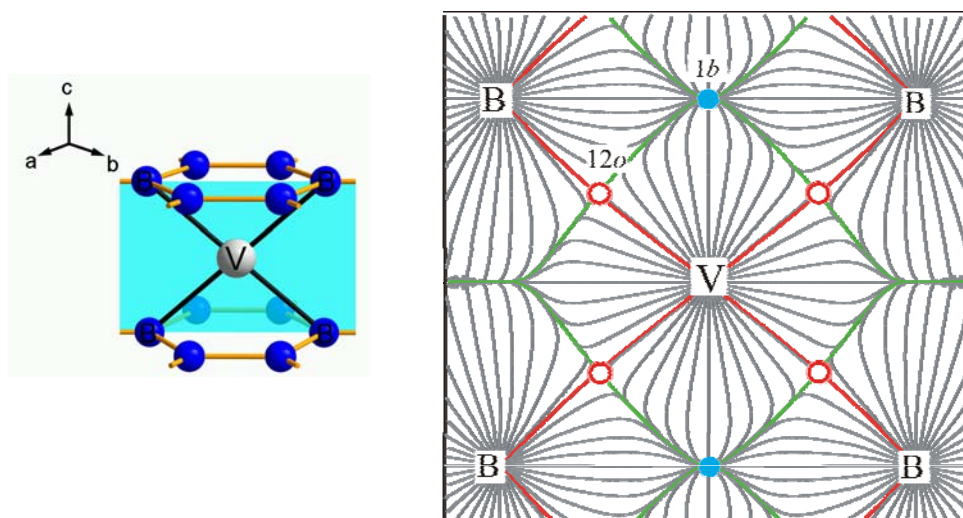


**Figure 4.8** Gradient field of the ED in  $\text{VB}_2$  in the  $(1\bar{1}0)$  plane. The red lines are the bond paths whereas the interatomic surface is drawn in green. The B–V bcp at  $12o$  position and the ccp at  $1b$  position are denoted by red and blue circles, respectively.

A cage critical point is located in the middle of six-membered boron ring as shown in Figure 4.8. The ED at this ccp is characterized with small positive Laplacian and considerably small ED value. The presence of this critical point indicates the distribution ED over a wide cage surfaces formed by vanadium and boron atoms.

The 3D representation of the density Laplacian indicates that the penultimate shell of vanadium is distorted and there are two charge concentrations located above and below the (001) plane (Figure 4.9). The structurization in the penultimate shell supports the participation of  $3d$  orbitals in B–V bonding.

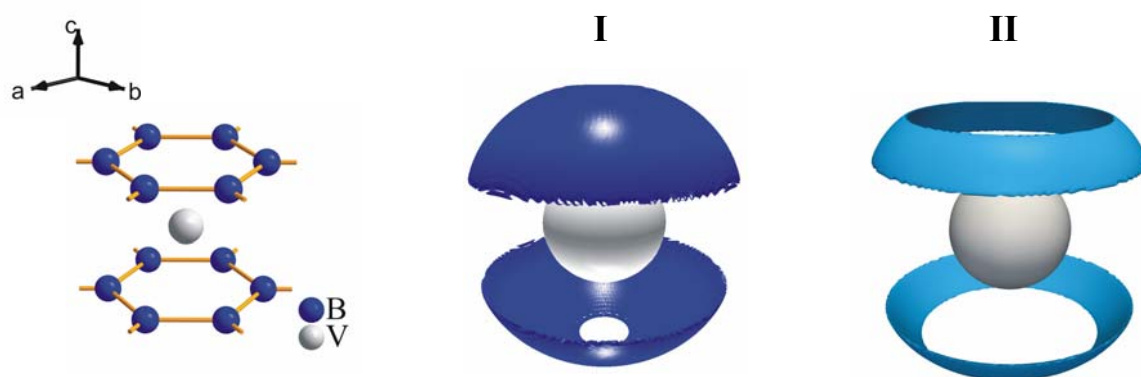


**Figure 4.9** Experimental (I) and theoretical (II) 3D representation of the  $\nabla^2\rho$  distribution in the penultimate shell of the V atom in  $\text{VB}_2$ . The isosurface Laplacian value is  $-295 \text{ e } \text{\AA}^{-5}$ .

### 4.2.3 Atomic electron populations

Atomic electron populations can be determined by the integration of the ED over an atomic basin bounded by the zero-flux surface of the ED gradient. The deviations from the neutral atomic electron populations originate from charge transfer between the atoms. According to the experimental and theoretical results a charge transfer from vanadium of *ca.* 0.5 e and 0.6 e takes place per boron atom, respectively. The experimental e-counts obtained from the integration are remarkably in agreement with the total number of electrons in the unit cell. The integrated charges are given in Table 4.6.

**Table 4.6** Atomic volumes (V) and electron populations ( $\bar{N}$ ) in VB<sub>2</sub>.

	V(M) (Å <sup>3</sup> )	V(B) (Å <sup>3</sup> )	$\bar{N}$ (M)	$\bar{N}$ (B)	$\bar{N}$ in the unit cell
Exp.	8.72	7.52	21.97	5.51	33.00
Theory	8.56	7.60	21.85	5.57	32.99

### 4.3 The electric field gradient

Owing to the symmetry, the EFG at the B nuclei is determined by only one independent component. Table 4.7 shows the principal component  $\nabla E_{zz}$  of the boron EFG tensor obtained by NMR experiment and from the multipole model using the equation 2-34. It has to be noted that the asymmetry parameter  $\eta = (|\nabla E_{xx}| - |\nabla E_{yy}|) / |\nabla E_{zz}|$  which describes the symmetry of the EFG is equal to zero for the B position in the AlB<sub>2</sub>-type structures.

**Table 4.7** Experimental boron EFGs  $\nabla E_{zz}$  (in  $\times 10^{21}$  V/m<sup>2</sup>) in VB<sub>2</sub>.

$\nabla E_{zz}$ (X-ray)	$\nabla E_{zz}$ (NMR)	$\nabla E_{zz}$ (theory)
0.39	0.41	0.39

A good agreement is obtained between the EFG value deduced from the <sup>11</sup>B NMR experiment and the theoretical value. According to the multipole model the calculated value of the electron contributions to the boron EFG  $\nabla E_{zz}^{\text{el}}$  is  $0.01 \times 10^{21}$  V/m<sup>2</sup> which is quite small compared to the lattice EFG contribution ( $\nabla E_{zz}^{\text{lat}} = 0.38 \times 10^{21}$  V/m<sup>2</sup>).<sup>[132]</sup> However,

when taking the lattice EFG contribution into account which is in general larger for the d-diborides than the s and p-diborides, a perfect agreement is obtained with the theoretical value since the variation of EFG for diborides covers two orders of magnitude despite their similar crystal structure. This result confirms indirectly the accuracy of the reconstructed ED.

#### 4.4 Summary on VB<sub>2</sub>

The ED in VB<sub>2</sub> is successfully reconstructed from high-resolution X-ray data. Resolution limit achieved up to  $\sin \theta / \lambda = 1.72$  by single crystal X-ray diffraction experiment allows to recover the fine details in ED. Both theoretical and experimental results indicate the same number and type of critical points. In general, there are some minor differences in the ED at critical points  $\rho(r_{cp})$  between two methods. This kind of agreement is not very surprising since the charge density is based on the model ED that is reconstructed with the multipole parameters and density functions which are smoothly varying in the algorithm used. This is advantageous over the ED obtained simply by Fourier transform of the structure factors of the experimental data. The latter method creates artefacts such as local maxima and minima, *i.e.* critical points arising from the experimental noise and series truncation errors owing to the finite resolution. Those artefacts can dominate the topology unlike in case of the model density used in the present thesis which does not suffer from these drawbacks and provides a more suitable basis for the topological analysis.

The B–B bcp clearly indicates a shared type interaction between boron atoms with a significant bond ellipticity in [001] direction. Taking the energetic characteristics of ED at the B–V bcp into account along with the displacement of the B–V bcp toward the boron atom, the boron vanadium interaction can be described as polar covalent. Both experiment and theory indicate the deformation in the penultimate shell which is presumably an indication of participation of 3*d* electrons in the B–V bonding. Not any sign of localised V–V bond is observed.



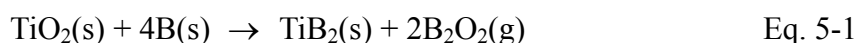
## 5 SYNTHESIS, CHARACTERIZATION AND RECONSTRUCTED ELECTRON DENSITY IN TiB<sub>2</sub>

In this Chapter first the preparation of the TiB<sub>2</sub> single crystals will be explained. This is followed by a description of conventional and multipole refinements of the TiB<sub>2</sub> structure using high resolution X-ray single-crystal diffraction data. Finally, the ED features will be analysed in terms of QTAIM. The results obtained from the reconstruction of the experimental ED will be compared with quantum chemical calculations.

### 5.1 Synthesis

Diborides of group-IV metals are reported to be the most stable among the AlB<sub>2</sub>-type transition metal diborides according to their thermodynamic and thermomechanical properties also supported by cohesive energy and formation energy calculations.<sup>[37e, 133]</sup> This is also well reflected in the melting points of these compounds which are larger than diborides of other groups. According to the most recent compilation on the Ti–B system published by Murray *et al.* TiB<sub>2</sub> is the only congruent melting phase with the reaction temperature of 3225 ± 25 °C.<sup>[134]</sup> Correspondingly, high temperature synthesis methods are usually exploited for its production using the following experimental conditions:

1) TiB<sub>2</sub> powders are synthesized by a borothermic reduction of titania at temperatures above 1000 °C where additional carbon is generally used in order to reduce the oxygen content of the titanium diboride.<sup>[135]</sup>



2) Another technique is the self-spreading high temperature (SHS) method according to which the material is produced by thermal energy generated during the chemical reaction of aluminothermic or magnesiothermic reduction of mixtures of metal oxide and boron oxide.<sup>[136]</sup>



3) Gas-phase-combustion synthesis of TiB<sub>2</sub> is reported according to the following flame reaction<sup>[137]</sup>



4) Carbothermic reduction of metal oxide yields TiB<sub>2</sub>:<sup>[138]</sup>



Other synthesis techniques for TiB<sub>2</sub> powders are fused-salt electrolysis,<sup>[139]</sup> solution processing,<sup>[140]</sup> mechanochemical synthesis<sup>[141]</sup> or chemical vapor deposition.<sup>[105, 142]</sup>

In this study TiB<sub>2</sub> crystals are prepared both using high-temperature solution method as well as by arc-melting. The starting materials are titanium powder, crystalline (for Al flux experiments) and amorphous (for arc-melting experiments) boron powder, aluminium metal chips (Purity grades: Ti—99.99 %; crystalline B—99.995 %; amorphous B—95 %, Mg max. 0.8%). For the recrystallization from the melt, aluminium (Purity grade: 99.995 %) is used as flux material. The same experimental procedure has been applied as for the synthesis of VB<sub>2</sub> described in Chapter 3. TiB<sub>2</sub> crystals are isolated from the melt when atomic ratios B/V=1.3-2.7 were used. The crystals grown in the Al melt exhibit generally a shiny metallic surface with well-defined faces. The size of the crystals is mostly below 100  $\mu\text{m}$ .

## 5.2 Characterization

The samples are analysed by X-ray powder diffraction. The X-ray diffractograms indicate the presence of Al<sub>2</sub>O<sub>3</sub>, AlN as by-products in samples obtained from the Al melt (Figure 5.1). In addition, WC is detected in all samples ground in WC mortar which points to the extreme hardness of the material.

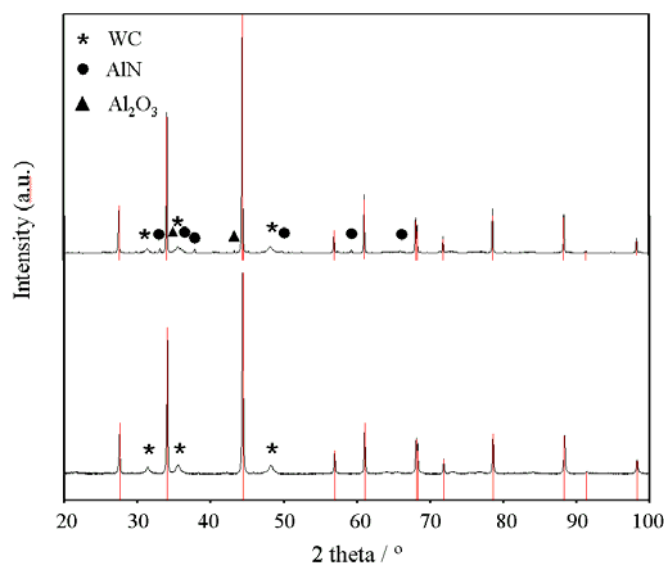


**Figure 5.1** Observed X-ray powder diffraction data and calculated diffraction peak's positions lines from single crystal refinement (red) for TiB<sub>2</sub>. Upper part: sample recrystallized from Al melt; lower part: arc-melted sample.

Unit cell parameters are obtained by least squares fitting of Bragg's equation to the positions of the diffraction lines. The unit cell dimensions  $a = 3.0309(2)$  and  $c = 3.2298(2)$  are in good agreement with previously published data.<sup>[96, 122a]</sup> According to the reported phase diagram the homogeneity range of  $\text{TiB}_2$  is quite narrow.<sup>[134, 143]</sup> Rudy and Windisch<sup>[144]</sup> claim that it extends between 65.2 and 67 at. % B, while Fenish<sup>[145]</sup> and Thebault *et al.*<sup>[146]</sup> reported 65.5–67 at. % B and 65.5–67.6 at. % B, respectively. The respective results are derived from ternary systems in these studies. Accordingly, small variation in the stoichiometry may originate from contamination effects. In the present study,  $\text{TiB}_2$  samples with different nominal compositions do not reveal any significant change in their unit cell parameters (Figure 5.2). Similar to vanadium borides, the unit cell parameters of  $\text{TiB}_2$  show small changes with respect to the B/Ti ratio. But a clear trend is not present. Slight variations in the unit cell parameters may originate from the nonequilibrium state of the samples. According to WDXS analysis, the composition of diboride is  $\text{Ti}_{1.00(1)}\text{B}_{2.02(1)}$ .

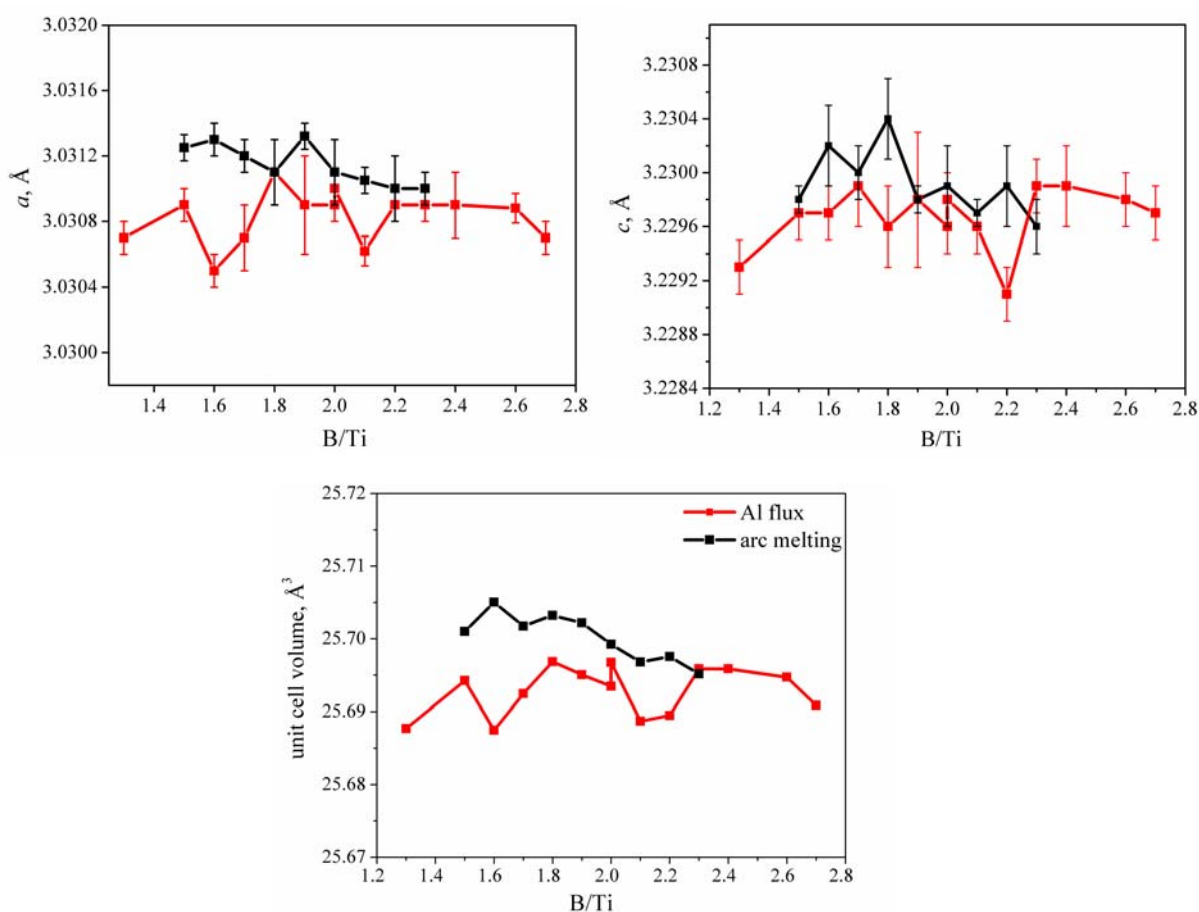


**Figure 5.2:** Cell volumes and cell parameters vs. B/Ti molar ratio in  $\text{TiB}_2$  samples. Data obtained from samples synthesized by Al flux and arc-melting are denoted as red and black squares, respectively. The error bars are smaller than the square-shaped data points of the of the unit cell volumes.

### 5.3 High-resolution single-crystal X-ray diffraction experiment

X-ray single-crystal diffraction measurements are carried out at room temperature using micro-focus (100 $\mu$ m) rotating anode generator, Ag  $K\alpha$  radiation ( $\lambda = 0.56087$  Å), mirror optics and image-plate detector in Weissenberg-type arrangement. The data set extends to  $\sin \theta_{max} / \lambda = 1.724$  (Å<sup>-1</sup>). The data collection and evaluation information is given in Table 5.1. The unit cell parameters used in the single crystal refinement are obtained from the X-ray powder diffraction data.

**Table 5.1** Crystallographic data of TiB<sub>2</sub>.

Space group	<i>P6/mmm</i>
Unit cell parameters (Å) (powder diffraction data)	$a = 3.0309(2)$ , $c = 3.2298(2)$
Unit cell volume (Å <sup>3</sup> )	25.695(5)
No. of formula units, $Z$	1
No. of measured/unique reflections	3199 / 269
Measured range	$-9 \leq h \leq 10$ ; $-7 \leq k \leq 6$ ; $-11 \leq l \leq 11$
$2 \theta_{max} (^{\circ}) / (\sin \theta_{max} / \lambda) (\text{\AA}^{-1})$	149.38 / 1.724
$R_{(int)}$	0.015
Completeness (%)	99,6

\* $R_{(int)}$  is simply the  $R$ -factor between the amplitudes of Friedel pairs.

### 5.4 Conventional IAM refinement

The refined parameters for TiB<sub>2</sub> are the scale factor of the observed intensities, the vibration mean square amplitudes of both titanium and boron atoms and finally two width parameters of a Gaussian mosaic distribution for anisotropic extinction according to the Becker-Coppens formalism. The same conventional refinement procedure is applied as described in Chapter 3.4 for vanadium borides. Table 5.2 summarizes the reliability factors  $R_{(F)}$  obtained at different stages of the refinement. The isotropic description of atomic displacement already leads to a reduction of the reliability factor  $R_{(F)}$  to 1.36%. An important remark is that the extinction correction does not have a reducing effect on  $R_{(F)}$  which can be attributed to the crystal size which is small enough to avoid extinction effects. A small achievement is obtained applying the anharmonic description of atomic displacement pa-

rameters up to fourth tensor. The occupancy of both atoms does not indicate any deviation from the ideal stoichiometry. The data is merged prior to the multipole refinement of the structure.

**Table 5.2**  $R_{(F)}(\%)$  values at different refinement steps of TiB<sub>2</sub> structure. The final  $R_{(F)}$  value is obtained after data merging.

Isotropic description of ADPs	Anis. extinction correction	Anis. description of ADPs	Anharm. description of ADP (3 <sup>rd</sup> rank)	Anharm. description of ADP (4 <sup>th</sup> rank)	Final $R_{(F)}$
1.36	1.37	1.31	1.31	1.31	1.26

Figure 5.3 shows the ratio of observed and calculated structure factors according to IAM refinement of TiB<sub>2</sub> structure with respect to the variation of  $\sin \theta / \lambda$ . The discrepancy between the observed and calculated structure factors at very high resolution data is considerably smaller than that observed for vanadium borides (Chapter 3.4). Accordingly, all reflections are taken into account for the model calculations of TiB<sub>2</sub>.

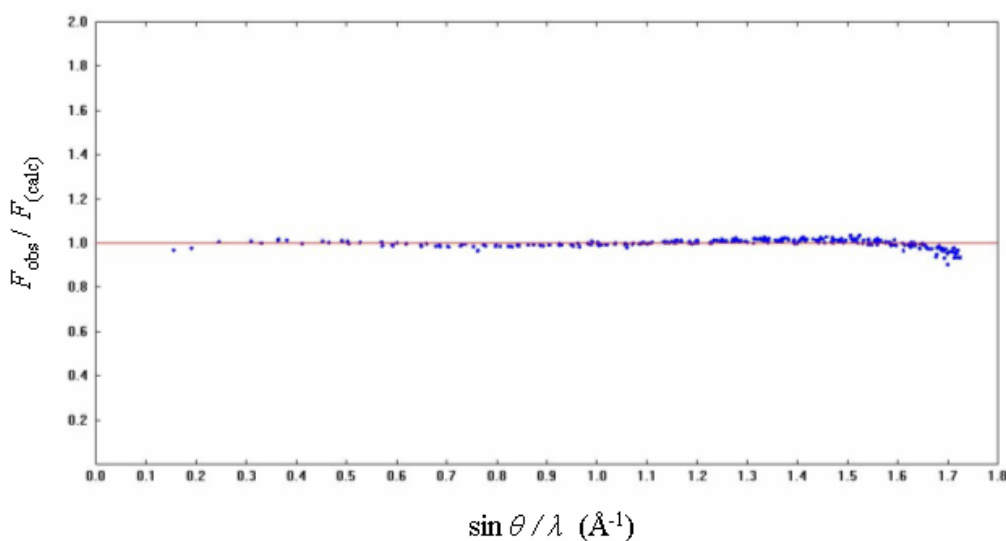


**Figure 5.3**  $F_{\text{obs}} / F_{\text{calc}}$  vs.  $\sin \theta / \lambda$  according to IAM refinement of TiB<sub>2</sub> structure.

## 5.5 Crystal structure of TiB<sub>2</sub>

The fundamental units in TiB<sub>2</sub> are triangular prisms formed by metal atoms like all other AlB<sub>2</sub>-type structure. The boron atom is located at the center of this trigonal prism unit. A comparison between the crystal structures of diborides of titanium and vanadium which differ only by one electron in the valence region, reveal that the interatomic distances of

TiB<sub>2</sub> is larger. The most considerable difference is due to the interatomic distance between the respective metal atoms along the [001] axis. On the other hand, the difference between the respective B–B and M–M distances in the (001) plane is relatively small (Figure 5.4).

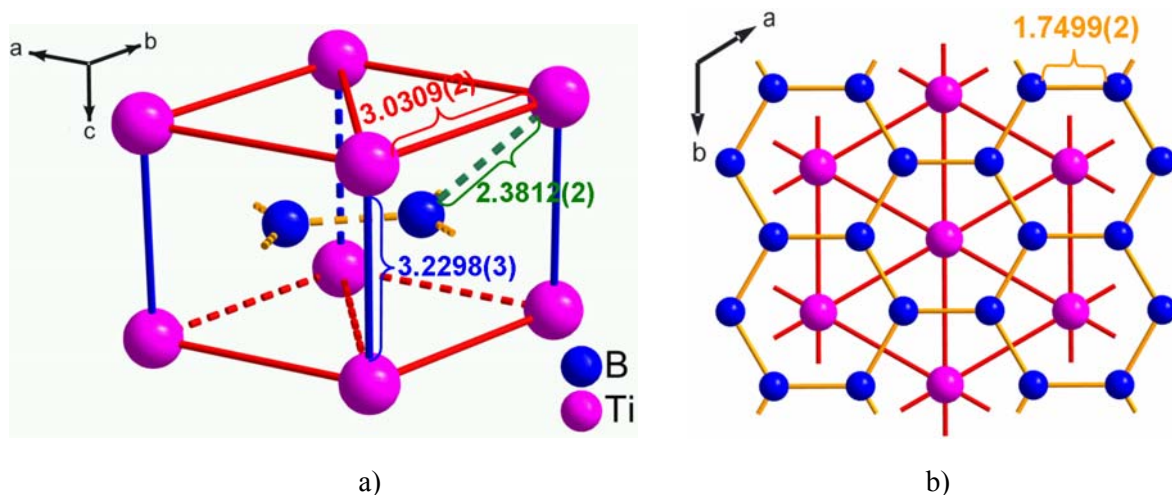


**Figure 5.4** The interatomic distances (Å) in TiB<sub>2</sub>. The views are parallel (a) and perpendicular (b) to the B-atom plane.

In general, the ADP values of TiB<sub>2</sub> are relatively large as compared to those in VB<sub>2</sub>. However, they follow the same trend. In general, the movement of the metal atoms is more restricted than that of the boron atoms which vibrate more easily along the [001] axis in comparison to other directions (Table 5.3). Owing to the symmetry restrictions there is no third-order anharmonic contribution for the metal position. Introducing the anharmonic description up to the fourth order reduces the  $R_{(F)}$  value only for titanium atom whereas no substantial improvement is achieved for boron beyond harmonic approximation. Similar to VB<sub>2</sub>, the use of multipole model decreases the harmonic ADPs of the metal atom whereas those of boron atoms are increased slightly.

**Table 5.3** The harmonic (Å<sup>2</sup>) and anharmonic (Å<sup>4</sup>) ADPs of TiB<sub>2</sub> according to IAM and multipole model refinement.

		$B(\text{eq})^*$	$B_{11}$	$B_{33}$	$D_{1111}$	$D_{3333}$	$D_{1133}$
Spherical refinement	Ti	0.210(2)	0.169(3)	0.223(6)	-0.5(3)	-0.2(2)	–
	B	0.314(4)	0.233(7)	0.37(1)	kept fixed		
Multipole refinement	Ti	0.186(3)	0.147(3)	0.196(4)	-1.0(2)	-0.1(1)	-0.1(1)
	B	0.321(5)	0.239(6)	0.380(8)	kept fixed		

\*  $B(\text{eq}) = 1/3[B_{11}a^{*2}a^2 + \dots + 2B_{23}b^*c^*bc \cos \alpha]$

### 5.6 Multipole refinement

The Ti and B atoms have site symmetry  $6/mmm$  and  $\bar{6}m2$ , respectively. Therefore, the multipole refinement is performed up to hexadecapoles for each atom. The contributing multipoles for Ti atoms are  $P_v$ ,  $P_{20}$  and  $P_{40}$ , whereas for B atoms  $P_v$ ,  $P_{20}$ ,  $P_{33}$ - and  $P_{40}$  multipoles are allowed by symmetry. Both core and valence EDs are obtained from the Hartree-Fock wavefunctions taken from Clementi and Roetti.<sup>[130]</sup> The valence functions are constructed using the scattering contributions of  $4s^2$ ,  $3d^2$  and  $2s^2$ ,  $2p^1$  states for Ti and B, respectively, which gives electron populations ( $P_v$ ) of  $4e^-$  for Ti and  $3e^-$  for B as starting values. The radial-function parameters are chosen to  $n_2 = 4$ ,  $n_4 = 4$  and  $\zeta_v = 2.71$  for Ti and  $n_2 = 2$ ,  $n_3 = 3$ ,  $n_4 = 4$  and  $\zeta_B = 2.53$  for B.

First, thermal parameters and the scale factor are refined for both atoms using the whole data set ( $R_{(F)} = 0.99\%$ ). After this, the  $P_v$  parameters are refined for both atom positions using low order data ( $\sin \theta/\lambda \leq 0.8 \text{ \AA}^{-1}$ ) keeping  $\kappa$ ,  $\kappa'$  and all multipole parameters fixed. The electron populations for both atoms indicate that there is charge transfer from titanium to boron. The  $P_{lm\pm}$  parameters together with  $\kappa$  and  $\kappa'$  are refined using  $\sin \theta/\lambda \leq 0.8 \text{ \AA}^{-1}$ . Subsequently, multipole parameters are fixed followed by refining again the  $P_v$  and the atomic displacement parameters. This procedure is repeated until the final convergence is achieved ( $R_{(F)} = 0.85\%$ ). The multipole, expansion and contraction parameters are summarized in Table 5.4.

	Ti (in $6/mmm$ )	B (in $\bar{6}m2$ )
$P_v$	3.532	3.234
$P_{20}$	-0.122(2)	-0.025(2)
$P_{33}$	—	0.166(2)
$P_{40}$	-0.030(2)	-0.019(2)
$\kappa$	0.990(2)	0.968(2)
$\kappa'$	0.939(2)	1.052(2)

**Table 5.4** Multipole, expansion and contraction parameters of TiB<sub>2</sub>.

The use of multipole model instead of spherical treatment of atoms reduces the  $R_{(F)}$  for the reflections up to  $\sin \theta/\lambda = 0.8 \text{ \AA}^{-1}$  from 1.09% to 0.75%. Data analysis after the multipole refinement reveals that most pronounced improvement in fitting  $F_{\text{obs}}$  to  $F_{\text{calc}}$  is achieved for the few strongest low order reflections (Figure 5.5).

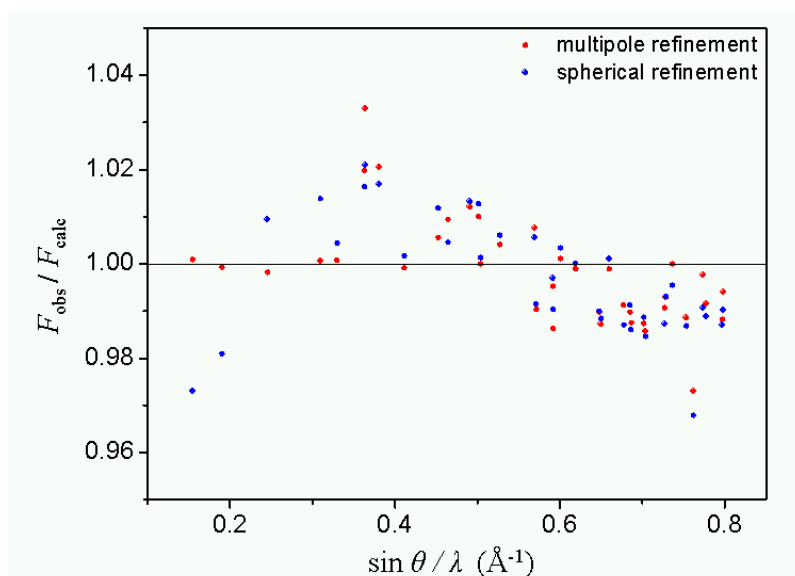


**Figure 5.5**  $F_{\text{obs}}/F_{\text{calc}}$  vs.  $\sin \theta / \lambda$ . Values according to spherical and multipole refinement of the crystal structure of  $\text{TiB}_2$  are denoted as blue and red dots, respectively.

IAM refinement of  $\text{TiB}_2$  structure is not sufficient to account for some features particularly in the vicinity of borons as well as B–B internuclear regions (Figure 5.6). These residuals almost disappear with the use of multipole model. The minimum and maximum values of the residual densities in the B–B network plane are  $-0.140 / 0.481$  and  $-0.045 / 0.054$  after the use of IAM and multipole model, respectively.

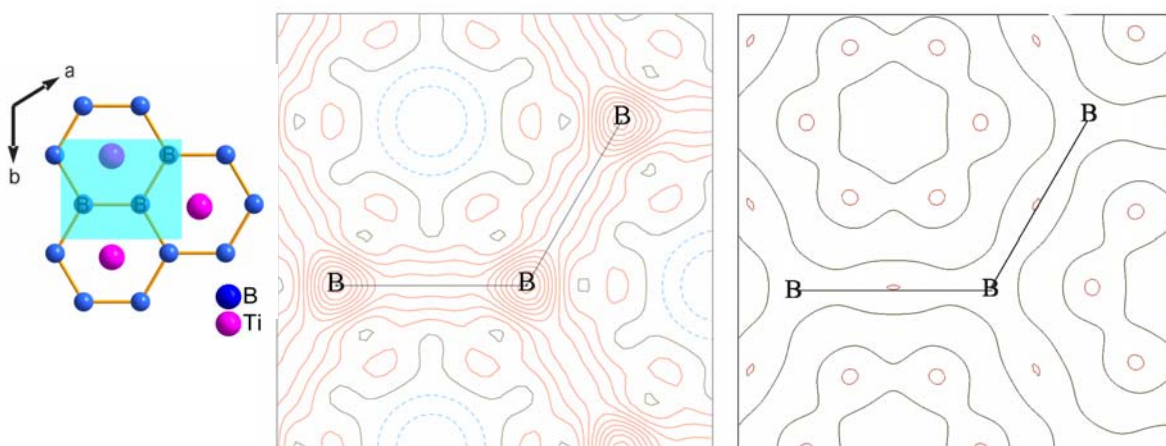


**Figure 5.6** Residual density distributions in boron network plane in  $\text{TiB}_2$  after IAM (left) and multipole (right) refinement; data cut-off at  $\sin \theta / \lambda = 0.9$ ; contour level step width of  $0.05 \text{ e}\text{\AA}^{-3}$ . Solid red and dashed blue lines correspond to positive and negative values, respectively, whereas solid black line is the zero contour.





All types of cps are observed in both experimental and theoretical ED. The number of different cps obeys Poincare-Hopf condition. Some of their positions are restricted by the space group symmetry. No non-nuclear attractors are found. There are some discrepancies due to cps found between experiment and theory which can be attributed to the flatness of the ED. Experimental calculations indicate at the  $2c$  position a ccp instead of a bcp found in theory (Table 5.5). The ED at this bcp is very small and two principle curvatures are close to zero. Furthermore, experimentally found rcp at the  $3f$  position is replaced by ccp according to theory. Moreover, theoretically obtained rcp at the  $6l$  position is not reproduced in experiment. Experimental topological descriptors agree with the values of theory by  $\pm 0.03 \text{ e } \text{\AA}^{-3}$  for  $\rho(r_{cp})$  and  $\pm 0.21 \text{ e } \text{\AA}^{-5}$  for  $\nabla^2 \rho(r_{cp})$ . The most considerable quantitative disagreement for  $\rho(r_{cp})$  is observed in B–B interatomic region reflected by relatively larger ED value at the bcp on the B–B bond path ( $3g$  position) according to the experiment in comparison to theory.

**Table 5.5** Topological characteristics of the critical points in ED for TiB<sub>2</sub> determined from reconstructed experimental data and theoretical calculations. Theoretical values are denoted by an asterisk.

Wyckoff notation and position of cp	$\rho(r_{cp})(\text{e } \text{\AA}^{-3})$	$\nabla^2 \rho(r_{cp})(\text{e } \text{\AA}^{-5})$	$\lambda_1(\text{e } \text{\AA}^{-5})$	$\lambda_2(\text{e } \text{\AA}^{-5})$	$\lambda_3(\text{e } \text{\AA}^{-5})$	cp type
$3g(0, 0.5, 0.5)$	0.847	-4.196	-3.810	-2.506	2.121	3, -1
$3g(0, 0.5, 0.5)^*$	0.817	-4.405	-3.152	-2.728	1.475	3, -1
$12o(0.175, 0.350, 0.241)$	0.323	2.672	-0.771	-0.058	3.502	3, -1
$12o(0.167, 0.334, 0.250)^*$	0.334	2.487	-0.798	-0.141	3.429	3, -1
$2c(0.333, 0.666, 0)^*$	0.197	0.641	-0.003	-0.003	0.647	3, -1
$6l(0.330, 0.660, 0)^*$	0.197	0.641	-0.007	0.002	0.645	3, +1
$12n(0, 0.698, 0.245)$	0.320	2.589	-0.764	0.070	3.282	3, +1
$12n(0, 0.715, 0.257)^*$	0.328	2.533	-0.790	0.140	3.183	3, +1
$3f(0, 0.5, 0)$	0.204	0.903	-0.058	0.410	0.551	3, +1
$3f(0, 0.5, 0)^*$	0.194	0.954	0.024	0.441	0.489	3, +3
$2c(0.333, 0.667, 0)$	0.195	0.762	0.084	0.084	0.593	3, +3
$1b(0, 0, 0.5)$	0.149	1.087	0.188	0.448	0.448	3, +3
$1b(0, 0, 0.5)^*$	0.175	1.239	0.128	0.554	0.554	3, +3

### 5.7.1 The B–B interaction

The topology of the deformation ED reveals a single maximum picture in the region between the boron atoms in (001) plane (Figure 5.8). The covalency of B–B interaction is approved by the sign of the Laplacian  $\nabla^2\rho(r_b) < 0$  at the bcp which is found between the boron atoms in the relevant plane, indicating typically a shared-type interaction. Similar to VB<sub>2</sub> the bond path in TiB<sub>2</sub> is not curved due to symmetry restriction. The B–B bcp is located at a distance of 0.875 Å from both boron atoms. The ED Laplacian distribution  $\nabla^2\rho(r)$  along the B–B bond path reveals some differences between experiment and theory as also observed in VB<sub>2</sub>. In general, theoretically derived curve is less contracted in comparison to experiment indicating a more homogeneous distribution of ED in the internuclear region of boron atoms. On the other hand, experimentally derived Laplacian distribution indicates a more pronounced valence shell.

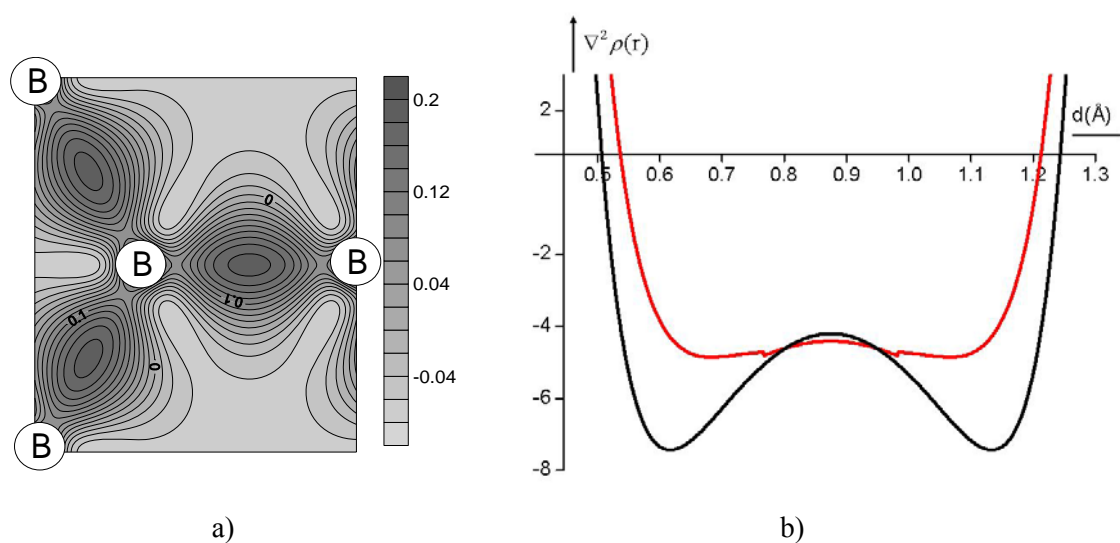


**Figure 5.8** (a) The deformation ED map of TiB<sub>2</sub> in the B-atom plane (the isoline interval is 0.02 e a.u.<sup>-3</sup>). (b) Experimentally (black) and theoretically (red) calculated  $\nabla^2\rho(r)$  distribution along the B-B bond path. The bcp is located at a distance of 0.875 Å from both B-atoms (at 0 Å and 1.7499 Å, respectively) exactly in the middle of the bond path. The non-continuous behaviour of the theoretical values in the same region is an artefact originating from the APW basis set used for the theoretical calculation.

Some selected topological properties of the B–B bond in TiB<sub>2</sub> are given in Table 5.6. There are some discrepancies in the bond critical point properties between experiment and theory concerning the higher derivatives of ED. The most significant deviation is due to

the ellipticity value. Experimentally observed ellipticity value is relatively higher in comparison to the theoretical one as also observed in  $\text{VB}_2$ .

**Table 5.6** Topological properties of the B–B bonds in  $\text{TiB}_2$ .

	$\rho(r_b)$ ( $\text{e } \text{\AA}^{-3}$ )	$\nabla^2 \rho(r_b)$ ( $\text{e } \text{\AA}^{-5}$ )	$\lambda_1(\text{e } \text{\AA}^{-5})$	$\lambda_2(\text{e } \text{\AA}^{-5})$	$\lambda_3(\text{e } \text{\AA}^{-5})$	$\mathcal{E}(r_b)$	$ \lambda_1 /\lambda_3$
Exp.	0.847	-4.196	-3.810	-2.506	2.121	0.519	1.80
Theory	0.817	-4.405	-3.152	-2.728	1.475	0.155	2.14

Both experimentally and theoretically derived values of the first principal curvature of the ED  $\lambda_1$  is explicitly dominating  $\lambda_3$  suggesting that the perpendicular contraction at the bcp is more pronounced than the parallel concentration along the bond path towards the nuclei which is typical for shared type interactions ( $|\lambda_1| / \lambda_3$  ratio  $> 1$ ). In spite of the large variation between experiment and theory ellipticity value above zero points to a deviation from the cylindrical symmetry. It points presumably toward the relevant  $\pi$ -density contribution to the B–B bond. The deviation from the spherical symmetry of the B–B bond in  $\text{TiB}_2$  is illustrated in deformation ED maps of  $(1\bar{1}0)$  plane. The ED is elongated along the  $[001]$  direction. As a result, it is spread between the boron layers as shown in Figure 5.9.

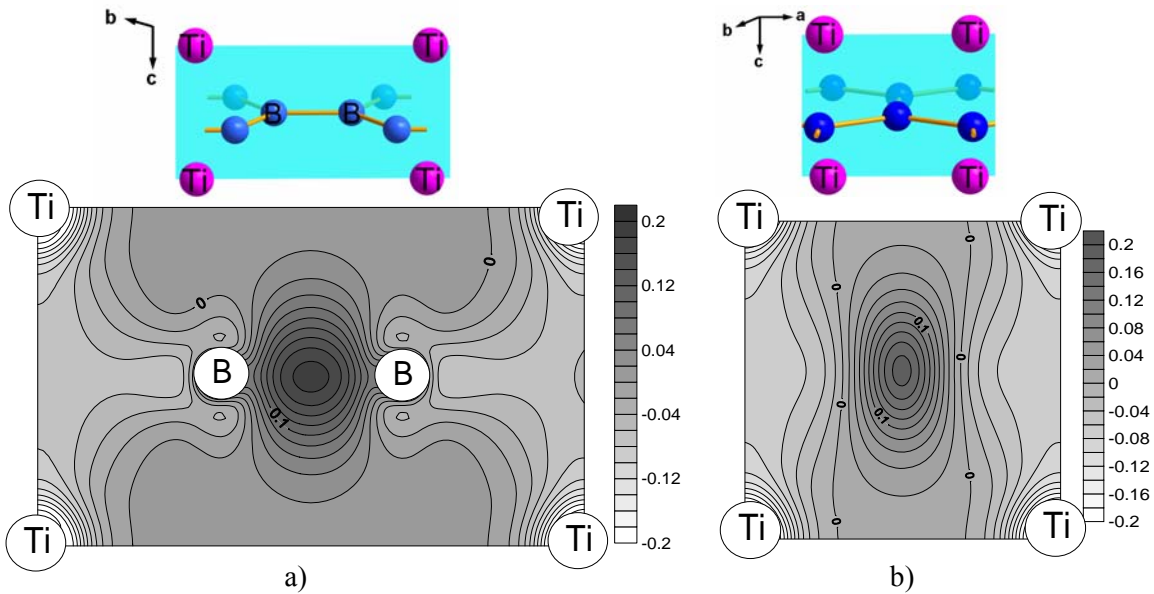


**Figure 5.9** The deformation ED of  $\text{TiB}_2$  structure a) in  $(1\bar{1}0)$  plane; b) in  $(100)$  plane. The isoline interval is  $0.02 \text{ e.u.}^{-3}$

### 5.7.2 The B–Ti interaction

Topological analysis of ED in  $\text{TiB}_2$  structure indicates a bcp in the B–Ti interatomic region at the  $12o$  position (Figure 5.10). The bcp is slightly shifted along the bond path towards boron indicating the polarity of the B–Ti bond. The distances from the B–Ti bcp to Ti and B nuclei are 1.204 Å and 1.180 Å, respectively. The bond path is slightly curved.

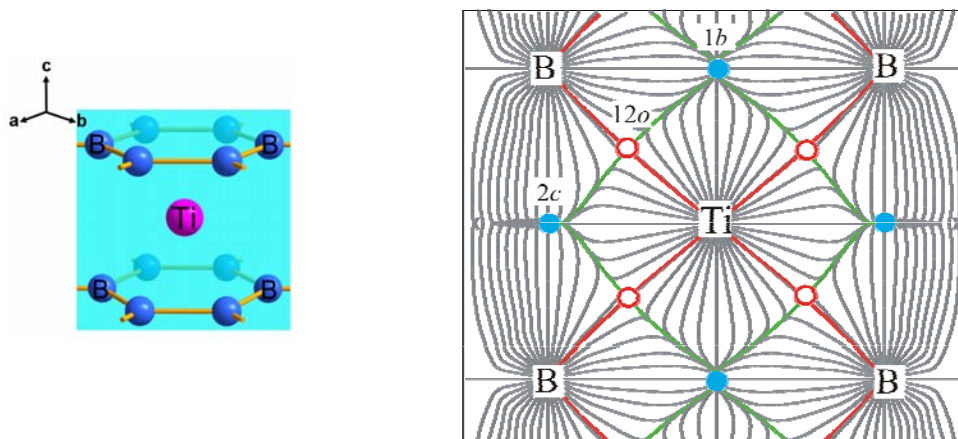


**Figure 5.10** The  $\nabla\rho$  field of the ED in  $\text{TiB}_2$ . The section shown belongs to  $(1\bar{1}0)$  plane. The red line is the B–Ti bond path whereas the interatomic surface path is drawn in green. The B–V bcp at  $12o$  position is denoted by red circle. The ccp at  $1b$  and  $2c$  positions are denoted by blue circles.

The topological properties of the B–Ti bond are summarized in Table 5.7. The positive curvature at the bcp dominates other two negative principal curvatures. One of the principal negative curvatures is close to zero as also observed at the B–V bcp which leads to very high ellipticity values.

**Table 5.7** Topological properties of B–Ti the bond in  $\text{TiB}_2$  according to experiment and theory.  $d(\text{bcp})$  is the distance between the B–Ti bcp and the B–Ti interatomic line.

	$d(\text{bcp})$ (Å)	$\rho(r_b)$ ( $\text{e}\text{Å}^{-3}$ )	$\nabla^2\rho(r_b)$ ( $\text{e}\text{Å}^{-5}$ )	$\lambda_1(\text{e}\text{Å}^{-5})$	$\lambda_2(\text{e}\text{Å}^{-5})$	$\lambda_3(\text{e}\text{Å}^{-5})$	$\varepsilon(r_b)$
Exp.	0.053	0.323	2.672	-0.771	-0.058	3.502	12.293
Theory	0	0.334	2.487	-0.798	-0.141	3.429	4.660

Further information about the B–Ti bonding is extracted from the energetic considerations of the ED. Experimental calculations suggest small negative value for the local

energy density  $H(r) = -0.009$  a.u at the B–Ti bcp. This result indicates that B–Ti bonding is of covalent nature similar to B–V interaction in  $\text{VB}_2$ .

Both experimental and theoretical representation of the ED Laplacian distribution in the vicinity of the titanium atom does not indicate any structurization in the penultimate shell (Figure. 5.11). This is in contradiction with presence of a deviation from sphericity of the metal in  $\text{TiB}_2$  as detected by Hegenscheidt on base of the deformation ED.<sup>5</sup>

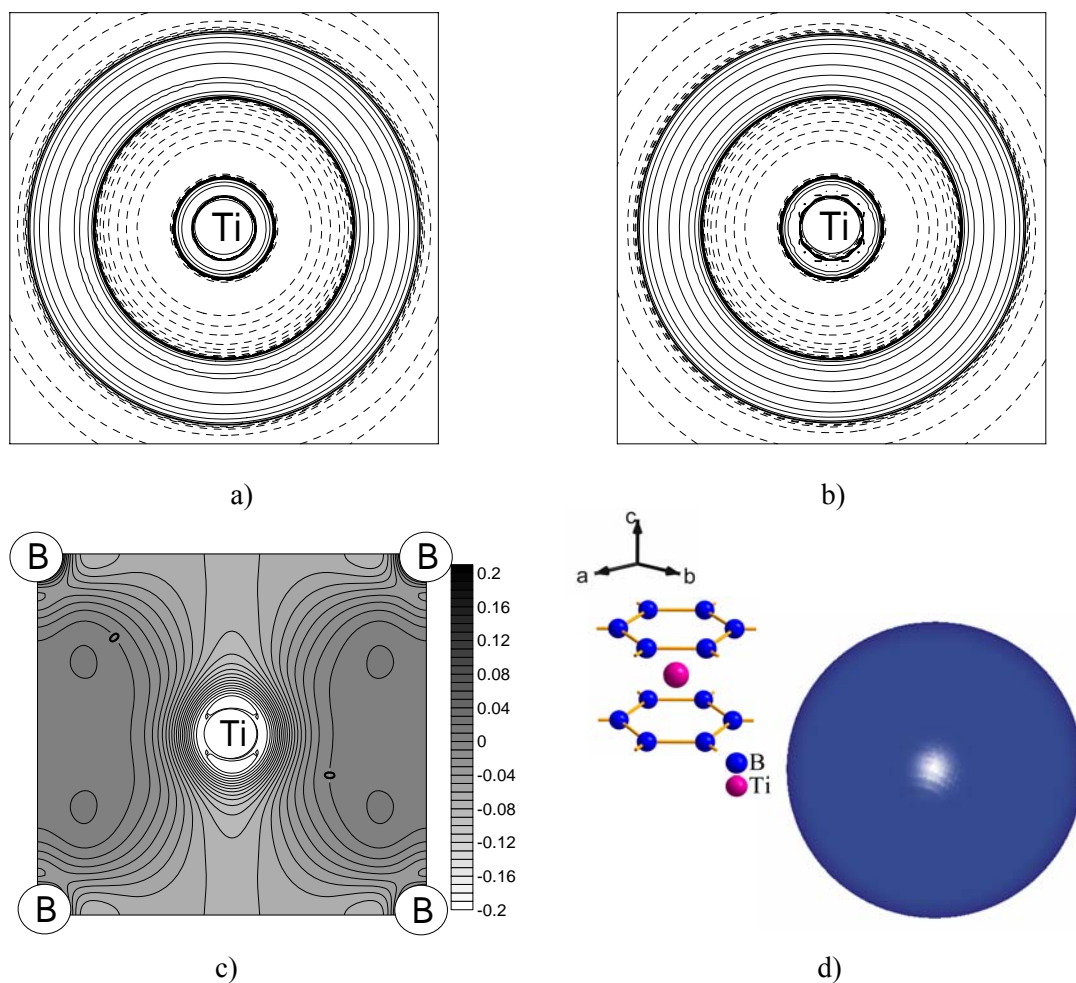


**Figure 5.11** The ED Laplacian of Ti atom in  $\text{TiB}_2$  in  $(1\bar{1}0)$  plane reconstructed from experiment in a); calculated by DFT in b). Solid and broken lines represent negative and positive values, respectively. The Isoline intervals are  $\pm 2 \times 10^n$ ,  $4 \times 10^n$ ,  $8 \times 10^n$  e  $\text{\AA}^{-5}$  where  $n = 0, 4, 3, 2, 1$ . Additional isolines are -140 and 185 e  $\text{\AA}^{-5}$  c) The deformation ED map in the same plane as in a) and b). The isoline interval is 0.01 e a.u.<sup>-3</sup>. d) The 3D ED Laplacian distribution of the Ti atom. The isosurface value for the Laplacian is -200 e  $\text{\AA}^{-5}$ .

The flatness of the ED in the B–Ti nuclear region is well reflected in deformation ED map in  $(1\bar{1}0)$  plane. It is evident that the ED is depleted in the Ti–Ti internuclear region

along the [001] axis. Both experimental as well as theoretical results do not indicate any bcp in Ti–Ti interatomic region.

### 5.7.3 Atomic electron populations

Both the atomic volumes as well as the number of electrons in Ti and B basins are given in Table 5.8. The Integration of the ED over the atomic basins yields a charge transfer from Ti to B of 0.56 e and 0.68 e per boron atom based on experiment and theory, respectively.

**Table 5.8** Atomic volumes (V) and electron populations ( $\bar{N}$ ) in TiB<sub>2</sub>.

	V(Ti) (Å <sup>3</sup> )	V(B) (Å <sup>3</sup> )	$\bar{N}$ (Ti)	$\bar{N}$ (B)	$\bar{N}$ in the unit cell
Exp.	9.27	8.21	20.88	5.56	32.00
Theory	8.81	8.42	20.63	5.68	31.99

### 5.8 The electric field gradient

The EFG value deduced from X-ray diffraction, <sup>11</sup>B NMR and theoretical calculations are summarized in Table 5.9. The multipole model yields for the B nuclei the EFG value ( $\nabla E_{zz}^{\text{el}}$ ) =  $-0.40 \times 10^{21}$  V/m<sup>2</sup>. When taking into account the lattice EFG contribution ( $\nabla E_{zz}^{\text{lat}} = 0.31 \times 10^{21}$  V/m<sup>2</sup>)<sup>[132]</sup>, the total value becomes ( $\nabla E_{zz}$ ) =  $-0.09 \times 10^{21}$  V/m<sup>2</sup>.

**Table 5.9** Boron EFGs,  $V_{zz}$  (in  $\times 10^{21}$  V/m<sup>2</sup>) for TiB<sub>2</sub>.

$\nabla E_{zz}$ (X-ray)	$ \nabla E_{zz} $ (NMR)	$ \nabla E_{zz} $ (theory)
-0.09	0.35	0.38

## 5.9 Summary on $\text{TiB}_2$

Suitable single crystals are synthesized for a charge density analysis of the  $\text{TiB}_2$  structure. The use of Ag radiation along with very small crystals prevents severe extinction effects as also reflected by the minor improvement in reliability factor  $R_{\text{(F)}}$  due to extinction correction. X-ray powder diffraction analysis does not indicate any homogeneity range for  $\text{TiB}_2$ . Furthermore, both the WDXS as well as the refinement of the structure on base of single crystal X-ray diffraction data confirm that there is not any deviation from ideal stoichiometry.

The use of the multipole refinement provides a very good agreement between the calculated and observed structure factors as evidenced by close to featureless residuals. The topological aspects of the total ED from both theory and experiment are generally in a good agreement with respect to  $\rho(r_{\text{cp}})$  values. However, discrepancies due to some rcp and ccp are observed. In addition, a theoretically found bcp between the boron layers is not reproduced by experiment which can be attributed to the flatness of ED in corresponding interatomic region. Topological analysis does not yield any Ti–Ti bcp. The bcp found between the boron atoms in the B–network indicate typically a shared type interaction with significant ellipticity. On the other hand, the B–Ti bcp properties reveal an interaction which is of polar covalent nature. However, the participation of  $3d$  electrons in B–Ti bonding is uncertain due to the non-structurized penultimate shell of the metal according to the ED Laplacian. In addition, a charge transfer is obtained from titanium to boron. These results support that the B–Ti interaction points to a bonding situation which is intermediate between shared and closed-shell type.



## 6 ELECTRON DENSITY IN VB

This Chapter describes the topological aspects of experimental electron density (ED) in vanadiummonoboride reconstructed on base of the multipole parameters obtained from high-resolution single-crystal X-ray diffraction data. Besides, the reconstructed ED is compared with quantum chemical calculations.

### 6.1 Multipole refinement

The ED in VB is reconstructed using a multipole model in which both vanadium and boron atoms are refined up to hexadecapoles. Both atoms have the site symmetry  $m2m$ . Accordingly, the same multipoles ( $P_v, P_{20}, P_{22}, P_{31}, P_{33-}, P_{40}, P_{42}$  and  $P_{44}$ ) are contributing to ED. The core as well as valence EDs are obtained from the Hartree-Fock wavefunctions taken from Clementi and Roetti.<sup>[130]</sup> The respective radial functions used are  $n_2 = 4, n_3 = 4, n_4 = 4$  and  $\zeta_V = 4.4$  for V;  $n_2 = 2, n_3 = 3, n_4 = 4$  and  $\zeta_B = 2.53$  for B.

In the multipole model atomic orbital scattering contributions of  $4s^2, 3d^3$  and  $2s^2, 2p^1$  states are used for V and B, respectively. These give electron populations ( $P_v$ ) of  $5e^-$  for V and  $3e^-$  for B as starting values. First, the displacement parameters and the scale factor are refined for both atoms using the whole data set. The  $R_{(F)}$  value droppes to 1.21%. The  $P_v$  parameters are refined for both atom positions using low order data ( $\sin \theta/\lambda \leq 0.8 \text{ \AA}^{-1}$ ) keeping  $\kappa, \kappa'$  and all multipole parameters fixed. The  $P_{lm\pm}$  parameters together with  $\kappa$  and  $\kappa'$  are refined using  $\sin \theta/\lambda \leq 0.8 \text{ \AA}^{-1}$ . Subsequently, first  $P_v$  parameters and then the thermal parameters are refined again. This procedure is repeated until the final convergence is achieved. The final reliability factor  $R_{(F)}$  referring to all observations droppes to 1.16%. The electroneutrality condition is imposed for the unit cell. The electron populations for both atoms indicated that there is charge transfer from vanadium to boron. The observations are weighted according to their counting statistical variances ( $w = 1/\sigma^2 F_{\text{obs}}$ ). The multipole, expansion and contraction parameters are summarized in Table 6.1.

**Table 6.1** Multipole, expansion and contraction parameters of VB.

	V (in $m2m$ )	B (in $m2m$ )
$P_v$	4.638(2)	3.362(8)
$P_{11-}$	-0.3809(4)	-0.0339(4)
$P_{20}$	0.0(2)	0.0116(2)
$P_{22}$	-0.0030(4)	-0.0035(4)
$P_{31}$	-0.1969(4)	0.0923(4)
$P_{33-}$	0.1303(4)	0.0172(4)
$P_{40}$	-0.0049(4)	-0.0019(4)
$P_{42}$	0.0043(4)	0.0048(4)
$P_{44}$	-0.0139(4)	0.0175(4)
$\kappa$	1.0000(4)	0.9961(4)
$\kappa'$	0.9232(4)	0.8201(4)

The use of multipole model instead of IAM reduces the  $R_{(F)}$  value calculated for the strongest 100 low order reflections ( $\sin \theta / \lambda \leq 0.8 \text{ \AA}^{-1}$ ) from 0.54% to 0.40% (Figure 6.1).

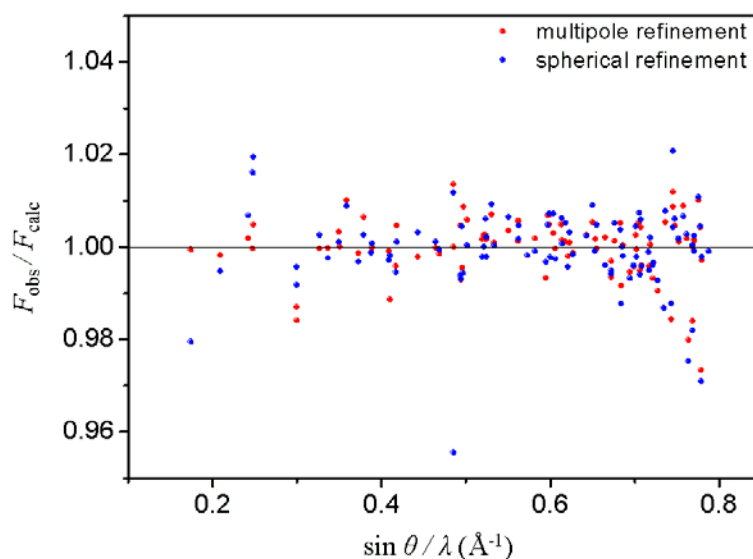


**Figure 6.1**  $F_{\text{obs}} / F_{\text{calc}}$  vs.  $\sin \theta / \lambda$  in VB. The values according to the spherical (blue) and multipole (red) refinement are denoted as blue and red circles, respectively.

The residuals of the ED in the B–B interatomic region which cannot be accounted for by the IAM refinement get considerably smaller but not completely disappear as illustrated in Figure 6.2. Other residual features are randomly distributed and can be mainly assigned to experimental noise. The minimum and maximum values of the residuals are -0.210 / 0.258 and -0.127 / 0.125 e  $\text{\AA}^{-3}$  after the IAM and multipole refinement, respectively.

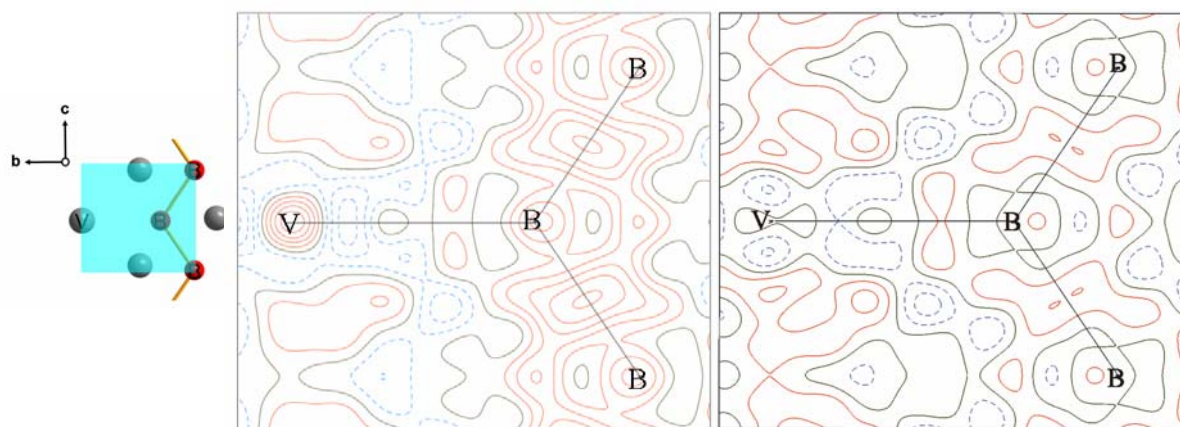


**Figure 6.2** Residual density maps for VB after the IAM (left) and multipole (right) refinement in plane as shown; data cut-off at  $\sin \theta/\lambda=0.9$ ; contour level step width of  $0.05 \text{ e } \text{\AA}^{-3}$ . Solid red and dashed blue lines correspond to positive and negative values, respectively, whereas solid black line shows the zero contour.

Table 6.2 summarizes the ADPs according to a conventional spherical and the multipole refinement. The use of multipole model decreases the harmonic ADPs of V position and whereas those of B atoms are slightly increased.

**Table 6.2** The harmonic ( $\text{\AA}^2$ ) and anharmonic ( $\text{\AA}^4$ ) ADPs of VB according to spherical and multipole refinements.

ADP	Spherical refinement		Multipole refinement	
	V	B	V	B
$B(eq)^*$	0.134(2)	0.285(5)	0.114(2)	0.299(5)
$B_{11}$	0.140(4)	0.301(8)	0.121(3)	0.317(8)
$B_{22}$	0.122(4)	0.292(9)	0.103(3)	0.305(8)
$B_{33}$	0.139(4)	0.261(8)	0.117(3)	0.274(7)
$D_{1111}$	-1.6(1)		-1.8(1)	
$D_{2222}$	—		—	
$D_{3333}$	1.5(1)	kept fixed	-1.8(1)	kept fixed
$D_{1122}$	—		—	
$D_{1133}$	-0.46(4)		-0.55(4)	
$D_{2233}$	—		—	

\*  $B(eq) = 1/3[B_{11} a^{*2} a^2 + \dots + 2 B_{23} b^* c^* b c \cos \alpha]$

## 6.2 Topological analysis of the electron density

The total ED features obtained from experiment and theory are shown in Figure 6.3. Obviously, The ED in the vicinity of the core is more distorted according to the experiment whereas it has rather a spherical shape according to theory.

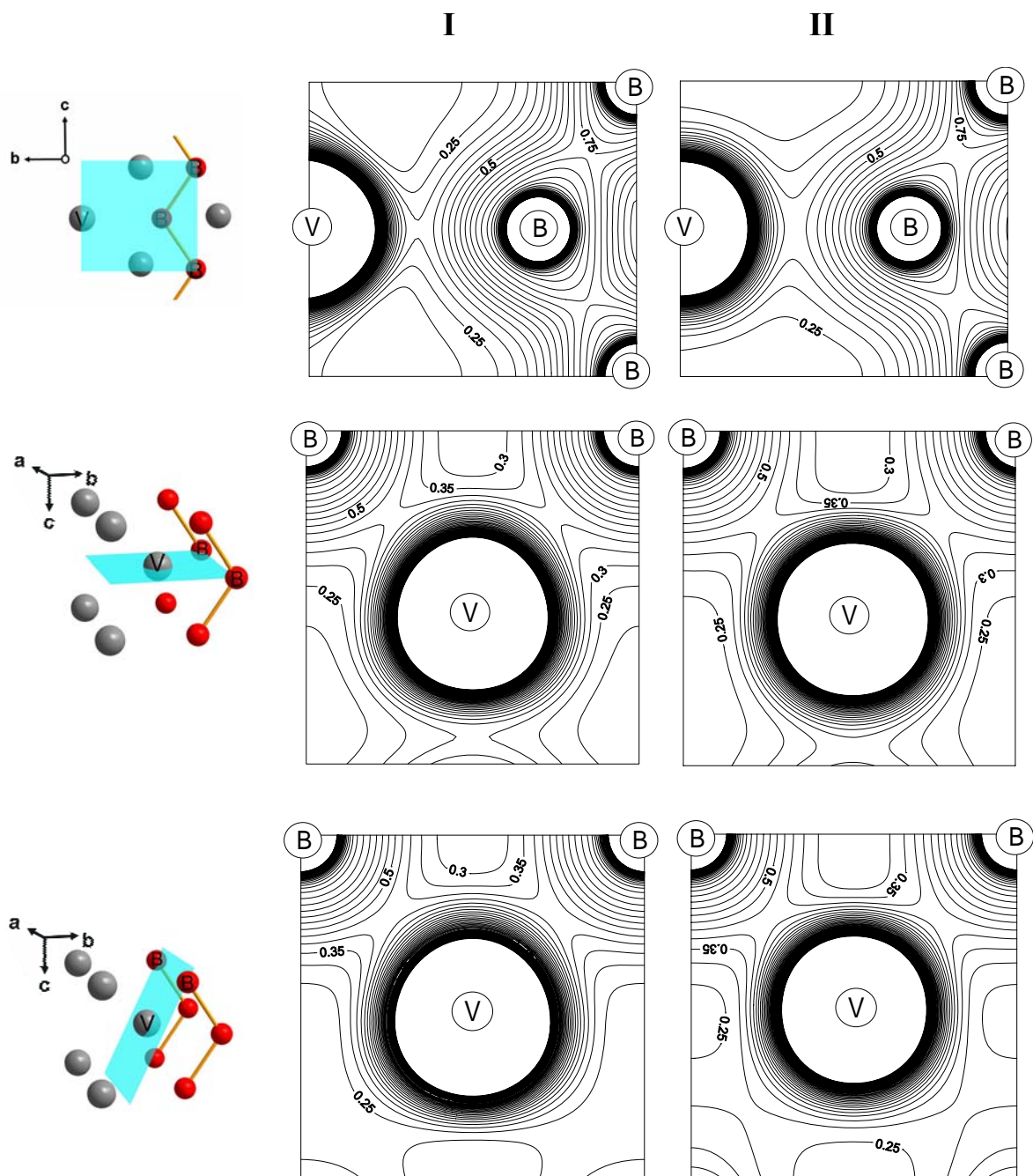


**Figure 6.3** Total electron density maps of VB structure in planes as shown: (I) reconstructed from the X-ray data, (II) calculated by DFT method. The isoline interval is  $0.05 \text{ e } \text{\AA}^{-3}$ .

All of the critical point (cp) types are observed according to both experiment and theory (Table 6.3). The number of different cp types fulfills the Poincare-Hopf condition. No non-nuclear attractors are found. Experimental topological descriptors agree with the values of theory by  $\pm 0.08 \text{ e } \text{\AA}^{-3}$  for  $\rho(r_{\text{cp}})$  and  $\pm 1.4 \text{ e } \text{\AA}^{-5}$  for  $\nabla^2 \rho(r_{\text{cp}})$ . Both number and positions of bcps are in a good agreement according to both methods. Furthermore,  $\rho(r_b)$  at the respective bcps are generally very close to each other except for one  $\rho(r_b)$  value found at  $4c$  position. It has to be noted that discrepancies due  $\rho(r)$  values at rcps are larger than at bcps mostly. An experimentally observed rcp at the  $4c$  position is replaced with a ccp according to theory. Additionally, experimentally found ccp at the  $8f$  position is not reproduced by theory.

**Table 6.3** Topological characteristics of the critical points in VB determined from reconstructed experimental data and theoretical calculations. Theoretical values are denoted by an asterisk.

Wyckoff notation and position of cp	$\rho(r_{\text{cp}})(\text{e } \text{\AA}^{-3})$	$\nabla^2 \rho(r_{\text{cp}})(\text{e } \text{\AA}^{-5})$	$\lambda_1(\text{e } \text{\AA}^{-5})$	$\lambda_2(\text{e } \text{\AA}^{-5})$	$\lambda_3(\text{e } \text{\AA}^{-5})$	Type of cp
$4b (0.5, 0.0, 0.5)$	0.748	-1.341	-2.224	-1.935	2.820	3, -1
$4b (0.5, 0.0, 0.5)^*$	0.740	-2.750	-2.364	-2.010	1.622	3, -1
$16h (0.243, -0.085, 0.489)$	0.431	2.855	-0.978	-0.680	4.511	3, -1
$16h (0.242, -0.01, 0.499)^*$	0.433	2.133	-1.162	-0.622	3.916	3, -1
$8g (0.243, 0.03, 0.250)$	0.405	3.417	-0.783	-0.137	4.335	3, -1
$8g (0.257, -0.04, 0.250)^*$	0.408	2.497	-0.952	-0.193	3.641	3, -1
$4c (0, -0.285, 0.75)$	0.303	3.430	-0.935	-0.320	4.687	3, -1
$4c (0, -0.209, 0.75)^*$	0.378	2.289	-0.581	-0.651	3.521	3, -1
$16h (0.256, -0.04, 0.635)$	0.401	3.088	3.627	-0.776	0.239	3, +1
$16h (0.267, -0.05, 0.641)^*$	0.404	2.627	3.294	-0.928	0.260	3, +1
$8d (0.25, -0.25, 0.50)$	0.197	1.050	-0.333	1.174	0.209	3, +1
$8d (0.25, -0.25, 0.50)^*$	0.276	1.203	-0.361	1.545	0.019	3, +1
$4a (0, 0, 0.5)$	0.304	2.048	0.075	2.270	-0.296	3, +1
$4a (0, 0, 0.5)^*$	0.265	1.268	0.434	0.937	-0.104	3, +1
$4c (0.5, -0.263, 0.75)$	0.163	0.314	-0.101	0.174	0.243	3, +1
$4c (0.5, -0.286, 0.75)^*$	0.213	0.516	0.260	0.055	0.200	3, +3
$8f (0, 0.239, 0.585)$	0.155	1.319	0.275	0.287	0.757	3, +3

### 6.2.1 The B–B interaction

The most prominent structural feature of the VB structure, namely the B–B zig-zag chain is well reflected in the topology of the deformation ED map. The sign of the Laplacian function ( $\nabla^2\rho(r_{cp}) < 0$ ) at the bcp found between the boron atoms of the zig-zag chain points to a shared-type interaction. Figure 6.4 shows the ED Laplacian according to theory and experiment in the plane which includes the boron-zig-zag chain. The Laplacian distribution  $\nabla^2\rho(r)$  along the B–B bond path in the same plane is also shown. The theoretically determined curve is relative less contracted in comparison to experimental one. This result indicates that the valence shell is more pronounced according to experiment.

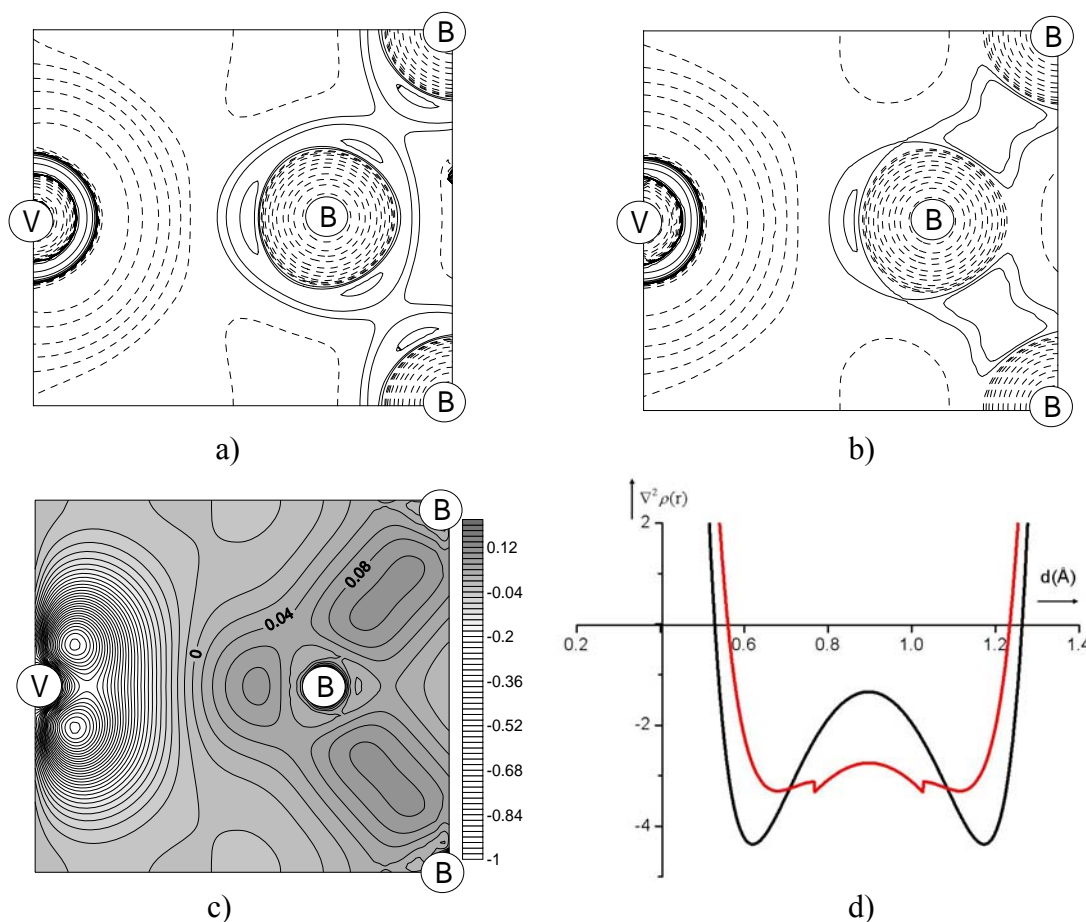


**Figure 6.4** The ED Laplacian in VB according to a) experiment and b) theory in (100) plane. Solid and broken lines represent negative and positive Laplacian values, respectively. The isoline values are  $\pm 2 \times 10^n$ ,  $\pm 4 \times 10^n$ ,  $\pm 8 \times 10^n$  e  $\text{\AA}^{-5}$  where  $n = 0, 4, 3, 2, 1$ . c) The deformation ED map of VB in the same plane as shown in a) and b). The isoline interval is  $0.02$  e a.u. $^{-3}$ . d) The ED Laplacian distribution (e  $\text{\AA}^{-5}$ ) along the B–B bond path. Experimental and theoretical results are given by black and red curves, respectively. The non-continuous behaviour of the theoretical values is an artefact originating from the APW basis set used for the calculation.

Some topological properties of the B–B bond are given in Table 6.4. According to the experiment, the parallel concentration along the bond path towards the nuclei which is measured by  $\lambda_3$ , dominates the first principal curvature  $\lambda_1$  as reflected in the  $|\lambda_1| / \lambda_3$  ratio. In contrary, theoretical calculations suggest that the perpendicular contraction at the bcp is more pronounced. The corresponding bond path is not bent due to symmetry restriction applied to boron atom. The bcp is located at a distance of 0.897 Å from both boron atoms.

**Table 6.4** Topological properties of the ED at B–B bcp in VB according to experiment and theory.

	$\rho(r_b)$ (e Å <sup>-3</sup> )	$\nabla^2 \rho(r_b)$ (e Å <sup>-5</sup> )	$\lambda_1$ (e Å <sup>-5</sup> )	$\lambda_2$ (e Å <sup>-5</sup> )	$\lambda_3$ (e Å <sup>-5</sup> )	$\varepsilon(r_b)$	$ \lambda_1  / \lambda_3$
Exp.	0.748	-1.341	-2.224	-1.935	2.820	0.149	0.789
Theory	0.740	-2.750	-2.364	-2.010	1.622	0.176	1.457

Ellipticity values obtained both from theory and experiment are in agreement. Figure 6.5 shows deformation ED in plane perpendicular to the boron layer including the B–B bond axis. The DD in plane perpendicular to the former one and spanned by the metal atoms is also shown. Deviation from the cylindrical symmetry of the B–B bond in VB is less pronounced as compared to that observed for the B–B bond in both VB<sub>2</sub> and TiB<sub>2</sub>. This indicates that the relevant  $\pi$ -density contribution to the B–B bond is presumably less than those for diborides.

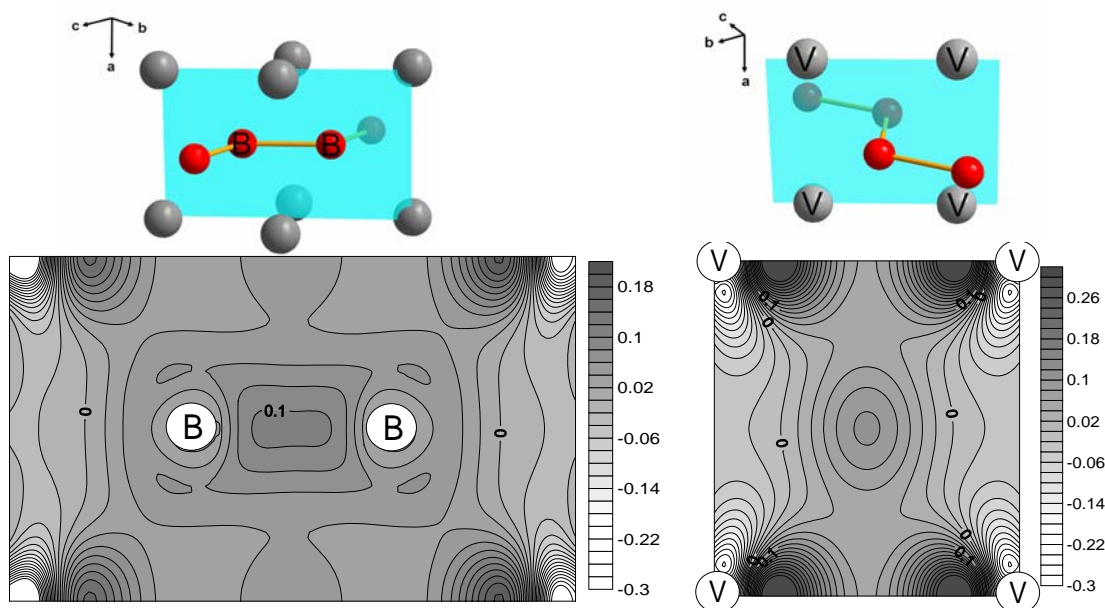


**Figure 6.5** Deformation electron density maps in VB structure in planes as shown. The isoline interval is 0.02 e a.u.<sup>-3</sup>



### 6.2.2 The B–V interaction

As stated previously in Chapter 3, vanadiummonoboride structure can be well described by double metal layers containing the  $BV_6$  prisms. Taking the similar metal boron distances both in the same and neighbouring trigonal prim units into account additional boron metal interaction is expected arising from neighbouring trigonal prims. This is evidenced by the bcp (at the  $4(c)$  position) found on the bond path between boron and vanadium atoms each belonging to two different neighbouring  $BV_6$  prisms in addition to two bond critical points located in the same  $BV_6$  prisms (at the  $16(h)$  and  $8(g)$  positions, respectively) as shown in Figure 6.6.

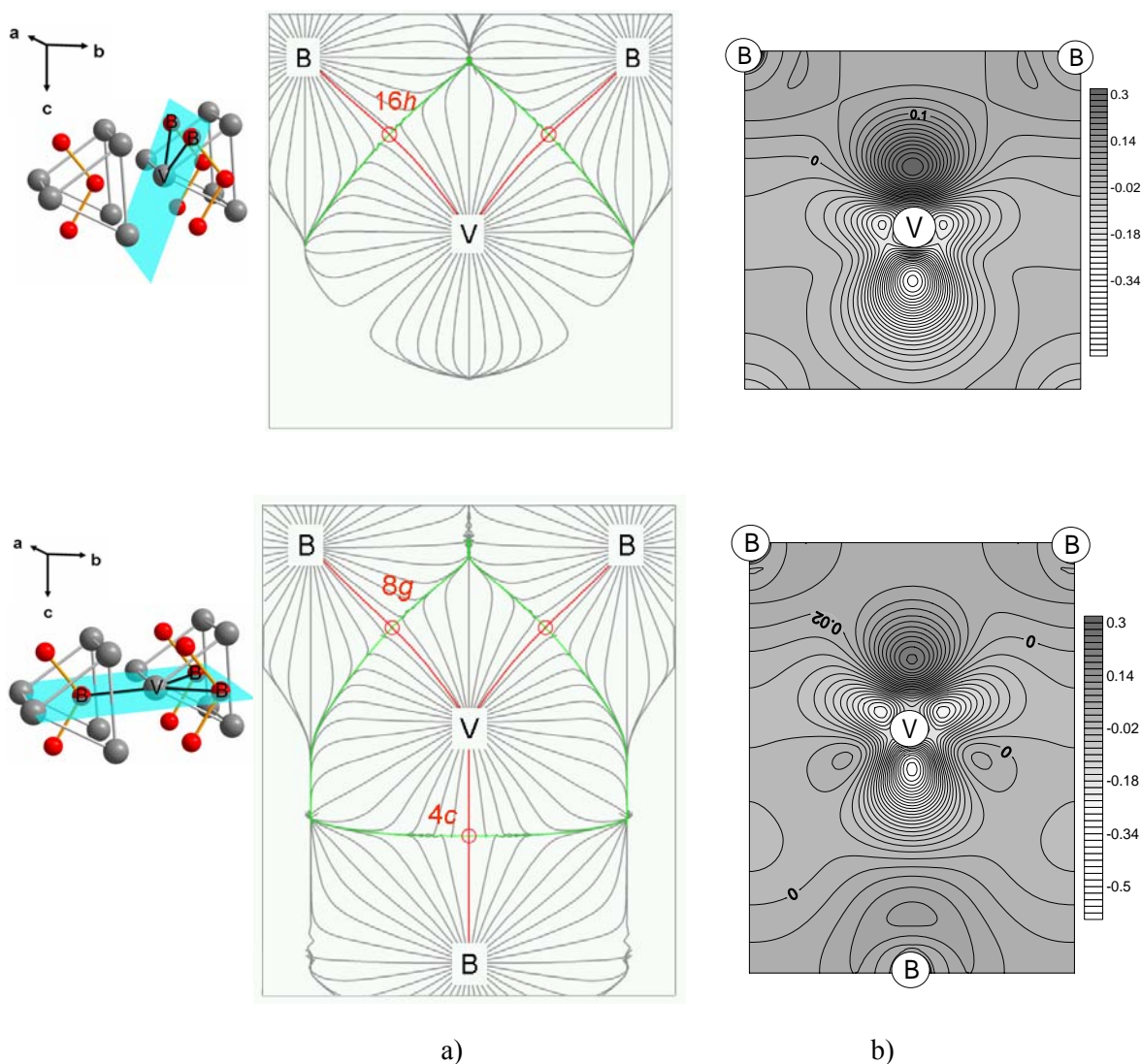


**Figure 6.6** a) The  $\nabla\rho(r)$  field of the ED in VB structure in planes as shown. The bond path and the interatomic surface path are drawn in red and green, respectively. b) The deformation ED in VB structure in the same planes as shown in a). The isoline interval is 0.02 e a.u.<sup>-3</sup>



The bond paths which are placed in the same  $BV_6$  prism are slightly curved. On the other hand, the bond path between neighbouring trigonal prism units is not curved and the corresponding bcp is shifted towards the vanadium atom in contrary to other B–V bcps which are shifted to the nearest boron atoms. These results indicate the polarity of the respective B–V interactions.

The charge asphericities of the vanadium atom can be manifested by the deformation ED maps. As evidenced in Figure 6.6 the ED is highly deformed in the vicinity of the metal atom. The boron atoms are placed not directly to the charge concentrations around the vanadium core.

Some selected topological properties of the B–V bonds are summarized in Table 6.5. The properties of ED at the B–V bcp are perfectly fitting to the unique set of characteristics observed by those in  $VB_2$  and  $TiB_2$ . These are small  $\rho(r_b)$ , small positive  $\nabla^2\rho(r_b)$  and small negative  $H(r)$ . Accordingly, some degree of covalency is evidenced by B–V interactions due the energetic considerations.

**Table 6.5** Topological properties of ED at the B–V cp in VB. The ED  $\rho(r_b)$ , the density Laplacian  $\rho(r_b)$ ,  $G(r)$  kinetic energy density and  $H(r)$  local energy densities are given in atomic units.  $d(bcp)$  is the distance between the B–V bcp and the B–V interatomic line.

Wyckoff notation and position of cp	$d(bcp)$ (Å)	$\rho(r_b)$	$\nabla^2\rho(r_b)$	$G(r)$	$H(r)$
16h (0.243, -0.085, 0.489)	0.155	0.064	0.118	0.049	-0.019
8g (0.243, 0.03, 0.250)	0.063	0.060	0.142	0.050	-0.015
4c (0, -0.285, 0.75)	0	0.045	0.142	0.040	-0.004

The 3D representation of both experimental as well as theoretical ED Laplacian shows that the penultimate shell of the metal atom is distorted (Figure 6.7). However, both methods indicate some discrepancies in the number and location of the charge concentrations. Experimentally and theoretically derived  $\nabla^2\rho(r)$  distribution revealed four and eight significant charge concentrations in the penultimate shell, respectively. They are presumably related to the participation of 3d orbitals of the metal atom at the B–V interaction both in the same as well as between the neighbouring trigonal prism units.

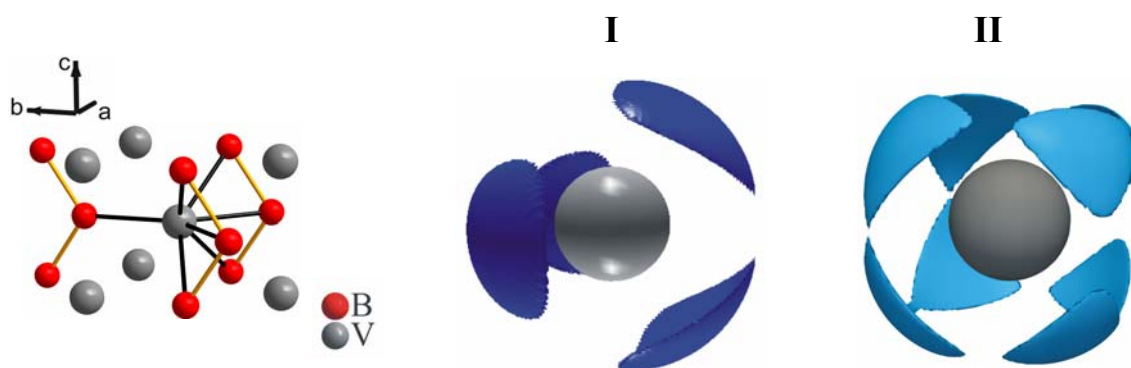


**Figure 6.7** Experimental (I) and theoretical (II) 3D representation of the  $\nabla^2\rho(r)$  distribution in the penultimate shell of the metal atom in VB. The isosurface value is  $\nabla^2\rho(r) = -295 \text{ e } \text{\AA}^{-5}$ .

### 6.2.3 Atomic electron populations

Transferred number of electrons from V to B atom is calculated by integration of the ED over the respective QTAIM basins (Table 6.6). According to the experiment a charge transfer of 0.8 e from a basin volume assigned to vanadium [ $9.76 \text{ \AA}^3$ ] to the zig-zag boron chain [ $V = 8.55 \text{ \AA}^3 / \text{atom}$ ] takes place. Theoretical calculations yield a charge transfer of 0.9 e.

**Table 6.6** Atomic volumes (V) and electron populations ( $\bar{N}$ ) in VB.

	V(M) ( $\text{\AA}^3$ )	V(B) ( $\text{\AA}^3$ )	$\bar{N}$ (M)	$\bar{N}$ (B)	$\bar{N}$ in the unit cell
Exp.	9.76	8.55	22.20	5.79	111.98
Theory	9.52	8.80	22.08	5.92	112.00

### 6.3 Summary on VB

The ED in VB is successfully reconstructed from high-resolution single crystal X-ray data applying a multipole model. A good agreement between the observed and calculated structure factors is achieved. According to the topological analysis of the ED, all theoretically obtained bcps are reproduced. However, disagreements are observed due to positions of some ring- and cage critical points. Four bond critical points are found, one corresponds to the B–B interaction in the zig-zag chain and the remaining three are related to the B–V interaction. The ED properties of the B–B bcp reveal that the B–B interaction has a covalent character. Moreover, the respective ellipticity value is found to be less in comparison to those observed in diborides. The B–V bcp properties reveal that the B–V bonding is of polar covalent nature similar to that observed in diborides. This result is supported by the significant structurization in the vicinity of metal atom according to both deformation ED and the Laplacian despite some discrepancies between theory and experiment. Furthermore, vanadium atom is not only interacting with borons in the same trigonal prism unit but also with those in the neighbouring ones according to a B–V bcp found. Finally, the analysis of the QTAIM population in the atomic basins reveals a charge transfer from vanadium to the boron zig-zag chain.



## 7 ELECTRON DENSITY IN V<sub>3</sub>B<sub>4</sub>

In this Chapter the topological analysis of the experimentally reconstructed ED in V<sub>3</sub>B<sub>4</sub> is given in the light of QTAIM. The results are compared with the quantum chemical calculations.

### 7.1 Multipole refinement

The number of multipole parameters in V<sub>3</sub>B<sub>4</sub> to be refined is considerably higher than those in VB<sub>2</sub> and VB, since there are four atom positions; one with the site symmetry *mmm* and the other three *mm2*. The multipole expansion is terminated at the hexadecapole level for each atom. That gives 29 contributing multipole coefficients in addition with two valence and two expansion as well as contraction parameters per each atom to be refined against 169 low-order reflections ( $\sin \theta/\lambda \leq 0.8 \text{ \AA}^{-1}$ ). Core and valence functions used for the reconstruction of the ED are obtained from the Hartree-Fock wavefunctions taken from Clementi and Roetti.<sup>[130]</sup> The respective radial-function parameters used are  $n_2 = 4$ ,  $n_4 = 4$  and  $\zeta_V = 4.4$  for V1;  $n_2 = 4$ ,  $n_3 = 4$ ,  $n_4 = 4$  and  $\zeta_V = 4.4$  for V2;  $n_2 = 2$ ,  $n_3 = 3$ ,  $n_4 = 4$  and  $\zeta_B = 2.53$  for B1 and B2.

The procedure used for the multipole refinement of V<sub>3</sub>B<sub>4</sub> is similar to that applied for other structures refined in this thesis. The valence electron populations  $P_v$  of 5 e<sup>-</sup> for V and 3 e<sup>-</sup> for B are used as starting values. First only displacement parameters and the scale factor are refined using all data. After this, the  $P_v$  for each atom is refined together with  $\kappa$  using low order data ( $\sin \theta/\lambda \leq 0.8 \text{ \AA}^{-1}$ ) keeping  $\kappa'$  and all multipole parameters fixed. The valence electron populations indicate that there is charge transfer from vanadium to boron. The  $P_{lm\pm}$  parameters are refined using  $\sin \theta/\lambda \leq 0.8 \text{ \AA}^{-1}$  whereas  $P_v$  and  $\kappa$  are kept fixed. The  $R_{(F)}$  value drops to 1.76%. To keep the number of refined coefficients as low as possible a more rigid multipole model is used by which  $\kappa'$  is not refined. Furthermore, some multipole coefficients are close to zero, thus they are insignificant to be included in the final model for reconstruction of the ED. Refined multipole parameters and atomic coordinates are given in Table 7.1.

**Table 7.1** Multipole, expansion and contraction parameters together with the atomic coordinates in V<sub>3</sub>B<sub>4</sub>.

	V1 (in <i>mmm</i> )	V2 (in <i>mm</i> 2)	B1 (in <i>mm</i> 2)	B2 (in <i>mm</i> 2)
<i>x/a</i>	0	½	0	½
<i>y/b</i>	0	0	0	0
<i>z/c</i>	0	0.31249(1)	0.43443(3)	0.13641(3)
<i>P<sub>v</sub></i>	4.556(6)	4.256(6)	3.631(6)	3.334(6)
<i>P<sub>10</sub></i>	-	-0.0558(4)	0.0186(4)	0.0558(4)
<i>P<sub>20</sub></i>	0.0	0.0	0.0186(4)	0.0
<i>P<sub>22</sub></i>	-0.0186	-0.0186(4)	0.0	0.0
<i>P<sub>30</sub></i>	-	-0.0186(4)	-0.0744(4)	0.0744(4)
<i>P<sub>32</sub></i>	-	0.1116(4)	-0.0372(4)	-0.0372(4)
<i>P<sub>33-</sub></i>	-	-	-	-
<i>P<sub>40</sub></i>	0.0	0.0	0.0186(4)	0.0140(4)
<i>P<sub>42</sub></i>	0.0	0.0	0.0	0.0372(4)
<i>P<sub>44</sub></i>	0.0186	0.0	0.0186(4)	0.0163(4)
<i>κ</i>	0.9144(4)	0.9144(4)	1.0156(4)	1.0156(4)

Table 7.2 shows harmonic and anharmonic ADPs due to conventional and multipole refinement. The use of multipole model slightly decreases the ADPs. The changes are smaller than those observed for other vanadium borides.

**Table 7.2** Harmonical (Å<sup>2</sup>) and anharmonic ADPs (Å<sup>4</sup>) due to spherical and multipole refinement for the crystal structure of V<sub>3</sub>B<sub>4</sub>.

ADP	Spherical refinement				Multipole refinement			
	V1	V2	B1	B2	V1	V2	B1	B2
<i>B(eq)*</i>	0.123(3)	0.130(2)	0.270(7)	0.296(7)	0.120(2)	0.122(2)	0.268(6)	0.290(6)
<i>B<sub>11</sub></i>	0.096(5)	0.094(43)	0.26(1)	0.29(1)	0.096(4)	0.090(4)	0.26(1)	0.28(1)
<i>B<sub>22</sub></i>	0.136(4)	0.163(3)	0.28(1)	0.29(1)	0.132(4)	0.153(3)	0.28(1)	0.29(1)
<i>B<sub>33</sub></i>	0.137(4)	0.133(3)	0.27(1)	0.31(1)	0.132(4)	0.125(3)	0.257(9)	0.304(9)
<i>D<sub>1111</sub></i>	-2.0(4)	-2.1(3)			-1.7(1)	-2.1(2)		
<i>D<sub>2222</sub></i>	-2.4(3)	-1.2(2)			-2.4(2)	-1.4(2)		
<i>D<sub>1122</sub></i>	-0.8(1)	-0.5(1)	kept fixed		-0.7(1)	-0.6(1)	kept fixed	
<i>D<sub>1133</sub></i>	—	—			—	—		
<i>D<sub>2233</sub></i>	—	—			—	—		

\*  $B(eq) = 1/3 [B_{11} a^{*2} a^2 + \dots + 2 B_{23} b^* c^* b c \cos \alpha]$

Figure 7.1 shows the ratio of the observed and calculated structure factors according to the spherical and the multipole refinement of V<sub>3</sub>B<sub>4</sub> referring to low order data up to  $\sin \theta / \lambda = 0.8$ . In general, the improvement achieved in the fitting of observed structure factors to the calculated ones with the use of the multipole model instead of simple spherical atom model is less compared to other vanadium borides.

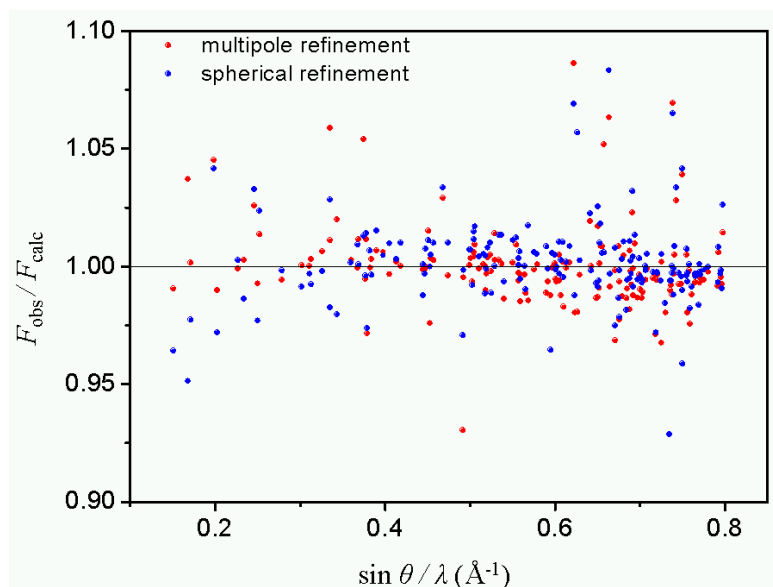


**Figure 7.1**  $F_{\text{obs}} / F_{\text{calc}}$  vs.  $\sin \theta / \lambda$  according to spherical (blue) and multipole (red) refinement of V<sub>3</sub>B<sub>4</sub> structure.

Table 7.3 summarizes the variation in  $R_{\text{(F)}}$  values in V<sub>3</sub>B<sub>4</sub>, VB and VB<sub>2</sub> according to both IAM and multipole refinement taking into account only low-order reflections ( $\sin \theta / \lambda \leq 0.8 \text{ \AA}^{-1}$ ). In general, the  $R_{\text{(F)}}$  values increase with the increase of reflection number.

**Table 7.3**  $R_{\text{(F)}}$  values after IAM and multipole refinement.  $\overline{N}$  is the number of reflections.

	$\overline{N}$	IAM Refinement	Multipole refinement
VB <sub>2</sub>	35	0.46	0.38
VB	100	0.54	0.49
V <sub>3</sub> B <sub>4</sub>	169	0.88	0.84

Figure 7.2 shows the residual density maps of V<sub>3</sub>B<sub>4</sub> according to spherical and multipole refinement. Obviously, the density is not completely flat and featureless with the use of multipole model. Unlike other compounds examined, in case of V<sub>3</sub>B<sub>4</sub> some features cannot

be described by the multipole model located in the B1–B2 internuclear region, in particular. The maximum and minimum values of the residuals are  $-0.412 / 0.451$  and  $-0.337 / 0.229 \text{ e } \text{\AA}^{-3}$  due the IAM and multipole model, respectively. All following results should be considered solely as a first attempt of the reconstruction of ED from the diffraction data for  $V_3B_4$ .

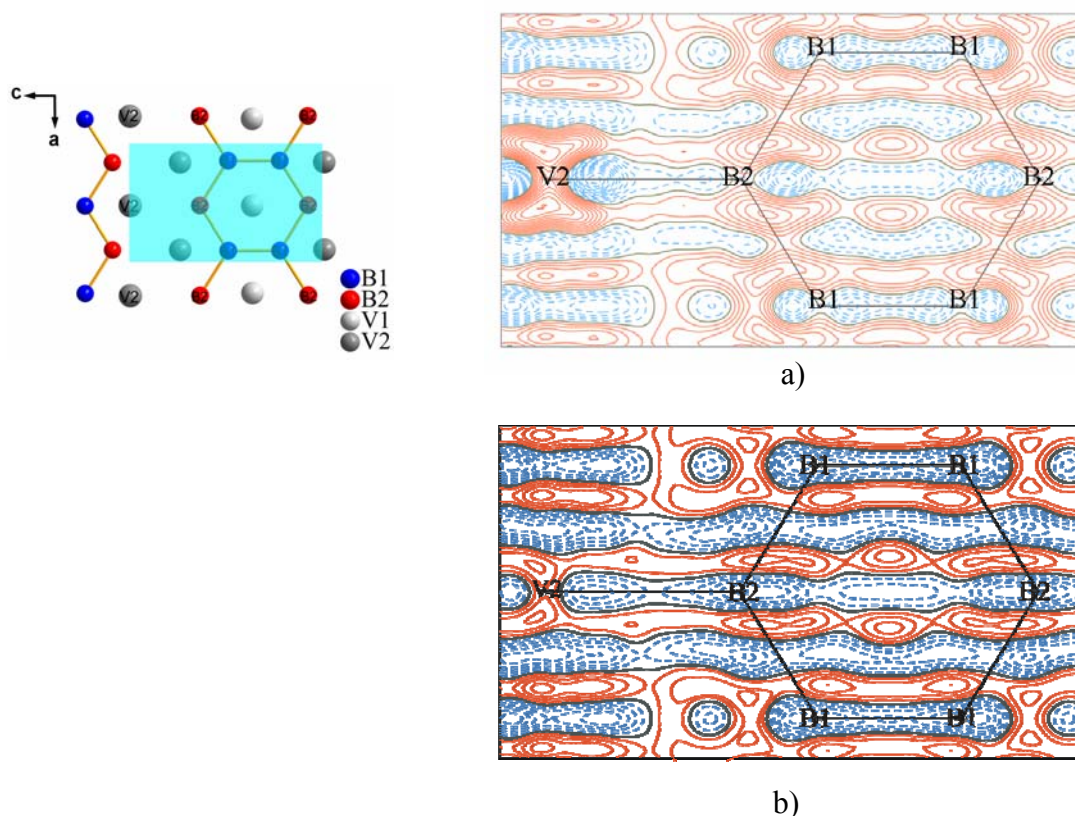


**Figure 7.2** Residual density maps in  $V_3B_4$  structure according to the IAM in a) and multipole refinement in b). The data cut-off at  $\sin \theta / \lambda = 0.9$ ; contour level step width:  $0.05 \text{ e } \text{\AA}^{-3}$ . Solid red and dashed blue lines correspond to positive and negative values, respectively, whereas solid black line is the zero contour.

## 7.2 Topological analysis of the electron density

Experimentally reconstructed total ED maps for  $V_3B_4$  in some selected planes are presented in Figure 7.3. Theoretical ED maps are also given for the sake of comparison. All of cp types are present in the ED of  $V_3B_4$ . No nonnuclear attractors are found. The Poincare-Hopf condition is fulfilled according to both theoretical and experimental analysis of ED. All the theoretically found bcps are reproduced by experiment (Table 7.4).



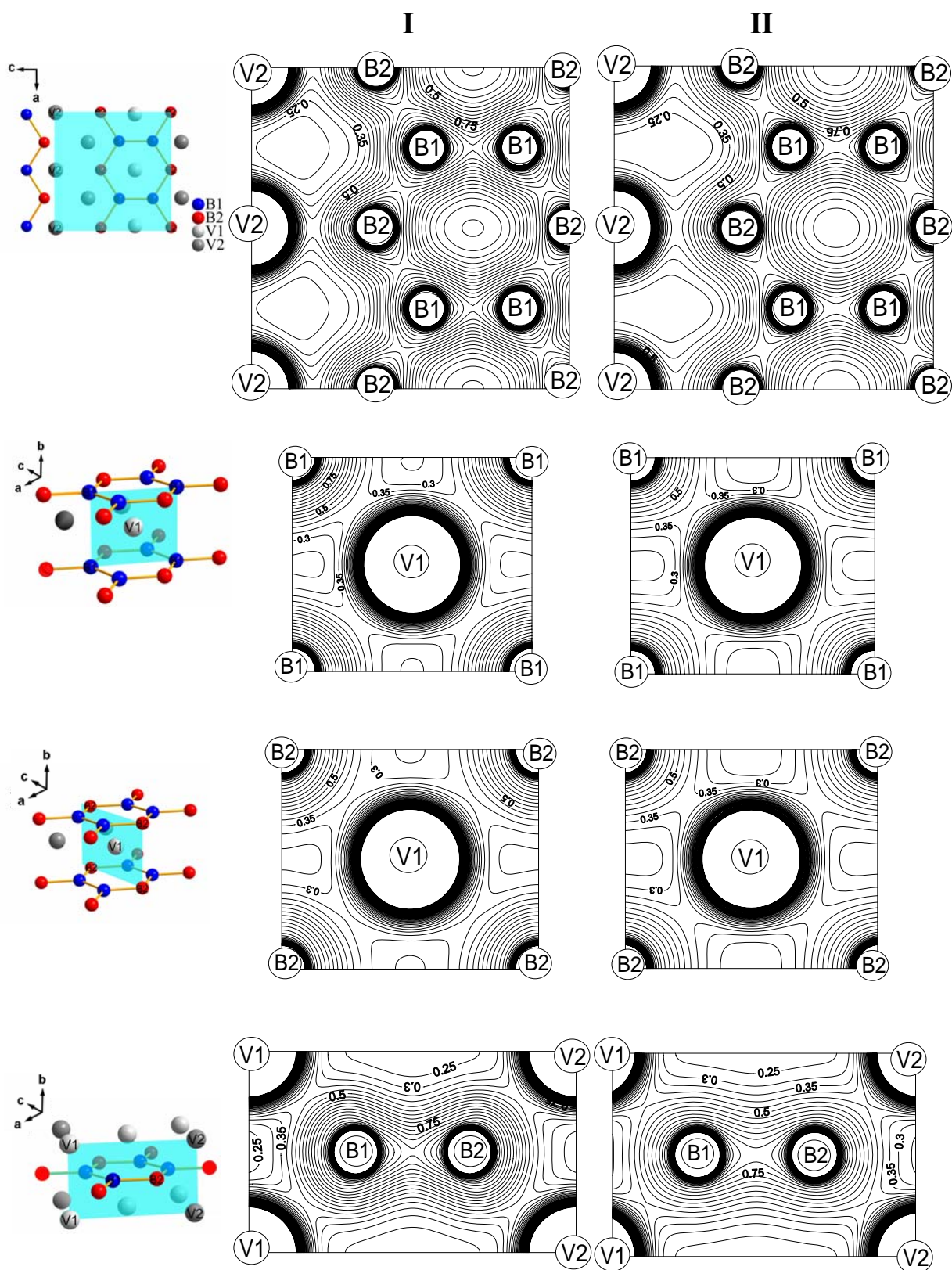


**Figure 7.3** Total electron density in  $V_3B_4$  structure in planes as shown. (I) ED reconstructed from the X-ray diffraction data, (II) calculated by APW method. The isoline interval is  $0.05 \text{ e } \text{\AA}^{-3}$ .

**Table 7.4** Topological characteristics of the critical points determined from reconstructed experimental ED and theoretical calculations. Theoretical values are denoted by an asterisk.

Wyckoff notation and position of cp	$\rho(r_{cp})(e \text{ \AA}^{-3})$	$\nabla^2 \rho(r_{cp})(e \text{ \AA}^{-5})$	$\lambda_1(e \text{ \AA}^{-5})$	$\lambda_2(e \text{ \AA}^{-5})$	$\lambda_3(e \text{ \AA}^{-5})$	Type of cp
2c (0.5, 0.5, 0)	0.904	-3.000	-3.316	-2.930	3.249	3, -1
2c (0.5, 0.5, 0)*	0.814	-4.118	-2.918	-2.658	1.458	3, -1
8l (0.5, 0.245, 0.106)	0.752	-0.691	-2.162	-1.940	3.410	3, -1
8l (0.5, 0.249, 0.103)*	0.785	-3.535	-2.718	-2.340	1.521	3, -1
8m (0.250, 0, 0.375)	0.436	4.423	-0.918	-0.523	5.863	3, -1
8m (0.237, 0, 0.375)*	0.447	2.487	-1.306	-0.386	4.176	3, -1
16o (0.266, 0.290, 0.149)	0.402	3.605	-0.815	-0.077	4.497	3, -1
16o (0.264, 0.260, 0.155)*	0.437	2.265	-1.275	-0.424	3.964	3, -1
16o (0.255, 0.253, 0.031)	0.376	3.558	-0.708	-0.255	4.523	3, -1
16o (0.258, 0.256, 0.032)*	0.391	2.248	-0.998	-0.229	3.545	3, -1
4j (0.5, 0, 0.226)	0.363	2.878	-0.969	-0.774	4.617	3, -1
4j (0.5, 0, 0.225)*	0.382	2.273	-0.713	-0.581	3.567	3, -1
8m (0.249, 0, 0.068)	0.381	2.925	-0.803	-0.419	4.145	3, -1
8m (0.256, 0, 0.068)*	0.363	2.234	-0.795	-0.046	3.077	3, -1
16o (0.272, 0.307, 0.145)	0.402	3.602	-0.807	0.075	4.335	3, +1
16o (0.275, 0.343, 0.138)*	0.429	2.716	-1.200	0.159	3.615	3, +1
8n (0.267, 0.281, 0)	0.367	3.435	-0.704	0.231	3.909	3, +1
8n (0.272, 0.283, 0)*	0.381	2.509	-0.993	0.229	3.270	3, +1
16o (0.271, 0.147, 0.057)	0.361	2.939	-0.681	0.378	3.244	3, +1
16o (0.259, 0.063, 0.067)*	0.362	2.280	-0.793	0.080	2.993	3, +1
8k (0.25, 0.25, 0.25)	0.215	1.420	-0.253	0.118	1.557	3, +1
8k (0.25, 0.25, 0.25)*	0.276	1.203	-0.378	0.036	1.545	3, +1
8l (0.5, 0.138, 0.430)	0.239	1.171	-0.072	0.496	0.747	3, +1
8l (0.5, 0.213, 0.328)*	0.242	1.125	-0.084	0.547	0.665	3, +1
4l (0.5, 0.5, 0.328)*	0.236	0.974	-0.058	0.361	0.678	3, +1
4l (0.5, 0.5, 0.379)*	0.213	0.971	0.043	0.142	0.786	3, +3
2d (0, 0.5, 0)	0.230	1.137	0.089	0.458	0.588	3, +3
2d (0, 0.5, 0)*	0.218	1.104	0.063	0.472	0.569	3, +3
2b (0.5, 0, 0)	0.228	1.281	0.313	0.369	0.598	3, +3
2b (0.5, 0, 0)*	0.210	1.309	0.357	0.388	0.564	3, +3
4l (0.5, 0.5, 0.253)	0.169	0.461	0.113	0.142	0.207	3, +3
4l (0.5, 0.5, 0.224)*	0.209	0.583	0.074	0.227	0.280	3, +3

Theoretically obtained ring and cage critical point at the 4l positions are not reproduced by experiment. Variation of ED values at cp between theory and experiment are in the range of  $\pm 0.09 e \text{ \AA}^{-3}$  for  $\rho(r_{cp})$  and  $\pm 2.8 e \text{ \AA}^{-5}$  for  $\nabla^2 \rho(r_{cp})$ , respectively.

### 7.2.1 The B–B interaction

The topology of the DD map indicates ED accumulation located both in B1–B2 internuclear region as well as in B1–B1 internuclear region. The B1–B1 atoms are responsible for linking both B1–B2 zig-zag chains. However, no single maxima are observed in regions of density accumulation, instead two maxima are separated and each one is located close to the other nucleus (Figure 7.4). The boron atoms are completely enveloped by the negative region of  $\nabla^2\rho(r)$ . The negative values for  $\nabla^2\rho(r_b)$  both at the B1–B1 and B1–B2 bcp indicate a shared-type interaction.

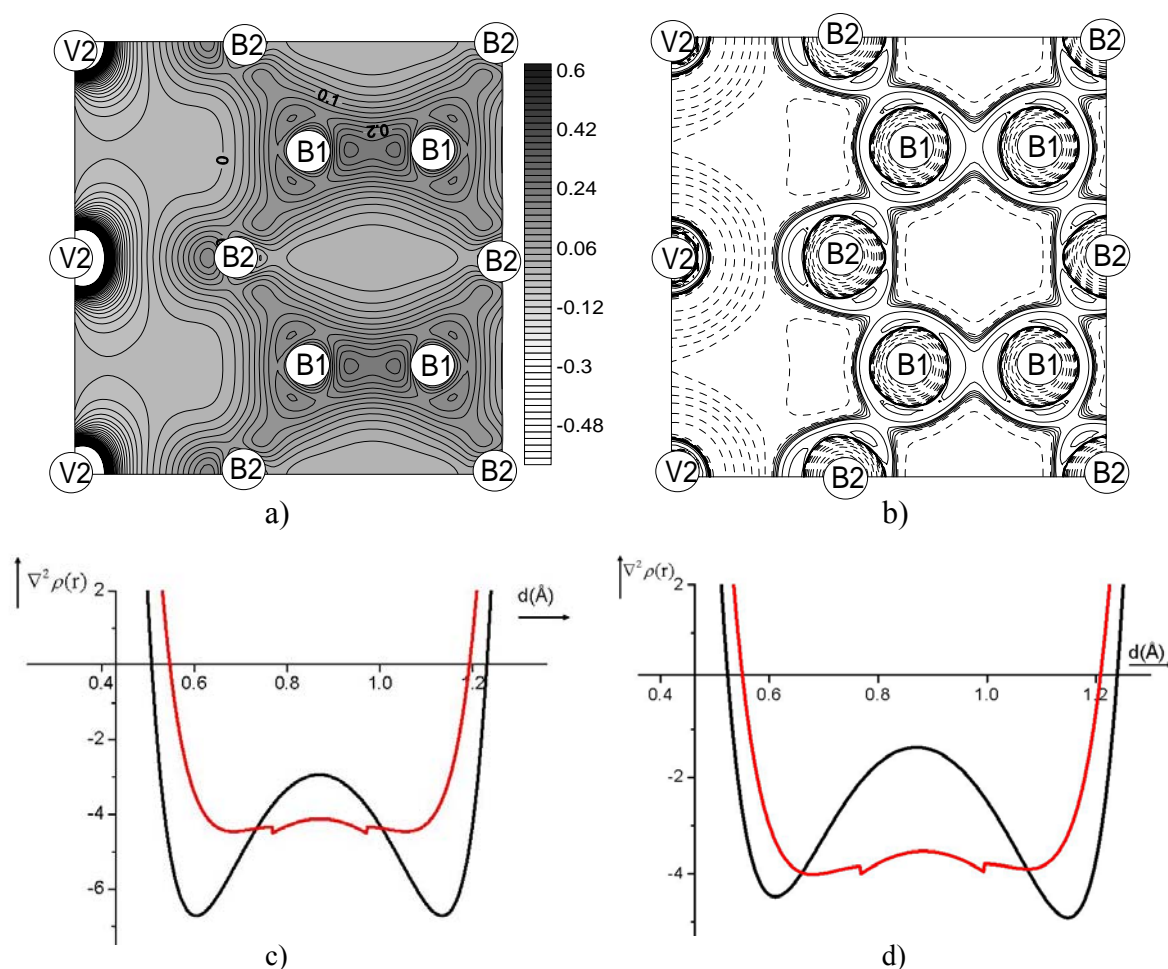


**Figure 7.4** a) The deformation ED in  $V_3B_4$  in plane of B-B double zig-zag chain. The isoline interval is  $0.02 \text{ e a.u.}^{-3}$  b) The ED Laplacian in  $V_3B_4$  in the same plane as in a). The isoline intervals are  $\pm 2 \times 10^n$ ,  $\pm 4 \times 10^n$ ,  $\pm 8 \times 10^n \text{ e \AA}^{-5}$  where  $n = 0, 4, 3, 2, 1$ . c) Experimentally (black) and theoretically (red) calculated  $\nabla^2\rho(r)$  (e  $\text{\AA}^{-5}$ ) distribution along the B1–B1 bond path. d) Experimentally (black) and theoretically (red) calculated  $\nabla^2\rho(r)$  (e  $\text{\AA}^{-5}$ ) distribution along the B1–B2 bond path. The non-continuous behaviour of the theoretical values is an artefact originating from the APW basis set used for the calculation.

In general, experimentally determined ED Laplacian  $\nabla^2\rho(r)$  along both B–B bond paths reveals a double minima picture with a significant "contraction" indicating a quite pronounced charge concentration comparable to C–C bonds in a phenyl ring.<sup>[147]</sup> This result differs from the theoretically predicted shape of Laplacian distribution between the boron atoms which is supposed to have a less pronounced valence shell (Figure 7.4). According to experiment, the bcp at the  $2c$  position is exactly in the middle of the interatomic line due to symmetry restrictions applied to B1 atom whereas the bcp at the  $8l$  position is located near to B2.

Some other topological properties of B1–B1 and B1–B2 bcps are summarized in Table 7.5. Experimental and theoretical  $\rho(r_b)$  value at the B1–B2 bcp at  $8l$  position is less than that of the B1–B1 bcp at  $2c$  position. The variation between theoretically and experimentally derived  $\rho(r_b)$  values is larger for the latter bcp. The ellipticity values varying in the range of 0.098–0.161 may be indication of  $\pi$ -density contribution to the bond. A comparison of  $|\lambda_1| / \lambda_3$  ratios at both B1–B1 as well as B1–B2 bcp between experiment and theory reveal that the parallel concentration along the bond path toward both nuclei is more pronounced according to experiment.

**Table 7.5** Experimentally and theoretically determined properties of B–B bonds in  $V_3B_4$ . Theoretical values are denoted with an asterisk.  $d(B-B)$  is the B–B interatomic distance whereas  $d(B-bcp)$  is the distance between the respective boron atoms and the bcp.

Wyckoff notation of the bcp	$d(B-B)$ (Å)	$d(B-bcp)$ (Å)	$\rho(r_b)$ (e Å <sup>-3</sup> )	$\nabla^2\rho(r_b)$ (e Å <sup>-5</sup> )	$\varepsilon(r_b)$	$ \lambda_1  / \lambda_3$
B1-B2 in $V_3B_4$ , $8l$	1.7942(3)	0.941, 0.858	0.752	-0.691	0.114	0.634
B1-B2 in $V_3B_4$ , $8l^*$			0.785	-3.535	0.162	1.788
B1-B1 in $V_3B_4$ , $2c$	1.7341(6)	0.867, 0.867	0.904	-3.000	0.132	1.021
B1-B1 in $V_3B_4$ , $2c^*$			0.814	-4.118	0.098	2.001

### 7.2.2 The B–V interaction

Topological analysis of ED according to both theory and experiment reveals that there are five bcps in B–V interatomic regions. Some selected topological properties of B–V bonds are summarized in Table 7.6. The slight shifts of the bcps away from the midpoint of the bond paths indicate the polarity of the B–V bonds. It has to be noted that the topological properties of the ED at different B–V bond critical points are quite close to each other.

These properties are generally relatively low value of  $\rho(r_b)$ , small positive  $\nabla^2\rho(r_b)$  value and small negative value for local energy density  $H(r)$ ; thus coincides generally with those observed in  $VB_2$ ,  $TiB_2$  and  $VB$ . These bcp indices point to covalent nature of the B–V interactions in  $V_3B_4$ .

**Table 7.6** Topological properties of ED at B–V bcp in atomic units.  $d(B\text{--}bcp)$  is the distance between the respective boron atom and the B–V bcp whereas  $d(V\text{--}bcp)$  is the distance between the respective metal atom and the B–V bcp.

Wyckoff notation and position of cp	$d(B\text{--}bcp)$ (Å)	$d(V\text{--}bcp)$ (Å)	$\rho(r_b)$	$\nabla^2\rho(r_b)$	$G(r)$	$H(r)$
B1–V2, $8m$ (0.250, 0, 0.375)	1.088	1.109	0.065	0.184	0.060	-0.015
B2–V2, $16o$ (0.266, 0.290, 0.149)	1.180	1.150	0.060	0.150	0.051	-0.014
B1–V1, $16o$ (0.255, 0.253, 0.031)	1.147	1.160	0.056	0.148	0.048	-0.011
B2–V2, $4j$ (0.5, 0, 0.226)	1.185	1.143	0.054	0.119	0.042	-0.012
B2–V1, $8m$ (0.249, 0, 0.068)	1.173	1.170	0.056	0.121	0.044	-0.014

The charge asphericities in the vicinity of V1 and V2 atoms can be detected by deformation electron density maps as shown in Figure 7.5. In general, the ED around V1 is less distorted and more homogeneously distributed in comparison to V2. The charge accumulations around V2 are located opposite to B1 atoms.

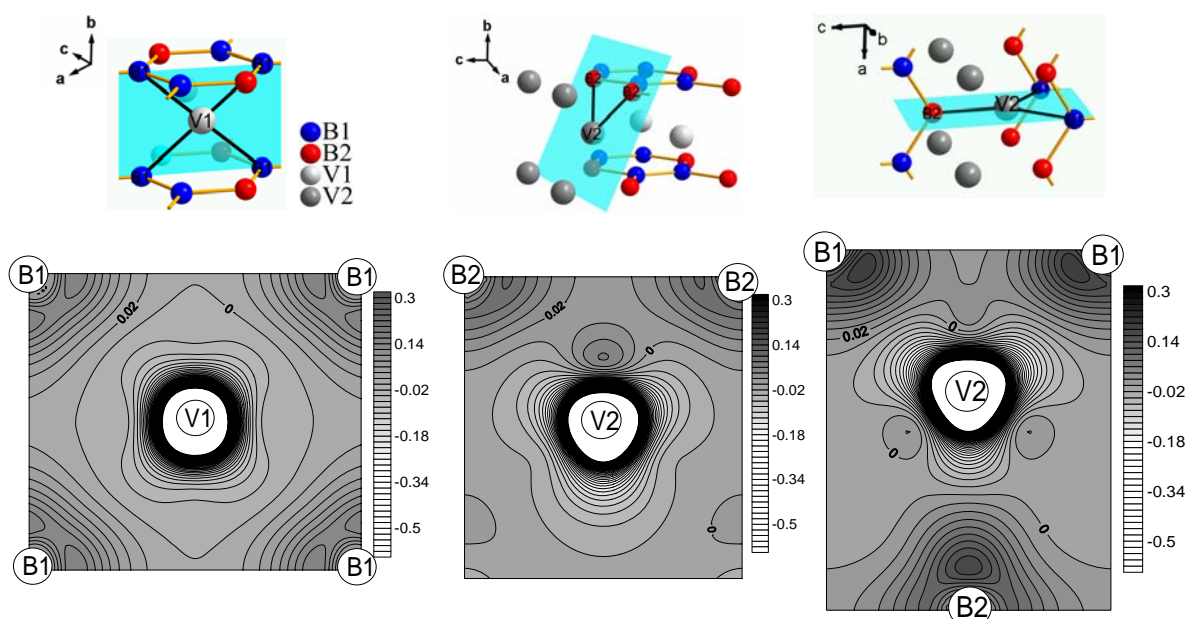


**Figure 7.5** Deformation densities in  $V_3B_4$  in planes as shown. The isoline interval is  $0.02 \text{ e a.u.}^{-3}$ .



The gradient field of the ED  $\nabla\rho(r)$ , inclusive the B–V bond paths in the relevant planes are shown in Figure 7.6. The bcp found at  $4j$  position confirms that the B–V interaction exists not only in the same trigonal prism unit but also between neighbouring trigonal prism units. Consequently, B2 atoms are shifted from the center of the trigonal prism towards to V2 in the neighbouring sheet.

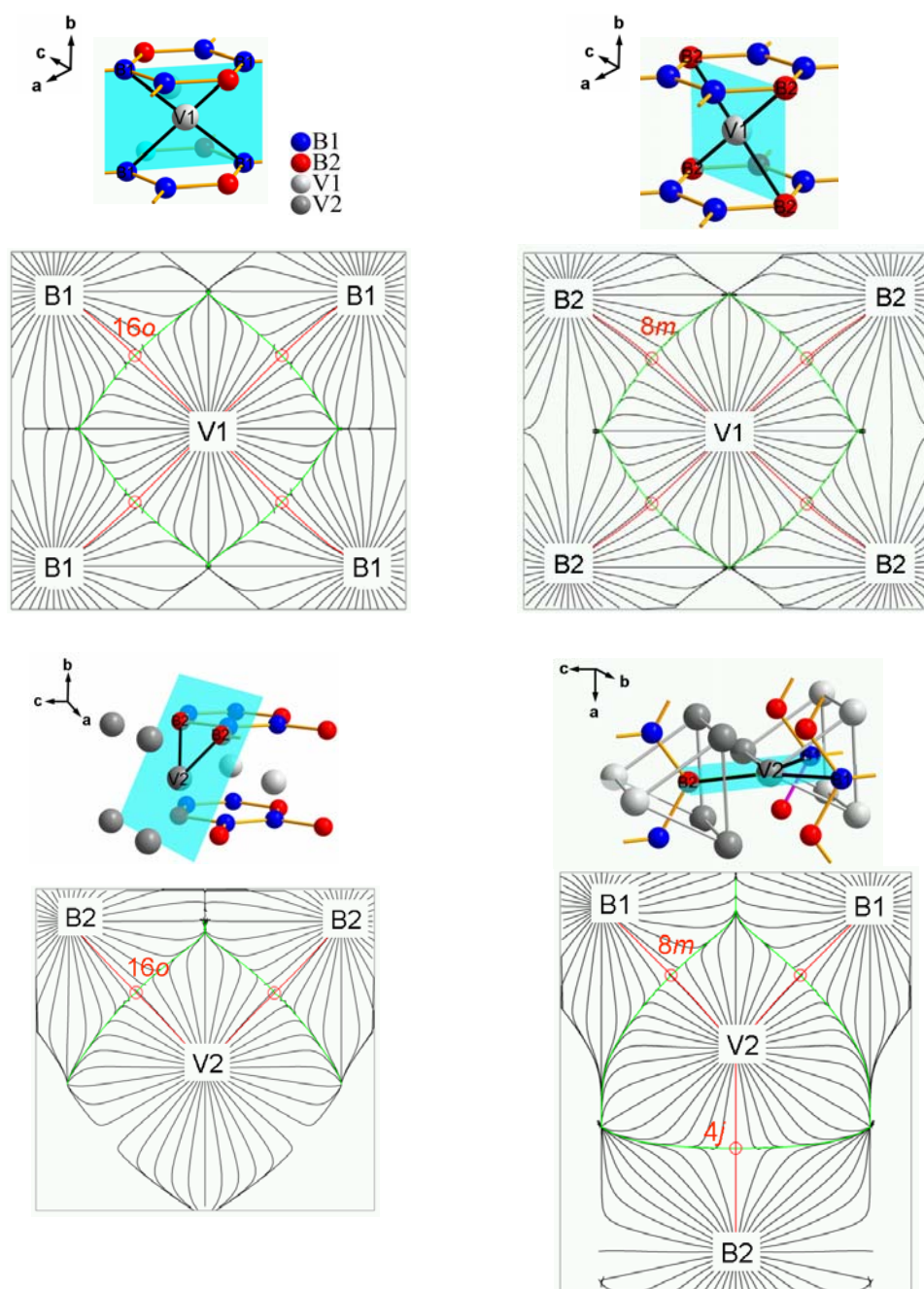


**Figure 7.6** The gradient field  $\nabla\rho(r)$  of the ED in the planes as shown in  $V_3B_4$ . The bond path and the interatomic surface path are drawn in red and green, respectively. The bond critical points are denoted by red circles.

The 3D representation of the experimentally derived topology of the Laplacian  $\nabla^2\rho(r)$  around the V atom is not in agreement with the theory (Figure 7.7). Both methods confirm the structurization of the penultimate shell away from a spherical shape. However, there are differences in the position of charge concentrations.

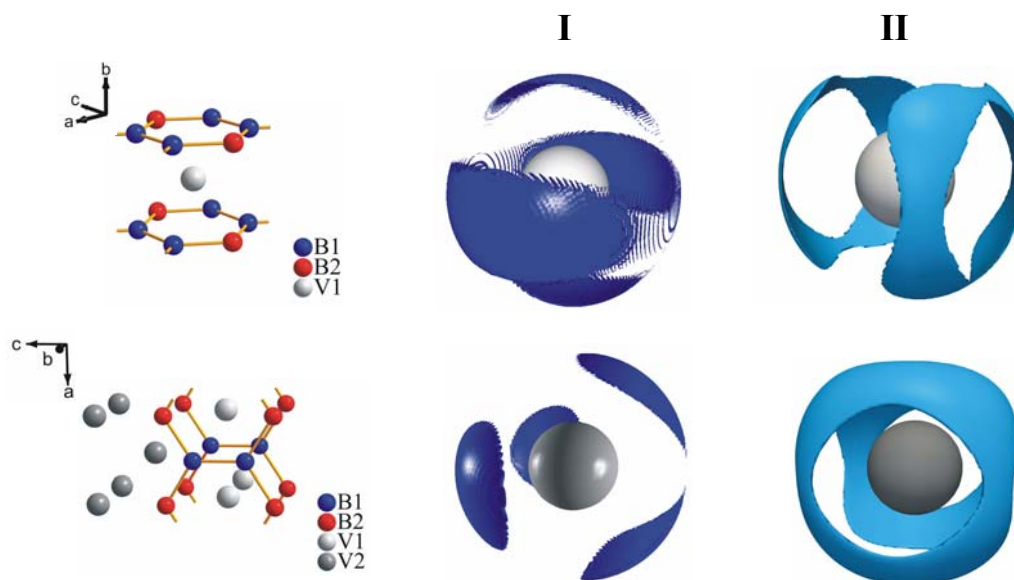


**Figure 7.7** Experimental (I) and theoretical (II) 3D representation of the ED Laplacian for the metal atoms in  $V_3B_4$ . The isosurface  $\nabla^2\rho$  values are  $-300 \text{ e } \text{\AA}^{-5}$  (I) and  $-288 \text{ e } \text{\AA}^{-5}$  (II).

### 7.2.3 Atomic Electron Populations

The atomic electron populations are estimated by integration of the model ED over the atomic basins (Table 7.7). Experimental calculations yield a charge transfer of *ca.* 3.72 e from  $V_3$  to  $B_4$ , i.e.,  $[V_3]^{3.7+} [B_4]^{3.7-}$  whereas theoretical calculations reveal a transfer of *ca.* 3.11 e. The agreement of AIM charges and the atomic volume within the given atom types are  $\pm 0.43 \text{ e}$  and  $\pm 0.27 \text{ \AA}^3$ , respectively.

**Table 7.7** Atomic volumes (V) and electron populations in atomic basins ( $\bar{N}$ ).

	V ( $\text{\AA}^3$ )				$\bar{N}$				$\bar{N}$ (unit cell)
	V1	V2	B1	B2	V1	V2	B1	B2	
Exp.	8.36	9.60	7.97	8.41	21.72	21.78	6.10	5.75	177.96
Theory	8.57	9.50	7.70	8.69	21.85	22.08	5.67	5.82	178.00

Experimentally obtained charge transfer to B1 in  $V_3B_4$  ( $\sim 1.1$  e) is found to be considerably higher than the theoretical value ( $\sim 0.7$  e) as well as electrons transferred to B2 ( $\sim 0.8$  e). The location of B1–B2 bcp away from the midpoint of the B1–B2 bond path supports the transfer of electrons to B1 not only from the metal but also presumably to a smaller extent from B2. Large amount of charge transfer to B1 in  $V_3B_4$  is also reflected by the ED value at B1–B1 bcp which is found to be higher in comparison to that at the B1–B2 bcp.



### 7.3 Summary on $V_3B_4$

A detailed description of the ED features in  $V_3B_4$  is derived in terms of a multipole model using high resolution X-ray diffraction data. Residual density maps indicate some features in B–B interatomic region which cannot be properly described by the multipole model. Nevertheless, all theoretically obtained critical points are experimentally reproduced except for a ring and a cage critical point. No sign of directed V–V bonding is found. Discrepancies are observed especially by comparison of some bcp descriptors concerning the higher derivatives of ED. Theoretically determined ED Laplacian distributions along the B–B bond paths indicate that the boron valence shell is less pronounced in comparison that found according to the experiment. The ED properties at the B–V bcp indicate a polar covalent interaction between vanadium and boron. This result is supported by the participation of  $3d$  orbitals at B–V bonding evidenced by the structured penultimate shell of both vanadium atoms according the ED Laplacian. It has been approved that the metal interacts with borons not only in the same but also from neighbouring trigonal prism units. Finally, topological analysis indicates a charge transfer from vanadium atoms to borons.



## 8 ON SIMILARITIES AND DIFFERENCES BETWEEN THE ELECTRONIC STRUCTURES OF $\text{TiB}_2$ , $\text{VB}_2$ , $\text{VB}$ AND $\text{V}_3\text{B}_4$

In this Chapter, the electron density properties of the resembling fragments in  $\text{TiB}_2$ ,  $\text{VB}_2$ ,  $\text{VB}$  and  $\text{V}_3\text{B}_4$  are compared. For the identification of the resembling fragments, the B–B and the B–M interactions in addition to net charges of the atomic basins are analysed.

### 8.1 The B–B interaction

The ED Laplacian indicates a significant charge concentration in the B–B interatomic regions which is typical for covalent bonds as shown in the structurally relevant planes of  $\text{TiB}_2$ ,  $\text{VB}_2$ ,  $\text{VB}$  and  $\text{V}_3\text{B}_4$  (Figure 8.1).

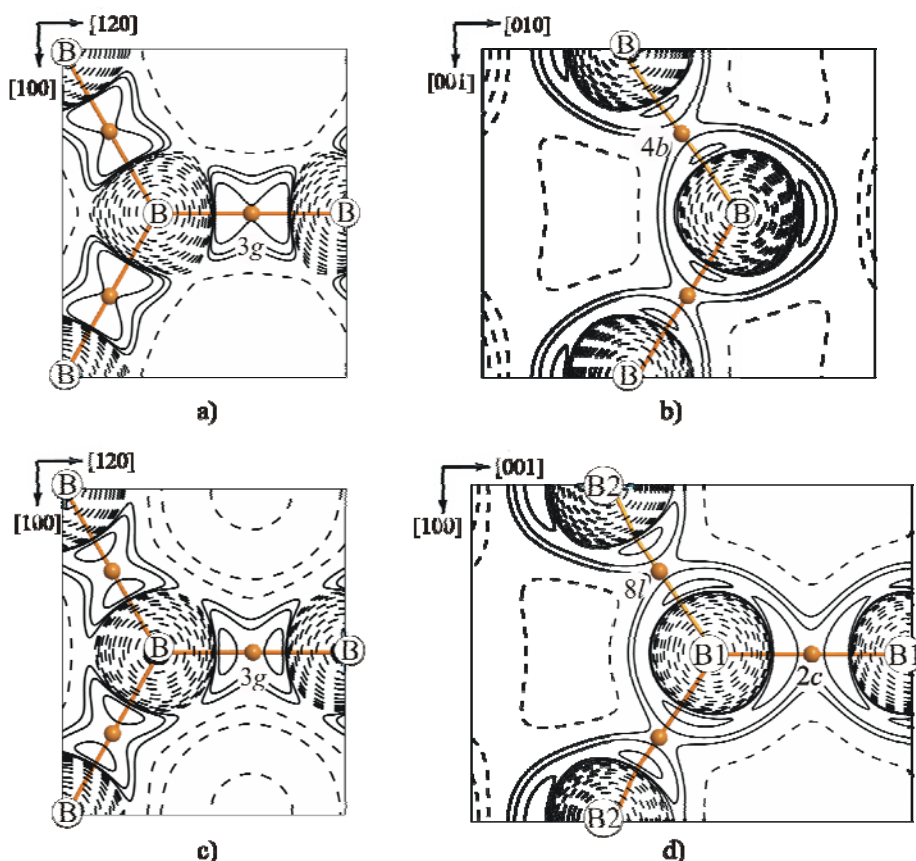


**Figure 8.1** Contour maps of experimentally reconstructed ED Laplacian together with the bond paths in structurally relevant B-atom planes of  $\text{TiB}_2$  (a),  $\text{VB}$  (b),  $\text{VB}_2$  (c) and  $\text{V}_3\text{B}_4$  (d). Negative contour levels are drawn at  $-1, -2, -4 \text{ e } \text{\AA}^{-5}$ ; positive levels at  $1, 2 \times 10^n, 4 \times 10^n, 8 \times 10^n \text{ e } \text{\AA}^{-5}$ , where  $n = 3, 2, 1, 0$ . Positive and negative values are marked by solid and dashed lines, respectively. The bond critical points are denoted by closed circles.

As discussed in Chapter 3 there are two distinct B–B distances in  $\text{V}_3\text{B}_4$  structure. The first one (B1–B2) which is a part of the zig-zag chain and extends along  $[100]$ , is similar to that in  $\text{VB}$ ; the other one (B2–B2) which links both chains resembles that in  $\text{VB}_2$ . A closer inspection of the associated B–B interactions via charge density analysis reveals that the ED values at the B–B bcps reflect these variations (Table 8.1). In general, the magnitudes of  $\rho(r_b)$  and  $\nabla^2\rho(r_b)$  at B–B bcps are increasing with the decrease of B–B distances. Accordingly, in  $\text{V}_3\text{B}_4$  structure, both experimental and theoretical  $\rho(r_b)$  between B1–B2 at the  $8(l)$  position (resembling more that in  $\text{VB}$ ) is less than  $\rho(r_b)$  between B1–B1 at the  $2(c)$  position (resembling more that in  $\text{VB}_2$ ). The most considerable disagreement between experiment and theory is due to  $\rho(r_b)$  of the latter bcp in  $\text{V}_3\text{B}_4$  for which experiment suggests a higher value than theory. Taking into account that the B1–B1 distance of *ca.*1.734 Å in  $\text{V}_3\text{B}_4$  is slightly larger as compared to the B–B distance of *ca.*1.731 Å in  $\text{VB}_2$ , experimental  $\rho(r_b)$  at the B1–B1 bcp is presumably overestimated.

**Table 8.1** Experimentally and theoretically determined B–B bcp properties in  $\text{VB}_2$ ,  $\text{VB}$  and  $\text{V}_3\text{B}_4$ . Wyckoff notations and the positions of the B–B bcps are also given.  $d(\text{B–B})$  is the B–B interatomic distance whereas  $d(\text{B–bcp})$  is the distance between the respective boron atoms and the bcp. The ellipticity of the bonds is given by  $\varepsilon = \lambda_1 / \lambda_2 - 1$  where  $\lambda_1$  and  $\lambda_2$  are the negative principle curvatures of the ED at bcp.  $|\lambda_1| / \lambda_3$  is the ratio of the magnitude of the smallest negative principle curvature and the positive principle curvature at bond critical point. Note that a bcp at  $2(c)$  position in  $\text{TiB}_2$  is not reproduced by experiment.

Bond		$d(\text{B–B})$ (Å)	$d(\text{B–bcp})$ (Å)	$\rho(r_{\text{cp}})$ (e Å <sup>-3</sup> )	$\nabla^2\rho(r_{\text{cp}})$ (e Å <sup>-5</sup> )	$\varepsilon(r_{\text{cp}})$	$ \lambda_1  / \lambda_3$
B–B in VB,	exp.	1.7933(6)	0.897, 0.897	0.748	-1.341	0.149	0.789
4b, (0.5, 0.0, 0.5)	theory			0.740	-2.750	0.176	1.457
B1–B2 in $\text{V}_3\text{B}_4$ ,	exp.	1.7942(3)	0.926, 0.839	0.752	-0.691	0.114	0.634
8l, (0.5, 0.25, 0.11)	theory			0.785	-3.535	0.162	1.788
B1–B1 in $\text{V}_3\text{B}_4$ ,	exp.	1.7341(6)	0.869, 0.869	0.904	-3.000	0.132	1.021
2c, (0.5, 0.5, 0)	theory			0.814	-4.118	0.098	2.001
B–B in $\text{VB}_2$ ,	exp.	1.7307(2)	0.865, 0.865	0.812	-3.098	0.731	1.578
3g, (0.5, 0.5, 0.5)	theory			0.831	-4.48	0.131	2.237
B–B in $\text{TiB}_2$ ,	exp.	1.7499(2)	0.875, 0.875	0.847	-4.196	0.519	1.796
3g, (0.5, 0.5, 0.5)	theory			0.817	-4.405	0.155	2.137
B–B in $\text{TiB}_2$ ,	theory	3.0309(2)	1.515, 1.515	0.197	0.641	0	0
2c, (0.33, 0.66, 0)							

Experimental  $\rho(r_b)$  for B–B at 3g position in  $\text{TiB}_2$  is slightly larger than the corresponding  $\rho(r_b)$  in  $\text{VB}_2$  whereas the opposite situation is valid for theory. The ED values at the B–B bcp in  $\text{VB}_2$  and  $\text{TiB}_2$  are very close to that reported for  $\text{Mg}_{1-x}\text{B}_2$  ( $\sim 0.8 \text{ e } \text{\AA}^{-3}$ ).<sup>[21f]</sup> These compounds show very slight changes in the B–B interatomic distances similar to those observed between  $\text{VB}_2$ ,  $\text{VB}$  and  $\text{V}_3\text{B}_4$ . In order to distinguish between the topological properties of the respective B–B interactions, examination of higher derivatives of ED is necessary, the accuracy of which depends both on the data quality as well as the flexibility of deformation radial density functions used in the multipole model.

The variation between theoretically and experimentally derived bonding descriptors based on higher derivatives of the ED is larger. Nevertheless, some trends can still be observed. For example, experimentally calculated  $|\lambda_1| / \lambda_3$  ratios which are generally smaller than the theoretical ones, reveal that the concentration of the ED along the bond path towards borons is more pronounced for B1–B2 than for B1–B1 in  $\text{V}_3\text{B}_4$  ( $|\lambda_1| / \lambda_3$  for B1–B2 is smaller than for B1–B1). A comparison between the same bcp descriptors for the resembling B–B interactions in  $\text{VB}$  and  $\text{VB}_2$  reveal a similar trend ( $|\lambda_1| / \lambda_3$  for B–B in  $\text{VB}$  is smaller than that of  $\text{VB}_2$ ). Ellipticity values in  $\text{VB}$  and  $\text{V}_3\text{B}_4$  cannot be distinguished clearly due to very small variation (0.098-0.176). In case of  $\text{VB}_2$  and  $\text{TiB}_2$ , experimentally obtained ellipticity values are considerably higher in comparison to theory. The experimental ellipticity value for B–B bcp in  $\text{VB}_2$  ( $\varepsilon = 0.73$ ) is larger than that in  $\text{TiB}_2$  ( $\varepsilon = 0.52$ ) whereas the opposite situation is valid for theory.

Both experimental as well as theoretical ED values of the B–B bcps obtained in the present work are considerably larger than those reported by Will<sup>[122b]</sup> and Hegenscheidt<sup>[148]</sup> in  $\text{TiB}_2$  ( $\sim 0.2 \text{ e } \text{\AA}^{-3}$ ). It has to be noted that in those works the quantitative analysis is based not on the ED itself but the deformation ED the interpretation of which depend crucially on the reference state. Both authors confirmed a significant concentration of the ED in B–B bond and concluded that boron atoms have a covalent interaction within the boron network.

The magnitudes of  $\rho(r_b)$  for B–B bcps found in this work are close to that reported for some two-center intracluster B–B bcps (0.78-0.95  $\text{e } \text{\AA}^{-3}$ ) in  $\alpha$ -boron as well as in the more recently discovered high pressure  $\gamma$ - $\text{B}_{28}$  modification of boron.<sup>[149]</sup> For the latter the ED at the respective bcp is significantly smaller than those at other two-center B–B bonds which are varying between 1.13-1.19  $\text{e } \text{\AA}^{-3}$ . The authors concluded that the former has to be a 1e-

2c bond in order to balance the electrons according to Wade's rule. Simple electron counting rules allow distinguishing between 1e-2c, 2e-2c and 2e-3c bonds in boron modifications since they are predominantly covalent in nature which is evidenced by the negative sign of  $\nabla^2\rho(r_{\text{cp}})$ . Such a comparison cannot be carried out for intermetallic borides straightforwardly since there are substantial differences between the topological properties of B–B bcps and other cps in these compounds. In general, the ring and cage critical points are characterized with small positive Laplacian and considerably small ED values. Furthermore, the ED is distributed over a wide ring and cage surfaces. Additional topological property of these ring and cage critical points is negative  $H(r)$ , besides the ratio  $G(r_b) / \rho(r_b)$  is less than unity as also observed by B–V bcp.

## 8.2 Transition metal-boron interactions

Topological analysis indicated that the B–V bcps in  $\text{VB}$  and  $\text{VB}_2$  are reproduced in the analogous interatomic regions of  $\text{V}_3\text{B}_4$  (Figure 8.2). Additional B–V bcps found in the resembling B–V interatomic regions of  $\text{VB}$  and  $\text{V}_3\text{B}_4$  confirm that transition metals form bonds with boron not only within the same trigonal prism unit but also between neighbouring trigonal prism formations. Consequently, boron atoms are shifted from the center of the trigonal prism towards to vanadium atoms in the neighbouring layer. This explains smaller B–B angles in  $\text{VB}$  and  $\text{V}_3\text{B}_4$  with respect to  $\text{VB}_2$  as discussed in Chapter 3.

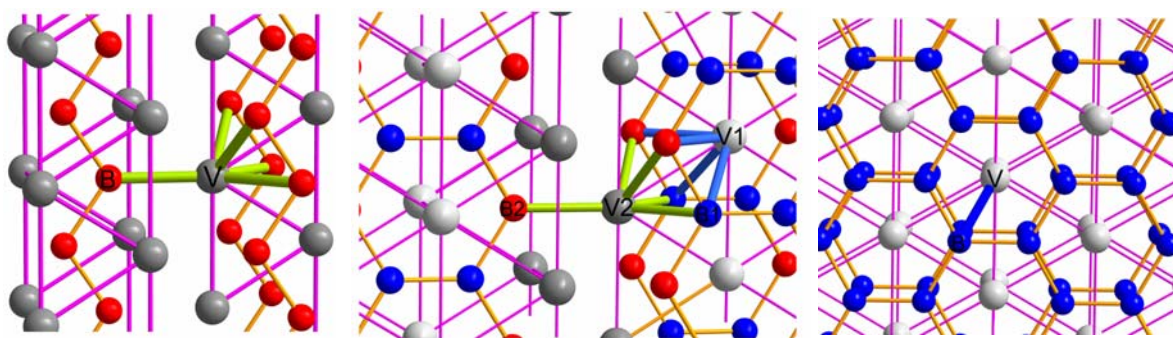


**Figure 8.2**  $\text{VB}$ ,  $\text{V}_3\text{B}_4$  and  $\text{VB}_2$  structures. The thick green and blue lines are symbolizing B–V interactions according to bcp analysis whereas the trigonal prism units are drawn in pink.

The DD maps in Figure 8.3 show coincident features of  $\text{V}_3\text{B}_4$  and  $\text{VB}$  structures in the metal environment. A similar comparison of the analogous regions between  $\text{V}_3\text{B}_4$  and  $\text{VB}_2$  reveal that the density in the vicinity of the core is almost featureless.

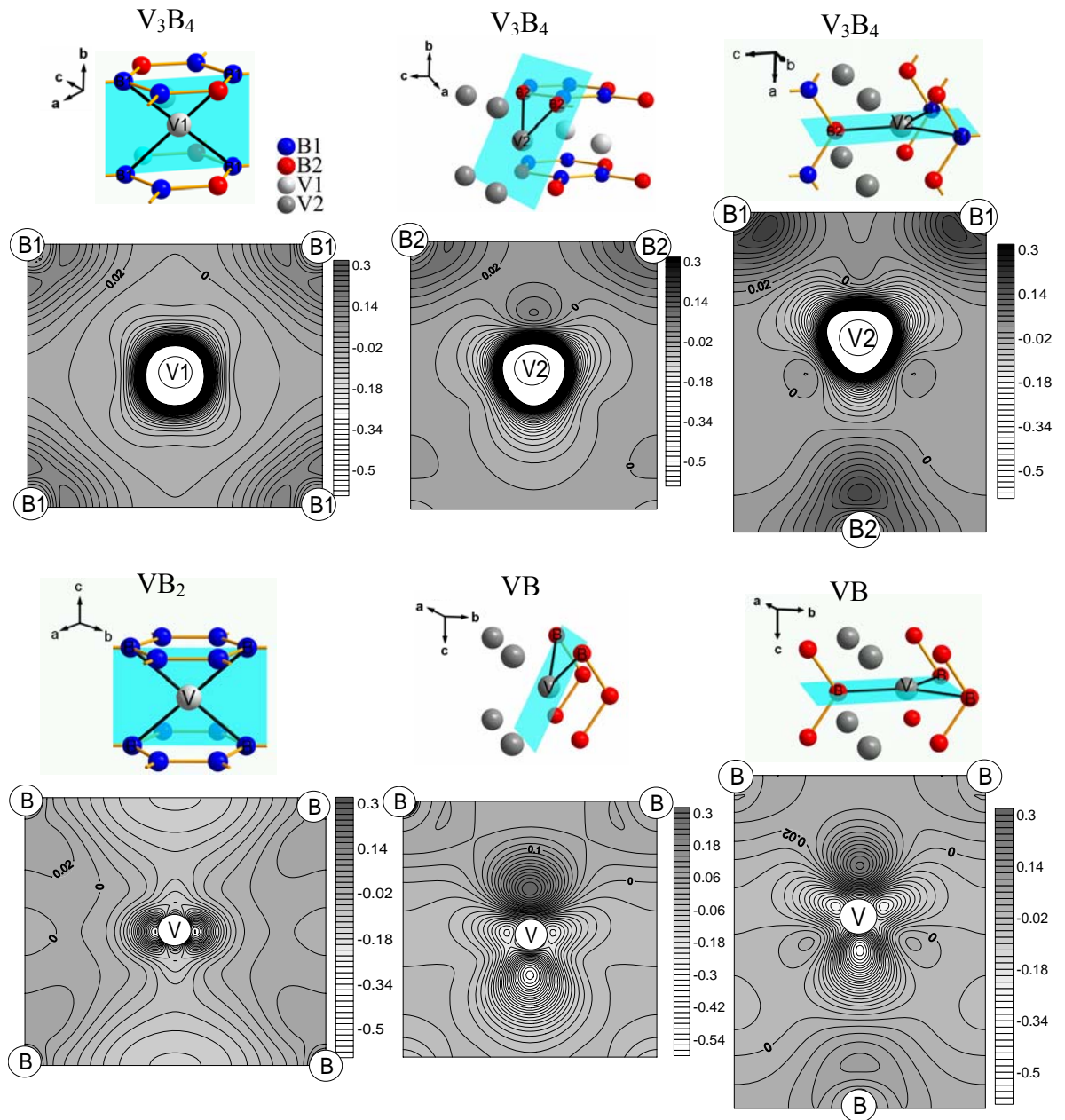


**Figure 8.3** Deformation electron densities in  $\text{V}_3\text{B}_4$ ,  $\text{VB}_2$  and  $\text{VB}$  in the structurally relevant planes. The isoline interval is  $0.02 \text{ a.u.}^{-3}$ .

All transition metal-boron (B–M) bcps in  $\text{TiB}_2$ ,  $\text{VB}_2$ ,  $\text{VB}$  and  $\text{V}_3\text{B}_4$  are characterized by low value for  $\rho(r_b)$  and small positive value for  $\nabla^2\rho(r_b)$  as shown in Table 8.2. The sign of the Laplacian is not informative about the bonding situation of transition metals. The B–V bonds can be assumed to have some degree of covalent nature evidenced by the magnitudes of  $\nabla^2\rho(r_b)$  which are considerably smaller in comparison to those of strong ionic bonds ( $\nabla^2\rho(r_b) \gg 0$ ). Furthermore, the bcps are slightly shifted to the respective boron at-

oms. The position of the bcp away from the midpoint of the respective bond paths may indicate the polarity of the bond.

Additional properties of the B–M bcps in TiB<sub>2</sub>, VB<sub>2</sub>, VB and V<sub>3</sub>B<sub>4</sub> derived from the experimental ED are small negative value for local energy density  $H(r_b)$ , besides the  $G(r_b) / \rho(r_b)$  is less than unity. These topological indexes also support that the B–M interaction is of covalent nature. Similar bond critical point properties are observed for carbon metal interactions in cyclopentadienyl complexes of Ge, Al<sup>+</sup> and Fe by Bader *et al.* for which the ED is distributed over a wide range between the metal atom and five membered carbon atom rings.<sup>[150]</sup>

**Table 8.2** Some selected topological properties of B–V interactions in VB<sub>2</sub>, VB and V<sub>3</sub>B<sub>4</sub>.  $d(B-V)$  is the B–V interatomic distance whereas  $d(bcp)$  is the distance between the B–V bcp and the B–V interatomic line. Wyckoff notation and the position of the B–V bcp are also given.

Bond	d(B–M) (Å)	d(bcp) (Å)		$\rho(r_b)$ (e Å <sup>-3</sup> )		$\nabla^2 \rho(r_b)$ (e Å <sup>-5</sup> )	
		exp.	theory	exp.	theory	exp.	theory
TiB <sub>2</sub>							
B–Ti, 12 <i>o</i> (0.18, 0.35, 0.24)	2.3812(2)	0.052	0	0.323	0.334	2.672	2.487
VB <sub>2</sub>							
B–V, 12 <i>o</i> (0.82, 0.18, 0.24)	2.3087(2)	0.059	0.063	0.364	0.393	2.953	2.299
VB							
B–V, 16 <i>h</i> (0.24, -0.09, 0.49)	2.2413(2)	0.155	0.130	0.431	0.433	2.855	2.133
B–V, 8 <i>g</i> (0.24, -0.03, 0.25)	2.2795(4)	0.063	0.049	0.405	0.408	3.417	2.497
B–V, 4 <i>c</i> (0, -0.29, 0.75)	2.3358(5)	0	0	0.303	0.378	3.430	2.289
V <sub>3</sub> B <sub>4</sub>							
B2–V2, 8 <i>m</i> (0.26, 0, 0.37)	2.1964(4)	0	0	0.436	0.447	4.423	2.487
B1–V2, 16 <i>o</i> (0.27, 0.29, 0.15)	2.2407(3)	0.244	0.195	0.402	0.437	3.605	2.265
B1–V1 in V <sub>3</sub> B <sub>4</sub> , 16 <i>o</i> (0.25, 0.25, 0.03)	2.3057(3)	0.025	0.056	0.376	0.391	3.558	2.248
B2–V2 in V <sub>3</sub> B <sub>4</sub> , 4 <i>j</i> (0.5, 0, 0.23)	2.3286(5)	0	0	0.363	0.382	2.878	2.273
B2–V1 in V <sub>3</sub> B <sub>4</sub> , 8 <i>m</i> (0.25, 0, 0.07)	2.3406(4)	0	0	0.381	0.363	2.925	2.234

The properties of B–M bcp reveal that in case of the examined compounds, for the density itself the theory predicts larger values whereas experimentally obtained Laplacian



values are larger in comparison to theory. For polar bonds of main group elements, in particular, similar systematic deviations in the topological properties of ED at the bcp are reported between theory and experiment.<sup>[19, 151]</sup> This effect can be attributed to insufficient flexibility of the radial functions used in the multipole model which cannot account for fine details of ED. For all multipoles of a given  $l$ , the same set of Slater-type radial functions are used which maxima is controlled by both the parameter  $n_l$  and the single Slater exponent  $\zeta_l$ . The starting values of these parameters are modified by a single optimized  $\kappa'$  parameter. The increase in the number of variables used for the radial functions would doubtlessly provide a more flexible model but also increase the correlations between the parameters refined.

A comparison between theory and experiment indicates that the deviations of the B–M bcp values in TiB<sub>2</sub>, VB<sub>2</sub>, VB and V<sub>3</sub>B<sub>4</sub> are varying in the range of  $\pm 0.075 \text{ e } \text{\AA}^{-3}$  for  $\rho(r_b)$  and  $\pm 1.936 \text{ e } \text{\AA}^{-5}$  for  $\nabla^2\rho(r_b)$ , respectively. This kind of spread would normally indicate a high degree of transferability for the respective bond-topological properties of light atom molecules but not for the present case. The reason is that light-atom molecules are generally characterized by high and clearly distinguished ED values at bond critical points as well as other bonding descriptors with a very broad spectrum. On the other hand, B–M bonds exhibit very similar bcp properties indicated by  $\rho(r_b)$  and  $\nabla^2\rho(r_b)$  values, in spite of being in different environments, as generally observed for transition metal bonding.<sup>[80]</sup> Therefore, additional criteria are necessary in order to distinguish between different B–M bonds.

As is evident from Figure 8.4, all of the B–V bond paths in the structurally relevant planes of VB<sub>2</sub>, VB and V<sub>3</sub>B<sub>4</sub> are inwardly curved with respect to the interatomic lines forming the three-membered ring except for the bond path in VB<sub>2</sub> which is outwardly curved. Table 8.2 shows the shifts of the bond critical point from the B–V interatomic line for quantification of bond bending. The so-called strained bonds usually cause the internuclear distances to appear shorter than normal. Obviously, such a correlation exists for B–V bonds in VB but not explicitly in V<sub>3</sub>B<sub>4</sub> according to both experiment and theory. A close inspection of B–V bond path topology in VB<sub>2</sub>, VB and V<sub>3</sub>B<sub>4</sub> reveals that the bcp shifts allow a differentiation between several B–V interactions which can hardly be distinguished due to very similar  $\rho(r_b)$ . For example, as also observed by the B–B distances, V<sub>3</sub>B<sub>4</sub> have two distinct B–V distances (2.241 Å and 2.307 Å, respectively) resembling either that in

$\text{VB}$  (2.241 Å) or that in  $\text{VB}_2$  (2.309 Å). An analogous situation can be found for the associated bcp shifts. The distance between the B–V interatomic line and the respective bcp at  $16h$  position in  $\text{VB}$  ( $d(\text{bcp}) = 0.155$  Å) is comparable to the distance between the B2–V2 interatomic line and the B2–V2 bcp at  $16o$  position in  $\text{V}_3\text{B}_4$  ( $d(\text{bcp}) = 0.244$  Å). A similar situation can be found for the B–V bcp shifts in the structurally relevant planes of  $\text{VB}_2$  and  $\text{V}_3\text{B}_4$  in which the bending of the respective B–V bond paths are relatively less pronounced. It has to be also mentioned that these bond paths are curved in opposite directions. Nevertheless, for all other B–V interactions, it is not possible to find such a good agreement together for the interatomic distances, bcp shifts and  $\rho(r_b)$ . As a result, topological analysis of ED allows identification of two different types of B–V interactions in  $\text{V}_3\text{B}_4$ : one resembles more that in  $\text{VB}$ ; the other one more that in  $\text{VB}_2$  despite some slight qualitative as well as quantitative differences in the associated topological properties of ED.

In case of  $\text{TiB}_2$ , experimental results, unlike the theory, indicate that the B–Ti bond is slightly bent as evidenced by the distance between the B–Ti bcp and the B–Ti interatomic line (0.052 Å). However, both methods are in agreement in terms of ED value at B–Ti bcp which is smaller in comparison to that found in  $\text{VB}_2$ . This result correlates with the respective B–M interatomic distances  $d(\text{B–M})$  in these compounds (Table 8.2). There is an inverse relationship between  $d(\text{B–M})$  and  $\rho(r_b)$  at B–M bcp.

In  $\text{VB}_2$ ,  $\text{VB}$  and  $\text{V}_3\text{B}_4$ , there are some ring critical points (rcp) located on the three-membered ring surfaces that result from the formation of B–B and B–V bond paths (Figure 8.4). The quantitative differences between these associated bcps and rcps are generally small considering the ED value as reported in the previous Chapters. Furthermore, one of the principle curvatures of the ED  $\lambda_2$ , is of relatively smaller magnitude for both cp types. Similarities between the topological properties of ED at these bond and ring critical points suggest that the density is smeared over a wide range of the ring surface. These bonding situation presumably differs from that exists in the ring surfaces of electron-deficient boranes which are characterized by comparable ED values at rcp and bcp together with negative  $\nabla^2\rho(r)$  at rcp.<sup>[152]</sup> The reason is that for vanadium borides the Laplacian is only negative at the B–B bcp. Accordingly, the ED is predominantly accumulated in the B–B interatomic region.

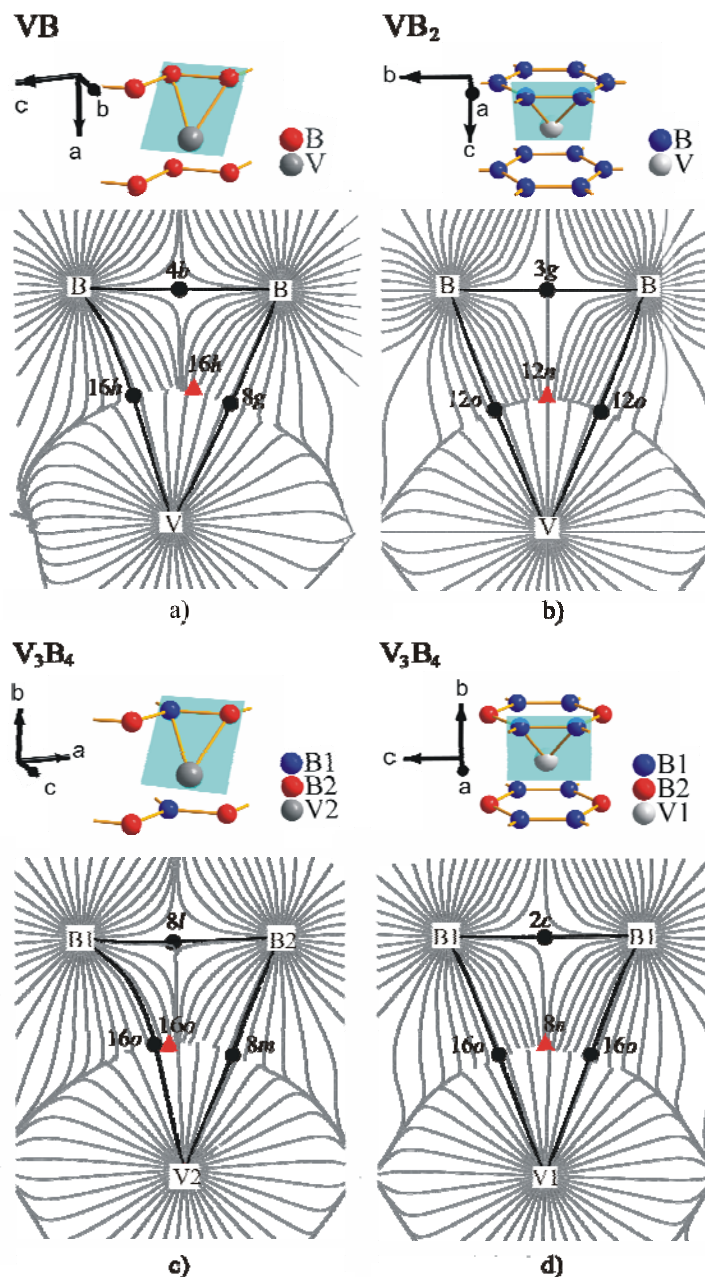


**Figure 8.4** Gradient field of the experimentally reconstructed ED of VB (a),  $\text{VB}_2$  (b) and  $\text{V}_3\text{B}_4$  (c) and (d) in structurally relevant planes containing the three-membered ring surfaces. Black circles and red triangles are attributed to bcps and rcps, respectively whereas the black solid lines are the bond paths. The B–V bond path in VB and the B1–V2 bond path in  $\text{V}_3\text{B}_4$  are relatively more curved. Note the proximity of the rcp at  $16o$  position to the strongly curved B1–V2 bond path (c). The rcp at  $16h$  position in VB is shifted to the bond path curved to a lesser extent. The rcps (b) and (d) are located at equal distances to the B–V bond paths due to symmetry restrictions for the atomic sites involved.

Topological analysis of the structurally relevant ring surfaces in  $\text{VB}_2$ , VB and  $\text{V}_3\text{B}_4$ , reveals slight differences in the morphology of the charge distribution (Figure 8.4). In VB,

the rcp is shifted slightly to the bond path curved to a lesser extent whereas in  $\text{V}_3\text{B}_4$ , the rcp at 16(o) position is located relatively close to the strongly curved bond path. As shown in the structurally relevant planes of  $\text{VB}_2$  and  $\text{V}_3\text{B}_4$ , the rcp has equal distances to the B–V bond paths due to the symmetry restrictions for the atomic sites involved. Owing to the strongly curved B1–V2 bond path in  $\text{V}_3\text{B}_4$ , bond and ring critical point are located in immediate proximity to each other. Similar situation is observed for the B–M bond path in  $\text{Mg}_{1-x}\text{B}_2$  for which the bcp shift from boron-metal interatomic line is found to be  $d(\text{bcp}) = 0.21 \text{ \AA}$ .<sup>[21f]</sup> It is worth to mention that in  $\text{Mg}_{1-x}\text{B}_2$  the magnitude of the smallest principle curvature of the ED,  $|\lambda_2|$ , is  $0.01 \text{ e \AA}^{-5}$  at the respective bcp and rcp. On the other hand, according to both experiment and theory,  $|\lambda_2|$  is relatively large for the relevant critical points in  $\text{VB}_2$ ,  $\text{VB}$  and  $\text{V}_3\text{B}_4$  varying in the range of  $0.1\text{--}0.2 \text{ e \AA}^{-5}$ ,  $0.1\text{--}0.3 \text{ e \AA}^{-5}$  and  $0.1\text{--}0.3 \text{ e \AA}^{-5}$ , respectively. In general, for nuclear motions that result in migration of a critical point along an axis associated with relatively small curvatures of the ED, less energy is sufficient.<sup>[17]</sup> In a ring structure, such a motion leads to coalescence of the bond and ring critical point thereby first breaking of the respective bond and opening the ring structure. Topological properties of the associated ring and bond critical points indicate that more energy is required in order to open the respective ring structure in  $\text{VB}_2$  as compared to that for  $\text{Mg}_{1-x}\text{B}_2$ . This result is in line with the respective cohesive energies,  $E_{\text{coh}}$  which is a measure of the stability of a system relative to that of noninteracting atoms. The maximum  $E_{\text{coh}}$  values were reported for group IV and Vd-metal diborides *i.e.* for  $\text{VB}_2$  and  $\text{TiB}_2$  while the minimum  $E_{\text{coh}}$  was obtained for  $\text{Mg}_{1-x}\text{B}_2$ .<sup>[47]</sup>

The ED Laplacian unravels the most remarkable difference between  $\text{TiB}_2$  and  $\text{VB}_2$  structures. The penultimate shell of vanadium is distorted into a non-spherical shape in contrary to titanium which is non-structurized (Figure 8.5). Both theoretically as well as experimentally derived topologies of  $\nabla^2\rho(\mathbf{r})$  in  $\text{VB}$ ,  $\text{V}_3\text{B}_4$  and  $\text{VB}_2$  reveal distortion in the penultimate shell of vanadium atoms. Both methods show a very good agreement for  $\text{VB}_2$  and  $\text{TiB}_2$  whereas discrepancies are observed in  $\text{VB}$  and  $\text{V}_3\text{B}_4$  due to the location of charge concentrations. Notwithstanding these differences, both experimental and theoretical calculations reveal that the topology of the penultimate shell of V in  $\text{VB}$  and V2 in  $\text{V}_3\text{B}_4$  are coincident. On the other hand, a similar comparison between the penultimate shell of V in  $\text{VB}_2$  and V1 in  $\text{V}_3\text{B}_4$  indicated differences according to both methods.

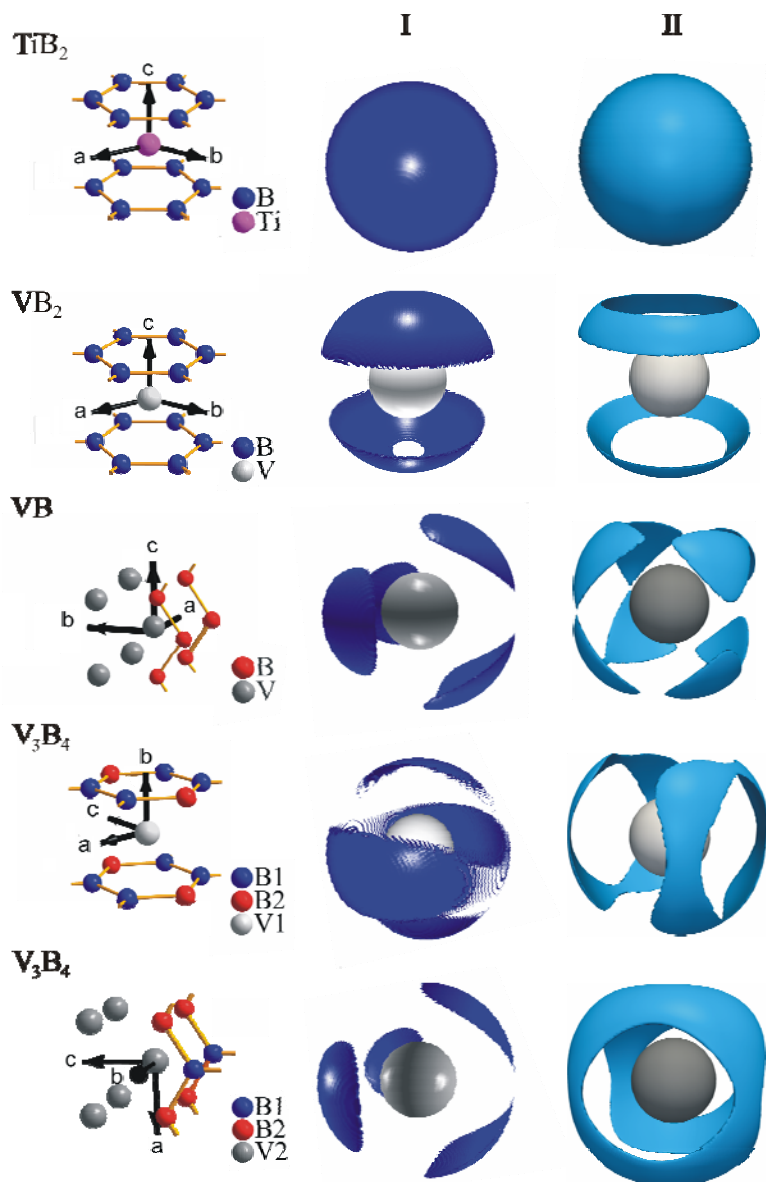


**Figure 8.5** Experimental (I) and theoretical (II) 3D representation of  $\nabla^2\rho(r)$  of the penultimate shell for transition metal atoms in the descending order in  $\text{TiB}_2$ ,  $\text{VB}_2$ ,  $\text{VB}$  and  $\text{V}_3\text{B}_4$ . The isosurface values in the same order: -200, -290, -288, -290 and -300  $\text{e} \text{ \AA}^{-5}$ , respectively.

Additional properties of the B–M bcps in  $\text{TiB}_2$ ,  $\text{VB}_2$ ,  $\text{VB}$  and  $\text{V}_3\text{B}_4$  derived from the experimental ED are small negative values for local energy density  $H(r_b)$ , besides the  $G(r_b)/\rho(r_b)$  is less than unity. These topological indexes indicate that B–M interaction is of covalent nature. Similar bcp properties are also observed for carbon metal interactions in cyclopentadienyl complexes of Ge,  $\text{Al}^+$  and Fe by Bader *et al.* for which the ED is distributed over a wide range between the metal atom and five membered carbon atom rings.<sup>[150]</sup>

### 8.3 Atomic electron populations

The electron populations are determined by the integration of the model ED over the atomic basins defined by the zero-flux surfaces as shown in Figure 8.6.

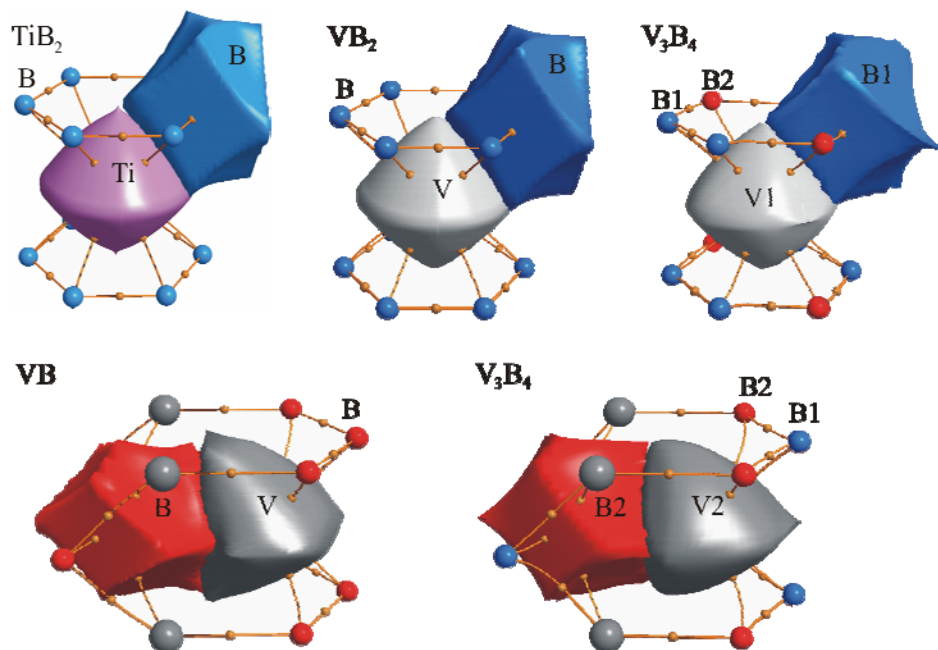


**Figure 8.6** Atomic basins in the electron density distribution in  $\text{TiB}_2$ ,  $\text{VB}$ ,  $\text{VB}_2$  and  $\text{V}_3\text{B}_4$  as determined from X-ray diffraction data. The B–B and B–V bond paths are also given. The bond critical points are denoted by small orange spheres.

The electrons transferred from metal to B-network in  $\text{TiB}_2$  are found slightly higher than that obtained in  $\text{VB}_2$  according to both theory and experiment (Table 8.3). Both the atomic volume and the electron population of the metal in  $\text{VB}_2$  are slightly less than in  $\text{VB}$ . The same trend is observed for the resembling metal atoms in  $\text{V}_3\text{B}_4$ . Theoretical calculations reveal that the electron populations of the boron atom in  $\text{VB}_2$  and the resembling B1 atom in  $\text{V}_3\text{B}_4$  are less than those of the boron atom in  $\text{VB}$  and the resembling B2 in  $\text{V}_3\text{B}_4$ . This result is not reproduced by experiment according to which the electron population of B1 in  $\text{V}_3\text{B}_4$  is overestimated. For all other boron atoms experimentally obtained electron populations are less in comparison to those from theory. This necessitates a further examination of the multipole model on the charges in QTAIM.

**Table 8.3** Atomic volumes ( $\text{\AA}^3$ ) and electron populations ( $\bar{N}$ ) in TiB<sub>2</sub>, VB<sub>2</sub>, VB and V<sub>3</sub>B<sub>4</sub>.

		V(M) ( $\text{\AA}^3$ )	V(B) ( $\text{\AA}^3$ )	$\bar{N}$ (M)	$\bar{N}$ (B)	$\bar{N}$ in the unit cell
TiB <sub>2</sub>	exp.	9.27	8.21	20.88	5.56	32.00
	theory	8.81	8.42	20.64	5.68	32.00
VB <sub>2</sub>	exp.	8.72	7.52	21.97	5.52	33.00
	theory	8.56	7.60	21.85	5.57	32.99
VB	exp.	9.76	8.55	22.20	5.79	111.98
	theory	9.52	8.80	22.08	5.92	112.00
V <sub>3</sub> B <sub>4</sub>	exp.	8.36(V1)	7.97(B1)	21.72(V1)	6.10(B1)	177.96
		9.60(V2)	8.41(B2)	21.78(V2)	5.75(B2)	
	theory	8.57(V1)	7.70(B1)	21.85(V1)	5.67(B1)	178.00
		9.50(V2)	8.69(B2)	22.08(V2)	5.82(B2)	

## 8.4 Summary

The electronic structure in  $\text{TiB}_2$ ,  $\text{VB}$ ,  $\text{VB}_2$  and  $\text{V}_3\text{B}_4$  can be characterized by a charge transfer from the metal to boron together with two predominant atomic interactions. These are the typical shared type B–B and the polar covalent B–V interactions. Topological analysis yields not any significant interaction between the metal atoms. The basic assumption of the Zintl-Klemm concept which is the fulfilling of the octet rule by a full formal transfer of the valence electrons from the electropositive to the electronegative component is not valid for  $\text{TiB}_2$ ,  $\text{VB}$ ,  $\text{VB}_2$  and  $\text{V}_3\text{B}_4$  due to the covalency of the B–V bond.

The participation of  $3d$  orbitals in B–V bonding is evidenced by the structurized penultimate shell of the metal according to ED Laplacian despite some discrepancies observed between experiment and theory which needs further investigation. The density Laplacian unraveled the most remarkable difference between  $\text{VB}_2$  and  $\text{TiB}_2$  structures where for the latter the penultimate shell of the metal is not distorted. Considering the physical properties of these materials such as extreme hardness appreciable directed bonding is expected not only between the boron atoms but also for the transition metal boron interaction for all compounds investigated. The topological properties of the B–M interactions in the present work, on the other hand, do not clearly indicate such a bonding situation. Obviously, the topological analysis is successful for the characterization of homoatomic boron interactions but not sufficient to explain existing forces originating from the interaction with the transition metal bonding.

Topological properties of ED concerning the B–B and B–V interactions are compared for  $\text{TiB}_2$ ,  $\text{VB}$ ,  $\text{VB}_2$  and  $\text{V}_3\text{B}_4$  structures using both experimentally reconstructed ED and theoretical calculations. In general, the magnitudes of the B–B  $\rho(r_b)$  and  $\nabla\rho(r_b)$  have an inverse relationship with the B–B distances. The small spread of ED values at B–M bcp complicates the differentiation between several fragments. Nevertheless, slight differences in B–M interactions left traces in the respective bond paths exhibiting different degree of bending. These slight differences may originate from a change in the electronic structure of the neighbouring atoms but also from experimental error. As a result, the resembling bond properties of the examined compounds cannot be treated as equivalent. Accordingly, they are not transferable in terms of multipole populations.



## CONCLUSIONS AND OUTLOOK

In this thesis, the electron density in  $\text{TiB}_2$ ,  $\text{VB}_2$ ,  $\text{VB}$  and  $\text{V}_3\text{B}_4$  is successfully reconstructed from single crystal X-ray diffraction intensities applying Hansen & Coppens multipole model. The topological aspects of the experimental ED features are analysed in terms of Bader's Quantum Theory of Atoms in Molecules (QTAIM)<sup>[17]</sup> and compared with those obtained from quantum chemical calculations.

The crystals being subject to a charge density analysis are synthesized using both Al flux technique as well as arc-melting. In case of  $\text{TiB}_2$ ,  $\text{VB}_2$  and  $\text{VB}$ , X-ray powder diffraction experiments ensure that there is not any significant change of lattice parameters, thus any significant variation of composition also supported by WDXS. On the other hand, WDXS indicates small variations from the ideal stoichiometry for other vanadium borides which are increased along the series  $\text{V}_3\text{B}_4$ - $\text{V}_2\text{B}_3$ - $\text{V}_5\text{B}_6$ . The determination of the respective accurate lattice parameters are mostly hampered by the overlapping X-ray powder diffraction lines of both additional vanadium borides as well as some other by-products.

The diffraction limits of the crystals investigated are varying in the range of  $(\sin \theta / \lambda) = 1.67$ - $1.72$ . The reliability factors  $R_{\text{(F)}}$ , in case of IAM refinements of the examined structures, generally increase with the number of reflections collected but never exceed 2%. A reliability factor smaller than 1% is achieved for  $\text{VB}_2$  referring to all observations. At the very high resolution of the data set the disagreement between the observed and calculated structure factors becomes pronounced in case of all vanadium borides investigated. The use of both very small single crystals ( $20$ - $50 \mu\text{m}$ ) as well as Ag radiation for the X-ray diffraction measurement remarkably reduces extinction or absorption effects. The reflections of  $\text{TiB}_2$  crystal are almost not extinction-affected.

The crystal structures of  $\text{TiB}_2$ ,  $\text{VB}_2$ ,  $\text{VB}$ ,  $\text{V}_2\text{B}_3$  and  $\text{V}_3\text{B}_4$  are reinvestigated and compared on base of spherical refinement. The similarities and differences between the atomic arrangements of different vanadium borides are well reflected in B-B distances and angles. The crystallographic analyses reveal that B-B distances decrease slightly with increasing boron content in the structure.

The use of multipole model provides a better agreement between the observed and calculated structure factors which is well reflected in the residual densities for all structures

investigated. Close to featureless residuals are obtained particularly in the B–B interatomic region for  $\text{TiB}_2$  and  $\text{VB}_2$  whereas the maximum value of residuals increases along with VB and  $\text{V}_3\text{B}_4$ .

Anharmonic description of the ADPs up to the fourth tensor drops the  $R_{\text{(F)}}$  value for only metal atom for all compounds investigated. An important fact which renders the physical significance of the anharmonic motion doubtful is the very small anisotropic ADPs. Furthermore, for the model refinements of all structures which include only anisotropic description of atomic displacement, the respective residual densities does not reveal any characteristic sign reflecting the absence of anharmonic motion in the vicinity of the metal core. Accordingly, the improvement in the fit can be explained with the flexibility of the current model provided by the anharmonic displacement parameters which is able to represent systematic errors of the experimental data.

A comparison between theory and experiment reveal that the same number and type of critical points are obtained for  $\text{VB}_2$  but only minor quantitative differences in the ED at critical points  $\rho(r_{\text{cp}})$  are observed. A similar comparison indicates some disagreements in  $\text{TiB}_2$ , VB and  $\text{V}_3\text{B}_4$ , by positions of ring and cage critical points, in particular but all theoretically obtained bond critical points are reproduced in experiment except for one found between the boron layers (at  $2c$  position) in  $\text{TiB}_2$ . In case of all compounds examined, the variations of the experimentally and theoretically found ED values at the critical points are in the range of  $\pm 0.08 \text{ e } \text{\AA}^{-3}$  for  $\rho(r_{\text{b}})$ , and  $\pm 2.1 \text{ e } \text{\AA}^{-5}$  for  $\nabla^2\rho(r)$ , respectively. Further confidence in the results comes from the comparison between the EFG values at the boron nucleus derived from single crystal X-ray diffraction experiment,  $^{11}\text{B}$  NMR experiment and theoretical calculations for  $\text{TiB}_2$  and  $\text{VB}_2$ .

A close inspection of the density Laplacian distribution along B–B bond path indicates systematic differences between experiment and theory for all compounds studied. Furthermore, B–M bcp properties reveal that for the density itself the theory predicts larger values whereas experimental  $\nabla^2\rho(r)$  is larger in comparison to theory. Similar discrepancies are observed by the investigation of the atomic electron populations. These systematic deviations can be traced back on the inadequacy of the multipole model which is mostly criticized because of the inflexibility of the deformation radial density functions.

Both experimental and theoretical calculations confirm a model containing both B–B as well as B–M bonding interactions for  $\text{TiB}_2$ ,  $\text{VB}_2$ ,  $\text{VB}$  and  $\text{V}_3\text{B}_4$ . The corresponding bcp properties reveal that the former interaction is typical shared-type with significant  $\pi$ -density contribution whereas the B–M interactions are of polar covalent nature. In general, the topological analysis of ED according to QTAIM is more successful for the characterization of homoatomic boron interactions than the bonding situation where the transition metal is involved. Integration of the ED over the atomic basins reveals that there is a charge transfer from metal to boron for all compounds studied.

In general, the resembling features in the crystal structures of  $\text{TiB}_2$ ,  $\text{VB}$ ,  $\text{VB}_2$  and  $\text{V}_3\text{B}_4$  structures show correlations in their ED properties. Similarities between the boron sublattices of different vanadium borides are well reflected by the ED values at the respective bond critical points. The differentiation between several fragments containing the transition metal bonding is mostly difficult due to the small spread of ED values at B–M bcp. Nevertheless, these features provide some correlations in their bond paths exhibiting different degree of bending. In general, a good agreement is achieved between experimentally reconstructed ED and theoretical calculations but the variation is still comparable to the small spread of different atomic and bond properties of vanadium borides examined. Accordingly, the pseudoatomic density of the resembling features can not be treated as equivalent for a transferable model within the accuracy of the experiment

Based on the present results a charge density analysis for  $\text{V}_2\text{B}_3$  will be of crucial importance since this compound contains also independent metal and boron sites as  $\text{V}_3\text{B}_4$ , thus it offers additional features for detailed comparison. The density study shall explain if  $\text{V}_2\text{B}_3$  possesses similar building blocks with respect to  $\text{VB}$ ,  $\text{V}_3\text{B}_4$  and  $\text{VB}_2$ .

The most remarkable difference between B–M interaction in  $\text{VB}_2$  and  $\text{TiB}_2$  is that the penultimate shell of the Ti atom is not structurized in contrary to V atom. Taking into account the extreme hardness of both materials this result indicates that the density Laplacian is not sufficient for the characterization of the transition metal bonding. For unravelling the differences with respect to transition metal bonding other tools are necessary. For a development of a more general bonding model for intermetallic compounds with the crystal structure of  $\text{AlB}_2$  charge density analyses along the series  $\text{ScB}_2$ - $\text{TiB}_2$ - $\text{VB}_2$ - $\text{CrB}_2$ - $\text{MnB}_2$  have to be completed. The topological analysis of the ED is expected to indicate similarities or differences with respect to charge transfer from metal to the boron network. Furthermore,

the non-stoichiometry effect on the electronic structure for this class of compounds can be investigated by a charge density analysis of diborides of heavier group V *d* metals  $\text{Nb}_{1-x}\text{B}_2$  and  $\text{Ta}_{1-x}\text{B}_2$  ( $x = 0.01-0.5$ ).<sup>[153]</sup>

## REFERENCES

- [1] T. Lucretius Carus, R. Latham, *The nature of the universe*, Penguin Books ; Whitefriars Press, Harmondsworth ; London, **1951**.
- [2] W. Friedrich, P. Knipping, M. von Laue, Sitzungsberichte der math-phys. Klasse der k.-b. Akad. der Wissenschaften zu München, **1912**, 303-322.
- [3] W. H. Bragg, W. L. Bragg, *P. R. Soc. Lond. A-Conta.* **1913**, 88, 428-428.
- [4] P. Debye, *Ann.. Phys.(Berlin)* **1915**, 46, 809-823.
- [5] L. Pauling, *J. Am. Chem. Soc.* **1932**, 54, 988-1003
- [6] a) G.C. Verschoo, E. Keulen, *Acta Crystallogr. B* **1971**, B 27, 134-135; b) Y. Wang, R. H. Blessing, F. K. Ross, P. Coppens, *Acta Crystallogr. B* **1976**, 32, 572-578; c) P. Coppens, *Acta Crystallogr. B* **1974**, 30, 255-261; d) P. Coppens, A. Vos, *Acta Crystallogr. B* **1971**, 27, 146-158; e) T. Koritsanszky, R. Flaig, D. Zobel, H. G. Krane, W. Morgenroth, P. Luger, *Science* **1998**, 279, 356-358; f) F. K. Larsen, *Acta Crystallogr. B* **1995**, 51, 468-482; g) M. J. Hardie, K. Kirschbaum, A. Martin, A. A. Pinkerton, *J. Appl. Crystallogr.* **1998**, 31, 815-817.
- [7] a) A. Martin, A. A. Pinkerton, *Acta Crystallogr. B* **1998**, 54, 471-477; b) B. B. Iversen, F. K. Larsen, A. A. Pinkerton, A. Martin, A. Darovsky, P. A. Reynolds, *Acta Crystallogr. B* **1999**, 55, 363-374.
- [8] J. J. Demarco, R. J. Weiss, *Phys. Rev.* **1965**, 1, 1869-1871.
- [9] B. Dawson, *Proc. R. Soc. Lon. Ser. A* **1967**, 298, 255-263.
- [10] Kurkisuo.K, *Acta Crystallogr. A* **1968**, A 24, 379-390.
- [11] a) R. F. Stewart, *J. Chem. Phys.* **1968**, 48, 4882-4889; b) R. F. Stewart, *J. Chem. Phys.* **1969**, 51, 4569-4577; c) R. F. Stewart, *J. Chem. Phys.* **1973**, 58, 1668-1676.
- [12] F.L. Hirshfeld, *Acta Crystallogr. B* **1971**, B 27, 769-781.
- [13] N. K. Hansen, P. Coppens, *Acta Crystallogr. A* **1978**, 34, 909-921.
- [14] P. Coppens, *Angew. Chem. Int. Edit.* **2005**, 44, 6810-6811.
- [15] P. Hohenberg, W. Kohn, *Phys. Rev. B* **1964**, 136, 864-871.
- [16] a) R. F. W. Bader, P. J. Macdougall, C. D. H. Lau, *J. Am. Chem. Soc.* **1984**, 106, 1594-1605; b) R. F. W. Bader, P. J. Macdougall, *J. Am. Chem. Soc.* **1985**, 107, 6788-6795; c) K. B. Wiberg, R. F. W. Bader, C. D. H. Lau, *J. Am. Chem. Soc.* **1987**, 109, 985-1001; d) R. F. W. Bader, R. J. Gillespie, P. J. Macdougall, *J. Am. Chem. Soc.* **1988**, 110, 7329-7336.
- [17] R. F. W. Bader, *Atoms in molecules: a quantum theory*, Clarendon Press, Oxford, **1990**.
- [18] P. Coppens, D. Feil, *NATO ASI Ser. Ser. B* **1991**, 250, 7-22.
- [19] A. Volkov, Y. Abramov, P. Coppens, C. Gatti, *Acta Crystallogr. A* **2000**, 56, 332-339.
- [20] A. Fischer, D. Tiana, W. Scherer, K. Batke, G. Eickerling, H. Svendsen, N. Bindzus, B. B. Iversen, *J. Phys. Chem. A* **2011**, 115, 13061-13071.
- [21] a) Z. W. Lu, A. Zunger, A. G. Fox, *Acta Metall. Mater.* **1994**, 42, 3929-3943; b) W. Jauch, M. Reehuis, *Acta Crystallogr. A* **2005**, 61, 411-417; c) Z. W. Lu, S. H. Wei, A. Zunger, *Acta Metall. Mater.* **1992**, 40, 2155-2165; d) A. Ohno, S. Sasaki, E. Nishibori, S. Aoyagi, M. Sakata, B. B. Iversen, *Phys. Rev. B* **2007**, 76, 064119; e) P. K. Lam, M. L. Cohen, *Phys. Rev. B* **1981**, 23, 6371-6376; f) V. Tsirelson, A. Stash, M. Kohout, H. Rosner, H. Mori, S. Sato,

- S. Lee, A. Yamamoto, S. Tajima, Y. Grin, *Acta Crystallogr. B* **2003**, *59*, 575-583; g) T. Ohba, Y. Kitano, Y. Komura, *Acta Crystallogr. C* **1984**, *40*, 1-5.
- [22] a) A. I. Baranov, *From the electron density to electron pairing, localizability and chemical bonding*, DFG-SPP 1178, **2010**; b) J. P. Perdew, Y. Wang, *Phys. Rev. B* **1992**, *45*, 13244-13249; c) Program Elk, version 1.0.00, <http://elk.sourceforge.net>, **2010**; d) M. Kohout, Program DGrid, version 4.6, Radebeul, Germany.
- [23] a) N. N. Greenwood, A. Earnshaw, *Chemistry of the elements*, 2nd ed., Butterworth-Heinemann, Oxford; Boston, **1997**; b) D. Emin, *Boron-rich solids*, American Institute of Physics, New York, **1991**.
- [24] S. Lassoued, R. Gautier, A. Boutarfaia, J. F. Halet, *J. Organomet. Chem.* **2010**, *695*, 987-993.
- [25] a) H. J. Juretschke, R. Steinitz, *J. Phys. Chem. Solids* **1958**, *4*, 118-127; b) R. Kiessling, *Acta Chem. Scand.* **1950**, *4*, 209-227; c) R. Kiessling, *Powd. Metallurg. Bull.* **1950**, *3*, 177-184; d) D. A. Robins, *Powd. Metallurg. Bull.* **1958**, *2*, 172-176; e) E. Dempsey, *Philos. Mag.* **1963**, *8*, 285-299; f) J. Callaway, *Phys. Rev.* **1961**, *121*, 1351-1354; g) Y. S. Tyan, L. E. Toth, Y. A. Chang, *J. Phys. Chem. Solids* **1969**, *30*, 785-792.
- [26] a) A. H. Silver, P. J. Bray, *J. Chem. Phys.* **1960**, *32*, 288-292; b) A. H. Silver, T. Kushida, *J. Chem. Phys.* **1963**, *38*, 865-872; c) R. W. Johnson, A. H. Daane, *J. Chem. Phys.* **1963**, *38*, 425-432; d) H. Krebs, *Acta Crystallogr.* **1956**, *9*, 95-99; e) D. W. Fischer, W. L. Baun, *J. Appl. Phys.* **1968**, *39*, 4757-4777; f) S. A. Nemnonov, A. Z. Menshiko, K. M. Kolobova, E. Z. Kurmayev, V. A. Trapeznii, *T. Met. Soc. Aime.* **1969**, *245*, 1191-1198; g) L. Ramqvist, B. Ekstig, E. Kallne, E. Noreland, R. Manne, *J. Phys. Chem. Solids* **1969**, *30*, 1849-1860; h) L. Ramqvist, K. Hamrin, G. Johansson, A. Fahlman, C. Nordling, *J. Phys. Chem. Solids* **1969**, *30*, 1835-1847.
- [27] G. V. Samsonov, Y. M. Goryachev, E. B. A. Kovenskaya, Y. Telnikov, *Sov. Phys. J.* **1972**, *15*, 809-813.
- [28] Y. M. Goryachev, B. O. Kovenskaya, G. V. Samsonov, *Izv. Vuz. Fiz.* **1974**, *8*, 35-41.
- [29] a) R. M. Minyaev, R. Hoffmann, *Chem. Mater.* **1991**, *3*, 547-557; b) B. D. Hanson, M. Mahnig, L. E. Toth, *Z. Naturforsch. Pt. A* **1971**, *26*, 739-746; c) A. Kohm, H. Merz, *Phys. Status Solidi B* **1974**, *61*, 147-161.
- [30] a) J. Etourneau, J. P. Mercurio, R. Naslain, P. Hagenmuller, *J. Sol. State Chem.* **1970**, *2*, 332-338; b) R. W. Mar, N. D. Stout, *J. Chem. Phys.* **1972**, *57*, 5342-5349; c) I. Fischerhjalmar, S. Flodmark, *J. Chem. Phys.* **1954**, *22*, 1950-1950; d) H. C. Longuethiggins, M. D. Roberts, *Proc. R. Soc. Lon. Ser. A* **1954**, *224*, 336-347; e) S. Flodmark, *Ark. Fys.* **1959**, *14*, 513-550; f) W. N. Lipscomb, D. Britton, *J. Chem. Phys.* **1960**, *33*, 275-280; g) V. V. Odintsov, Y. B. Paderno, Y. M. Goryachev, *Zh. Strukt. Khim.* **1971**, *12*, 323-325; h) Z. Fisk, R. N. Castella, P. H. Schmidt, A. S. Cooper, *Mater. Res. Bull.* **1972**, *7*, 285-88.
- [31] a) Y. Yu, L. E. Tergenius, T. Lundstrom, S. Okada, *J. Alloy. Compd.* **1995**, *221*, 86-90; b) A. B. Riabov, V. A. Yartys, B. C. Hauback, P. W. Guegan, G. Wiesinger, I. R. Harris, *J. Alloy. Compd.* **1999**, *295*, 93-100.
- [32] E. Rudy, F. Benesovsky, L. Toth, *Z. Metallkd.* **1963**, *54*, 345-353.
- [33] V. I. Matkovich, *Boron and refractory borides*, Springer-Verlag, Berlin; New York, **1977**.
- [34] J. Nagamatsu, N. Nakagawa, T. Muranaka, Y. Zenitani, J. Akimitsu, *Nature* **2001**, *410*, 63-64.
- [35] a) A. F. Guillermet, G. Grimvall, *J. Less-Common Met.* **1991**, *169*, 257-281; b) G. E. Grechnev, N. V. Ushakova, P. D. Kervalishvili, G. G. Kvachantiradze, K. S. Kharebov, *Low Temp. Phys.* **1997**, *23*, 217-219; c) D. C. Tian, X. B. Wang, *J. Phys. Condens. Mat.* **1992**, *4*,

- 8765-8772; d) S. H. Liu, L. Kopp, W. B. England, H. W. Myron, *Phys. Rev. B* **1975**, *11*, 3463-3468; e) P. Vajeeston, P. Ravindran, C. Ravi, R. Asokamani, *Phys. Rev. B* **2001**, *63*, 045115; f) W. Chen, J. Z. Jiang, *Solid State Commun.* **2010**, *150*, 2093-2096; g) N. Hamdad, N. Benosman, B. Bouhafs, *Physica B* **2010**, *405*, 540-546; h) V. A. Gasparov, N. S. Sidorov, I. I. Zver'kova, M. P. Kulakov, *Jetp. Lett.* **2001**, *73*, 532-535.
- [36] a) Y. F. Han, Y. B. Dai, D. Shu, J. Wang, B. D. Sun, *J. Alloy. Compd.* **2007**, *438*, 327-331; b) B. Mouffok, H. Feraoun, H. Aourag, *Mater. Lett.* **2006**, *60*, 1433-1436; c) P. G. Perkins, A. V. J. Sweeney, *J. Less-Common Met.* **1976**, *47*, 165-173.
- [37] a) A. L. Ivanovskii, *Phys. Solid State* **2003**, *45*, 1829-1859; b) J. Kortus, *Physica C* **2007**, *456*, 54-62; c) N. I. Medvedeva, A. L. Ivanovskii, J. E. Medvedeva, A. J. Freeman, *Phys. Rev. B* **2001**, *64*, 020502; d) G. Satta, G. Profeta, F. Bernardini, A. Continenza, S. Massidda, *Phys. Rev. B* **2001**, *64*, 104507; e) T. Oguchi, *J. Phys. Soc. Jpn.* **2002**, *71*, 1495-1500; f) P. Ravindran, P. Vajeeston, R. Vidya, A. Kjekshus, H. Fjellvag, *Phys. Rev. B* **2001**, *64*, 224509; g) I. R. Shein, N. I. Medvedeva, A. L. Ivanovskii, *Phys. Solid State* **2001**, *43*, 2213-2218.
- [38] a) A. Cely, L. E. Tergenius, T. Lundstrom, *J. Less-Common Met.* **1978**, *61*, 193-198; b) G. Levchenko, A. Lyashchenko, V. Baumer, A. Evdokimova, V. Filippov, Y. Paderno, N. Shitsevalova, *J. Solid. State Chem.* **2006**, *179*, 2949-2953.
- [39] S. Okada, T. Atoda, I. Higashi, Y. Takahashi, *Nippon Kagaku Kaishi* **1985**, 1-8.
- [40] B. Terlan, L. Akselrud, A. I. Baranov, H. Borrmann, Y. Grin, **2012** (unpublished results).
- [41] a) A. Serquis, Y. T. Zhu, E. J. Peterson, J. Y. Coulter, D. E. Peterson, F. M. Mueller, *Appl. Phys. Lett.* **2001**, *79*, 4399-4401; b) D. G. Hinks, J. D. Jorgensen, H. Zheng, S. Short, *Physica C* **2002**, *382*, 166-176; c) R. A. Ribeiro, S. L. Bud'ko, C. Petrovic, P. C. Canfield, *Physica C* **2003**, *385*, 16-23; d) O. Perner, J. Eckert, W. Hassler, C. Fischer, J. Acker, T. Gemming, G. Fuchs, B. Holzapfel, L. Schultz, *J. Appl. Phys.* **2005**, *97*, 056105.
- [42] a) I. Loa, K. Kunc, K. Syassen, P. Bouvier, *Phys. Rev. B* **2002**, *66*, 134101; b) U. Burkhardt, V. Gurin, F. Haarmann, H. Borrmann, W. Schnelle, A. Yaresko, Y. Grin, *J. Solid State Chem.* **2004**, *177*, 389-394.
- [43] A. Yamamoto, C. Takao, T. Masui, M. Izumi, S. Tajima, *Physica C* **2002**, *383*, 197-206.
- [44] S. M. Kazakov, R. Puzniak, K. Rogacki, A. V. Mironov, N. D. Zhigadlo, J. Jun, C. Soltmann, B. Batlogg, J. Karpinski, *Phys. Rev. B* **2005**, *71*, 024533.
- [45] a) I. Higashi, Y. Takahashi, T. Atoda, *J. Cryst. Growth* **1976**, *33*, 207-211; b) I. Higashi, Y. Takahashi, S. Okada, *J. Less-Common Met.* **1986**, *123*, 277-283; c) S. Okada, T. Atoda, I. Higashi, Y. Takahashi, *J. Mater. Sci.* **1987**, *22*, 2993-2999; d) H. Klesnar, T. L. Aselage, B. Morosin, G. H. Kwei, A. C. Lawson, *J. Alloy. Compd.* **1996**, *241*, 180-186; e) E. Storms, B. Mueller, *J. Phys. Chem.* **1977**, *81*, 318-324; f) I. R. Shein, A. L. Ivanovskii, *Phys. Rev. B* **2006**, *73*, 144108; g) K. Kudaka, K. Lizumi, T. Sasaki, S. Okada, *J. Alloy. Compd.* **2001**, *315*, 104-107; h) S. A. Kuznetsov, S. V. Kuznetsova, E. Rebrov, M. J. M. Mies, K. de Croon, J. C. Schouten, *Surf. Coat. Tech.* **2005**, *195*, 182-188.
- [46] G. P. Shveikin, A. L. Ivanovskii, *Usp. Khim.* **1994**, *63*, 751-775.
- [47] A. L. Ivanovskii, I. R. Shein, N. I. Medvedeva, *Russ. Chem. Rev.* **2008**, *77*, 467-486.
- [48] M. Born, *Zeitschrift Für Physik* **1926**, *A 38*, 803-827.
- [49] W. R. Busing, H. A. Levy, *Acta Crystallogr.* **1957**, *10*, 180-182.
- [50] W. Massa, *Crystal structure determination*, 2nd ed., Springer, Berlin; New York, **2004**.
- [51] W. H. Zachariasen, *Theory of X-ray diffraction in crystals*, J. Wiley & Sons, Chapman & Hall, Ltd., New York, London, **1945**.

- [52] C. G. Darwin, *Philos. Mag.* **1922**, *43*, 800-829.
- [53] W.H. Zachariasen, *Acta Crystallogr. A* **1967**, *23*, 558-564
- [54] S. A. Werner, *Acta Crystallogr. A* **1969**, *A 25*, 639
- [55] J. L. Lawrence, *Acta Crystallogr. A* **1972**, *A 28*, 400-404
- [56] a) P. J. Becker, P. Coppens, *Acta Crystallogr. A* **1974**, *A 30*, 129-147; b) P. J. Becker, P. Coppens, *Acta Crystallogr. A* **1974**, *A 30*, 148-153; c) P. Becker, *Acta Crystallogr. A* **1977**, *33*, 243-249.
- [57] P. J. Becker, P. Coppens, *Acta Crystallogr. A* **1975**, *31*, 417-425.
- [58] H. R. Hoche, H. Schulz, H. P. Weber, A. Belzner, A. Wolf, R. Wulf, *Acta Crystallogr. A* **1986**, *42*, 106-110.
- [59] B. Raghoeamachar, G. Dhanaraj, J. Bai, M. Dudley, *Microsc. Res. Techniq.* **2006**, *69*, 343-358.
- [60] a) J. M. Cowley, D. J. Smith, *Acta Crystallogr. A* **1987**, *43*, 737-751; b) R. F. Klie, Y. Zhu, *Micron* **2005**, *36*, 219-231; c) M. Dudley, J. Bai, X. Huang, W. M. Vetter, G. Dhanaraj, B. Raghoeamachar, *Mat. Sci. Semicon. Proc.* **2006**, *9*, 315-322.
- [61] a) W. Cochran, *Acta Crystallogr. A* **1969**, *25*, 95-101; b) J. Harada, M. Sakata, *Acta Crystallogr. A* **1974**, *A 30*, 77-82; c) E. D. Stevens, *Acta Crystallogr. A* **1974**, *A 30*, 184-189.
- [62] R. H. Blessing, *Crystallogr. Rev.* **1987**, *1*, 3-58.
- [63] a) M. L. Crow, G. Schupp, W. B. Yelon, J. G. Mullen, A. Djedid, *Acta Crystallogr. A* **1987**, *43*, 638-645; b) C. Ghezzi, A. Merlini, S. Pace, *Nuovo Cimento B* **1969**, *64*, 103-116; c) Y. Kashiwase, M. Minoura, *Jpn. J. Appl. Phys.* **2** **1983**, *22*, L49-L51; d) K. Krec, W. Steiner, P. Pongratz, P. Skalicky, *Acta Crystallogr. A* **1984**, *40*, 465-468.
- [64] N. Nilsson, *Ark. Fys.* **1957**, *12*, 247-257.
- [65] P. Coppens, T. N. Gururrow, P. Leung, E. D. Stevens, P. J. Becker, Y. W. Yang, *Acta Crystallogr. A* **1979**, *35*, 63-72.
- [66] R. F. Stewart, *Israel J. Chem.* **1977**, *16*, 124-131.
- [67] D. M. Collins, *Nature* **1982**, *298*, 49-51.
- [68] a) S. van Smaalen, J. Netzel, *Phys Scripta* **2009**, *79*, 048304; b) L. Palatinus, S. van Smaalen, *Acta Crystallogr. A* **2002**, *58*, 559-567.
- [69] B. Dittrich, C. B. Hubschle, J. J. Holstein, F. P. A. Fabbiani, *J. Appl. Crystallogr.* **2009**, *42*, 1110-1121.
- [70] G. A. Jeffrey, D. W. J. Cruickshank, *Q. Rev. Chem. Soc.* **1953**, *7*, 335-376.
- [71] a) B. M. Craven, R. K. McMullan, *Acta Crystallogr. B* **1979**, *35*, 934-945; b) C. Scherlinger, A. Kutoglu, D. Mullen, *Acta Crystallogr. A* **1978**, *34*, 481-483.
- [72] P. Coppens, *Angew. Chem. Int. Edit.* **1977**, *16*, 32-40.
- [73] a) J. M. Savariault, M. S. Lehmann, *J. Am. Chem. Soc.* **1980**, *102*, 1298-1303; b) J. D. Dunitz, P. Seiler, *J. Am. Chem. Soc.* **1983**, *105*, 7056-7058.
- [74] W. J. Hehre, *Ab initio molecular orbital theory*, Wiley, New York, **1986**.
- [75] a) G. R. Runtz, R. F. W. Bader, R. R. Messer, *Can. J. Chem.* **1977**, *55*, 3040-3045; b) R. F. W. Bader, S. G. Anderson, A. J. Duke, *J. Am. Chem. Soc.* **1979**, *101*, 1389-1395.
- [76] D. Cremer, E. Kraka, T. S. Slee, R. F. W. Bader, C. D. H. Lau, T. T. Nguyendang, P. J. Macdougall, *J. Am. Chem. Soc.* **1983**, *105*, 5069-5075.
- [77] H. Hopf, *Math. Ann.* **1927**, *96*, 209-224.



- [78] K. Collard, C. G. Hall, *Int. J. Quantum Chem.* **1977**, *12*, 623-637.
- [79] K. Meindl, R. Herbst-Irmer, J. Henn, *Acta Crystallogr. A* **2010**, *66*, 362-371.
- [80] P. Macchi, A. Sironi, *Coordin. Chem. Rev.* **2003**, *238*, 383-412.
- [81] C. Gatti, *Z. Kristallogr.* **2005**, *220*, 399-457.
- [82] a) R. P. Sagar, A. C. T. Ku, V. H. Smith, A. M. Simas, *J. Chem. Phys.* **1988**, *88*, 4367-4374; b) Z. Shi, R. J. Boyd, *J. Chem. Phys.* **1988**, *88*, 4375-4377.
- [83] D. A. Kirzhnits, *Sov. Phys. JETP-USSR* **1957**, *5*, 64-71.
- [84] R. F. W. Bader, P. M. Beddall, *J. Chem. Phys.* **1972**, *56*, 3320-3330.
- [85] a) R. F. W. Bader, H. Essen, *J. Chem. Phys.* **1984**, *80*, 1943-1960; b) R. F. W. Bader, *J. Phys. Chem. A* **1998**, *102*, 7314-7323.
- [86] D. Cremer, E. Kraka, *Angew. Chem. Int. Edit.* **1984**, *23*, 627-628.
- [87] a) C. Jelsch, V. Pichon-Pesme, C. Lecomte, A. Aubry, *Acta Crystallogr. D* **1998**, *54*, 1306-1318; b) B. Dittrich, T. Koritsanszky, P. Luger, *Angew. Chem. Int. Edit.* **2004**, *43*, 2718-2721; c) B. Dittrich, T. Koritsanszky, M. Grosche, W. Scherer, R. Flaig, A. Wagner, H. G. Krane, H. Kessler, C. Riemer, A. M. M. Schreurs, P. Luger, *Acta Crystallogr. B* **2002**, *58*, 721-727; d) B. Dittrich, S. Scheins, C. Paulmann, P. Luger, *J. Phys. Chem. A* **2003**, *107*, 7471-7474; e) B. Dittrich, C. B. Hubschle, M. Messerschmidt, R. Kalinowski, D. Girnt, P. Luger, *Acta Crystallogr. A* **2005**, *61*, 314-320; f) B. Dittrich, P. Munshi, M. A. Spackman, *Acta Crystallogr. B* **2007**, *63*, 505-509; g) V. Pichonpesme, C. Lecomte, H. Lachekar, *J. Phys. Chem.* **1995**, *99*, 6242-6250; h) R. Wiest, V. Pichonpesme, M. Benard, C. Lecomte, *J. Phys. Chem.* **1994**, *98*, 1351-1362; i) J. A. Ibers, W. A. Hamilton, *International Tables for X-ray Crystallography* **1974**, Vol IV, Birmingham: Kynoch; j) C. P. Brock, J. D. Dunitz, F. L. Hirshfeld, *Acta Crystallogr. B* **1991**, *47*, 789-797; k) P. Luger, *Org. Biomol. Chem.* **2007**, *5*, 2529-2540; l) P. M. Dominiak, A. Volkov, X. Li, M. Messerschmidt, P. Coppens, *J. Chem. Theory Comput.* **2007**, *3*, 232-247; m) A. Volkov, M. Messerschmidt, P. Coppens, *Acta Crystallogr. D* **2007**, *63*, 160-170.
- [88] P. Coppens, *X-ray charge densities and chemical bonding*, International Union of Crystallography; Oxford University Press, Chester, England, **1997**.
- [89] a) P. Groenew, J. Zeevalki, D. Feil, *Acta Crystallogr. A* **1971**, *27*, 487-491; b) J. Bentley, R. F. Stewart, *Acta Crystallogr. A* **1974**, *30*, 60-67.
- [90] Z. W. Su, P. Coppens, *Acta Crystallogr. A* **1992**, *48*, 188-197.
- [91] K. E. Spear, P. K. Liao, J. F. Smith, *V-B (Vanadium-Boron) Binary alloy Phase Diagrams, Vol. 1*, second ed., ASM International, Materials Park, Ohio, **1990**.
- [92] a) K. E. Spear, P. W. Gilles, *High Temp. Sci.* **1969**, *1*, 86-97; b) E. Rudy, S. Windisch, *Wright-Patterson Air Force Base, OH* **1966**, Part I, Vol. X, 330-334; c) H. Nowotny, F. Benesovsky, R. Kieffer, *Z. Metallkd.* **1959**, *50*, 258-261.
- [93] W. Rostoker, A. Yamamoto, *T. Am. Soc. Met.* **1954**, *46*, 1136-1167.
- [94] H. Blumenthal, *J. Am. Chem. Soc.* **1952**, *74*, 2942-2942.
- [95] B. B. de Lima, C. A. Nunes, G. C. Coelho, P. A. Suzuki, P. Rogl, *J. Phase Equilib. Diff.* **2004**, *25*, 134-139.
- [96] J. T. Norton, H. Blumenthal, S. J. Sindeband, *T. Am. I. Min. Met. Eng.* **1949**, *185*, 749-751.
- [97] R. Kieffer, F. Benesovsky, E. R. Honak, *Z. Anorg. Allg. Chem.* **1952**, *268*, 191-200.
- [98] B. Post, F. W. Glaser, D. Moskowitz, *Acta Metall. Mater.* **1954**, *2*, 20-25.

- [99] C. A. Nunes, B. B. de Lima, G. C. Coelho, P. Rogl, P. A. Suzuki, *J. Alloy. Compd.* **2004**, *370*, 164-168.
- [100] K. E. Spear, J. H. Blanks, M. S. Wang, *J. Less-Common Met.* **1981**, *82*, 237-243.
- [101] P. Peshev, L. Leyarovs, G. Bliznako, *J. Less-Common Met.* **1968**, *15*, 259-267.
- [102] J. J. Zuckerman, J. J., Hagen, A. P., Inorganic reactions and methods, Vol. 2, The formation of bonds to hydrogen Thompson, *Chem. Brit.* **1971**, *7*, 140.
- [103] a) M. F. Garbauskas, J. S. Kasper, G. A. Slack, *J. Solid State Chem.* **1986**, *63*, 424-430; b) Y. Wang, X. Y. Guang, Y. L. Cao, X. P. Ai, H. X. Yang, *J. Alloy. Compd.* **2010**, *501*, L12-L14; c) C. Bulfon, A. LeitheJasper, H. Sassik, P. Rogl, *J. Solid State Chem.* **1997**, *133*, 113-116.
- [104] Cueiller.J, G. Lahet, F. Thevenot, R. A. Paris, *J. Less-Common Met.* **1971**, *24*, 317.
- [105] I. E. Campbell, C. F. Powell, D. H. Nowicki, B. W. Gonser, *J. Electrochem. Soc.* **1949**, *96*, 318-333.
- [106] a) L. Rao, E. G. Gillan, R. B. Kaner, *J. Mater. Res.* **1995**, *10*, 353-361; b) L. A. Shi, Y. Gu, L. Y. Chen, Z. H. Yang, J. H. Ma, Y. T. Qian, *Mater. Lett.* **2004**, *58*, 2890-2892; c) J. W. Kim, J. H. Shim, J. P. Ahn, Y. W. Cho, J. H. Kim, K. H. Oh, *Mater. Lett.* **2008**, *62*, 2461-2464.
- [107] M. G. Kanatzidis, R. Pottgen, W. Jeitschko, *Angew. Chem. Int. Edit.* **2005**, *44*, 6996-7023.
- [108] a) R. Kieffer, Rassaert.H, O. Schob, *Monatsh. Chem. Verw. Tl.* **1965**, *96*, 685-694; b) G. Jangg, R. Kieffer, *Monatsh. Chem.* **1973**, *104*, 226-233; c) G. Jangg, A. Blaha, T. Sultan, R. Kieffer, *Z. Metallkd.* **1972**, *63*, 671-676; d) G. Jangg, R. Kieffer, L. Usner, *J. Less-Common Met.* **1968**, *14*, 269-277.
- [109] a) S. Okada, K. Kudou, I. Higashi, Lundstro.T, *Proc. 11th Int. Symp. Boron, Borides and Related Compounds, Tsukuba* **1993**, *JJAP Series 10*, 132-135; b) S. Okada, T. Atoda, *Nippon Kagaku Kaishi* **1984**, 416-421.
- [110] a) G. V. Samsonov, V. A. Neronov, L. K. Lamikhov, *J. Less-Common Met.* **1979**, *67*, 291-296; b) O. N. Carlson, *Al-B (Aluminium-Boron) Binary alloy Phase Diagrams, Vol. 1*, sec. ed., ASM International, Materials Park, Ohio, **1990**.
- [111] N.N. Greenwoo, R. V. Parish, P. Thornton, *Q. Rev. Chem. Soc.* **1966**, *20*, 441-464.
- [112] a) N.N. Greenwoo, R. V. Parish, P. Thornton, *J. Chem. Soc.* **1965**, 545-549; b) L. Andrieux, *Ann. Chim. France* **1929**, *11*, 423-507.
- [113] M. A. Dewan, M. A. Rhamdhani, J. B. Mitchell, C. J. Davidson, G. A. Brooks, M. Easton, J. F. Grandfield, C. Crc, *Mater. Sci. Forum* **2011**, *693*, 149-160.
- [114] L. G. Akselrud, Y. P. Zavalii, Y. N. Grin, V. K. Pecharskii, B. Baumgartner, W. E., *Mater. Sci. Forum* **1993**, *133-136*, 335-342.
- [115] C. R. Hubbard, *J. Appl. Crystallogr.* **1983**, *16*, 285-288.
- [116] H. Bolmgren, T. Lundstrom, L. E. Tergenius, S. Okada, I. Higashi, *J. Less-Common Met.* **1990**, *161*, 341-345.
- [117] R. H. Blessing, *J. Appl. Crystallogr.* **1986**, *19*, 412-412.
- [118] R. H. Blessing, *Crystallogr. Rev.* **1987**, *1*, 3-58.
- [119] J. D. Dunitz, Verlag Helvetica Chimica Acta; VCH, Basel Weinheim; Cambridge, **1995**.
- [120] P. R. Mallinson, T. Koritsanszky, E. Elkaim, N. Li, P. Coppens, *Acta Crystallogr. A* **1988**, *44*, 336-342.
- [121] H. B. Burgi, S. C. Capelli, H. Birkedal, *Acta Crystallogr. A* **2000**, *56*, 425-435.

- [122] a) S. Mohr, H. Müller-Buschbaum, Y. Grin, H. G. von Schnering, *Z. Anorg. Allg. Chem.* **1996**, 622, 1035-1037; b) G. Will, *J. Solid State Chem.* **2004**, 177, 628-631.
- [123] S. Okada, T. Atoda, I. Higashi, *J. Solid State Chem.* **1987**, 68, 61-67.
- [124] a) R. Kiessling, *Acta Chem. Scand.* **1949**, 3, 603-615; b) R. Kiessling, *Acta Chem. Scand.* **1950**, 4, 146-159.
- [125] L. Pauling, *J. Am. Chem. Soc.* **1947**, 69, 542-553.
- [126] a) D. Moskowitz, *T. Am. I. Min. Met. Eng.* **1956**, 206, 1325-1325; b) Y. Kuz'ma, P. K. Starodub, *Inorg. Mater.* **1973**, 9, 337-340; c) Y. Kuz'ma, V. S. Telegus, K. D.A., *Sov. Powder Metall. Met. Ceram.* **1969**, 8, 403-410.
- [127] M. Elfstroem, *Acta Chem. Scand.* **1961**, 15, 1178.
- [128] A. Stash, V. Tsirelson, *J. Appl. Crystallogr.* **2002**, 35, 371-373.
- [129] A. Volkov, P. Macchi, L. J. Farrugia, C. Gatti, P. Mallinson, T. Richter, T. Koritsanszky, "XD2006 - A computer program for multipole refinement, topological analysis of charge densities and evaluation of intermolecular interaction energies from experimental and theoretical structure factors", **2006**.
- [130] C. Roetti, E. Clementi, *Atomic Data and Nuclear Data Tables* **1974**, 14, 177-478.
- [131] A. M. Pendas, A. Costales, V. Luana, *Phys. Rev. B* **1997**, 55, 4275-4284.
- [132] N. I. Medvedeva, A. L. Ivanovskii, J. E. Medvedeva, A. J. Freeman, D. L. Novikov, *Phys. Rev. B* **2002**, 65, 052501.
- [133] A. L. Ivanovskii, I. R. Shein, N. I. Medvedeva, *Usp. Khim.* **2008**, 77, 491-511.
- [134] J. L. Murray, P. K. Liao, J. F. Smith, *B-Ti (Boron-Titanium) Binary alloy Phase Diagrams, Vol. I*, sec. ed., ASM International, Materials Park, Ohio, **1990**.
- [135] L. Barton, D. Nicholls, *J. Inorg. Nucl. Chem.* **1966**, 28, 1367-1372.
- [136] a) B. Shahbahrani, R. S. Maamoori, N. Ehsani, *Mater. Sci-Poland* **2007**, 25, 719-731; b) J. Y. Lok, K. V. Logan, J. J. Payyapilly, *J. Am. Ceram. Soc.* **2009**, 92, 26-31.
- [137] R. L. Axelbaum, D. P. DuFaux, C. A. Frey, K. F. Kelton, S. A. Lawton, L. J. Rosen, S. M. L. Sastry, *J. Mater. Res.* **1996**, 11, 948-954.
- [138] a) J. K. Walker, *Adv. Ceram. Mater.* **1988**, 3, 601-604; b) T. Saito, T. Fukuda, H. Maeda, K. Kusakabe, S. Morooka, *J. Mater. Sci.* **1997**, 32, 3933-3938; c) N. J. Welham, *J. Am. Ceram. Soc.* **2000**, 83, 1290-1292.
- [139] a) M. Makyta, V. Danek, G. M. Haarberg, J. Thonstad, *J. Appl. Electrochem.* **1996**, 26, 319-324; b) M. Makyta, T. Utigard, *Light Met.* **1992**, 1137-1144.
- [140] S. E. Bates, W. E. Buhro, C. A. Frey, S. M. L. Sastry, K. F. Kelton, *J. Mater. Res.* **1995**, 10, 2599-2612.
- [141] a) A. Calka, D. Oleszak, *J. Alloy. Compd.* **2007**, 440, 346-348; b) R. Ricceri, P. Matteazzi, *Mat. Sci. Eng. a-Struct.* **2004**, 379, 341-346.
- [142] J. J. Gebhardt, R. F. Cree, *J. Am. Ceram. Soc.* **1965**, 48, 262-268.
- [143] a) L. Kaufman, Sitzungsberichte der math-phys. Klasse der k.-b. Akad. der Wissenschaften zu München B. Uhrenius, D. Birnie, K. Taylor, *Calphad* **1984**, 8, 25-66; b) A. E. Palty, H. Margolin, J. P. Nielsen, *T. Am. Soc. Metal.* **1954**, 46, 312-328; c) D. J. Mcpherson, M. Hansen, *Z. Metallkd.* **1954**, 45, 76-82; d) S. S. Ordanyan, Y. B. Paderno, E. E. Nikolaeva, I. K. Khoroshilova, *Inorg. Mater.* **1984**, 20, 738-739.
- [144] E. Rudy, S. Windisch, *Wright-Patterson Air Force Base, OH* **1966**, Part II, Vol. XIII.
- [145] R. G. Fenish, *NRM* **1964**, 138, 1-37.

- [146] J. Thebault, R. Pailier, G. Bontempsmoley, M. Bourdeau, R. Naslain, *J. Less-Common Met.* **1976**, *47*, 221-233.
- [147] P. Macchi, D. M. Proserpio, A. Sironi, *J. Am. Chem. Soc.* **1998**, *120*, 13429-13435.
- [148] T. Hegenscheidt, *Doctoral Thesis*, Universität Karlsruhe, **1998**.
- [149] a) M. Fujimori, T. Nakata, T. Nakayama, E. Nishibori, K. Kimura, M. Takata, M. Sakata, *Phys. Rev. Lett.* **1999**, *82*, 4452-4455; b) S. Mondal, S. van Smaalen, A. Schonleber, Y. Filinchuk, D. Chernyshov, S. I. Simak, A. S. Mikhaylushkin, I. A. Abrikosov, E. Zarechnaya, L. Dubrovinsky, N. Dubrovinskaia, *Phys. Rev. Lett.* **2011**, *106*, 215502
- [150] F. Corts-Guzman, R. F. W. Bader, *Coordin. Chem. Rev.* **2005**, *249*, 633-662.
- [151] J. Henn, D. Ilge, D. Leusser, D. Stalke, B. Engels, *J. Phys. Chem. A* **2004**, *108*, 9442-9452.
- [152] R. F. W. Bader, D. A. Legare, *Can. J. Chem.* **1992**, *70*, 657-676.
- [153] A. Yamamoto, C. Takao, T. Masui, M. Izumi, S. Tajima, *Physica C* **383** **2002**, 197-206.

### Awards

International Union of Crystallography (IUCR) Poster Prize, 25<sup>th</sup> *European Crystallography Meeting*, August 16-21, **2010**, Istanbul.

### Publications

3. On similarities and differences between the electronic structures of binary vanadium borides.

B.Terlan, L. Akselrud, A. I. Baranov, H. Borrmann, Yu. Grin, *Acta Crystallogr. B* **2013** (submitted).

2. Experimental QTAIM analysis of the electron density in TiB<sub>2</sub>.

B.Terlan, L. Akselrud, A. I. Baranov, H. Borrmann, Yu. Grin, *Z. Anorg. Allg. Chem.*, **2013** (accepted).

1. Monomer reactivity ratios of *N*-isopropylacrylamide-itaconic acid copolymers at low and high conversions.

C. Erbil, B. Terlan, O. Akdemir, A.T. Gökceören, *Eur. Polym. J.*, **2009**, 45, 1728-1737.

### Oral and poster presentations

8. B.Terlan, L. Akselrud, A. I. Baranov, H.Borrmann, Yu. Grin, "On similarities and differences of electronic structure for binary vanadium borides and structural analogues", 15 – 20 September, **2012**, *European Charge Density Meeting 6*, Štrbské Pleso, High Tatras, Slovakia (**Oral**).

7. B.Terlan, L. Akselrud, A. I. Baranov, H.Borrmann, Yu. Grin, "Topological analyses of intermetallic borides from high-resolution single-crystal diffraction data", *International Symposium on Boron, Borides and related Materials*, September 11 – 17, **2011**, Istanbul, Turkey (**Oral**).

6. B.Terlan, L. Akselrud, A. I. Baranov, H.Borrmann, Yu. Grin, "Experimental electron density in intermetallic borides", 26<sup>th</sup> *European Crystallographic Meeting*, 29 – 2 August, **2010**, Darmstadt, Germany (**Oral**).

5. B.Terlan, L. Akselrud, A. I. Baranov, H.Borrmann, Yu. Grin, "Topological Analysis of Vanadium Borides from High Resolution Single-crystal Diffraction Data", 25<sup>th</sup> *European Crystallography Meeting*, August 16 – 21, **2010**, Istanbul, Turkey (**Poster**).

4. B.Terlan, L. Akselrud, A. I. Baranov, H.Borrmann, Yu. Grin, "X-ray charge density analysis of vanadium diboride: A comparison of experiment and theory", July 11 – 16, **2010**, *Gordon Research Conference*, Mount Holyoke College, USA (**Oral**).
3. B.Terlan, L. Akselrud, A. I. Baranov, H.Borrmann, Yu. Grin, "Experimental electron density in vanadium borides and structural analogues", Juni 18 – 21, **2010**, *Baltic Boat Conference*, Stockholm, Sweden (**Oral**).
2. B.Terlan, L. Akselrud, H.Borrmann, Yu. Grin, "Experimental electron density as to key to the understanding of chemical interactions", *DFG meeting*, February 2 – 4, **2009**, Kloster Banz, Germany (**Poster**).
1. B.Terlan, L. Akselrud, H.Borrmann, Yu. Grin, "Electron density and chemical bonding in intermetallic Borides and Structural Analogues", *5<sup>th</sup> European Charge Density Meeting*, June 6 – 11, **2008**, Gravedona, Italy (**Poster**).

## **Versicherung**

Hiermit versichere ich, dass ich die vorliegende Arbeit ohne unzulässige Hilfe Dritter und ohne Benutzung anderer als der angegebenen Hilfsmittel angefertigt habe; die aus fremden Quellen direkt oder indirekt übernommenen Gedanken sind als solche kenntlich gemacht. Die Arbeit wurde bisher weder im Inland noch im Ausland in gleicher oder ähnlicher Form einer anderen Prüfungsbehörde vorgelegt.

Die vorliegende Dissertation wurde unter Betreuung durch Herrn Prof. Juri Grin und Herrn Dr. Horst Borrmann am Max-Planck-Institut für Chemische Physik fester Stoffe in Dresden angefertigt.

Es haben keine früheren erfolglosen Promotionsverfahren stattgefunden.

Ich erkenne die Promotionsordnung der Fakultät Mathematik und Naturwissenschaften der Technischen Universität Dresden vom 23. 02. 2011 in vollem Umfang an.

Dresden, den

A handwritten signature in black ink, appearing to read 'Terlan', with a horizontal line above it.

(Bürgehan Terlan)